Karlsruher Institut für Technologie

Hierarchical imaging of the dynamics during pulsed laser ablation in liquids

Zur Erlangung des akademischen Grades
Doktor der Naturwissenschaften (Dr. rer. nat.)
von der KIT-Fakultät für Physik des
Karlsruher Institut für Technologie (KIT)

genehmigte
Dissertation
von

M. Sc. Stefan Reich

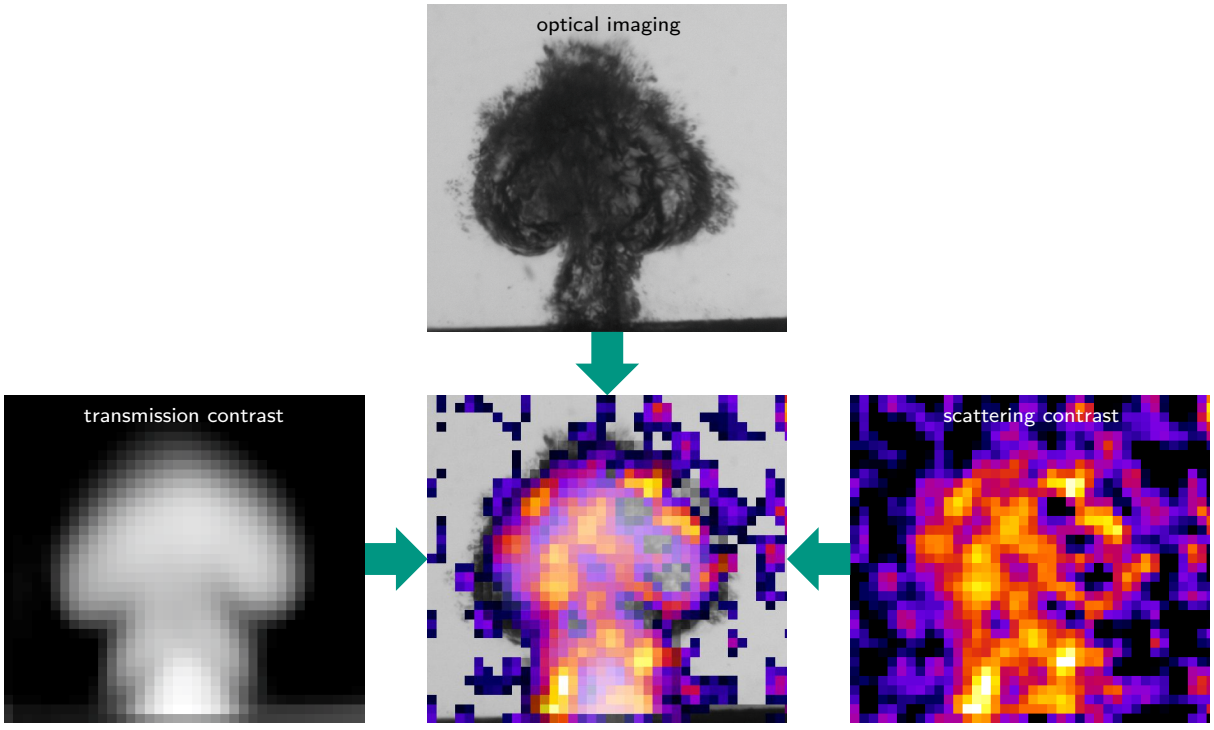

Tag der mündlichen Prüfung:	24. Mai 2019
Referent:	Prof. Dr. Tilo Baumbach
Korreferent:	PD Dr. habil. Anton Plech

”Some people - some companies and some decision makers in particularly - have known exactly what priceless values they are sacrificing to continue making unimaginable amounts of money. And I think many of you who are here today belong to this group of people.”

Greta Thunberg, World Economic Forum 2019

Cover image: Images of optical imaging and X-ray multi-contrast imaging of the first cavitation bubble rebound of an ablation on a free zinc wire with a diameter of 1 mm. The ablation was performed in pure water with a laser of 7 ns pulse duration, a wavelength of 1064 nm and a pulse energy of 11 mJ. The multi-contrast imaging was performed on an imaging beamline of the synchrotron at KIT with a compound array refracting lens as optical element. In optical imaging a predominantly opaque mushroom-like rebound is visible. The X-ray imaging proves that the rebound consists of a vapor cavity containing many microbubbles.

Abstract

With Pulsed Laser Ablation in Liquids (PLAL) it is possible to produce nanoparticles (NPs) that are directly dispersed in liquid and no residual surfactants or reactants do contaminate these NPs. After laser excitation of the target, a millimeter-sized cavitation bubble is formed in which the NPs are confined. Using a series of complementary measurement techniques and *in situ* hierarchical imaging, this work examines the fundamental processes during PLAL.

The laser-matter interaction is investigated by optical imaging of the cavitation bubble and the ignited plasma in combination with absorption spectroscopy. A direct correlation between these three parameters is identified which allows indirect conclusions to be drawn about the ablation process. The incubation effect occurring on pristine targets and the presence of a plasma threshold fluence indicate that efficient ablation requires either pre-irradiated targets or fluences above the threshold. An ablation with low fluences on pristine targets leads to strong loss mechanisms, which results in a strongly reduced energy localization and thus a low ablation rate. It is found that the energy dose required for stable and efficient ablation depends on material parameters such as the Young's modulus and the enthalpy required for material heating and evaporation. As soon as the plasma threshold fluence is exceeded, the material parameters have a minor influence. For nanosecond laser ablation above the threshold, most of the pulse energy is absorbed by the plasma. Below the threshold, the loss mechanisms dominate, which leads to a strongly reduced ablation efficiency.

For the *in situ* detection of NPs during the lifetime of the cavitation bubble X-ray methods are used. The NP size distribution is examined with high temporal resolution by Small-angle X-ray Scattering (SAXS), while Wide-angle X-ray Scattering (WAXS) measures the crystalline domain size. The early appearance of large NPs with large crystal domain sizes confirms the recent models of the ablation process. The multimodal NP size distribution is caused directly by film lift-off and Rayleigh instabilities on the liquid metal surface. Furthermore, the temporal distribution of the NPs confirms that NPs are located at or even in front of the cavitation bubble boundary, as well as the almost homogeneous filling of the bubble with NPs. Two different mechanisms of emergence of large NPs are also identified. Spherical NPs are produced directly from the molten target, while the agglomeration of small NPs occurs mainly during bubble collapse.

A multiplexing of the SAXS measurements to directly obtain a 2D image of the NP distribution is performed by Hartmann mask-like multi-contrast imaging. For this purpose, a broad X-ray beam is divided into a 2D array of beamlets by a custom Hartmann mask respectively the newly developed Compound Array Refractive Lenses (CARLs). The transmission and scattering contrast of this Single-Exposure Multi-Contrast Imaging (SEMCI) technique is used for the hierarchical imaging of the ablation process. The *in situ* quenching capabilities of gold NPs with inorganic electrolytes and macromolecular ligands are investigated. It is found that the quenching mechanisms of the two additives are different. Electrolytes act *in situ* in the cavitation bubble, while ligands do not. By changing the scattering sensitivity from NPs

to the micrometer range, the nature of the first bubble rebound of an ablation on a free wire target is clarified. This detached rebound consists of micrometer-sized bubbles and contains no significant amounts of NPs anymore.

The X-ray efficiency of the SEMCI is improved by replacing the commonly used Hartmann masks with lens arrays. These CARLs are produced by embossing 2D arrays with 100×100 concave lenses in polymer films. The pitches are around 50 µm and the apex radii of the parabolic lenses are around 8 µm. The positioning accuracy of the beamlets is less than 1 µm. By stacking up to six lens array foils, focal lengths between 60 cm and 125 cm are achieved at X-ray energies of 9 keV. The maximum visibility is about 0.5. Beside the NP detection by the scattering contrast, the wavefront distortion of samples or X-ray optics can be analyzed with a resolution of 0.2 µrad.

Kurzfassung

Mittels gepulster Laserablation in Flüssigkeiten (Pulsed Laser Ablation in Liquids, PLAL) ist es möglich, Nanopartikel (NP) herzustellen, die direkt in der Flüssigkeit dispergiert und nicht durch verblie-bene Tenside oder Reaktanden verunreinigt sind. Nach der Laseranregung des Targets bildet sich eine millimetergroße Kavitationsblase, in der die NP verteilt und größtenteils gefangen sind. In dieser Arbeit werden die fundamentalen Prozesse während PLAL mit einer Reihe von komplementären Messtechniken und hierarchischer *in situ* Bildgebung untersucht.

Die Laser-Materie-Wechselwirkung wird durch optische Abbildung der Kavitationsblase und des gezündeten Plasmas in Kombination mit Absorptionsspektroskopie untersucht. Es wird eine direkte Korrelation zwischen diesen drei Parametern gezeigt, die es erlaubt, indirekte Rückschlüsse auf den Ablationsprozess zu ziehen. Der Inkubationseffekt, der bei unversehrten Targets auftritt, und das Vorhandensein einer Plasma-Schwellfluenz zeigen, dass für eine effiziente Ablation entweder vorbestrahlte Targets oder Fluenzen oberhalb der Schwelle erforderlich sind. Eine Ablation mit geringen Fluenzen auf unversehrten Targets führt zu starken Verlustmechanismen, was in einer stark reduzierte Energielokalisation und damit niedrigen Ablationsrate resultiert. Es wird gezeigt, dass die für eine stabile und effiziente Ablation erforderliche Energiedosis von Materialparametern wie dem Elastizitätsmodul und der für die Materialerwärmung und -verdampfung erforderlichen Enthalpie abhängt. Sobald die Plasma-Schwellfluenz überschritten wird, haben die Materialparameter jedoch nur noch einen geringen Einfluss. Bei der Nanosekunden-Laserablation oberhalb der Schwellfluenz wird der größte Teil der Pulsenergie vom Plasma absorbiert. Unterhalb der Schwellfluenz dominieren die Verlustmechanismen, was zu einer stark reduzierten Ablationseffizienz führt.

Für den *in situ* Nachweis von NP während der Lebensdauer der Kavitationsblase werden Röntgenstreumethoden verwendet. Die NP-Größenverteilung wird mit hoher zeitlicher Auflösung mittels Röntgen-Kleinwinkelstreuung (Small-angle X-ray Scattering, SAXS) untersucht, während Röntgen-Weitwinkelstreuung (Wide-angle X-ray Scattering, WAXS) zur Messung der kristallinen Domänengröße verwendet wird. Das frühe Auftreten von großen NP mit großen Kristalldomänengrößen bestätigt die jüngsten Modelle des Ablationsprozesses. Die multimodale NP-Größenverteilung wird direkt durch Filmabhebung und Rayleigh-Instabilitäten auf der flüssigen Metalloberfläche hervorgerufen. Darüber hinaus bestätigt die zeitliche Verteilung der NP, dass sich NP an oder sogar vor der Kavitationsblasengrenze befinden, sowie die nahezu homogene Füllung der Blase mit NP. Zwei verschiedene Mechanismen der Entstehung von großen NP werden ebenfalls identifiziert. Sphärische NP entstehen direkt aus der Schmelze, während die Agglomeration von kleinen NP hauptsächlich während des Blasenkollapses stattfindet.

Ein Multiplexing der SAXS-Messungen, um direkt ein 2D-Bild der NP-Verteilung zu erhalten, erfolgt durch Hartmann-Blenden artiger Multikontrast-Bildgebung. Zu diesem Zweck wird ein breiter Röntgenstrahl durch eine maßgeschneiderte Hartmann-Blende beziehungsweise die neu entwickelten gestapelten

Röntgenlinsenarrays (Compound Array Refractive Lenses, CARLs) in ein 2D-Array von Teilstrahlen aufgeteilt. Für die hierarchische Abbildung des Ablationsprozesses werden die Kontraste Transmission und Streuung dieser Einzelbild Multikontrast-Bildgebung (Single-Exposure Multi-Contrast Imaging, SEMCI) verwendet. Die *in situ* Größenreduktion von NP aus Gold mit anorganischen Elektrolyten und makromolekularen Liganden wird untersucht. Es wird gezeigt, dass die Mechanismen der Größenreduktion der beiden Additive unterschiedlich sind. Elektrolyte wirken *in situ* in der Kavitationsblase, während Liganden dies nicht tun. Durch die Änderung der Streuempfindlichkeit von NP auf den Mikrometerbereich wird die Zusammensetzung der zweiten Blasenoszillation einer Ablation an einem freien Draht geklärt. Diese vom Draht losgelöste zweite Oszillation besteht aus mikrometergroßen Blasen und enthält keine signifikanten Mengen an NP mehr.

Die Röntgeneffizienz der SEMCI wird verbessert, indem die üblicherweise verwendeten Hartmann-Blenden durch Linsenarrays ersetzt werden. Diese CARLs werden durch Prägen von 2D-Arrays mit 100×100 konkaven Linsen in Polymerfolien hergestellt. Die Linsenabstände liegen bei 50 µm und die Scheitelradien der Parabollinsen bei 8 µm. Die Positioniergenauigkeit der Teilstrahlen ist geringer als 1 µm. Durch das Stapeln von bis zu sechs Linsenarray-Folien werden Brennweiten zwischen 60 cm und 125 cm bei Röntgenenergien von 9 keV erreicht. Die maximale Sichtbarkeit beträgt etwa 0,5. Neben der NP-Detektion durch den Streukontrast kann auch die Wellenfrontverzerrung durch Proben oder Röntgenoptiken mit einer Auflösung von 0,2 µrad analysiert werden.

Contents

Abstract . . . iii

Kurzfassung . . . v

1 Introduction . . . 1

2 Fundamentals of pulsed laser ablation . . . 5
2.1 From laser matter interaction to designed nanoparticles . . . 5
2.1.1 Laser absorption in water column . . . 7
2.1.2 Reflection and absorption of the laser at the target surface . . . 7
2.1.3 Material heating and disintegration . . . 8
2.1.4 Plasma ignition and heating . . . 9
2.1.5 Cavitation bubble formation . . . 10
2.1.6 Nanoparticle genesis and distribution . . . 14
2.2 Criteria for improved nanoparticle yield . . . 18

3 Basics of X-ray scattering and imaging methods . . . 23
3.1 The interaction of X-rays with matter . . . 23
3.2 X-ray scattering . . . 25
3.2.1 Small-angle X-ray scattering (SAXS) . . . 25
3.2.2 Wide-angle X-ray scattering (WAXS) . . . 28
3.3 X-ray absorption imaging . . . 28
3.4 X-ray multi-contrast imaging . . . 29
3.4.1 Grating interferometry . . . 31
3.4.2 Single-exposure measurement with Hartmann mask-like setups . . . 32
3.4.3 Absorption contrast . . . 34
3.4.4 Scattering contrast . . . 34
3.4.5 Phase contrast . . . 41
3.5 X-ray focusing by refractive lenses . . . 42
3.6 X-ray sources . . . 45

4 Experimental setups . . . 49
4.1 Setups for *in situ* analysis of the laser ablation process . . . 49
4.1.1 Lasers used in this work . . . 49
4.1.2 Ablation chambers . . . 50
4.1.3 Optical imaging setup . . . 52
4.1.4 X-ray scattering imaging setup . . . 53

4.2 Implementation of multi-contrast reconstruction methods . . . 56
4.2.1 Contrast retrieval by Gaussian fitting . . . 57
4.2.2 Contrast retrieval by Fourier transformation . . . 59
4.2.3 Decorrelation to remove transmission crosstalk . . . 60
4.2.4 Phase reconstruction by zonal wavefront estimation . . . 61
4.2.5 SH-WaveRecon as published reconstruction software for multi-contrast images . 62
4.3 Simulation of scattering imaging . . . 62
4.3.1 Influence of beamlet width on visibility and fitted beamlet parameters . . . 63
4.3.2 Influence of steep transmission changes on beamlet parameter reconstruction . . 65
4.3.3 Pre-analysis pedestal correction to reduce problems during reconstruction . . . 67
4.3.4 Scattering sensitivity distribution . . . 69
4.4 Comparison of the abilities of different reconstruction algorithms . . . 72

5 Production of Compound Array Refractive Lenses for hard X-rays . . . 81
5.1 Fabrication of 2D lens arrays . . . 81
5.1.1 Serial embossing with a single needle . . . 82
5.1.2 Single-step embossing with a 2D needle array . . . 87
5.1.3 Stacking for focal length reduction . . . 90
5.2 Focal length and homogeneity determination of CARLs . . . 92
5.3 Summary and definition of optimal production parameters . . . 97

6 Summary of new insights of the hierarchical processes of pulsed laser ablation . . . 99
6.1 Laser-matter interaction leading to threshold and incubation effects . . . 100
6.1.1 Fluence threshold for efficient ablation . . . 101
6.1.2 Incubation promoting the ablation . . . 103
6.2 Mechanisms of nanoparticle genesis . . . 107
6.2.1 Early appearance of crystalline nanoparticles . . . 107
6.2.2 Nanoparticle agglomeration during bubble collapse . . . 110
6.3 Hierarchical imaging for nanoparticle localization during ablation . . . 111
6.3.1 Size quenching of nanoparticles by electrolytes already in the cavitation bubble . 112
6.3.2 Micrometer-sized air bubbles after ablation of a free wire target . . . 114

7 Conclusion and Outlook . . . 117

List of Experiments . . . 121

References . . . 135

A Publications . . . 151

B Source Code . . . 153
B.1 2D Gaussian fitting and image moment . . . 153
B.2 Fourier-analysis . . . 157
B.3 Visibility . . . 162

B.4 Decorrelation of absorption and scattering contrast 164
B.5 Modified Southwell-algorithm for phase reconstruction 166

List of figures **169**

List of tables **173**

List of equations **175**

List of abbreviations **177**

1 Introduction

The possible production of Nanoparticles (NPs) by Pulsed Laser Ablation in Liquids (PLAL) has been known for more than a quarter of a century.[1] The knowledge about the ablation process has strongly improved during this time.[2,3] However, the fundamental processes during ablation are not yet fully understood.

NPs are of interest in many fields and can contribute, at least in part, to solving key society challenges such as energy, mobility and information technology. NPs improve water oxidation by catalyzing the water splitting process.[4–6] They can increase the absorption in photovoltaic devices.[7] NPs added to mineral oils improve friction and wear and can therefore reduce resource consumption in the mobility sector.[8] In the field of medicine, NPs can help to improve medical examinations by acting as a contrast agent.[9] In addition, they can be used for improved disease treatment such as cancer through photothermal therapy[10,11] or improved durability of neuronal electrodes.[12]

For many applications it is important to achieve clean and ligand free NPs.[13] The synthesis of NPs wet chemically allows high productivity, but there always remain additives in the suspension.[14] PLAL however leads to a clean production of NPs. At first glance, the ablation process is simple. The solid target to be dispersed is placed in the liquid of interest and excited by the laser. The laser pulse deposits a large amount of energy in a relatively small volume of the target, which leads to the disintegration of the material. In detail, however, many more processes are involved. Either NPs are generated directly or they are generated by merging of small particles.[3,15] This allows PLAL to be considered as a combination of top-down and bottom-up synthesis. First, the bulk target is dispersed into NPs, clusters and atoms and then the particles grow again.

Since there are no other elements than the target and the liquid components, the NPs are ligand free. They can only consist of the elements involved in the ablation. For pure targets immersed in water (H_2O), only an oxidation of NPs can occur, since H_2O is split during the harsh conditions of ablation.[16] If an organic liquid is used, a carbon shell can form around the NPs.[17]

In addition to the disintegration of the target material, a plasma is ignited and then a hemispherical cavitation bubble is generated by liquid evaporation.[18] The maximum bubble size and lifetime depends on the laser pulse energy and the target surface state and material. It is shown here that the bubble size correlates with ablation efficiency and plasma intensity. While the bubble size is a good indirect measure for the ablation efficiency, it also limits the maximum achievable productivity through bubble shielding.[19–21] The maximum productivity reached so far is 4 g/h achieved by using high repetition rate lasers and a polygon scanner to bypass the cavitation bubble.[22,23]

For application purposes the control of NP properties such as size distribution, morphology and crystallinity is required.[14] In *ex situ* investigations mainly a bimodal size distribution is observed, consisting of primary NPs with sizes of roughly 10 nm and secondary NPs with sizes of 20 nm to 80 nm.[24–27] Only recently also nanoclusters were observed in the suspension.[28] From an application point of view *ex situ*

investigations are suitable. However, if the fundamental processes within the lifetime of the cavitation bubble are to be investigated, *in situ* techniques with high temporal and spatial resolution are required. Furthermore, an undisturbed view into the bubble interior is required, which cannot be performed with visible light due to the strong refraction at the liquid bubble interface.[2]

In this work, mainly X-ray scattering methods are used for *in situ* detection of NP. These investigations were performed on synchrotrons in cooperation with S. Barcikowski and A. Letzel from the Institute of Technical Chemistry I of the University of Duisburg-Essen. Small-angle X-ray Scattering (SAXS) allows to study the NP size and the relative mass distribution with a high temporal resolution.[27,29–31] In these earlier publications, it was made clear that the cavitation bubble is almost homogeneously filled with primary and secondary NPs, with the secondary NPs concentrated slightly higher at the top of the bubble. Furthermore, most of the NP mass is trapped in the bubble and is only released during bubble collapse.[27,31] In this work, the temporal resolution is increased below 10 µs to prove the early occurrence of large solid NPs proposed by simulations.[3,32,33] In combination with Wide-angle X-ray Scattering (WAXS), which determines the crystal domain size of the NPs,[34] it is validated that these early discovered NPs have comparable large grain sizes.

A hierarchical imaging of the ablation process is performed with the Single-Exposure Multi-Contrast Imaging (SEMCI) technique based on the Hartmann mask-like multi-contrast imaging.[35,36] In contrast to the more common Grating Interferometry (GI),[37,38] it allows to reconstruct the different contrasts from a single sample image and no stepping of optical elements or the sample is required. While the transmission contrast shows the macroscopic scale of the cavitation bubble, a scattering contrast sensitivity can be selected to detect the NPs.[39] Simulations of typical scattering data show that Fourier analysis[35] is the only useful one in the case of PLAL. Other algorithms, such as the Gaussian fitting,[40] the image moment analysis[41] or the change in visibility contrast, show unstable scattering contrasts.

The size control of NPs can be achieved by using additives such as polymers or electrolytes in the liquid.[42–44] The amount of secondary NPs gets strongly reduced and the mean sizes of the two size fractions decrease. In this work and the dissertation of A. Letzel,[45] carried out in collaboration, the size reduction with additives in low concentrations in the range from µM to mM is studied. It is shown that size quenching processes differ between electrolytes and macromolecular ligands. The scattering contrast of SEMCI showed that electrolytes already act in the cavitation bubble, whereas macromolecular ligands can only act when the NPs are dispersed in the liquid.

During laser ablation on free wire targets, bubble dynamics change compared to flat targets.[46,47] On flat targets, the first bubble and the subsequent rebounds are more or less hemispherical bubbles attached to the target surface.[27] On free wire targets, however, the first collapse is already detached from the target surface and the rebounds are located in the fluid with a net velocity away from the target.[46,47] In optical imaging, the first rebound appears only as a dark object, which does not allow conclusions to be drawn about its composition. This has been investigated in this work by SEMCI.

In SEMCI so far mainly absorbing optical elements in the form of hole gratings have been used for beam patterning.[35,36] Thus, the major part of the X-ray flux does not contribute to image generation. Due to the Babinet's principle, inverted Hartmann masks made of absorbing rods can also be used for SEMCI.[48,49] With the inverted Hartmann masks, a considerable amount of flux is still absorbed by the optical element. In order to use almost the entire incident flux, the beam structuring must be performed with 2D lens arrays, as done in this work.

Refractive X-ray lenses have been known for more than 20 years.[50] Due to the low refractive power of typical lens materials, a stack of lenses is required to achieve short focal lengths. They are called Compound Refractive Lens (CRL).[51] Apart from a few publications[52,53] only single CRLs or 1D arrays of CRLs have been realized.[51,54–57] This work demonstrates the production of scalable large area 2D lens arrays, the Compound Array Refractive Lenses (CARLs). An iterative embossing with a needle and a single-step embossing with a 2D needle arrays in plastic foils with subsequent stacking of several of these lens foils are developed. They are characterized with regard to focal length, regularity and visibility of the pattern. Beyond that they are used for SEMCI of PLAL.

Chapter 2 discusses the several aspects of the PLAL process, from the partial absorption of the laser in the liquid over the laser-matter interaction to the NP genesis and cavitation bubble dynamics. In chapter 3 the fundamentals of X-ray imaging and scattering methods required for this work are explained. In addition to the process on which SAXS is based, the formation of the different contrasts in X-ray multi-contrast imaging is also presented. This is followed by the description of the experimental setup in chapter 4. In addition, the reconstruction algorithms used and their usefulness for scatter imaging are explained. Measurements and simulated scattering data are used for this purpose. The production of the CARLs together with their characterization is discussed in chapter 5. The results obtained in this work on the PLAL process are presented in chapter 6.

2 Fundamentals of pulsed laser ablation

The PLAL as a process to produce NPs dispersed in a liquid phase does exist since more than 25 years.[1] A broad understanding of the ablation process is established nowadays. In this chapter the fundamental processes occurring during the ablation process as well as the ripening of the NPs dispersed in the liquid are described. The ablation is a multi-scale process ranging over several length scales. There are many aspects such as pulse duration or the specific fluid environment that can change the ablation process. It is therefore important to distinguish between the specific ablation setups, as not all statements about the ablation process can be directly applied to all setups.

Much information, especially about the early processes directly after laser excitation, comes from ablation in air or vacuum or from simulations with femtosecond laser pulses. Information is still missing for ablation with nanosecond laser pulses, especially for the early time scales immediately after the laser excitation event.

In this chapter the different processes occurring during PLAL are presented starting with the laser traveling through the liquid, the laser-matter interaction leading to material disintegration, the plasma ignition and consequent cavitation bubble formation. Furthermore, the NP genesis and spatial distribution are explained. Furthermore, some aspects to increase the ablation efficiency in sense of NP production rate are presented. A high ablation yield is important for the *in situ* NP detection by the X-ray multi-contrast imaging techniques established in this work.

Parts of this chapter are results achieved in the context of this work. Most of them have already been published.[15, 58–61] Details of measurement are listed in the "List of Experiments" and are referenced in the text in bold square brackets, e.g. ***[OI1]****.*

2.1 From laser matter interaction to designed nanoparticles

For PLAL only very few components are needed: the laser, some laser optics like lenses and mirrors, the target and the solution in which the ablation should take place. During the ablation process only the deposited energy of the laser, the target material and the liquid molecules are involved. One could imagine a simple process to get from bulk material to dispersed NPs, but this is not the case. There are many processes involved that run on several time and length scales.[14] Just looking at the product suspension after an ablation of a few seconds or even minutes in a beaker is only half the story. There are many pitfalls that can never be seen if the actual ablation process is not examined on the early time scale after the laser excitation event. The parameter space for efficient ablation is very large, which needs a deep understanding of the basic processes that take place during ablation. This knowledge can decrease the space significantly.

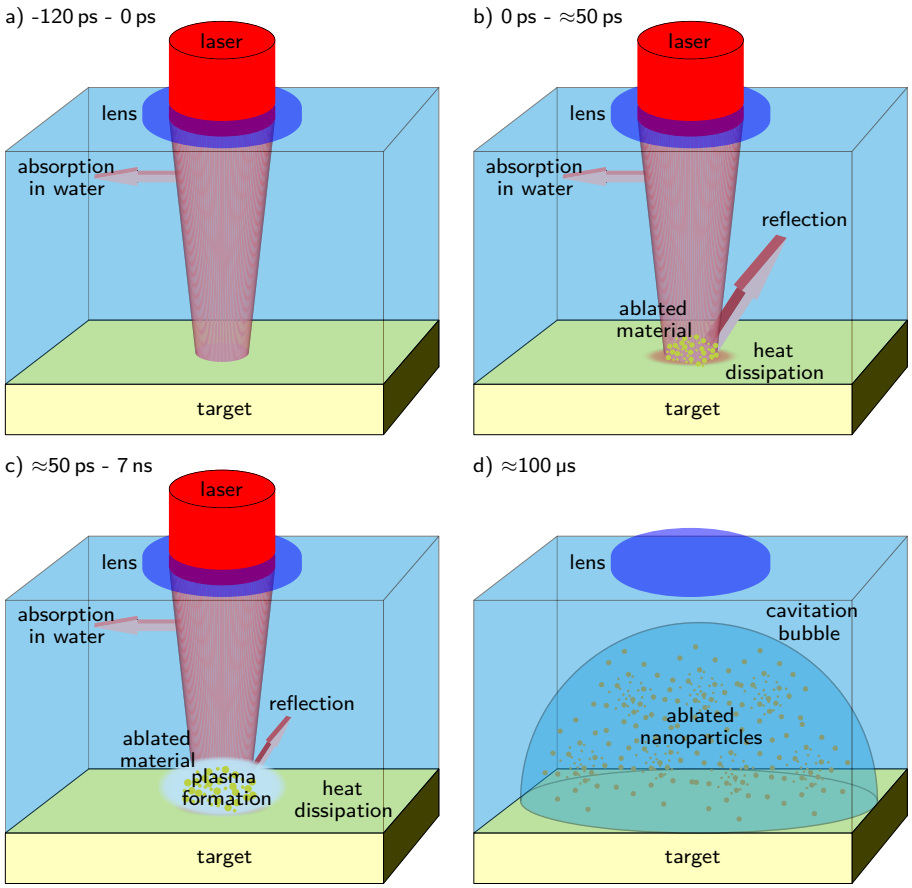

Fig. 2.1: Schematic illustration of the main processes after pulsed laser ablation with a nanosecond laser divided into four time periods. In (a) the time when the laser travels through the liquid before it reaches the target. Absorption occurs reducing the energy reaching the target. In (b) the laser interacts with the target. Parts of the laser light is reflected, energy is dissipated into the target and the first material is ablated. Then a plasma is ignited reducing the reflection as shown in (c). After the laser pulse has finished, a cavitation bubble is created due to water evaporation. This bubble contains most of the ablated material as illustrated in (d).

In the following the known and understood processes during the PLAL are explained in chronological order beginning with the laser energy lost mechanisms over the laser matter interaction and the target destruction to the NP genesis and release into the liquid. Fig. 2.1 shows schematically the ablation process during PLAL divided into four time intervals. As example, a laser with a wavelength of 1064 nm and a pulse width of 7 ns was assumed. In brief the four intervals consist of:

(a) The laser travels through the liquid layer and gets attenuated by absorption.
(b) The laser hits the target and gets partly reflected. Additionally, the disintegration of material and a minor heat dissipation into the target starts.
(c) A plasma is ignited which absorbs most of the trailing laser pulse and thereby gets heated. The plasma heats up the target to further ablate material.
(d) A cavitation bubble develops containing most of the ablated material. It has a distinct temporal evolution with collapses and rebounds. The bubble dynamics depend strongly on the target geometry.

The following description of the ablation process also mentions the differences to lasers with different wavelengths and pulse duration. The ablation setup consists of the laser guided by some optics to the

ablation chamber filled with the liquid and the target. To reduce problems of optics damage due to high laser fluences the laser is focused in the last step before the target. In many cases this is done by a lens standing free above the liquid. In this work the lens acted also as a chamber wall. The coupling in of the laser by the lens has the advantage that no corrugated liquid surface can change the laser profile. This is required for a stable and repetitive ablation. In this configuration the subsequent absorption of the laser in the liquid might be higher as the water column traversed is typically larger. In addition, the changed focal length compared to focusing in the air must be taken into account.

2.1.1 Laser absorption in water column

During PLAL the laser has to travel a certain length trough the liquid phase, in most cases water. In this work this is the complete focal length of the used focusing lens as the lens acts as a chamber sealing. The laser gets absorbed by the liquid as illustrated in Fig. 2.1 (a). The absorption can easily lead to an energy loss of up to 50 %, depending on the liquid, laser wavelength and focal length of the lens.[62] When focusing, it must be ensured that no optical breakdown occurs in the liquid.[24,58,63] This would lead to the creation of a plasma inside the liquid phase in front of the target. Consequently, most of the laser energy is absorbed by the plasma ignited in the liquid phase in front of the target. This inhibits an efficient ablation.[58] For laser pulse duration of picoseconds or longer, optical breakdown does not occur if the laser beam is unfocused. Therefore, an optical breakdown in the liquid can only occur in the focus point. For a pulse duration of femtoseconds, however, nonlinear effects such as self-focusing can occur even at low fluences of unfocused beams.[24] In general, a certain threshold fluence must not be exceeded to prevent optical breakdown. This fluence increases with pulse duration.[26]

2.1.2 Reflection and absorption of the laser at the target surface

When the laser hits the target several processes occur. The laser-target interaction is mainly studied in literature for ablation in air or vacuum.[64–66] Only occasionally are investigations carried out under liquid.[66–68]

Parts of the laser beam are reflected at the surface[66,69,70] due to the discontinuity in the real part of the index of refraction.[71] This is one of several loss mechanisms of laser energy that will be discussed later in section 2.2. The reflectivity, in general, depends on the polarization, the angle of incidence and the refractive indices of the two materials at the interface.[71] In the case of ablation, the reflectivity also changes depending on the laser pulse duration and the state of the target surface. With pulses that are longer than the plasma ignition time, the reflectivity is significantly reduced,[70] as explained later. Pulses shorter than the plasma ignition time can get reflected during the whole pulse duration. It should be emphasized that the reflectivity changes over time even in the picosecond time domain.[66] The second crucial point for reflection is the roughness of the target surface. Pristine and smooth surfaces reflect much stronger than corrugated ones.[60,69] The influence of target corrugation on the ablation efficiency will be discussed in subsection 6.1.2.

The non-reflected laser light gets absorbed by the target. The linear absorption follows the Beer-Lambert law:[72]

$$I(z) = I_0 \cdot e^{-\mu z} \quad \text{with} \quad \mu = \frac{4\pi\beta}{\lambda_0} \,. \tag{2.1}$$

Here $I(z)$ is the intensity in the depth z of the material, I_0 the intensity directly inside the material after the reflection losses and μ the absorption coefficient. The latter depends on the imaginary part imaginary part of the index of refraction (β) of the refractive index and the vacuum wavelength λ_0. The absorption depth is the inverse of μ and depends strongly on the material as well as on the wavelength. For metals it is typically in the range of around 10 nm for a wavelength of 1064 nm.[60,73] For semiconductors or insulators, in contrast, it can easily reach millimeters. In such cases an ablation is only possible if non-linear effects occur or absorption seeds in the form of dirt or beneficial surface structuring are present.[60] Especially short pulses are prone to non-linear effects due to the extremely high field intensities.

The electromagnetic wave of the laser interacts with the electrons of the material losing thereby its energy. The specific absorption process depends on the material.[71] In insulators and semiconductors, the absorbed photons mainly lead to intra-band excitation or to excitation from the valence band into the conduction band. These excited states release their energy over time to lattice phonons, which leads to a heating of the material. In metals, on the other hand, the photons interact with the free electrons.[64] This process is called inverse bremsstrahlung.

2.1.3 Material heating and disintegration

The absorbed energy gets thermalized in the electron subsystem and induces energy transfer to the lattice through electron-phonon coupling or electron heat transport into the target. For the detailed description of the processes occurring in the target material a differentiation between the different possible laser pulse lengths have to be done. There are three important time constants involved in these processes: (1) the laser pulse length τ_L itself, (2) the electron cooling time τ_e and (3) the lattice heating time τ_h. While τ_L can vary from femtoseconds up to nanoseconds, τ_e is in the order of 1 ps and $\tau_e \ll \tau_h$.[64]

If τ_L is in the order of femtoseconds it is smaller than τ_e. In this case, the entire laser energy is transferred to the electrons[64] and a multi-photon absorption is preferred leading to photoinduced ionization.[74] The electrons cannot transfer their energy to the lattice by electron-phonon coupling and do not thermalize. The material can be modified non-thermally. The heat-affected zone is minimized by the almost instantaneous evaporation.[74] This is referred to photochemical processing.[71] After the laser pulse, the electrons transfer their energy to the lattice, which then distributes the energy by thermal diffusion.

In the picosecond pulse regime the electrons can thermalize[75] and their temperature can be assumed as quasistationary.[64] As $\tau_L \ll \tau_h$ the target heats up during the complete pulse duration. The heat dissipation is still negligible as it is still in the range of the absorption depth. Therefore the lattice temperature at the end of the laser pulse is equivalent to femtosecond pulse duration.[64] If the target material gets molten, boiled or even evaporated within τ_L the simultaneous ongoing photoionization can lead to a larger affected volume of the target than defined by the spot area and absorption depth.[75,76]

In the third regime with nanosecond pulse duration both the electrons and the lattice are in a quasistationary regime and have the same temperature.[64] During the laser pulse duration the electrons absorb the energy from the photons but simultaneously deliver the energy to the lattice. Already for pulses below 10 ns the thermal diffusion length is in the range of 1 µm.[60] In this regime one can find material in all three phases. The top layer gets heated up first reaching the evaporation point while a liquid and the solid phase coexist in deeper regions.[64] Since the material is changed by thermal processes, this is called photothermal processing.[71]

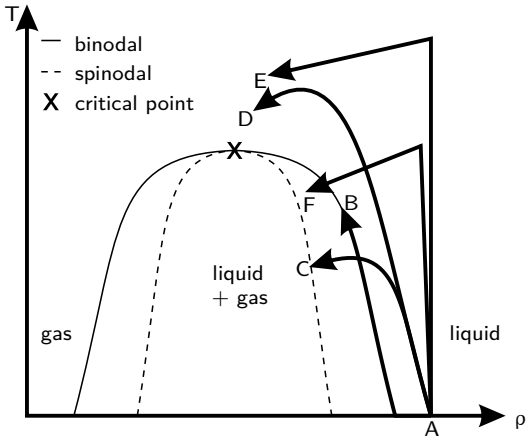

Fig. 2.2: Phase diagram of the ablation process. For long pulse duration ($\geq$ µs) the matter follows the binodal (A-B). At medium pulse duration (roughly ns), heating up and expansion occur simultaneously and the pulse energy decides whether the matter crosses the spinodal (A-C) or the critical point (A-D). For short pulse duration ($\leq$ ps) the matter is isochoricly heated and again the pulse energy decides where the matter ends (A-E and A-F). In accordance to Lorazo et al.[77]

Depending on the pulse duration, the material undergoes different paths in the temperature-density phase diagram as shown in Fig. 2.2. For long pulse lengths (microseconds or longer) the material is in thermodynamic equilibrium and follows the binodal (A-B) via a slow expansion and heating. If the energy is high enough the material reaches the critical point where phase separation takes place.[77] The material disintegration takes place by vaporization and boiling.[2] For shorter pulse (around nanoseconds) duration the material heats up faster while the density drops slower (A-C), which is called ”explosive boiling” or ”phase explosion”.[2,77,78] After rapid heating, the material expands and crosses the binodal and spinodal. This leads to phase separation of liquid and gaseous parts. The lower pulse duration limit for phase explosion was estimated to be around 10 ps.[77] If the pulse energy is high enough or the pulse duration short enough, the material may cross the critical point (A-D). Here the material directly changes from the liquid to the gaseous phase.[77] For the shortest pulses in the femtosecond range, the material is isochorically heated. Depending on the pulse energy the material crosses the critical point (A-E) or enters the binodal and spinodal (A-F).[77,79]

When the material gets expelled, the recoil pressure creates two shock waves traveling with supersonic velocity.[80] One goes into the target and one into the liquid.[78,81] The latter shock wave may promote detachment of material from the crater.[20]

2.1.4 Plasma ignition and heating

As already mentioned, a plasma ignites shortly after the beginning of the laser impact as shown in Fig. 2.1 (c). A time delay of a few tens of picoseconds after the laser impact is reported for ablation in air.[82,83] The ablated material consists of highly ionized material due to direct photoionization and the high temperature. Hence, the material is not in equilibrium and can be considered as a ”plasma plume”.[84] On the other hand, also ionized liquid molecules can ignite a plasma if an optical breakdown in the liquid happens.[25] Such a liquid plasma can absorb up to 96 % of the laser light depending on the laser parameters.[85] With increasing laser power and numerical aperture of the laser beam, the absorption of the plasma increases. In addition, the pulse duration is important for the amount of light absorbed.

It has been shown that picosecond pulses have the lowest absorption and increases with femtoseconds and especially with nanosecond pulses. The latter can be explained by the longer plasma duration while the former is ascribed to the increasing role of multi-photon ionization.[85]

It is important to mention that during PLAL the plasma behaves differently than for ablation in air or vacuum. Only for the very first time (up to around 1 ns) the plasma evolution is similar, but later the surrounding liquid strongly confines the plasma plume near the ablation spot.[86] This confinement is of advantage for the ablation yield. The target gets heated more efficiently compared to ablation in air or vacuum due to the better heat transfer from the plasma to the target. This results in a larger amount of material reaching the ablation threshold.[87–89] Hence, in PLAL one can consider the ablation to be driven by both, the laser energy deposition into the target material and the heat transfer from the plasma to the target.[90,91]

When the pulse duration of the laser is longer than the plasma ignition time (a few tens of picoseconds[82,83]) it gets heated up by the trailing part of the laser. Consequently, it shields the laser from reaching the target.[25] The plasma thus has two contributions to ablation. Firstly, efficient ignition of the plasma is advantageous for ablation. On the other hand, the plasma can also cause a reduction in laser energy reaching the target. The exact dependence of ablation on the two mechanisms is not fully understood until now.

Especially for nanosecond laser pulses the plasma plays an important role in the ablation process.[58,60] Hence, if most of the pulse energy is absorbed by the plasma the pure material properties (e.g. reflectivity) only play a minor role concerning the ablation process and efficiency. As shown in subsection 6.1.1 in more detail, a fluence threshold for bubble formation and ablation yield exists for nanosecond PLAL.[58,60] This threshold is directly linked to an efficient plasma ignition.[58] An efficient plasma ignition is mandatory for a productive ablation.

During the nanosecond PLAL the plasma reaches a maximum temperature of about 6000 K, as was stated in several reports.[46,92,93] The spectrum of the plasma is mainly dominated by the broad continuum black body radiation.[92] In special cases, nevertheless, also spectral lines of the materials present in the plasma are visible.[18,87] The lifetime differs a lot in literature from around 150 ns[46] over 600 ns[94,95] to more than 1 µs.[93]

The plasma is the important process for the following cavitation bubble and an efficient ablation.[58,60] It not only heats up the target for a more efficient ablation, it also heats up the surrounding liquid to roughly 10^3 K. This leads to a degradation, ionization and photolysis of liquid molecules.[87,88] Already in the plasma liquid species can be verified and might react with the ablated target material.[87,88] The strong heating of the liquid and subsequent evaporation is the genesis point of the cavitation bubble.

2.1.5 Cavitation bubble formation

After the laser impact on the target and the plasma formation a cavitation bubble develops. The bubble size depends on several parameters like pulse energy, target geometry, liquid pressure and material properties.[47,60,93] The bubble lifetime scales with the bubble size.[96,97]

Fig. 2.3 shows exemplarily the bubble dynamics for a 7 ns laser pulse with a wavelength of 1064 nm and a pulse energy of 3 mJ on a flat brass plate. In the first image (time 0 µs) one can see a bright spot, which is the plasma ignited by the laser. In the next image (time 5 µs) already an increasing bubble is

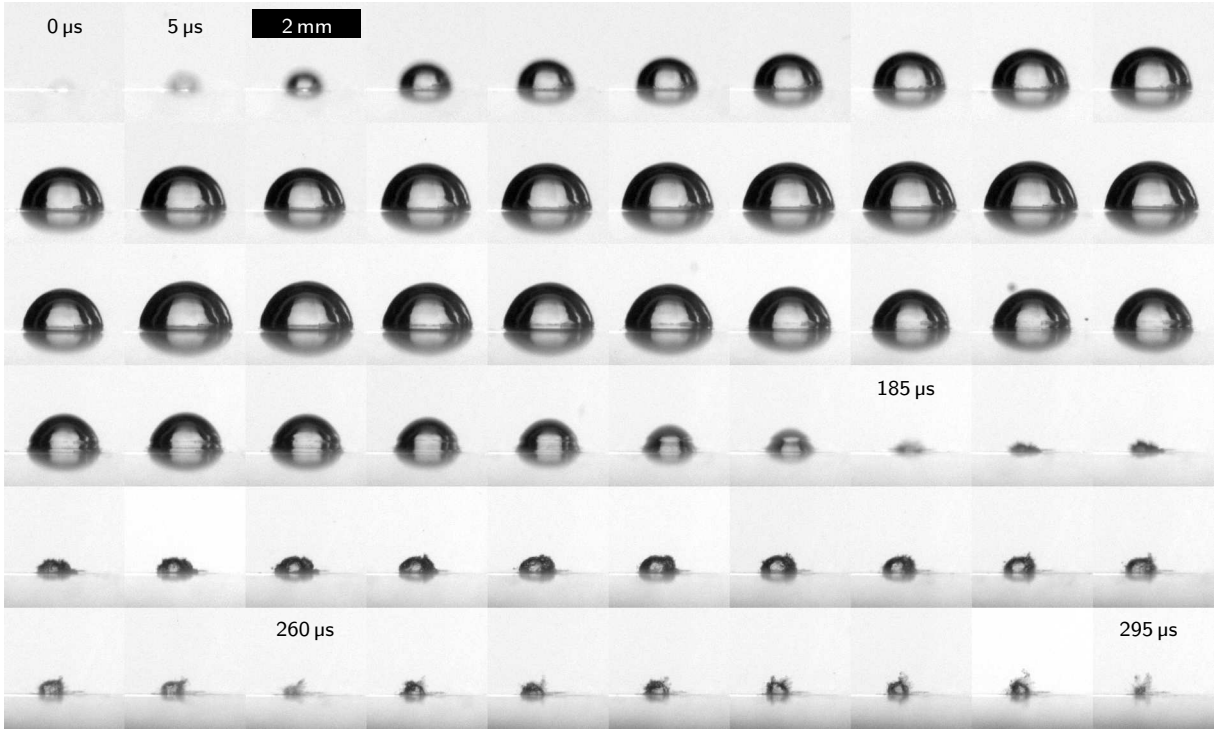

Fig. 2.3: Typical bubble dynamics during pulsed laser ablation under liquids on a flat target. After the laser impact (0 µs) an almost hemispherical bubble develops with a lifetime of 185 µs and a maximum diameter of around 2 mm. After the first collapse a first rebound with a collapse at 260 µs and a second rebound with a final collapse at 295 µs arise. Both rebounds do not have a smooth hemispherical shape anymore. A brass plate was ablated with a 1064 nm, 7 ns laser with a pulse energy of 3 mJ. **[OI1]**

visible. The edge of the bubble is blurred due to the fast expansion of the bubble compared to the camera exposure time. The cavitation bubble front velocity reaches roughly 50 m/s.[93] Later on the expansion velocity decreases until a stable maximum bubble is reached at around 90 µs. Afterwards the bubble size decreases again leading to a collapse at a time delay of 185 µs. During the shrinking phase, a rim develops near the bubble-target boarder and rises slowly. This rim indicates that the contact angle between the target surface and the bubble edge (measured in the liquid phase) is above 90° as shown by numerical calculations by Shima et al.[98] The backward flow of the liquid directly at the target surface is smaller than at a finite distance leading to a decreased collapse velocity for the bubble parts located at the target surface. As a result, the collapse is flattened, with the bubble radius being larger than the height.[15]

The first collapse is followed by a first rebound bubble with a much smaller size and consequently reduced lifetime (second collapse at 260 µs). Under ideal conditions also a second rebound can be observed with a further reduced size and lifetime (third collapse at 295 µs). After the third collapse no cavitation bubble in sense of a homogeneous bubble can be identified anymore. Only some persistent gas bubbles are formed due to liquid molecule splitting[15,16,99,100] as discussed later.

The first bubble is almost hemispherical. The sphericity (height divided by radius) is only slightly above unity as shown in Fig. 2.4. The minor fluctuations have to be addressed to the stroboscopic imaging mode (see for more details subsection 4.1.3). The first and second rebound however are no longer well defined hemispheres leading to a drastic change in sphericity.

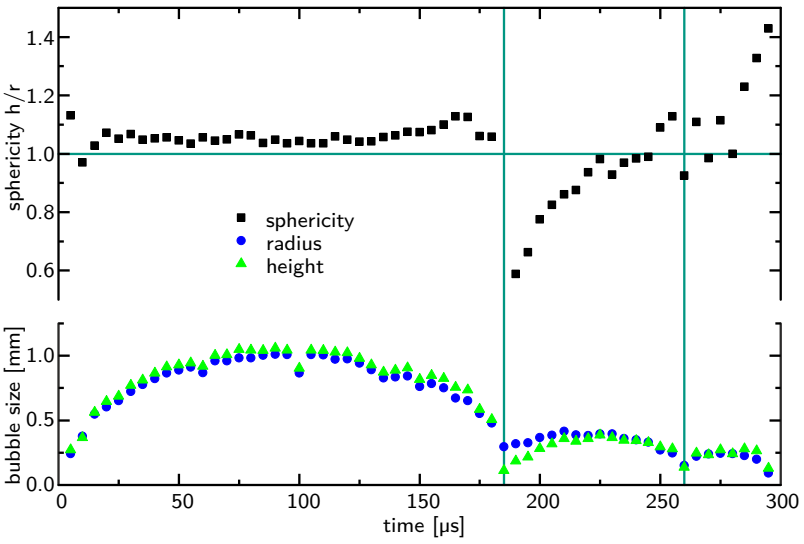

Fig. 2.4: Bubble sphericity and size development of the cavitation bubble of Fig. 2.3. While the first bubble is almost hemispherical for the whole time, the first and second rebound have an elongated shape. **[OI1]**

There are several models to fit the bubble dynamics used in literature.[15,96,97,101–105] The two mainly used ones are the Rayleigh-Plesset equations[97] and the Gilmore equations.[96] Both have their own limitations.[102,103] For the first bubble, both provide reasonable results. The collapse represents an extreme point that can hardly be considered in fitting algorithms. During collapse a lot of energy is released to the surrounding[85] and thus drastically reduces the size of the following rebound. This energy release is not considered in the Rayleigh-Plesset equation leading to a to large expected rebound.[102,103] The Gilmore equation, however, can predict the rebound better. It also takes into account the compressibility of the liquid and thus the loss of bubble energy during the collapse. This improves the Gilmore equation compared to the Rayleigh-Plesset equation.[102,103]

Changing the geometry of the target also modifies the bubble dynamics.[46,47,59] In Fig. 2.5 the evolution of the cavitation bubble on a wire target is shown. The wire target positioned at the bottom was excited by the laser from the top. In the top and middle row the wire is perpendicular to the imaging direction and parallel in the bottom row. The upper row shows X-ray images and the middle and lower rows stroboscopic optical images.

The increase of the cavitation bubble size is almost identical to that on a flat target. The bubble is developing as a mostly spherical one. Only the radius of the bubble is slightly reduced due to the fact that the bubble wraps around the wire a bit (see Fig. 2.5 bottom row 70 µs). The stored energy in the bubble is proportional to the bubble volume.[85] During the shrinking phase again the rim due to hydrodynamic discontinuities arises starting from the bubble-wire interface. However, this rim develops differently on the wire target. It generates an increased flow along the target leading to an effective movement of the bubble center away from the wire. As clearly shown in the middle column of Fig. 2.5 the collapse is located in front of the wire. Consequently the first and second rebound are also detached from the wire with a continuous net movement of the bubble center.[46,59]

In Fig. 2.5 both optical imaging and X-ray imaging are shown. The optical imaging is a standard technique that can be performed easily in normal labs while fast X-ray imaging is an exclusive technique performed at synchrotrons. With optical imaging a higher temporal resolution can be achieved because

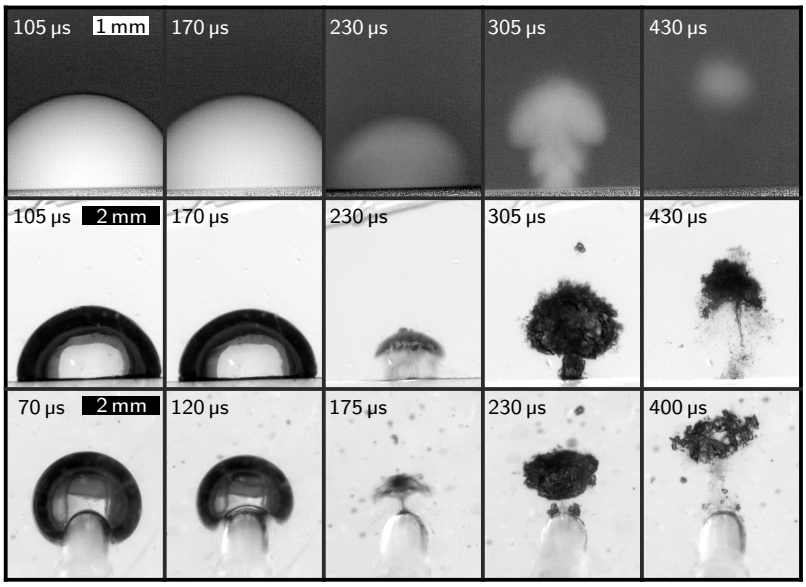

Fig. 2.5: Typical bubble dynamics during pulsed laser ablation under liquids on a free wire target. Top and middle row imaging perpendicular to the wire (wire at bottom), top X-ray imaging and middle stroboscopic imaging. Bottom row stroboscopic imaging parallel to the wire target. From left to right: first maximum bubble, shrinking bubble with rim development, first collapse, first rebound and second rebound. The slight temporal differences originate from the different used ablation chambers. A zinc wire with 1 mm diameter was ablated with a 1064 nm, 7 ns laser with a pulse energy of 11 mJ. Reproduced from Reich et al.[59] **[XRI1] [OI2]**

the absorption losses are much weaker and the illumination intensity can easier be increased compared to X-ray imaging. Optical imaging, however, has the great disadvantage of strong refraction of light at the bubble-liquid interface. Therefore the interior of the bubble can not be imaged completely. Even the bright area inside the bubble must be considered to be displaced compared to their real origin. The almost rectangular bright area in the first image in the middle row of Fig. 2.5 displays the back window of the ablation chamber with a size of 1 cm $\times$ 1 cm. This illustrates clearly the strong displacement of the imaged bubble interior parts.

In contrast to that, the X-ray imaging is (almost) refraction free. If the sample-to-detector distance is small (4.5 cm in Fig. 2.5), the low refracting power of a water-air interface in the X-ray regime only leads to sub-pixel sized X-ray displacements. This allows to evaluate the interior of the bubble.[15,27,58,59] One can clearly see that the first bubble is a homogeneous vapor bubble without internal structures. The first and second rebound, which appear black in optical imaging, also show a strong increase in transmission in X-ray imaging. This shows that the rebound still contains high amounts of vapor. The comparison with the optical imaging suggests that the vapor bubbles of the rebounds consist of a high amount of smaller bubbles. Maybe the first rebound also has a larger bubble in the interior, as the slightly increased transmission in the optical imaging indicates. In subsection 6.3.2 the existence of micrometer sized structures in the rebound will be proven with the help of X-ray scattering imaging.

The detachment of the cavitation bubble can also be provoked on a flat target by increasing the liquid pressure as shown by Dell'Aglio et al.[93] The initial bubble wall velocity is the same, but the further dynamics change compared to the ambient pressure. The maximum bubble size is smaller, collapse takes place earlier and the collapse velocity increases with increasing liquid pressure.[93]

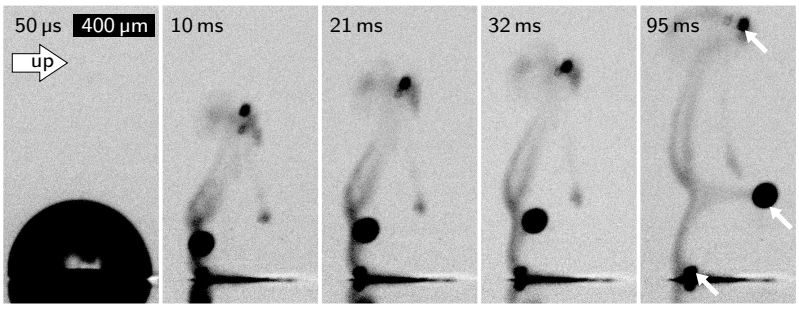

Fig. 2.6: Videografic images after laser excitation (from top) of a brass plate with a 7 ns laser pulse of 1 mJ pulse energy and a wavelength of 1064 nm. The first image (50 µs) shows the cavitation bubble almost at her maximum extent. The following images (10 ms to 95 ms) show the emergence of elongated clouds containing nanoparticles as well as three persistent gas bubbles (white arrows). The persistent bubbles move upwards (images rotated by 90°). **[OI3]**

After the final collapse of the cavitation bubble and the rebounds often persistent gas bubbles remain.[15, 16] In Fig. 2.6 snapshots of a movie after a single laser shot on a flat target are shown. In the first image (50 µs) the cavitation bubble at almost the maximum expansion is shown. In the following images (10 ms to 95 ms) three persistent bubbles can be seen (highlighted by green arrows). First they are expelled from the ablation spot before flowing up against gravity (images rotated by 90°). It was shown in literature that these persistent bubbles contain all possible species of molecules that can occur after the splitting of the liquid phase. For ablation in water, only H_2 and O_2 are observed in a ratio of 2:1. This fits well to the ratio of the atomic appearance in water molecules. After ablation in organic liquids also molecules like carbon monoxide and hydro carbonates are detected.[16, 100]

Besides the gas bubbles grayish clouds are observed after bubble collapse. No structures like small bubbles are observed in these clouds. Hence, the structures leading to this extinction must be below the camera resolution of 2.2 µm/px. Cavitation bubbles of this size would collapse within microseconds.[106] Therefore, these clouds must consist of small persistent gas bubbles and the ablated NPs. The latter are first captured in the cavitation bubble and get released into the liquid during bubble collapse, as will be explained in the following section.

2.1.6 Nanoparticle genesis and distribution

In subsection 2.1.3 some phenomenological processes how the target material can get disintegrated were explained. The material can either undergo heating, melting and evaporation along the binodal for long laser pulses, explosive boiling for medium pulse duration or fragmentation for very short pulses. Here the origin of NPs will be described in more detail.

The target material gets disintegrated after the laser impact. A real imaging of the ablation process is not possible with the investigation techniques available at the moment. However, there are several simulations of the ablation with short pulse duration published in literature by the group of Zhigilei.[3, 33, 76, 107, 108] One successful simulation method is a hybrid atomistic-continuum model. It combines the classical molecular dynamics method[107, 108] with a continuum description of the laser excitation and subsequent relaxation of the conduction band electrons based on the so-called two-temperature model.[109] So far, these simulations can only be carried out for short pulse duration of up to 100 ps and also the time span after the laser impact is limited to some nanoseconds. However, they helped to de-

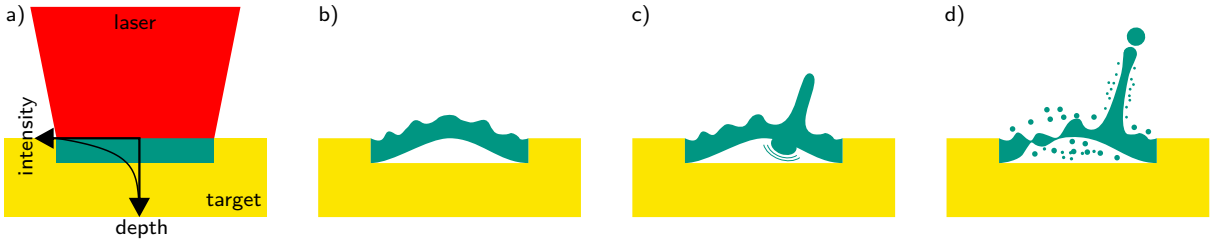

Fig. 2.7: Schematic drawing of the material disintegration for short laser pulses. Note that the vertical direction is strongly stretched. (a) The laser gets absorbed in the top layer of the target and increases the temperature and pressure in this volume (green area). (b) To expand the laser affected layer it lifts up forming a void underneath. Rayleigh-Taylor instabilities lead to a roughened layer surface. (c) When a droplet from deeper crater regions hits the lifted layer it induces a nanojet. (d) The nanojet separates into several droplets while also in the lifted surface droplets can be separated. The nanoparticles generated directly from the liquid layer are also shown in this image.

velop a picture of the ablation process as illustrated in Fig. 2.7. This figurative description should also be transferable to nanosecond ablation with only minor modifications.

When a laser beam hits a target, the processes in the target depend strongly on the laser fluence on the target surface. At fluences below the ablation threshold, the top layer of the target only melts and quickly resolidifies again. The stress exerted creates subsurface voids[110] and leads to a ”swelling” of the target surface.[111] The threshold fluence is reduced for subsequent laser pulses and is called ”incubation effect”. This can play an important role during PLAL and will be discussed in subsection 6.1.2 in more detail.

At fluences above the ablation threshold, the target surface not only melts, but also lifts off. During laser impact, the laser energy is absorbed within the first 10 nm in metallic targets[73] as shown in Fig. 2.7 (a). This leads to rapid heating of the material and thus to increased pressure, as the material can not expand quickly enough.[33,76] The increased localized pressure is the starting point of the two shock waves traveling through the liquid on top and the target. As long as the target is much thicker than the laser affected volume (green areas in Fig. 2.7) the only way for the heated material to expand is by moving away from the unaffected target as depicted in Fig. 2.7 (b). Cavities form underneath the lifting hot material.[3,112–114] In these cavities the pressure decreases very quickly, even below ambient pressure.[115] During this time, the material itself remains hot. This results in conditions leading to material evaporation.[3]

The interface between the lifted molten metal layer and the water gets roughened due to Rayleigh-Taylor instability.[3,33] When a droplet traverses the cavity and hits the lifted layer as shown in Fig. 2.7 (c), a pressure and temperature peak occurs in this layer. The impact of the droplets also leads to the appearance of a nanojet.[3,33] These nanojets get separated in the following into several droplets as depicted in Fig. 2.7 (d). The simulations suggest that some of the ejected droplets can reach the surrounding water phase.[3] This would result in material being emitted directly into the water phase without being confined inside the cavitation bubble. Some very recent results for picosecond laser pulses showed that some NPs indeed might be located in front of the cavitation bubble[61] and are shown in subsection 6.2.1. Measurements performed with nanosecond lasers, however, did not show ablated material in front of the cavitation bubble.[15,27]

Another possibility for NP genesis might be the separation of droplets out of the lifted molten layer. These droplets form relatively large NPs. Besides them also a large number of smaller NPs, clusters or

maybe even molecules and monomers are formed as indicated by some additionally NPs in Fig. 2.7 (d). The simulations suggest that a large amount of clusters and monomers are present right after the material disintegration.[32] Depending on the time scale of the material heating, parts of the material can pass directly into the vapor phase and thus be released directly from the target as vapor (see discussion to Fig. 2.2). Just recently it was shown experimentally that during PLAL with nanosecond lasers also a large amount of clusters are produced.[28] In fact, in number- and mass-weighted comparison the clusters with a diameter of roughly 1 nm are the dominant species in the final suspension.

The simulations for short laser pulses predict the existence of several size levels of NPs within the first nanoseconds. Experiments show also several size levels. Most of them being present in different weighting for PLAL with short and long pulse duration. A possible classification into five size levels can be made as follows, knowing well that this does not necessarily reflect all aspects of the ablation process:

- atoms and monomers;[32, 116]
- nanoclusters with diameters of about 1 nm to 3 nm[28, 33, 116] located inside the cavitation bubble and distributed in the liquid;
- primary particles with diameters between around 5 nm and 15 nm[25, 27, 30, 31] where the actual size varies somewhat with experimental conditions;
- secondary particles with diameters roughly between 20 nm and 80 nm,[25, 27, 30, 31] consisting of agglomerated and aggregated smaller NPs or solid spheres and often can be quenched efficiently by organic or inorganic additives;[44, 61, 117–119]
- micrometer sized fragments[32, 120] representing larger parts broken from the target without undergoing the ablation process but rather mechanical cracking.

Not all size levels can always be found, independent of the experimental parameters. For example, it is reported that no secondary particles can be found in femtosecond ablation with low fluences, whereas they are present at high fluences.[24] A decrease in average size with increasing fluence is also reported in literature.[121] The existence of nanoclusters was not observed in experiments due to the difficult detection in the past. Only recently they have been detected by analytical ultracentrifugation by Letzel et al.[28] For this reason, it is not always possible to deduce an absence from a non-detection.

The smaller ones (nanoclusters and monomers / atoms) are difficult to detect[88, 122] and therefore often not observed. The large chunks are less stable in suspension. If they can sediment before analysis, they are not observed. Therefore, the two most frequently discussed size levels are primary and secondary NPs. The two parts of this bimodal size distribution[30, 31] have shown a Gaussian[25] or log-normal[3, 121] shape. Predictions by using a residence time model neglecting coagulation also have shown the log-normal distributions.[123, 124]

If and how large differences in the ablation process on the short time scale do exist for short compared to long pulse duration is not clarified until now. The quite good agreement of the results of short pulse simulations with the observed size distributions, which were found experimentally for a long pulse duration, indicates that there are only small differences.[61]

After the first NP generation by phase explosion and droplet emission, the existing particle material can begin to aggregate and thus form larger particles.[116, 125–127] Depending on the precise process of the joining of several particles these processes are called ripening, coagulation, aggregation or agglomeration. This growth process can be prevented by using additives.[44, 117, 128] Some additives are able to

quench the growth already within the ablation bubble, while others can only quench the long term growth when the NPs are dispersed in the liquid. This has been investigated using X-ray scattering techniques within this work and is further explained in subsection 6.3.1.

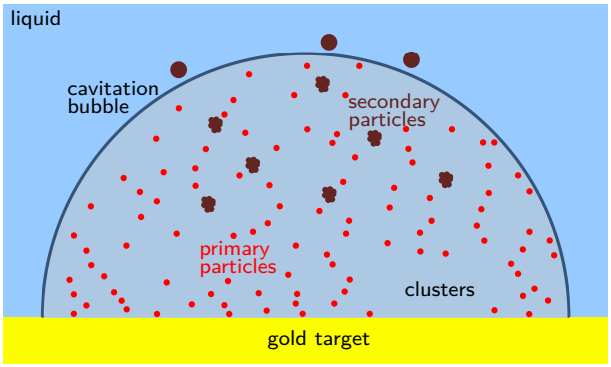

Fig. 2.8: Illustration of nanoparticle distribution at the maximum expansion of the cavitation bubble after laser ablation. Only the primary and secondary particles are *in situ* detectable at the moment and are shown as dots. However, one has to assume that also the other size levels such as clusters are present in this picture. Most of the ablated material is confined inside the cavitation bubble with only rare parts being directly injected into the liquid.

In several publications it was confirmed that most of the ablated material is confined inside the cavitation bubble.[15,27,30,31,61,125] This was proven for different pulse duration from picoseconds to nanoseconds. Fig. 2.8 illustrates the nowadays expected NP distribution for the cavitation bubble of maximum expansion. The bubble is homogeneously filled with primary particles, while the secondary ones are more in the upper part of the bubble.[15,27,30] Within this work it has been proven that some secondary particles may even be in front of the bubble.[61] So far the clusters have only been confirmed in the final suspension,[118] but no *in situ* investigation of their position in the cavitation bubble was possible.

The ablated mass is confined by the bubble. Hence it also gets retracted to the target during the shrinkage phase.[27,61] A high amount of NPs get only released into suspension during the collapse phase.[27,31] The harsh conditions during the collapse, when pressure and temperature rise again, lead to an increased growth. Thus a higher amount of secondary particles is observed in the first rebound[15,27,31] as shown in subsection 6.2.2. However, the presence of the high amount of nanoclusters in the suspension shows that significant parts of them do not grow.[28]

PLAL can be seen as a combination of top-down and bottom-up NP synthesis. The target is first dispersed into clusters and NPs, followed by a growth process. The size of NPs increases with the inclusion of atoms and clusters, but clusters can also connect and form new NPs. Surface atoms can rearrange themselves to improve the spherical shape, if the reduction of the surface is energetically more favorable.[2] Therefore, NPs with spherical shape are often found.[26,61,118,129]

One point that must not be forgotten is reirradiation of already existing NPs.[130] Only if the water column contaminated by NPs is exchanged between two laser shots one can exclude reirradiation. Most of the published investigations perform PLAL in a beaker or batch chambers with a slow water exchange for a large number of laser shots.[26,121,131,132] Therefore, these NPs must be considered as produced in two steps, first by ablation and then by reirradiation. The result is that not only the primary ablation parameters, but also the parameters of reirradiation, which may have occurred several times, led to the obtained NPs. A fragmentation by reirradiation, however, can be useful in some cases if the size distribution of the NPs thereby can be optimized.[130,133]

When the NPs are dispersed into a reactive environment they can undergo chemical changes.[59, 134–136] As an example the ablation of a pure zinc target with a subsequent oxidation of the NPs is explained. Immediately after ablation, the proportion of zinc in the NPs is still very high, as shown by X-ray spectroscopy.[59] The UV-Vis spectrum is dominated by the Drude-like behavior of metallic zinc at the beginning but changes within 10 min into the bandgap shape of zinc oxide.[59, 135, 136] This change from metallic zinc to zinc oxide was also observed in X-ray spectroscopy, but with a slightly lower kinetics. Additionally, it was revealed that zinc not only oxidizes to zinc oxide but also to hydrozincite ($Zn_5(CO_3)_2(OH)_6$). It is expected that the carbon in hydrozincite comes from dissolved carbon dioxide contained in the water that is split under the harsh conditions of laser ablation. Half an hour after ablation the NP suspension consists of roughly 10 % zinc, 45 % zinc oxide and 45 % hydrozincite.[59]

This shows that the NP ripen after ablation in the suspension.[127, 137, 138] They undergo chemical reactions and change size and shape with time. It is therefore not sufficient to look only at the end product to draw conclusions about the primary processes. Only an *in situ* investigation allows to make clear statements about the basic physical processes in the early phases of PLAL. In order to investigate the exclusive ablation process, it must also be ensured that no NPs are present at the site of investigation before. In this work this was ensured by using a flow-chamber with high flow rate and low repetition rate of the laser.

2.2 Criteria for improved nanoparticle yield

Compared to chemical NP synthesis the PLAL process is inefficient. Therefore the improvement of the ablation efficiency is an important point. Until now ablation rates up to 4 g/h were achieved.[22, 23] The strategies to improve the NP yield can be divided into two categories, first by increasing the number of laser pulses per time and second by improving the ablation rate per pulse.

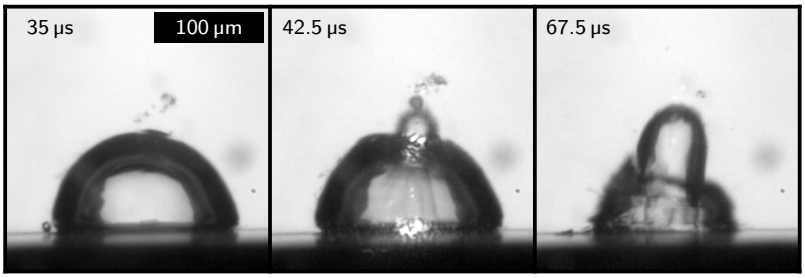

Fig. 2.9: Snapshots of the cavitation bubble evolution after two laser pulses (1064 nm, 12 ps, 1 mJ) of high repetition rate (26 kHz) showing the bubble shielding effect. The cavitation bubble of the first laser shot develops to a hemispherical bubble (35 µs). The energy of the second laser shot (arriving at 38.5 µs) is deposited at the water-bubble interface of the first bubble and not at the target surface. This generates a second bubble on top of the first one (42.5 µs). While the first bubble shrinks the second bubble increases (67.5 µs). **[OI4]**

The maximum laser repetition rate is limited for PLAL. Besides technical limits of some lasers also a phenomenological limit exists. The ablation productivity in the sense of mass per time saturates when the cavitation bubble of the previous laser shot is still alive at the time the next laser shot is fired.[3, 19–21] This effect is called bubble shielding. The laser energy is deposited at the interface of the previous bubble and the surrounding water as shown in Fig. 2.9. The second bubble starts to grow on top of the first one.

Some minor splashes can be seen penetrating the first bubble (middle image of Fig. 2.9). In this case, the first bubble was at its maximum expansion and shrinks while the second bubble grows.

The laser energy of the second laser pulse does not reach the target, so no additional ablation can occur. This is the reason why the ablation productivity saturates and the ablation rate per pulse decreases, respectively.[19–21] To overcome the problem of bubble shielding one can spatially bypass the cavitation bubble by the help of a laser scanner,[22,23] which have different technical limitations restricting the ablation productivity. If one can choose between a high repetition rate or higher pulse energies, the second was reported to be more productive.[129]

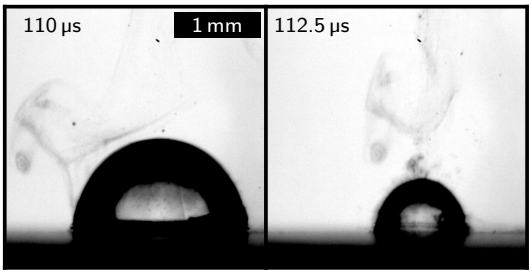

Fig. 2.10: Two snapshots of cavitation bubbles after laser ablation (1064 nm, 7 ns, 3 mJ) showing the strong bubble size reduction due to nanoparticle shielding. In the left image the laser path (coming from the top in the center of the bubble) was not contaminated by preexisting nanoparticles while it was contaminated for the right image. The bubble volume is reduced eightfold. The small difference in the delay time after the laser pulse (110 µs and 112.5 µs) is not of importance as the bubble in the left image is at her maximum expansion, which lasts much longer. **[OI5]**

One further problem are the already generated NPs themselves. As mentioned above, they have to be removed otherwise they also absorb parts of the laser intensity. This effect is called nanoparticle shielding.[21,58,130,131] As shown in Fig. 2.10, the NP cloud of a previous laser shot can have such a high optical density that the bubble volume is reduced (in this case) eightfold. Here the concentration of NPs is very high but even much lower concentrations have an effect on the laser transmission. Two processes contribute to the absorption, (i) the NPs themselves and (ii) micrometer sized cavitation bubbles around the NPs induced by the laser light absorption,[139–141] which only exists for a few nanoseconds.[106] This shows clearly that the generated NPs have to be removed fast enough to not absorb most of the laser intensity. In Fig. 2.10 the laser repetition rate was 0.5 Hz so the NP cloud was accidentally traversing the laser path. If the repetition rate is much faster a higher amount of NPs are generated increasing the probability of NP shielding. Hence, even if a laser scanner is used one has to ensure an efficient water flow to remove the high amount of generated NP.

The NP shielding in some cases might be of direct interest. If a reirradiation of the NPs is wanted to improve the NP properties, this is one possibility to produce them. However, it is not ensured that all NPs are reirradiated leading to a partially uncontrolled ablation process. A more controlled way of reirradiation represents the laser fragmentation in a liquid jet.[142]

Besides the improvement of the ablation environment also the ablation efficiency of a single laser shot can be improved. As already mentioned above at Fig. 2.5, a wire target has an improved ablation efficiency compared to a flat target.[21,47,59,143] The reason for this is a reduced or completely inhibited redeposition of ablated material onto the target during cavitation bubble collapse.[143]

A further optimization point is the lens-target distance of maximum ablation. For laser pulse duration in the picosecond range it was reported that the distance of maximum ablation is the focal length.[20,23]

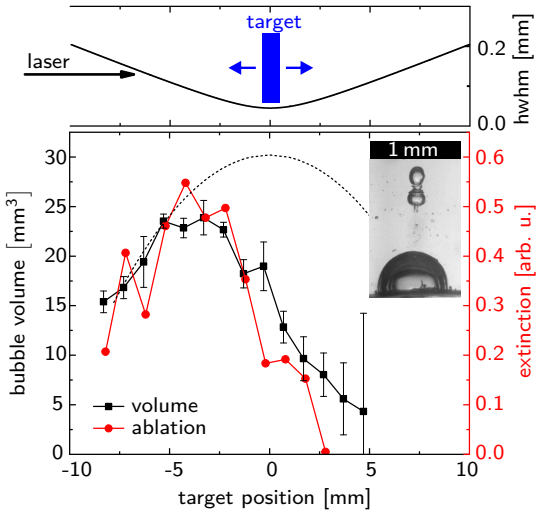

Fig. 2.11: Influence of the target position on the cavitation bubble volume and the ablation rate for nanosecond excitation (1064 nm, 7 ns, 10 mJ stroboscopy and 12 mJ spectroscopy). Top: The laser beam half-width at half-maximum (hwhm) in water (non-diffraction-limited). Bottom: Maximum bubble volume and colloidal extinction (400 nm to 420 nm) as function of the target position relative to the focal point. The dashed line represents the modeled bubble volume for a simple fluence threshold behavior that still peaks at the focus point. Both, the bubble volume and the extinction reach their peak when the target is around 4 mm in front of the focus point. The inset shows optical breakdown in the water when the target is 2.4 mm behind the focal point. Reproduced from Reich et al.[58] **[OI6]**

In contrast, the femtosecond pulse duration showed that the point of highest ablation efficiency is slightly ahead of the focus position.[25,42] This is in accordance with results obtained for nanosecond laser pulses.[58,129,144] Here also a shift of the target position in front of the focal point was found. This is shown in Fig. 2.11 for nanosecond ablation with a lens of focal length in air of 30 mm, which corresponds to around 38 mm in water. Both, the bubble volume and the ablated mass (expressed in colloidal extinction) peaks when the target is about 4 mm in front of the focal point. The focus was determined on the one hand by the lens parameters and on the other hand by determining the ablation point and the optical breakdown point in the water with minimal laser power. Besides the maximum ablation rate[25,58] also the plasma intensity is highest when the focus lies in the target.[25] The close correlation of the cavitation bubble size and the extinction additionally shows the close relation of both quantities during PLAL.

The shift of the point of maximum ablation can not be explained by a simple fluence threshold behavior above which the laser energy is transferred into the bubble. This assumption would lead to a peak efficiency still located at the focal point (see dashed line in Fig. 2.11). If the target is behind the focal point optical breakdown in the water phase can occur as shown in the inset of Fig. 2.11. This shields the trailing laser pulse from the target. The shift of the point of maximum efficiency can be explained by introducing an additional shielding factor.[58]

The difference in the point of maximum efficiency for different laser pulse duration may be explained by the two facts that (i) the plasma shielding is less pronounced for shorter pulse duration and (ii) that femtosecond pulses show a strong self-focusing effect leading to a shifted focal point.[145] Hence, for both, picosecond and femtosecond pulses, the point of maximum efficiency is the focal point. For the shorter impulses, the self-focusing effect must also be taken into account, which reduces the actual focal length compared to the lens parameters.

Two more important aspects for an efficient ablation are the fluence threshold effect[58] and the target roughness, which shows an incubation effect.[60] They are explained in section 6.1.

3 Basics of X-ray scattering and imaging methods

In this chapter the basics of X-ray scattering and imaging techniques are explained. Furthermore the focusing of X-rays to spots by refractive lenses and the generation of X-rays in synchrotrons is described.

In this work nanoparticles are investigated during the ablation process after laser excitation. As they are too small to be investigated by visible light due to the Abbe diffraction limit,[72] X-Rays are used. With X-ray scattering their size distribution as well as their spatial distribution can be analyzed. One powerful technique is the Small-angle X-ray Scattering (SAXS) as it allows to determine the size distribution. It probes only a single spot at once. On the other hand, X-ray imaging methods are being developed for a 2D investigation and can provide different contrast modalities. The scattering contrast allows to actually image the 2D nanoparticle distribution. One can obtain with a single measurement micro- and nanoscale features, such as the laser-induced cavitation bubble and the nanoparticle distribution by the transmission and the scattering contrast, respectively. The third contrast, the differential phase, can give additional information on material interfaces.

To improve the X-ray efficiency in Single-Exposure Multi-Contrast Imaging, in this work 2D lens arrays for hard X-rays were invented. The basics of X-ray focusing by lens array are explained. In the last section of this chapter the generation of X-rays by bending magnets, wigglers and undulators and their monochromatisation is explained briefly.

3.1 The interaction of X-rays with matter

X-rays interact with matter in two ways: they can be scattered or absorbed.[146] The fundamental process is that the electromagnetic wave accelerates the electrons in the atoms and they consequently radiate the scattered wave. In the classical approach, the scattering process is elastic. No energy is transferred to the electron and the scattered wave has the same wavelength as the incident one. In the quantum mechanical description, however, this is not the case. It is an inelastic process in which energy may be transferred to the electron and the scattered wave has a reduced energy. The elastic scattering is the main process if the photon momentum is taken up by atoms and the lattice rather than a single electron. Therefore a classical description is sufficient.[146] The inelastic scattering gets only important for high energies and large scattering angles. It gives only a smooth contribution to the scattering signal as it varies slowly with the scattering angle.[146]

The most elementary scattering object is a free electron. In the X-ray regime the photons are energetic enough that in first approximation also atomic electrons respond like free ones (with respect to resonances).[146] The total scattering length of a single atom can be calculated as the integral over all volume elements $d\boldsymbol{r}$ of the atom containing the electrons:[146]

$$-r_0 f^0(\boldsymbol{q}) = -r_0 \int \rho(r) \cdot e^{i\boldsymbol{q}\cdot\boldsymbol{r}} d\boldsymbol{r} \,, \tag{3.1}$$

where r_0 is the Thomson scattering length, $f^0(\boldsymbol{q})$ the atomic form factor, ρ the electron number density and $\boldsymbol{q}$ the wavevector transfer or scattering vector. The latter can be calculated by $\boldsymbol{q} = 4\pi \sin(\theta)/\lambda$ with 2θ being the angle between incident beam and scattering direction and λ the wavelength. To obtain the scattering amplitude of a molecule or a small particle one has to integrate over all atoms. The details of the Small-angle X-ray Scattering techniques will be given in subsection 3.2.1.

The second interaction of X-ray photons with matter is the attenuation. It occurs due to photoelectric absorption, incoherent Compton scattering and coherent Rayleigh scattering.[147,148] The linear attenuation coefficient μ thus can be decomposed into:

$$\mu = \mu_{pe} + \mu_{coh} + \mu_{incoh} \ , \tag{3.2}$$

where the index *pe* stands for the photoelectric, *coh* for the coherent and *incoh* for the incoherent effect, respectively. All processes depend on the photon energy. The cross section of Compton scattering varies slowly with energy and is the dominant process only at high energies. The coherent Rayleigh scattering has an lower cross section compared to the photoelectric absorption. Therefore the latter is the main absorption process in this work. The absorption follows the Beer-Lambert law as shown in equation (2.1). The absorption coefficient μ has a distinct photon energy dependence. It is inversely proportional to the energy with about the third power. The absorption is a process of expelling electrons from the atom shells this cross section strongly increases when the energy exceeds the binding energy of a deeper shell. Therefore the absorption is a fingerprint of the material. This effect is used in X-ray absorption spectroscopy.[146]

X-rays experience also refraction when entering a medium. As in the visible light range the index of refraction n is of central interest. In the X-ray regime it can be expressed as:[146]

$$n = 1 - \delta + i\beta \ . \tag{3.3}$$

Here δ is the decrement of n from unity and is assigned to refraction processes. It can be calculated by:[149]

$$\delta = \frac{\rho r_0 \lambda^2}{2\pi} \ , \tag{3.4}$$

with ρ the electron density (in matter typically of the order of 1 electron/Å^3), r_0 the Thomson scattering length and λ the wavelength. Normally the X-ray frequencies lie above various resonances of the electrons (photon energy higher than binding energy). Thus the electrons respond as free carriers to the electromagnetic forces. This is the reason why the real part of n is slightly lower than unity.

The imaginary part of the index of refraction β is smaller than δ in the hard X-ray regime. It is assigned to attenuation in matter. It is related to the absorption coefficient μ by:[146]

$$\beta = \frac{\mu\lambda}{4\pi} \ . \tag{3.5}$$

X-rays entering a medium are refracted away from the surface normal in contrary to the visible light regime where they are refracted towards it. This is of importance in this work as 2D arrays of X-ray lenses were developed. For grazing angles (below $\alpha_c = \sqrt{2\delta}$) one observes total external reflection. This is used on the one hand for focusing mirrors as discussed in section 3.5. On the other hand this is a

way for surface sensitive measurements as the evanescent wave only penetrates into the medium a few nanometers. This is much smaller than the normally observed penetration depth.

3.2 X-ray scattering

X-rays get scattered when inhomogeneous samples are investigated. The scattering vector (q) depends on the size of the inhomogeneities. Therefore, the genesis of NPs during laser ablation can be investigated by X-ray scattering methods.[27,30,31,61,117,119,150] A high time resolution of down to 100 ps can be achieved.[61] The scattering from NPs can be divided into two regions in q space: at low angle the scattering only sees a continuum of scattering length distribution. This is called Small-angle X-ray Scattering (SAXS).[146] Since the NPs can also have crystalline domains, a scattering at the atomic lattice can occur. Here the angles are much larger (the (111) Bragg angle of gold is around 20 ° for 15 keV). This crystalline scattering can be measured with Wide-angle X-ray Scattering (WAXS).[146] In Fig. 3.1 the different setups for measuring SAXS and WAXS are shown schematically. In the two following subsections both techniques will be explained in detail.

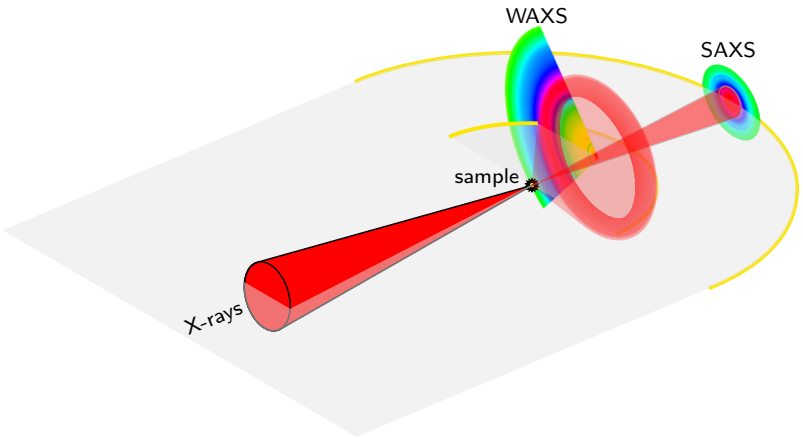

Fig. 3.1: Schematic illustration of wide-angle and small-angle X-ray scattering (WAXS and SAXS) methods. For WAXS the angles are around 20 ° and the sample-to-detector distance is roughly 10 cm while for SAXS the angles are in the µrad range and the sample-to-detector distance can exceed meters.

3.2.1 Small-angle X-ray scattering (SAXS)

Especially SAXS was the basis for the development of the multi-contrast imaging tool in this work and is therefore described in more details. The SAXS signal from an extended sample is the Fourier transform of scattering length density fluctuations across the probed sample. At the small q-values the probed length scale is much larger than atom sizes, so that the material is sensed as continuum. Hence, the scattering intensity is the average over the complete probed volume. The scattering intensity can thus be simplified by using only the averaged excess electron density ρ_{avg}:[146]

$$I^{SAXS}(\boldsymbol{q}) = \left| \int_V f \rho_{avg} \cdot e^{i\boldsymbol{q}\cdot\boldsymbol{r}} dV \right|^2 , \tag{3.6}$$

where f is the atomic scattering length and dV the probed volume element. The integral of this equation can be recognized as a Fourier transform of the electron density of the sample. The scattering amplitude of a solid sphere is therefore its Fourier transform, as depicted in Fig. 3.2. The measured intensity, in contrast, is the square of the absolute value.

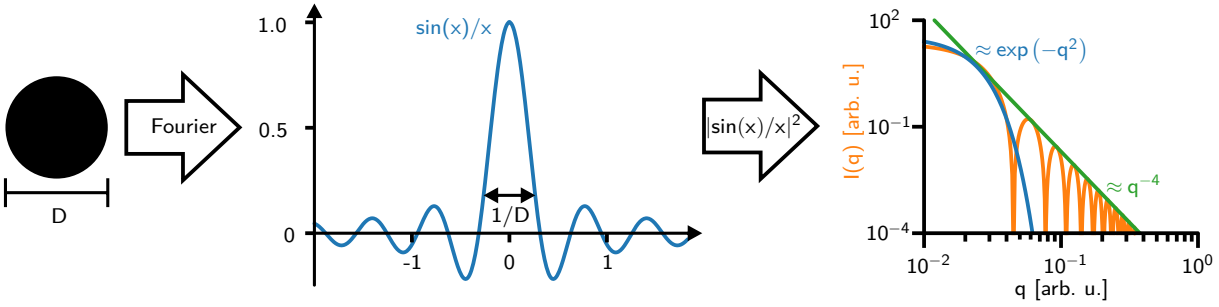

Fig. 3.2: Scattering distribution of a solid sphere. The scattering amplitude of a solid sphere of size D is the Fourier transform of it. The measurable scattering intensity I(**q**) is the square of the amplitude. The scattering intensity can be separated in two regions, the Guinier region for low values of **q** and the Porod region for high values of **q**, respectively.

The simplest sample, which also fits well to the here analyzed NPs, are diluted solid spheres in solution. Then any inter-particle correlations can be neglected. As only the change in electron density between the particle and the solution is of interest the scattering intensity can be rewritten with $\Delta\rho = f_p\rho_p - f_s\rho_s$, where the indexes p and s represent the investigated particle and the surrounding solvent, respectively, to:[146]

$$I^{SAXS}(\boldsymbol{q}) = \Delta\rho^2 V_p^2 |F(\boldsymbol{q})|^2 \ . \tag{3.7}$$

Here V_p is the volume of the particle and $F(\boldsymbol{q})$ the form factor. The latter can be calculated analytically for a solid spheres of radius r by:[146]

$$F(q)_{sphere} = 3 \cdot \left[\frac{\sin(q \cdot r) - q \cdot r \cdot \cos(q \cdot r)}{(q \cdot r)^3} \right] \ . \tag{3.8}$$

Here q and r can be assumed as scalars rather than vectors as the scattering distribution is rotational isotropic in space. If an interaction between the investigated particles exists one has to include a structure factor.[146, 151] Such a case is given if suspensions with high concentrations are investigated.

For small values of $q \cdot r$, the so called Guinier region[152] of the scattering distribution, the form factor can be simplified by an expansion of the trigonometric function leading to a scattering intensity of:

$$I_G^{SAXS}(q) \approx \Delta\rho^2 V_p^2 e^{(q \cdot r)^2/5} \qquad q \cdot r \ll 1 \ . \tag{3.9}$$

For values of $q \cdot r$ larger than unity, the so called Porod region,[153] the form factor can again be simplified and is approximated by:

$$I_P^{SAXS}(q) \approx 9\Delta\rho^2 V_P^2 \frac{1}{2} \frac{1}{q^4 \cdot r^4} \qquad q \cdot r \gg 1 \ . \tag{3.10}$$

Note that I_P^{SAXS} is strongly dependent on the shape of the particle and q has only the power of -4 for solid spheres, while it has the power of -2 for discs and -1 for rods, respectively.

Until now only particles with one defined size are considered. On laser ablation NPs with different sizes are generated. As pointed out before, the scattering intensity is the sum of the individual scattering contributions. Thus the scattering signal of several size levels is the sum of the individual ones. In Fig. 3.3 the scattering intensities of three size levels of NPs are shown. The scattering intensity from small NPs can be superseded by that of large NPs due to the V^2 dependence of the scattering cross section in SAXS.

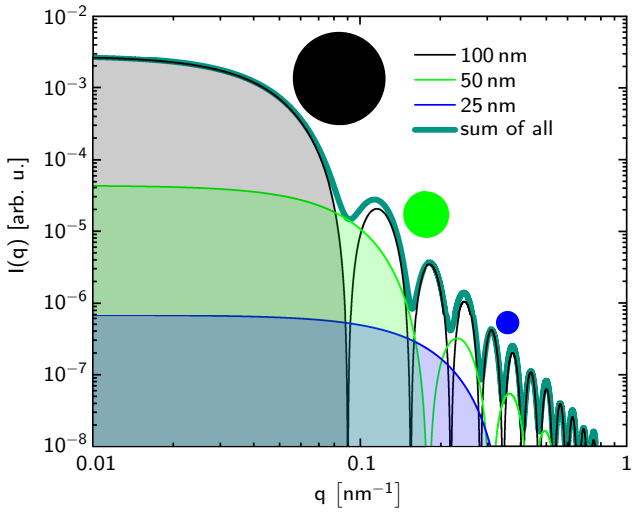

Fig. 3.3: Scattering intensity of spheres with three different sizes. If all sizes are contributing with an equal number of particles to the scattering signal their individual signal just add up.

Polydisperse NP distribution, as typically investigated in PLAL, can be analyzed the Unified fit introduced by Beaucage et al.[29,154,155] It is an empirical model based on the Guinier[152] and Porod[153] approximations. The summation of these two approximations can approximately determine the scatter from a multitude of systems. For one size level of solid sphere the summation is:[154]

$$I(q) = G \cdot \exp\left(\frac{-q^2 R_g^2}{3}\right) + B \cdot \left[\frac{erf\left(\frac{qR_g}{6^{1/2}}\right)^3}{q}\right]^{-4}, \tag{3.11}$$

where G is the exponential prefactor and is dependent to V_p^2, R_g it the radius of gyration which is $R_g = \sqrt{3/5} \cdot r$ for a spherical particle, B is a constant prefactor and depends on the surface area for the particle. The latter is dependent on the shape of the particle compared to the exponent in the Porod region. Thereby this Unified fit considers also clustering and roughness of the investigated particles.

As already mentioned, the scattering distribution of a sample with several size levels is the sum of the individual scattering curves. Therefore, a sum of the fit functions is also used in the Unified fit to determine the average radii and the relative volume contributions of the size levels.

The Porod invariant $P = \int I(q) \cdot q^2 dq$ can be used to determine the total mass of particles of a certain size. This reproduces in good approximation the total mass of the particles in the X-ray path and is independent of the shape and size distribution.[30,153]

3.2.2 Wide-angle X-ray scattering (WAXS)

With WAXS the Bragg peaks of the sample are measured so that their crystalline structure can be determined. The incident X-ray beam gets scattered at each crystal lattice plane leading to an overlay of many reradiated waves. For constructive interference of them the Bragg law of diffraction has to be fulfilled:[146]

$$2d\sin(\theta) = n\lambda \ . \tag{3.12}$$

Here d is the interplanar distance of two atomic layers, θ is the angle between the beam and the lattice planes, n is a positive integer and λ is the wavelength. In Fig. 3.4 the condition for constructive interference at two lattice planes is shown schematically.

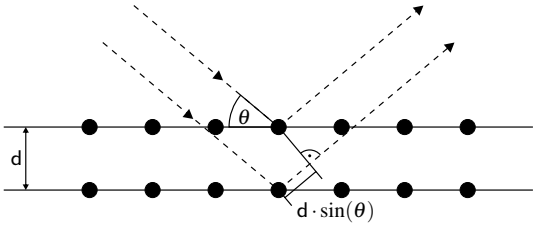

Fig. 3.4: Illustration of Bragg's law of diffraction. The incident beam is scattered at the atoms of the crystal and only at a certain angle θ constructive interference takes place.

At a fixed wavelength, the Bragg angle θ corresponds to a certain lattice distance d. For finite sized particles the width of the Bragg peak depends on the crystal mean size. Therefore one can calculate the crystal mean size τ from the Bragg peak width Δ (full-width at half-maximum) with the Scherrer equation:[156]

$$\tau = \frac{K\lambda}{\Delta\cos\theta} \ , \tag{3.13}$$

with K the Scherrer shape factor. K is slightly smaller than unit and depends not only on the crystal shape (cubic or non-cubic), but also on the instrumental parameters.[157] This broadening effect originates from the reducing number of lattice planes involved in the scattering process for decreasing particles sizes. After background subtraction the peak width can be fitted by a Gaussian function.

3.3 X-ray absorption imaging

The first X-ray absorption image was taken in 1895 by W. C. Röntgen and showed his wife's hand with her wedding ring. Especially the bones and the ring are visible while the soft tissue is only weakly recognizable. As discussed above, the absorption coefficient μ is material and X-ray energy dependent. In actual objects μ has to be assumed to be non-uniform. For an X-ray traveling in x-direction through a sample, the intensity $I(y,z)$ at pixel (y,z) of the detector is:[146]

$$I(y,z) = I_0 \cdot exp\left[-\int \mu(x,y,z)dx\right] \ , \tag{3.14}$$

where I_0 is the primary X-ray intensity. This means, that in absorption imaging only the projection of μ is detected. If one is interested in the 3D material distribution one has to perform a computed

tomography scan. There projections of many incident angles are taken and reconstructed by a Radon transformation.[146]

This direct projection of the sample absorption contrast only holds true as long as the imaging setup is in the contact region. This is valid if the sample-to-detector distance (L) is much smaller than D^2/λ, where D is the sample structure size. For a structure size of $D = 1\,\mu m$ with an X-ray energy of 12 keV ($\lambda = 0.1\,nm$) this condition is only fulfilled for $L \ll 10\,mm$. For samples with structure sizes of $D = 1\,mm$ the distance D^2/λ is equal to 10 km. Hence, for comparably large samples, like the cavitation bubbles in this work, one can still assume to be in the contact region without having problems of Fresnel ($L \approx D^2/\lambda$) or Fraunhofer ($L \gg D^2/\lambda$) diffraction.[146]

The soft tissue of the first X-ray image is hard to see due to the low absorption coefficient of tissue. Despite improvements in technology, it is still difficult to image soft tissue and other samples with low absorption contrast. Therefore several multi-contrast imaging techniques have been invented, where the phase and the scattering contrast improve the material differentiation.

3.4 X-ray multi-contrast imaging

With X-ray multi-contrast imaging not only the pure absorption contrast but also the phase (or differential phase) contrast and the scattering contrast can be measured simultaneously. There are many techniques for measuring both additional contrasts, not all of them provide all contrasts.

One common technique today is the X-ray Grating Interferometry (GI) first published in 2002 by David et al.[158] For phase contrast measurements, this technique is already used in commercial scanners[159] and is about to be implemented in clinical C-arm X-ray systems.[160] It will be explained in subsection 3.4.1 in detail to introduce the contrast formation in multi-contrast imaging. In brief, by a fine line grating as shown in Fig. 3.5 (a) a Talbot carpet is produced that is analyzed by stepping a second analyzer grating directly in front of the camera. The camera itself can not resolve the induced beam pattern. From changes of the step modulations of each pixel the different contrasts can be retrieved.[146]

The first phase contrast measurement technique was a crystal interferometer published in 1965 by Bonse and Hart.[164] Here the incident beam is split into two parts, both are reflected to coincide after one of them passing through the sample leading to interference changes due to the sample. Another pure phase contrast method is propagation-based imaging.[165, 166] The interference fringes in Fresnel diffraction introduced by the sample are measured. With *a priori* information on the sample the phase distortion can be recalculated. In some cases this technique can be used for a simple edge enhancement. In analyzer-based imaging a small X-ray beam intersects the sample and the rocking curve is measured with an additional analyzer crystal.[167] By the change of the rocking curve one can retrieve phase and scattering information.

In the recent past, multi-contrast methods with structured beams have been published. One of them is the edge illumination technique.[168–170] Here the primary beam is split into many beamlets by linear or square apertures. The beamlets pass the sample before they get detected by a masked detector. A perfect alignment of the setup is required so that the beamlets hit the edge of the detector mask. If the sample now changes the beamlet direction due to refraction, the intensity of the corresponding pixel changes. From the intensity change the shift of the beamlet and therefore the differential phase can be measured. When a scan of the apertures is performed, also the scattering signal can be obtained.[169, 170] There are even

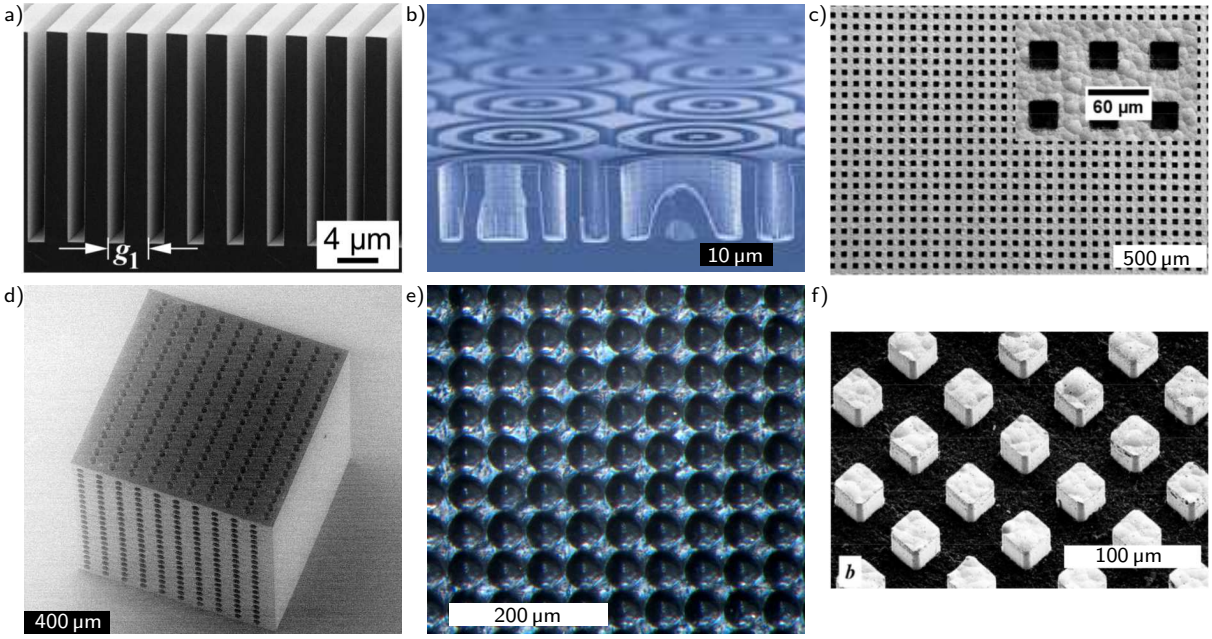

Fig. 3.5: Optical elements used in X-ray multi-contrast imaging techniques. (a) Phase grating[38] and (b) 2D array of circular gratings[161] used in grating interferometry. (c) Hartmann mask,[162] (d) 2D lens array produced by 3D laser writing of crossed cylindrical holes,[163] (e) 2D lens array embossed in polymer foil and (f) inverted Hartmann mask[162] for usage in Hartmann mask-like multi-contrast imaging. (a) ©2005 Optical Society of America. (b) Reprinted with permission from [M. Kagias, Z. Wang, P. Villanueva-Perez, K. Jefimovs, and M. Stampanoni. Phys. Rev. Lett., 116(9):093902, 2016.] Copyright 2016 by the American Physical Society. (d) Reprinted under CC BY 4.0 license. (c) and (f) courtesy of M. Zakharova.

realizations of the edge illumination technique that do not require a detector mask. Here the beamlets are precisely aligned into the intersection of neighboring pixels.[171] However this technique only allows to access the phase contrast.

A more random beam structuring is done in speckle-based multi-contrast imaging. Beam perturbations are introduced by e.g. a sandpaper.[172–174] This optical element must be located far enough from the detector to introduce the propagation based phase contrast of it into the beam. The optical element is scanned in one direction and the contrasts are retrieved by image correlation. The positional shift gives the differential phase contrast and the correlation coefficient corresponds to the scattering contrast.

The last multi-contrast imaging technique is the Hartmann mask-like Single-Exposure Multi-Contrast Imaging (SEMCI) technique. It is explained in detail in the subsection 3.4.2 as this is the technique used and further improved in this work. In short, a broad beam is divided into many beamlets that are detected by an area detector that resolves the beamlets. In Fig. 3.5 (b) to (f) different optical elements for beam division are shown shown. From the change of beamlet properties, the different contrasts can be retrieved. This is a true single exposure technique as no stepping of an optical element or the sample is necessary. Only the pattern change between a separately recorded undisturbed *flat* image and the sample disturbed *radio* image is necessary.

With exception of some publications for GI,[175–177] the SEMCI is the only technique allowing real single exposure imaging. All other multi-contrast techniques require the acquisition of several subimages. This means that several images must be recorded to obtain one set of images of different contrasts. The speckle technique in principle allows a single exposure but only the phase contrast could be sufficiently

reconstructed until now.[178, 179] For GI there is also the possibility to perform a single exposure measurement by a canted grating and moiré fringe analysis.[176, 177] Until now, this technique is not suitable for the mapping of fast processes, because only a 1 kHz frame rate was reached. Hence, it is not suitable for the NP detection during laser ablation. The only technique allowing single exposure combined with a high frame rate is measuring with Hartmann masks or the here developed 2D lens arrays. One further advantage of the Hartmann mask-like imaging are the low requirements on coherence. The imaging process itself does not require coherence as it is based on a pure optical propagation. Coherent illumination is only required for the scattering process on the samples themselves. Since these are in the nanometer size range, a much lower coherence is sufficient for this technique, compared with e.g. GI.

3.4.1 Grating interferometry

In Grating Interferometry (GI) the change of an interference pattern behind a grating is used to obtain the three contrasts absorption, differential phase and scattering simultaneously. In 1836 H. F. Talbot found the self imaging effect of a grating in the optical wavelength range.[180] This is a near-field diffraction effect, which nowadays is called Talbot effect. It was transferred to the X-ray system at the beginning of the 21^{st} century.[38, 158, 175]

In crystal diffractometry, the Ewald sphere construction is a common method for determining the Laue condition for constructive interference. It combines the real and reciprocal space where the intersections of the reciprocal lattice of the crystal and the Ewald sphere fulfills the Laue condition. In a certain way it can be assumed that the interference pattern formation in GI takes place analogously.[181] In reciprocal space a line grid has discrete lines. The positions of the intersections of these lines with the Ewald sphere correspond to the positions of the maxima of the Talbot carpet.[181] The Talbot effect in GI is a near field effect and the interference pattern does not change position with increasing distance from the grating.[146] The same Talbot carpet repeats itself identically until the near-field conditions are no longer met. The Laue condition on which the Ewald sphere construction is based, however, is a far field condition in which the points of constructive interference move at different distances from the diffraction object.

There are two kinds of gratings, absorption gratings and phase gratings. In the ideal case, the first only absorbs the X-ray intensity while the second only introduces a phase difference of $\pi/2$ or π. In GI normally a phase grating with a phase shift of π is used. It has no 0^{th} order while most of the diffracted waves is in the $\pm 1^{st}$ orders.[181] Additionally, the distance between the grating and the first self image is at $1/8$ of the Talbot distance while it is at $1/2$ for a $\pi/2$-phase grating and at the Talbot distance for a absorption grating.[146] Furthermore, for π-phase gratings the lateral period of the self image is half the size of the grating. The smaller distance to the first self image shortens the setup but on the other hand it decreases the phase sensitivity.[181]

A sample that introduces a certain phase shift into the propagating waves changes this interference pattern. This pattern change is imaged by a 2D camera, which determines the final spatial resolution by its pixels size. However, the resolution of cameras is too small to resolve the pattern. The most common routine to record the interference pattern is the phase stepping method. Therefore an analyzer grating (normally an absorption grating) is placed parallel to the first one in the plane of the self image directly in front of the camera. An oscillating intensity is recorded by scanning this grating orthogonal to the

optical axis and to the grating lines over one period. The intensity is highest when the grating is in registry with the self-image and lowest when it is in anti-registry.[146]

From a set of measurements with and without the sample one now can calculate the three contrasts. The sinusoidal intensity function of each pixel is analyzed for its own by a Fourier series.[182, 183] The absorption of the sample corresponds to a change in mean value. The differential phase contrast induced by a phase shift in the sample is obtained by the lateral shift of the intensity modulation.[184] If the sample also scatters X-rays, this leads to an overall increased background signal, which results in a reduced amplitude of the intensity modulation.[183] In comparison to visible light Fourier optics this can be retrieved by the first Fourier component. Quantitatively this is calculated by the visibility $V = (I_{max} - I_{min}) / (I_{max} + I_{min})$ where I_{max} and I_{min} stand for the maximum and minimum intensity, respectively. This is equal to the quotient of the first by the zeroth Fourier amplitude coefficient.[182]

The GI requires sufficient spatial coherent X-rays, otherwise no interference pattern is created. This can only be provided directly by synchrotrons or micro-focus X-ray tubes.[184] For conventional X-ray tubes an additional source grating is needed where each opening can be seen as an individual source leading to high coherence.[184, 185]

In the phase stepping method a complete set of subimages is necessary. Between each acquisition one grating or the sample must be moved precisely. This reduces the possible image repetition rate significantly.[186] There are published approaches allowing retrieval of the contrasts from one single image. With canted gratings one obtains moiré patterns, which can be analyzed by the Fourier transform method.[175–177] With this method, however, the spatial resolution, which depends on the inclination of the grids, is lost. Furthermore, the achieved frame rate of 1.000 Hz is still one order of magnitude too low to image the NPs inside the cavitation bubble after laser excitation.

3.4.2 Single-exposure measurement with Hartmann mask-like setups

Hartmann masks are well known in visible optics to analyze optical elements since 1900.[187] They consist of a regular arrangement of holes in an otherwise opaque foil. Hartmann mask-like setups in which the sample-induced change in beamlet properties is analyzed are inherently Single-Exposure Multi-Contrast Imaging (SEMCI) technology. It was transferred to the X-ray regime first by using line gratings[35, 188] and later by 2D hole gratings.[36, 189–191] To facilitate the reconstruction a regular 2D array is of advantage[36, 189] but also arbitrary arrangements are possible.[52]

The Hartmann mask is used as an example to explain the functional principle of the SEMCI technology. These basic considerations apply without restriction even when lens arrays are used as optical elements. Thanks to the Babinet's principle also the recently developed inverted Hartmann masks follow the same considerations.[48, 49, 162] These masks consist of free standing pillars instead of holes in an otherwise opaque foil.

The broad X-ray beam gets split into many beamlets by the apertures of the hole array as depicted in Fig. 3.6. The 2D beamlet pattern is detected by an area detector. Before introducing the sample into the beamlet pattern one reference image is taken. This image is valid until the setup is changed. From the change in intensity, position and width of each beamlet the three contrasts absorption, deflection (or differential phase) and scattering can be retrieved simultaneously as illustrated (separately for better visibility) in Fig. 3.6. This retrieval can be performed either by individual beamlet analysis (e.g. Gaussian

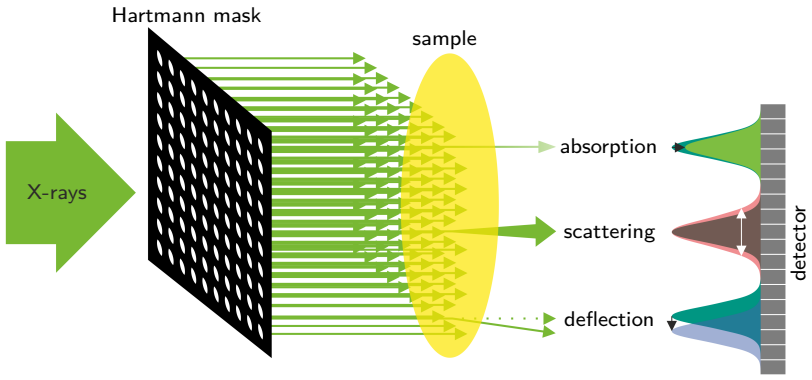

Fig. 3.6: Single-Exposure Multi-Contrast Imaging principle with a Hartmann mask as optical element. The broad X-ray beam gets divided into a 2D array of beamlets. The change of intensity, width and position due to the sample gives the contrasts absorption, scattering and deflection, respectively. Here the three contrast mechanisms are separately illustrated while in reality they are superimposed.

fitting) or by spatial harmonic analysis (e.g. Fourier analysis). The reconstruction of the contrasts is described in chapter 4.2 in detail.

The spatial resolution is not the one of the detecting camera, as in GI, but the beamlet pitch. Hence, there is no improvement in spatial resolution compared to moiré fringe GI but the mechanical robustness is much higher.[41] Only the hole mask has to be aligned to the camera and not two (or sometimes three) gratings have to be aligned to each other. Additionally, the production of a hole array mask with pitches of around 50 µm is much easier than the precise production of the gratings for GI (pitch of a few micrometer).

Additional restrictions for the choice of measurement setup is the time resolution. It is ultimately limited by the available X-ray flux. If lens arrays, as developed in this work, are used instead of absorption masks, the flux losses are reduced to a minimum. However, the camera is also a limiting factor. Sensor sizes of about 500 px × 500 px are required for imaging areas in the centimeter range with a high spatial resolution. Even with state of the art high speed cameras one is limited down to roughly 10 µs temporal resolution for such large sensor sizes.

One data point (for each contrast) can be calculated for one beamlet. For a proper sampling of the individual beamlets at least 3 px × 3 px per beamlet are required.[189] In this work a sampling of six or higher was used. The spatial resolution is the beamlet pitch and was 50 µm and 65 µm in this work. This was required to obtain a suitable NP size sensitivities. Details on the specific setup used in this work will be explained in more details in subsection 4.1.4.

For the reconstruction of the different contrasts of SEMCI several algorithms are proposed in the literature.[35, 40, 41, 52, 191, 192] In detail they will be explained in chapter 4.2. Two of them, the Fourier analysis[189] and the image moment analysis,[193] allow the reconstruction of higher order scattering channels. As simulations (see subsection 4.3.4) showed, these higher orders lead to a changed sensitivity on the scatterers size. This allows to increase the possible contrasts from the three well known one, transmission, differential phase and scattering, to more sophisticated scattering contrasts with several length scale sensitivities.

3.4.3 Absorption contrast

The conventional absorption imaging with X-rays was already described in section 3.3. The X-ray intensity is attenuated depending on the absorption coefficient distribution in the sample. This leads in SEMCI to a decreased intensity of the beamlets but no change in position and width. Two ways are possible to determine the absorption contrast in SEMCI. The peak height of the beamlets or the integral intensity of each beamlet zone can be calculated. When the optical element has a finite absorption additionally the background signal changes with absorption. This leads to an additional kind of absorption contrast, the offset, in Gaussian fitting.

Multi-contrast imaging was developed especially for samples with low absorption contrast. With the additional contrasts, additional information about the samples can be obtained.[188] Hence, normally no strong changes in the absorption are observed. Within this work, however, there is a high absorption contrast due to the induced cavitation bubble. The high absorption change of the cavitation bubble leads to problems with crosstalk between the different contrasts as will be shown in section 4.4. The NPs themselves introduce a very low X-ray absorption and are only visible if they are highly concentrated.[27] The NPs scatter the X-rays and are therefore detectable by the scattering contrast.

3.4.4 Scattering contrast

As described at the beginning of subsection 3.2.1, the X-rays get scattered when samples with an inhomogeneous electron density are investigated. The scattering intensity thereby depends on the scatterer size and shape.[146]

The scattering contrast in multi-contrast imaging is often attributed to small-angle scattering, hence electron density variations, of structures which are not resolvable by the detector.[35, 39, 194, 195] There are more contributions to the scattering contrast, which are not understood in all details until know.[196] X-rays also undergo refraction when passing through a sample. If these phase fluctuations are large enough to be imaged with the setup this leads to differential phase contrast and is explained in the next subsection. Descriptions of wave propagation with unresolvable phase fluctuations resulted in scattering signals equivalent to measurement data.[183] At least for image moment analysis it was shown that the scattering contrast scales similar irrespective if a Gaussian scattering distribution or a binary pure phase object is assumed.[197] It could be shown, that a primary scattering signal could be transferred into a differential phase signal when the magnification of a GI setup was increased.[198] This illustrates very figurative that an unresolvable phase fluctuation can lead to a scattering signal.

Further aspects that change the scatter signal should only be mentioned and not described in detail. Sharp edges in samples lead to an increased scattering signal as shown by simulations and measurement.[199, 200] A comparison of simulations and measurements revealed that not only elastic but also inelastic scattering contributes to the scattering contrast.[201] From simulations a second order derivative differential phase is supposed to change the scattering contrast.[202] Samples showing a lens effect, like the here investigated cavitation bubbles, lead to a changed period of the interference pattern in GI and hence to a certain scattering signal.[200]

Additional effects occur when a polychromatic X-ray source is used. Beam hardening due to an energy-dependent attenuation of the sample changes the visibility in GI and therefore produces an artificial

scattering signal.[203] When a sample generates phase contrast the energy dependent deflection of X-rays leads to a spurious scattering signal.[203,204]

An effect that changes the scatter signal, but is also known from conventional SAXS, is when the assumption of diluted scatterers no longer holds. In SAXS an additional structure factor must be introduced for densely packed scatterers. This leads to a decrease in intensity at small angles and an increase at larger angles at the inverse particle-particle distance.[146,151] In multi-contrast imaging this also leads to an overall decreased scattering signal.[151,201]

The numerous influencing factors on the scattering signal indicate that it does not only result from the often stated pure small-angle scattering. Most of the investigations were done by using GIs and not SEMCI-techniques. It is not yet known whether and to what extent they are also present in SEMCI. Effects like the beam hardening of phase shifts of unresolvable structures do occur in the investigation of the cavitation bubble and should be kept in mind. In the following, the process of SAXS is used to describe the measurement technique, as this is the interesting process for the NP investigation.

In SEMCI the scattering strength at each beamlet is analyzed and therefore it can be considered as a kind of SAXS multiplexing as many simplified SAXS measurements are performed in once. This contrast is often also called "dark-field contrast"[39,40,170,182,190,195,205] or "diffraction contrast".[189,206] Within this work the name ”scattering contrast” will be used exclusively.

The real scattering curves (see Fig. 3.3) can only be measured in detail by a proper SAXS measurement. The SEMCI lacks the appropriate sampling of each individual beamlet to map the distribution in detail, as is the case with a SAXS measurement. Hence, the scattering contrast only represents a strongly simplified SAXS measurement with the advantage of a simultaneous investigation of a whole bunch of positions, respectively a whole area.

In Fig. 3.7 arbitrary example curves of a SAXS measurement and a line section of two neighboring beamlets of a SEMCI setup are plotted. The much higher sampling of SAXS is obvious. In SEMCI the usable range of the scattering vector q is limited. Large q-values, hence small particles, are already placed in the zone of the next beamlet. Thus they can not be analyzed and might lead to disturbances of the neighboring zones. Very large particles are also not detectable as their small scattering vector lies within one pixel of the detector and therefore do not change the beamlet shape. By changing the setup parameters the q-range within each beamlet zone can be set to values suitable for the investigated sample, as discussed later.

This figurative description of the scattering sensitivity is now quantitatively explained. There are several publications dealing with the size sensitivity of scatter imaging.[35,39,183,188,194–196,206–208] There are two contradictory proposals for the scattering intensity for different scatterer sizes.[39,206] For a fixed measurement setup both propose a linear increasing scattering intensity with increasing particle size until a certain value (the auto-correlation length ξ) is reached. After this value Stein et al.[206] proposes a saturation while Lynch et al.[39] proposes a peak and decrease afterwards. The electron density Auto-Correlation Length (ACL) ξ for scattering imaging setups is:[35]

$$\xi = \frac{\lambda \cdot L}{p} \,, \tag{3.15}$$

with L the sample-to-detector distance and p the pitch of the modulated X-ray beam on the detector. It defines the length scale of the structures, which can be investigated with a certain setup. In literature it

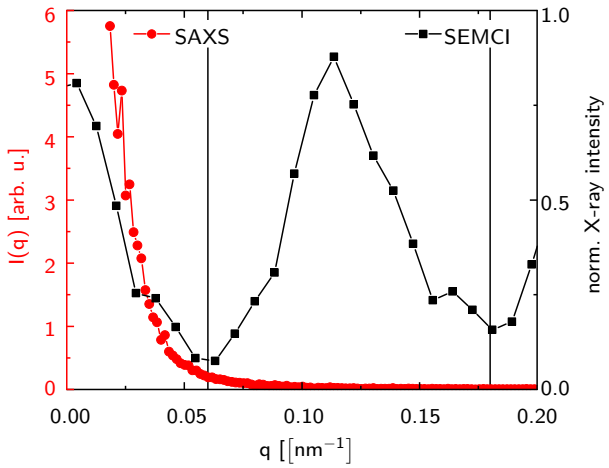

Fig. 3.7: Typical distributions of a Small-angle X-ray Scattering (SAXS) curve and a line section of the beamlets in scattering imaging (SEMCI). The sampling in SAXS is much higher than in SEMCI. The size of the beamlet zones in scattering imaging is shown by the vertical lines.

is often also called scattering length, which must not be confused with the Thomson scattering length. Therefore only the term auto-correlation length is used in this work.

It is worth mentioning that the sample can be placed before and behind the optical element. The theoretical expressions are valid for both geometries with the only exception that L changes to grating-to-detector distance, if the sample is in front of the grating. This interchangeability will be explained later for the phase contrast in more details. In this work the sample is always placed between the optical element and the detector.

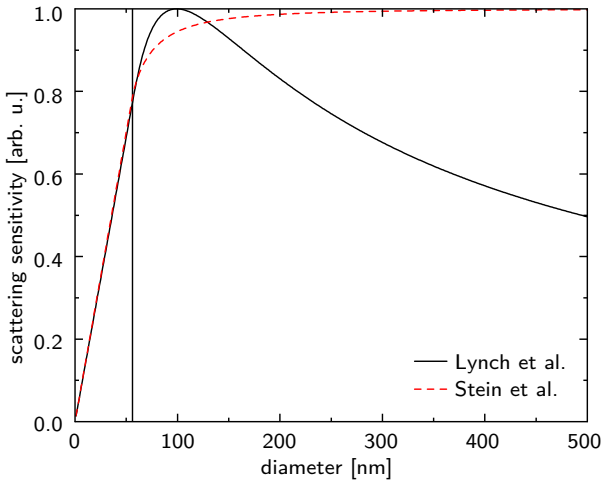

Fig. 3.8: Comparison of normalized scattering sensitivities reported in literature. Lynch et al.[39] belongs to the calculated "Dark-Field Extinction Coefficient" and Stein et al.[206] to the calculated "Diffraction Image Intensity". The auto-correlation length for both is 56 nm (vertical line). Below this value both propose a linear increase with rising scatterer diameter but above Stein et al.[206] propose a saturation while Lynch et al.[39] propose a peak with following decline in sensitivity.

Fig. 3.8 shows the two differently proposed scattering intensity distributions mentioned above for the same ACL. The proposal of Stein et al.,[206] to the best knowledge of now, seems to be wrong.[208] Qualitatively, one would expect that the scattering signal in the limit of very large particles would decay, as the scattering angles of them are very small. At least if the beam broadening due to a particle is smaller

than the detector pixel size one can estimate the scattering function as a δ-distribution leading to an unchanged image. Both images, the undisturbed *flat* and the sample *radio* image, should be identical (except of some absorption) and no scattering signal can be detected. Therefore, the proposal by Stein et al.[206] is problematic. This is further underlined by measured size dependencies in the literature.[208] The Dark-Field Extinction Coefficient (DFEC) was derived for GI where a scattering signal leads to a decreased visibility of the interference pattern. Therefore it is called "extinction coefficient". In SEMCI however, the scattering signal is represented by an increased beamlet width. The DFEC μ_ξ can be calculated by:[39]

$$\mu_\xi = \underbrace{\frac{3\pi^2}{\lambda^2}\varphi\,|\Delta\chi|^2}_{const.} \begin{cases} D\,, & \text{for } D \leq \xi\,; \\ D - \sqrt{D^2-\xi^2}\left(1+\left(\frac{D}{\xi}\right)^2/2\right)+\ldots & \\ \left(\frac{\xi^2}{D}-\frac{\xi^4}{4D^3}\right)\cdot\ln\left[\frac{\frac{D}{\xi}+\sqrt{\left(\frac{D}{\xi}\right)^2-1}}{\frac{D}{\xi}-\sqrt{\left(\frac{D}{\xi}\right)^2-1}}\right]\,, & \text{for } D > \xi\,. \end{cases} \tag{3.16}$$

Here φ is the volume fraction of the scattering structure, $\Delta\chi$ the difference of the complex index of refraction from the sample and the surrounding environment and D the diameter of the scattering structure. Lynch et al.[39] showed the derivation of the DFEC in detail. In short, the disturbance of a flat incident wavefront by the sample is divided into a resolvable and an unresolvable part. Based on wave function calculations, which are again divided into a resolvable and an unresolvable part, it is shown that the visibility of the GI changes according to an exponential decay with the constant μ_ξ.

The derivation was established for a grating interferometer setup. The measured data, however, were obtained with a Ronchi grating and a Hartmann mask and show a good agreement with the calculated DFEC for both parts, below and above the ACL.[39] The simulations in subsection 4.3.4, which are based on the scatter intensity calculated by equation (3.7), additionally prove the approach of the DFEC.

Also for GI a good agreement of the scattering distribution with the DFEC is published by Miller et al.[208] The scattering contrast of glass spheres of different sizes (7 µm to 725 µm) embedded in air and water was measured. The slope of scattering intensity per unit absorption for both conditions was calculated. These slopes display the scattering intensity irrespective of the sample thickness, hence amount of scatterers probed. In Fig. 3.9 the normalized slopes are plotted together with the expected DFEC for their setup. The slopes were normalized in the way that the values for the smallest and largest sample size (7 µm and 725 µm) fit to the DFEC. For both, the slopes in air and water, the values fit quite well to the expected DFEC showing a decrease for samples with sizes above the ACL. Note that the normalization is highly sensitive to the exact scattering intensity of the 7 µm spheres.

Also from the measurements of Prade et al.[194] on silica spheres of different sizes with a grating interferometer one can guess that the scattering intensity drops for samples larger than the ACL. All these results show, that the DFEC calculated by Lynch et al.[39] is a suitable parameter for estimating the scattering intensity of a sample in a certain setup. Furthermore, simulations of the scattering imaging show a good agreement of the DFEC with the retrieved scattering intensity by Fourier analysis as shown in subsection 4.3.4. In consequence, the calculations of Stein et al.[206] for the scattering sensitivity must be considered to be problematic. Nevertheless the idea of measuring at two different ACLs to improve

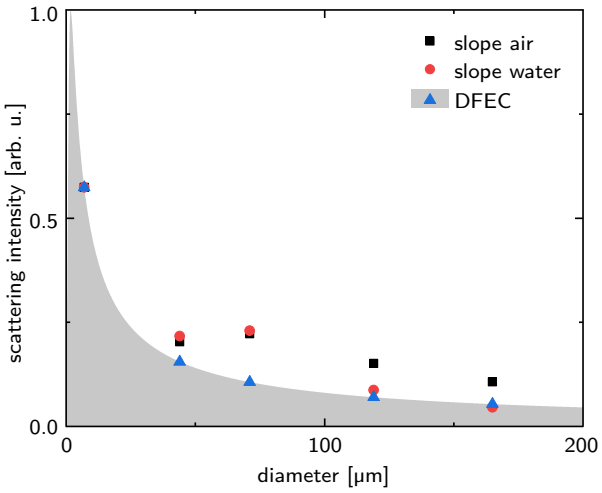

Fig. 3.9: Evaluation of the measured scattering intensities (given as slope of "scatter per unit absorption") obtained by Miller et al.[208] The measured values were normalized to the Dark-Field Extinction Coefficient (DFEC) (for details see text). The scattering intensities for measurements in air and water fit well to the DFEC calculated from Lynch et al.[39] supporting the correctness of this formula. The auto-correlation length of the setup was given as 1 µm.

the sensitivity, which is the main issue of the paper of Stein et al.,[206] is correct and will be used within this work.

The DFEC thus can be used as a proper parameter to calculate the scattering sensitivities for different sample sizes and setup configurations (expressed by different ACLs). Furthermore, it can be used for SEMCI with Ronchi grids and Hartmann masks as well as for GI.

The maximum value of the DFEC is at $D \approx 1.77\xi$. It can be calculated in simplified expression from the setup parameters by:

$$\mu_{\xi}^{max}[\mu\text{m}] = 21.96 \cdot \frac{L[\text{cm}]}{E[\text{keV}] \cdot p[\mu\text{m}]} \ . \tag{3.17}$$

Also ξ can be expressed in simplified version:

$$\xi[\mu\text{m}] = 12.4 \cdot \frac{L[\text{cm}]}{E[\text{keV}] \cdot p[\mu\text{m}]} \ . \tag{3.18}$$

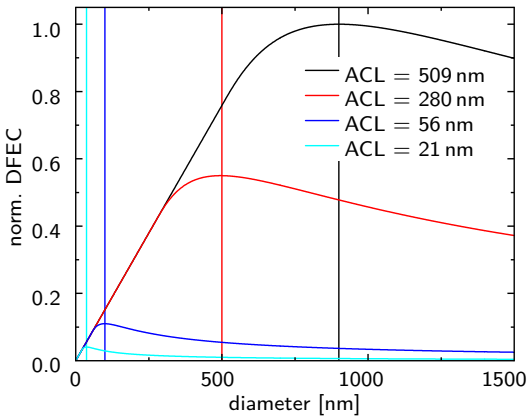

Fig. 3.10: The Dark-Field Extinction Coefficient (DFEC) as function of scatterer diameter for different Auto-Correlation Lengths (ACLs). The volume fraction was kept constant for all curves. The scatterer sizes of maximum extinction coefficient are 37 nm, 100 nm, 500 nm and 900 nm, respectively, as indicated by the vertical lines.

By varying the setup parameters one can change the ACL and thereby the DFEC distribution. Fig. 3.10 shows DFEC curves for four different ACLs. One can clearly see the common linear behavior of all below their specific ACL. The maximum value for the different ACLs increases linearly with the increasing ACL when the volume fraction is kept constant. Therefore, samples with double the diameter result in a doubled scattering intensity. Note that for an equal volume fraction an eightfold increased number of the smaller particles is necessary. Consequently, with decreasing particle size the scattering intensity decreases rapidly making their detection more challenging.

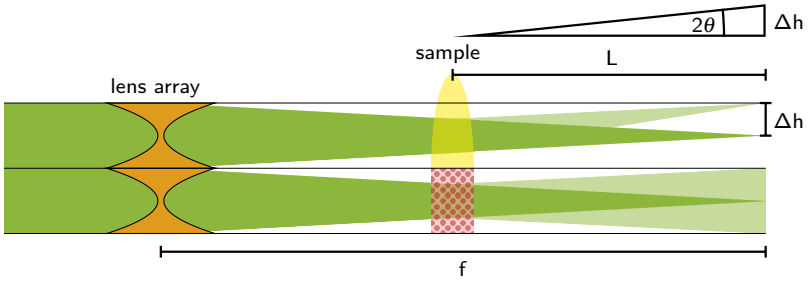

Fig. 3.11: Schematic drawing of the multi-contrast imaging parameters. The X-rays are divided into beamlets by lenses with the focal points laying in the detector plane. The maximum beam deflection (top sample part) is Δh and the maximum scattering width (bottom sample part) is 2Δh.

The q-range of a SEMCI setup is limited, even more than in SAXS. This results from the small scattering angles, which can be detected inside the zone of one beamlet and the low sampling. In Fig. 3.11 the geometrical limits of the SEMCI setup are illustrated for both, beam deflection (top beamlet) and beam broadening (bottom beamlet). One can directly see the limited accessible angle within the beamlet zone. When considering the beamlet size at the sample position being small compared to the beamlet zone the maximum scattering angle θ is:

$$\tan(2\theta) = \frac{\Delta h}{L} \,, \tag{3.19}$$

where Δh is the deviation from the original position on the detector plane. The corresponding scattering vector is then:

$$q = \frac{4\pi \cdot \sin(\theta)}{\lambda} \,. \tag{3.20}$$

With the equations (3.17), (3.19) and (3.20) one can find a direct link between the maximum accessible scattering vector q and the maximum DFEC μ_ξ^{max}, hence the auto-corellation length ξ:

$$q = \pi \cdot \frac{1.77}{\mu_\xi^{max}} \qquad \text{and} \qquad q = \pi \cdot \frac{1}{\xi} \,. \tag{3.21}$$

This allows for a comparison of the scattering curve of a particle with the beamlet of a SEMCI setup. In Fig. 3.12 (a) the scattering curve of a particle with a diameter of 100 nm is plotted with a logarithmic scale, as typical for SAXS data. In SEMCI the change of the direct beam is analyzed while at SAXS the primary beam is excluded. Thus the dynamic range on the detector is different and a linear plotting is more convenient for SEMCI. In Fig. 3.12 (b) the same scattering curve is plotted together with curves of two particles of 37 nm and 500 nm, respectively. Additionally the beamlet intensity of a setup with a $\mu_\xi^{max} = 100\,\text{nm}$ is plotted. The curves for 37 nm and 500 nm coincide with the half-maximum position

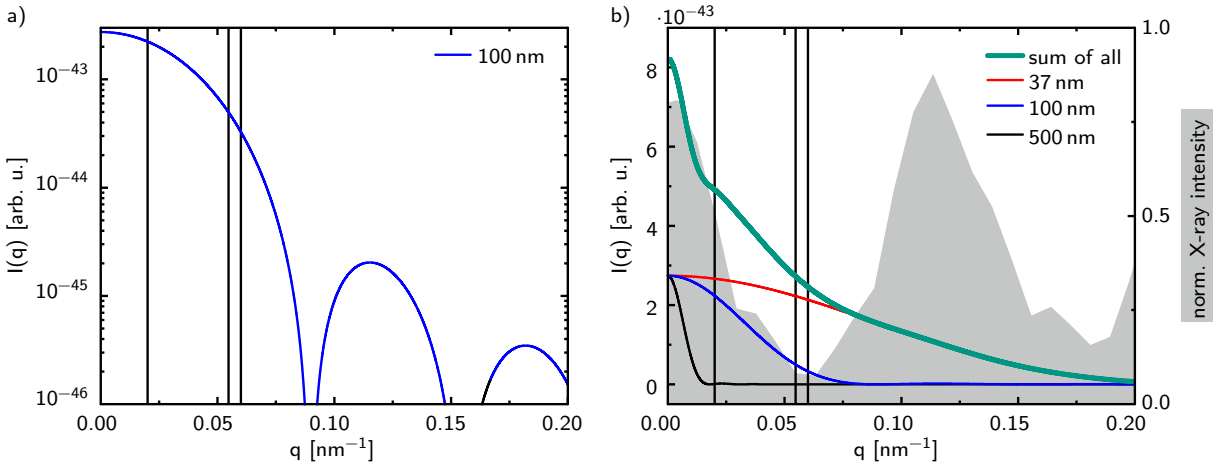

Fig. 3.12: (a) Scattering intensity of a particle with 100 nm diameter. (b) Normalized (to equal mass of the 100 nm particle) scattering intensity in comparison to particles with 37 nm and 500 nm diameter and the sum of all three intensities. In gray the intensity profile of two neighboring beamlets is plotted from a typical experimental setup. The three vertical lines in (a) and (b) represent values of $q \cdot r = 1$, $q \cdot r = 0.056$ and $q \cdot r = 3$ (from left to right) corresponding to the upper limit of the Guinier region, the q-limit of the scattering imaging setup and the lower limit of the Porod region.

of the DFEC of the 100 nm curve. The scattering for $q = 0\,\mathrm{nm}^{-1}$ was kept constant for all three particle sizes implying different particle concentrations.

It is evident that the small size fraction gives an almost constant contribution inside the zone of one beamlet. The scattering distribution of the large size fraction is only located at very small q-values and therefore would lead to a very small change in the beamlet shape. The 100 nm size fraction, for which this setup is optimized, has a scattering distribution lying well inside the beamlet zone. As already pointed out the scattering curve has two regions. The Guinier region at low q-values and the Porod region for high q-values.[209] The q-size of each beamlet zone ($q = 0.056\,\mathrm{nm}^{-1}$) is almost equivalent with the beginning of the Porod region ($q \approx 0.06\,\mathrm{nm}^{-1}$). The Porod region is not of interest in SEMCI as it is mainly sensitive on the scatterer shape and not the size.

The sensitivity in scatterer size is not as high as in SAXS. However, there are two ways to improve the sensitivity. For that purpose images at different ACLs have to be acquired. The first option is to measure at two different ACLs and subtract the resulting scattering signals.[35,206] In Fig. 3.13 (a) the DFEC for two ACLs are plotted together with the difference of them. The difference excludes all scatterer sizes below the lower ACL. This was demonstrated experimentally with two Ronchi grids of different pitches with a lab source.[206] If more size levels are to be distinguished, additional measurements on ACLs in between are required.

When the setup allows for a continuously change of the ACL one can determine the scatterer size of the sample by the fact that the DFEC saturates when the ACL reaches the particle diameter as shown in Fig. 3.13 (b). This was also demonstrated in literature for a grating interferometer[194] and a Hartmann mask.[195] If the sample contains several size levels the scattering signal in dependence of the ACL is the sum of the individual DFECs as shown by the sum-signal in Fig. 3.13 (b).

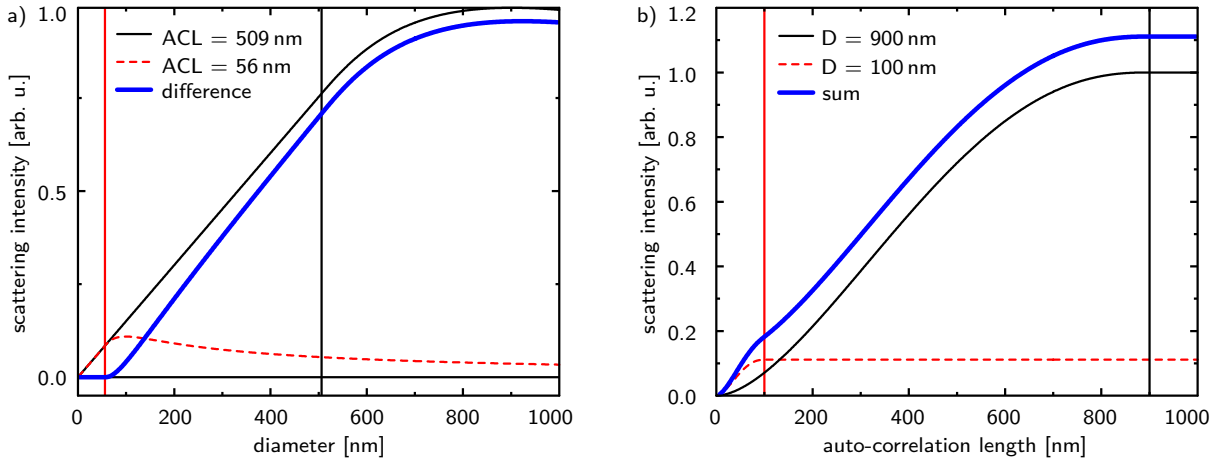

Fig. 3.13: Two possible realizations to improve the size sensitivity of the Single-Exposure Multi-Contrast Imaging. (a) By measuring at two different Auto-Correlation Lengths (ACLs) one can exclude scattering from small particles when subtracting both signals.[206] (b) By a fine scanning of the ACL a superposition of different size levels (diameters D) can be imaged. For all curves the volume fraction was kept constant.

3.4.5 Phase contrast

X-rays get refracted while transmitting through a sample as discussed in detail in section 3.5. The refraction angle depends on the material boundary slope and the index of refraction. The refraction angle α can be measured and is the gradient of the phase Φ of the refracted beam. They correspond to each other by:[146]

$$\alpha_x = \frac{\lambda}{2\pi}\frac{\partial\Phi(x,y)}{\partial x} \qquad \text{and} \qquad \alpha_y = \frac{\lambda}{2\pi}\frac{\partial\Phi(x,y)}{\partial y}\,, \tag{3.22}$$

for the x- and y-direction while assuming the incident beam to go along the z-direction. The phase can be reconstructed by integration and will be explained in detail in subsection 4.2.4.

In SEMCI the differential phase is measured by the displacement of the beamlets induced by the sample. The absolute values of α can be calculated with equation (3.19) with $\alpha = 2\theta$. For a high sensitivity either the detectable displacement has to be small or the sample-to-detector distance (L) has to be large. If lens arrays are used as optical elements this distance is limited. The lens array must be placed at a distance to the detector equal to the focal length. This is also the largest L that can be used. When the sample is positioned before the optical element the sample-to-detector distance interchanges with the grating-to-detector distance in equation (3.19). This is shown schematically in Fig. 3.14 for both, a Hartmann mask (a and c) and for a lens array (b and d).

Let's assume that the phase of the sample only varies slowly inside one beamlet zone and that L is much larger than the displacement Δh. Then the refraction angle α for a fixed Δh decreases inverse linearly with increasing L as shown in Fig. 3.14 (a) and equation (3.19). If the sample position now changes before the optical element the detected Δh stays the same for a certain α irrespective of the sample position as illustrated in Fig. 3.14 (c). Only the inspected point of the sample changes slightly. Hence the sensitivity of the setup is independent of the sample-to-detector distance. The same holds true if a lens array is used instead of a Hartmann mask as shown in Fig. 3.14 (b) and (d).

Comparable as the scattering contrast, also the phase contrast has an upper limit for the refraction angle. If one beamlet is shifted outside of his zone it might fall together with another one. Here the same

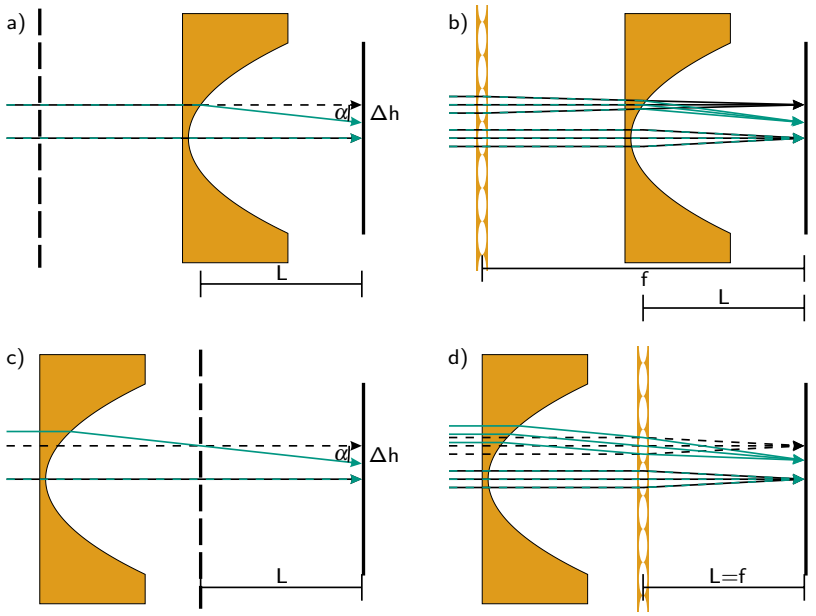

Fig. 3.14: Illustration of the interchangeable setup for phase contrast imaging. A parabolic concave structure (large lens in orange) is used as object here. In both setups, optical element before sample in (a) and (b) and sample before optical element in (c) and (d), the distance for the detected phase shift is the same. This holds true for Hartmann masks in (a) and (c) as well as for lens arrays in (b) and (d).

condition is valid as described for the scattering contrast as shown in Fig. 3.11. Only if the sample shows a strong deflection in combination with only a smooth change of the deflection, the beamlets can be detected well, even if they move into the next beamlet zone.

3.5 X-ray focusing by refractive lenses

The primary X-ray beams at synchrotrons have sizes in the millimeter range and are not suitable for micro- or even nano-probing as they are too large. One can to cut down the beam by a pinhole with the disadvantage of a high intensity loss. The more preferable way is to focus the beam down to the wanted probe size.

In the past decades several possibilities for the focusing of X-ray beams from synchrotrons have been developed. A good overview of the different focusing techniques can be found in Snigirev et al.[210] The advent of third generation storage rings such as the European Synchrotron Radiation Facility (ESRF) in Grenoble (France) made it possible to focus the beams efficiently. The focusing profits from the high brilliance, the low divergence and, in some cases, also the high coherence.

There are three physical effects that can be used for focusing of X-rays. The first process is total external reflection and was first used in 1948.[211] By using two bent orthogonal mirrors, the so called Kirkpatrick-Baez systems, a point focus can be achieved. One year later the focusing by a lead-glass capillary, in which the X-rays are reflected multiple times into a small point, was published.[212] Both setups can only provide single beam spots suitable for point investigations, e.g. SAXS.

The second process is diffraction. This is used in Fresnel zone plates first published in 1952.[213] Normally they consist of a circular diffraction grating leading to a point of constructive interference

when used in monochromatic light. Only if the coherence of the primary beam is equal or larger than the zone plate a diffraction limited focus can be obtained. By producing a 2D array of zone plates also a 2D array of beam spots was achieved and used for SEMCI recently.[161]

The third process is refraction. The index of refraction is only slightly smaller than unity. Thus, the same equations as for lenses in the visible light regime hold true and X-rays can be focused by lenses.[50] In contrast to visible light the lenses have to be concave for focusing. The refractive index and therefore the refractive power is wavelength dependent. Hence, only with monochromatic X-ray illumination really tight foci can be obtained. Using refractive lenses with polychromatic light leads to a chromatic blurring and a consequently broadened spot. The fabrication of 2D arrays of refractive lenses was one of the main goals of this work. Therefore, the working principle will be explained in the following in more detail.

The production of refractive X-ray lenses is a non-trivial task due to the required geometric properties. It was proposed by Suehiro et al.[214] in 1991 and first accomplished by Snigirev et al.[50] in 1996 in the group of Lengeler. These lenses were cylindrical holes in an aluminium alloy leading to a line focus. After the first proof of principle also point foci with spherical lenses[51] or crossed cylindrical lenses[215] were published.

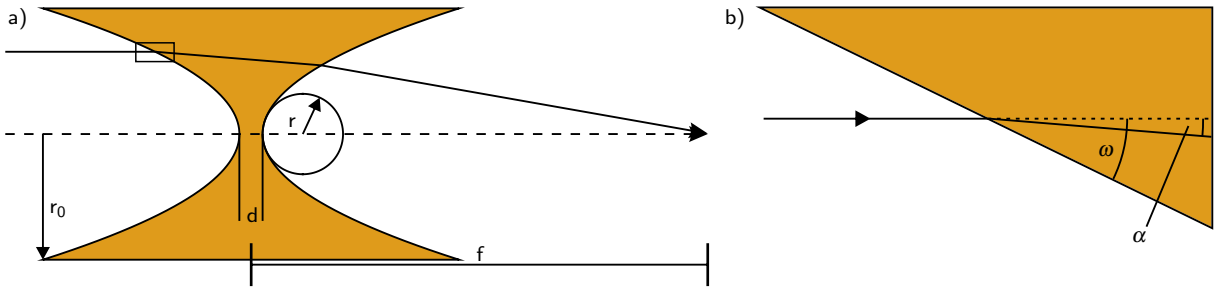

Fig. 3.15: (a) A parabolic focusing X-ray lens. The off-axis beam (solid line) gets deflected towards the optical axis and intersects the on axis beam (dashed line) in the focal length f. This depends on the apex radius r and the material parameter δ. The absorption of the lens depends on the thickness d and the aperture $2R_0$. (b) Detailed image of the entering point of the off-axis beam into the lens material illustrating the refraction of the beam by the angle α.

Parabolic lenses are of advantage compared to cylindrical ones because they do not show spherical aberrations.[51,57,215,216] Furthermore, they do not show pincushion distortion in X-ray micrograph imaging.[217] A schematic drawing of a parabolic X-ray lens in shown in Fig. 3.15 (a). Two beams, the on axis (dashed line) and off-axis (solid line) are coming in parallel from the left and penetrate the lens. The ordinary beam is not deflected while the extraordinary one gets deflected towards the optical axis. The refraction angle α depends on δ and the angle of the material boundary ω as shown in Fig. 3.15 (b). The refraction angle can then be calculated by:[146]

$$\alpha = \delta \cdot \tan(\omega) \; . \tag{3.23}$$

The focal length f of such a biconcave lens is defined as the distance from the middle of the lens to the point where both beams intersect and can be calculated by:[50]

$$f = \frac{r}{2N\delta} \; . \tag{3.24}$$

Here r is the radius of curvature at the apex of the parabola as shown in Fig. 3.15 and δ is the refractive index decrement of the lens material. N is the number of stacked biconcave lenses in a row that is needed to reduce the focal length. Due to the small value of δ, the focal length of a single lens is very large for typical lens materials. By stacking, focal lengths down to the region of tens of centimeters are achievable.[163,218] These stacked lenses are called Compound Refractive Lens (CRL).[219] Reducing the radius of curvature can also be done. The typical values are in the range of 10 µm to 100 µm. These curvatures are already difficult to produce and further reductions are often not feasible. By theoretical calculations it has also been shown that increasing the number of stacked lenses leads to a higher gain compared to decreasing the radius of the lenses.[219]

Besides the design values for the desired focal lengths also the absorption of the lens material is of importance. This is especially the case for materials with a high atomic number. They have the advantage of a higher value of δ but also the absorption coefficient is higher. This can limit the effective aperture of the lenses. Lenses with a kinoform profile do not have these limitations.[51,220,221] In this work only plastic (Kapton® and Mylar®) was used as lens material. They have low atomic numbers, so that the absorption of the lens material plays only a minor role. The effective apertures where the absorption exceeds the gain are much larger for polyimide than those used in this work.[222]

Most of the used CRLs at synchrotrons are made of several tens of lenses. In this case the beam size reduces considerably inside the CRL. When the smallest possible spot size is of interest, one has to change the lens aperture of the single lenses in the stack with the decreasing beam size. Such gradually changing lenses are called adiabatic lenses.[55,223] Only such adiabatic lenses allow a focusing of hard X-rays beyond the critical angle of total reflection.[224] Only stacks of a few lenses are used in this work. An adiabatic change of the lens size was therefore not necessary. On the other hand, this would have been almost impossible with the manufacturing process developed here.

The single lenses within one CRL have to be aligned precisely. Small errors in the positioning do not change the lens capabilities that much. Mostly only the total transmission increases leaving the focal length and spot size unchanged.[222,225]

A 2D lens array - the Compound Array Refractive Lens (CARL)

For a long time CRLs were only used to produce a single X-ray spot. Recently also 1D arrays of line foci[54,56] and point foci[55] were produced. For the aim of this work, the improvement of the SEMCI (see section 3.4), a 2D array of spots, hence point foci, is required. A 2D array of CRLs is shown in Fig. 3.16 and was proposed by Piestrup[226,227] but only a few realizations have been reported in the past.[52,53] One is a hexagonal packed array of polystyrene balls embedded in copper.[52] The second is a 3×3 array of crossed parabolic CRLs made by X-ray lithography.[53] The good focusing capabilities of such an array result in a high gain and small spot sizes. For an imaging tool, as required in this work, an array of only 3×3 spots is not suitable. Furthermore, the pitch of 1 mm of this array is much too large.

The expected parameters of the needed lens array for the SEMCI are a pitch of around 50 µm, a focal length of around 1 m and an array size of approximately 3 mm × 3 mm. The production of such a 2D lens array for the X-ray regime is challenging and could be fulfilled in this work. The production and characterization is shown in chapter 5.

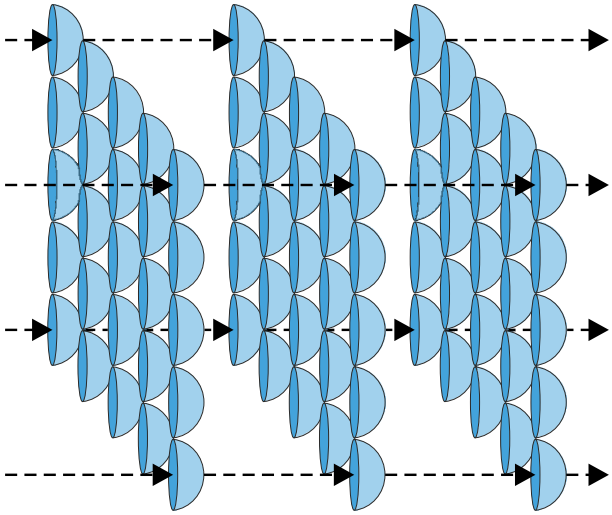

Fig. 3.16: Schematic drawing of a Compound Array Refractive Lens as required and developed in this work. The three 2D lens arrays are stacked on top of each other resulting in a 2D array of Compound Refractive Lenses.

Parallel to this work 2D lens arrays were realized by crossed cylinder lenses produced by 3D direct laser writing by dos Santos Rolo et al.[163] The usage of this lens array as a Shack-Hartmann sensor[228] for hard X-rays was demonstrated by measuring the wavefront of an X-ray diamond CRL. The size was limited to 1 mm × 1 mm × 1 mm, but further improvements in this approach are done at the Institute of Microstructure Technology (IMT) at KIT. First improvements in lens array size have recently been achieved.[218] The characterization of the lens arrays and data analysis were done in cooperation. Furthermore, first steps for 2D lens arrays produced by X-ray lithography are in progress.[229]

3.6 X-ray sources

X-rays are electromagnetic waves with a photon energy of about 100 eV to 1 MeV while there is no consensus about the upper limit.[146] A further differentiation is done between soft and hard X-rays with the border between 3 keV and 5 keV. The most widespread X-ray sources are X-ray tubes. Depending on the machine properties X-rays of characteristic wavelengths are emitted. This radiation is well suited for many applications. However, if high fluxes and (almost) parallel beams are required, synchrotron radiation facilities are required.

Synchrotron light sources are electron storage rings.[146] The electrons are accelerated up to relativistic velocities reaching kinetic energies of 2 GeV to 8 GeV. When these electrons are accelerated perpendicular to their movement, they emit electromagnetic radiation. Such an acceleration happens, in the simplest case, in so called bending magnets. They force the electrons to orbit on a circular path around the ring forced by the applied vertical magnetic fields. The wavelength of the radiation depends on the electron energy E_{el} and the magnetic field B. The critical energy of a bending magnet is:[230]

$$E_c = \hbar\omega_c = \frac{3}{2}\frac{\hbar\gamma^2 eB}{m} \,. \tag{3.25}$$

Here $\hbar$ is the reduced Planck constant, ω_c the critical frequency, $-e$ and m the electron charge and mass, respectively, and γ the relativistic factor $\gamma = E_{el}/(mc^2)$. The emitted spectrum of a bending magnet

is a broad spectrum around the critical energy with a fast decay for lower energies and a longer tail for higher energies. In Fig. 3.17 the characteristic spectrum of the Topo-Tomo instrument of the Synchrotron Radiation Source at KIT is plotted. Additionally, the spectrum after the typical filtering applied in the following experiments with 0.25 mm beryllium (Be) and 0.2 mm aluminum (Al) as well as the further beam hardening due to 5 mm H_2O (ablation chamber thickness) is shown. The opening angle of the beam is $1/\gamma$.[146] For the above mentioned beamline this divergence is 2×10^{-4}.

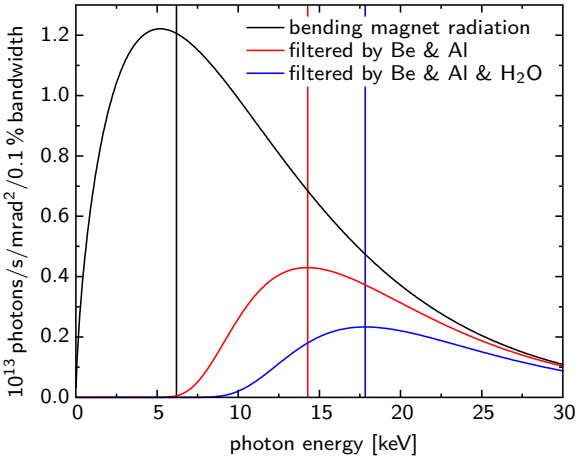

Fig. 3.17: Characteristic spectra of the Topo-Tomo instrument of the Synchrotron Radiation Source at KIT. The bending magnet radiation was calculated for an electron energy of 2.5 GeV, a ring current of 100 mA and a magnetic field of 1.5 T leading to the critical energy of 6.2 keV. After the filtering by 0.25 mm of beryllium (Be), 0.2 mm of aluminum (Al) the peak energy is 14.3 keV. After additional beam hardening due to 5 mm of water (H_2O) the peak energy shifts to 17.8 keV. The curves were obtained by.[231, 232]

Two more efficient ways to produce X-ray beams compared to bending magnets are wigglers and undulators.[146] These devices are inserted into straight sections of the storage rings laying between two bending magnets and are called insertion devices. Wigglers are in principle a stack of many alternately-poled bending magnets in a row. The electrons undergo many oscillations inside the wiggler instead of one in the bending magnet. This leads to an added up higher X-ray beam intensity while the spectrum stays the same.

Undulators also have an alternating magnet section but the electron beam bends are shallower due to smaller magnet periods. This leads on the one hand to a smaller opening angle compared to wigglers and bending magnets. On the other hand the emitted X-ray beams of the bends do overlap now and can interfere with each other. As only certain wavelengths can interfere constructively, the spectra is no longer broad. It has high peaks of particular wavelengths of the different harmonics. These harmonics can be shifted in wavelength by changing the gap in the undulator leading to a tunable device.

All the X-ray sources of a synchrotron do radiate X-rays of a certain bandwidth. The bandwidth of the bending magnets and wigglers is several tens of keV wide and the emitted beam is called "white beam". Undulators have a much smaller bandwidth of just a fraction of 1 keV. These beams are called "pink beam". A really monochromatic beam of just some eV bandwidth can only be obtained by using a monochromator.[233] They consist of crystals, mainly made of silicon. The Bragg's law mentioned in equation (3.12) defines a specific reflection angle for each wavelength. The wavelength of constructive interference can therefore be adjusted by the angle θ.

Often multilayers are used instead of single crystals.[234] Then d stands for the distance between the layer repeat unit. By selecting the appropriate multilayer material, period thicknesses and thickness gradients, almost any wavelength and bandwidth can be adjusted. They allow a higher flux with the expense of a higher bandwidth.[235] The advantage of a double monochromator with parallel mirrors in the opposite direction is that the beam direction after the monochromator remains constant for all wavelengths.

Many aspects play a role if the quality of an X-ray beam is characterized. Combining all of them leads to the brilliance of the beam, which can be calculated as:[146]

$$\text{brilliance} = \frac{\text{photons}/s}{mrad^2 \cdot (mm^2 \text{ source size}) \cdot (0.1\,\% \text{ bandwidth})} \,. \tag{3.26}$$

The first aspect of the brilliance is the intensity, which is equivalent to the amount of photons per second arriving at the sample. The second quantity is the collimation defining how much the beam diverges and is expressed in milli-radians for both, the horizontal and vertical direction. The source size (also in both directions) is of great importance, especially if the beam is to be focused strongly. Furthermore the energy spread is of interest. As discussed above the different sources produce different spectral distributions. The convention is to use the relative bandwidth of the beam used compared to 0.1 %.

4 Experimental setups

In this chapter the experimental setups, the multi-contrast reconstruction algorithms and simulations of the scattering imaging are presented. At the end a comparison of the different multi-contrast reconstruction algorithms with suggestions of their use is given.

For the *in situ* investigation of the ablation process several ablation chambers were designed and produced by 3D printing. The imaging of the ablation event was performed by optical and X-ray imaging in three different modes:

- Videographic mode: a sequence of images are recorded for one ablation event.
- Stroboscopic mode: each image corresponds to a new ablation event and time courses are produced by mounting images with shifted delays between laser excitation and image acquisition.
- Interleaving mode: combination of videographic and stroboscopic mode. Images from several videos captured in videographic mode with shifted delays (delay shift are a fractional of the delay steps in videographic mode) are interleaved to produce time courses with a higher frame rate than possible in videographic mode.

The X-ray multi-contrast imaging was performed at synchrotron beamlines providing an X-ray illumination of high flux and brilliance. The multi-contrast imaging was performed in interleaving mode with an additional averaging over several events.

For the retrieval of the different contrasts from the multi-contrast imaging several algorithms are known from literature. In this work the four algorithms (i) Gaussian fitting of single spots, (ii) Fourier analysis, (iii) image moment analysis of single spots and (iv) visibility calculation are examined for their abilities regarding NP detection. By simulating typical multi-contrast images in combination with measured data, the assets and drawbacks of the different reconstruction algorithms are pointed out. In addition, the agreement of the scattering intensities from the simulations based on scattering theory with the heuristic approach in the literature proves the validity of this approach.

In this chapter only the conceptional experimental setups are described. The detailed settings for each single measurement mentioned in the text are listed in the "List of Experiments" and are referenced in the text in bold square brackets, e.g. ***[Sim1]****.*

4.1 Setups for *in situ* analysis of the laser ablation process

4.1.1 Lasers used in this work

In this work four different lasers were used. In Table 4.1 they are listed together with their main parameters. For most of the experiments the Nd:YAG multimode laser "Continuum Minilite I" was used. It can be triggered externally, affecting either the flash lamp or the Q-switch. Especially for the X-ray scattering

Table 4.1: Lasers used in this work together with the used parameters.

type	pulse duration	wavelength	pulse energy	repetition rate
Continuum Minilite I ND:YAK multimode	7 ns	1064 nm	up to 11 mJ	up to 10 Hz
EdgeWave InnoSlab PX400-1-GM SN769	12 ps	1064 nm	1 mJ	1 kHz and 26 kHz
Coherent Legend Ti:Sa regenerative amplifier	2 ps	800 nm	2.7 mJ	1 kHz
EdgeWave HD-40I-E	6 ns	1064 nm	10 mJ	200 Hz

imaging this was of great advantage as the laser could be used as slave in the signal chain. The jitter is ±5 ns. For the SAXS experiments with high temporal resolution the ”EdgeWave InnoSlab” was used. In the free trigger mode one can trigger the amplifier by pulse picking on the seeder pulses (repetition rate 50 MHz). This leads to a maximum jitter of 20 ns, which is still acceptable for the investigations in this work, which are in the microsecond time range. The ”Coherent Legend” was used to investigate the crystallinity of the NPs. It is a laser system implemented into the beamline and the simultaneity of the X-ray beam and the laser was controlled with a dual detector. The ”EdgeWave HD-40I-E” was used for the X-ray scattering investigation of the NP distribution in the cavitation bubble and the agglomeration during bubble collapse.

4.1.2 Ablation chambers

Most of the ablation investigations published in literature are done in batch chambers (often beakers) with no water movement or in semi-batch chambers where the water is circulated but still accumulates a lot of NPs.[26,121,131,132] This leads inevitably to laser intensity reduction due to NP shielding and laser fragmentation of the already generated NPs, as discussed before. In this work the fundamental physical processes of the ablation are investigated and therefore batch chambers are not suitable.

For the *in situ* investigation of the ablation process an ablation chamber is required, which allows on the one hand a direct optical access to the ablation spot for X-rays and visible light. On the other hand each single ablation event has to occur under comparable conditions. This requires a refreshment of the ablation area between two laser shots by exchanging the water and moving the target to a new ablation spot. With the flow-chambers presented, this work is rather unique in the field of PLAL.

In Fig. 4.1 the different ablation chamber designs used within this work are shown. The three flow-chambers in (a) to (c) were used mostly as they can be used without intervention for hours. Especially for the X-ray scattering imaging measurements, where an averaging of about 1 h of continuous ablation was necessary, this was of huge advantage. The three chambers (d) to (f) were used for spectroscopy and optical imaging.

The flow-chambers in (a) to (c) have water channels with inlet at bottom and outlet at top (blue cylinders). The bottom-up water flow has been used to remove persistent gas bubbles that are either in the

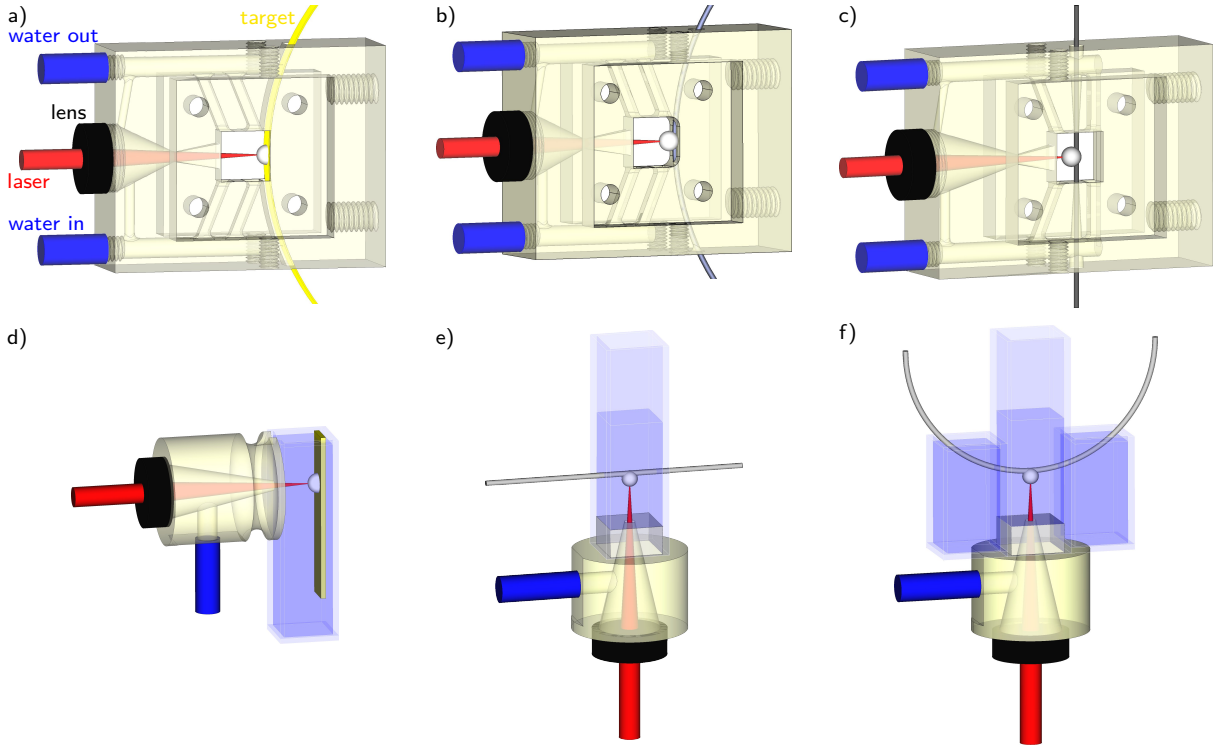

Fig. 4.1: The different ablation chamber designs used in this work. (a) to (c) are flow-chambers with optimized water channels while (d) to (f) only allow a minor liquid flow. (a) and (d) are for ribbon targets and (c), (d), (e) and (f) are for wire targets. (e) was specially designed for the *in situ* optical spectroscopy, while (f) was used for imaging in wire direction.

water or formed by water splitting during the ablation process.[16] The water was fed into and removed from the inner ablation volume of 10 mm × 10 mm × 0.5 mm via two channels each to reduce turbulences. The entrance and exit of the target was sealed with silicon plates fixated by frames. For access to the ablation point, the inner volume was sealed by glass and Kapton® windows for optical and X-ray examinations, respectively.

The laser was coupled in via a plan-convex lens (black cylinders). This lens (nominal focal length f = 30 mm, Thorlabs, LA-1289 C) focused the laser onto the target. The effective focal length in water with the planar side towards the target was calculated by "Winlens Basic" (Version 1.2.6, Qioptiq, Excelitas Technologies Corp., Waltham, USA) to be 38 mm behind the planar side. The distance between lens and target was just 35 mm because this is the position of the most efficient ablation (see section 2.2). An additional water channel ranged from the water entrance over the void behind the lens directly to the water exit to remove gas bubbles. Here the exiting channel was a bit smaller than the entrance to ensure a second flow along the laser path to prevent NPs to reach and contaminate the lens. The two windows perpendicular to the laser beam and the target were sealed by glass plates for optical imaging and by Kapton® foils for X-ray investigation, respectively. The windows were additionally sealed by a silicon plate and fixated by a frame.

The ablation chambers were printed by a 3D printer (ProJet® HD 3500 Plus, 3D Systems GmbH, Darmstadt, Germany) with a high resolution of below 35 µm. It prints volume filled structures while

channels are filled with wax. This can be removed thermally afterwards. The high resolution printing even allowed to directly print all threads needed.

The three other ablation chambers in Fig. 4.1 (d) to (f) were designed for individual optical imaging and spectroscopy needs. Here a suitable adapter to mount the focusing lens onto a standard cuvette was 3D printed. This adapter was also used to ensure a distance between the lens and the target of 35 mm. These cuvette chambers were designed to image rigid targets (d) and wires perpendicular (e) and also along (f) the wire direction.

One aspect that must be considered is the non-negligible absorption of water at the laser wavelength of 1064 nm. The extinction coefficient is 14.2 m^{-1} in this case.[236] This leads to only 60 % transmission after a laser path in water of 35 mm.

4.1.3 Optical imaging setup

The cavitation bubble, persistent gas bubbles, plasma and also plumes of NPs, all induced by the laser shot, were investigated with an optical imaging setup. It consisted of a camera, a flash lamp and a delay generator for synchronization.

As camera a visible-light monochromatic CMOS "Basler acA1300-60gm" with 1280 px × 1024 px was used. The pixel size is 5.3 µm × 5.3 µm and the maximum frame rate at full resolution is 60 Hz. As imaging lens a 50 mm "TV lens" (Ernitec) with a magnification of around 1.3 was mounted onto the camera. The camera is externally triggerable by a Transistor-Transistor Logic (TTL) signal. The minimal exposure time is 10 µs. To reduce this time, the camera trigger time was slightly shifted with respect to the illuminating flash lamp so that not the complete exposure time was illuminated. With this an exposure time of roughly 5 µs was achieved.

As flash lamp a Xenon lamp "Rheintacho RT-Strobe 3000" with 5 µs flash duration was used. An additional diffusor foil was used to ensure a homogeneous illumination. Alternatively shadowgraphic imaging with parallel illumination is possible, which prevents one to image the interior part of the bubble. Note that still with this setup not the complete interior of the bubble can be imaged. The bubble acts as a lens for the light leading to a black rim at the border of the bubble (see discussion to Fig. 2.5).

The triggering of the laser, the flash lamp and the camera were done with the delay generator "Research Instruments DG535". One important issue for the imaging of the complete time sequence of the ablation is a free triggerable laser as the internal delay times of the camera (around 70 µs) and the flash lamp (around 20 µs) are high. Therefore the trigger output of a laser is unusable for triggering the camera if the early stage of the cavitation bubble is of interest. The laser used mainly within this work was Q-switch and flash-lamp triggerable, which allowed all delay times of interest.

The frame rate of the camera is much slower than the ablation bubble dynamics occur. Hence, the imaging of the bubble dynamics was done in stroboscopic mode. For each image a new laser shot was applied to the target while the delay between the laser shot and the camera was shifted. The delay generator was operated remotely (over GBIP access with GPIB-ETHERNET (GPIB-LAN) Controller 1.2, Prologix, LLC) by a Python script. Movies of lower time resolution were acquired in pump-record mode. Here the delay generator only triggered the laser and a burst generator (33210A, Agilent), which then triggered the camera.

4.1.4 X-ray scattering imaging setup

For the scattering imaging the setup was similar to the optical imaging. The flow-chambers were used due to their reproducible ablation. As windows two thin Kapton® foils were used. The scattering imaging was performed at synchrotrons (ufo station at the Synchrotron Radiation Source at KIT, Karlsruhe, Germany and ID19 at the ESRF, Grenoble, France) as they provide an almost parallel X-ray beam of a high flux.

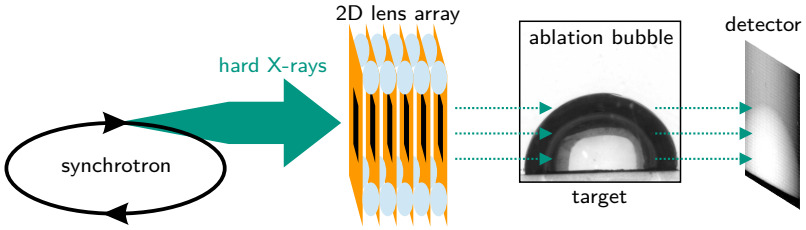

Fig. 4.2: Setup of the scattering imaging with a 2D lens array as optical element. The broad X-ray beam coming from the synchrotron is divided into many beamlets by the optical element before they interact with the sample (here the nanoparticle filled ablation bubble) and get detected by a scintillator coupled 2D camera.

Fig. 4.2 illustrates the scattering imaging setup. The synchrotron provides a broad X-ray beam, which is almost parallel at the experimental point. The distance from the source to the sample is in the order of several tens of meters while the investigating area is only some square millimeter large, the divergence is very small. The 2D lens array (as well as a 2D hole array) divides the broad X-ray beam into many tiny beamlets. They penetrate through the sample where they get distorted. The X-rays are detected indirectly. First they are transformed into visible light by a scintillator before this light is finally detected by a lens coupled camera. For details see the ”List of Experiments”.

When a CARL is used as an optical element, the distance between it and the detector must be around the focal length to achieve good beam focusing. For hole arrays there is no limitation in this point, since the beamlets are only generated by cutting the primary beam. To reduce blurring due to the divergence of the beam a short distance is of advantage. As discussed in subsection 3.4.4 the distance between the sample and the detector defines the scatterer size sensitivity of the setup. The position of the optical element should therefore be suitable for the required sample-to-detector distance. In this work the distance between the sample and the detector was between 3 cm and 40 cm.

Signal chain for triggering and acquisition scheme

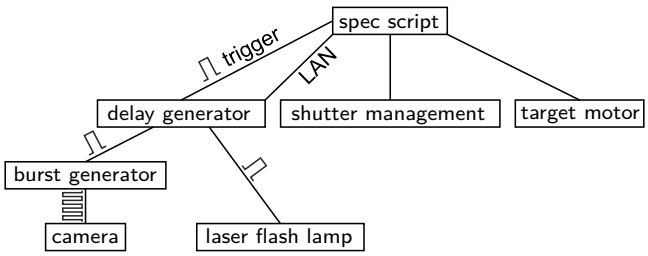

Fig. 4.3: Acquisition control chain for multi-contrast imaging at a synchrotron. The main control is done by a script in "spec". For the accurate timing between the laser and the camera acquisition a delay generator and a burst generator are used. The latter triggers each image acquisition of the camera, which runs in external trigger mode.

The standard control software at synchrotron beamlines is ”spec” (Certified Scientific Software, Cambridge, USA). For the SEMCI of the ablation event a script controlled the complete acquisition as illustrated in Fig. 4.3. The motor for target movement was turned on for a whole acquisition period to ensure a continuous refreshment of the ablation spot. It was stopped in between to save target material. The water, however, was pumped continuously without control by the script. The laser and camera were triggered by a delay generator to obtain a precise time delay between them. For each laser shot spec only sends a start signal to the delay generator, which then controlled the laser and image acquisition. This is necessary as the timing of the spec software is not precise enough. From the delay generator the laser flash lamp as well as a burst generator (33210A, Agilent) were triggered. The latter was used to give a defined number of pulses as acquisition trigger to the camera (pco.dimax). So for each trigger pulse of spec one laser shot was fired and a complete sequence of images were recorded by the camera. The delay between the laser and the camera was set by the delay generator. For a later interleaving of recorded videos the delay was changed via the LAN-connection to the delay generator.

One acquisition scheme consisted of several dark videos without X-rays, a number of bright videos with X-rays and again several dark videos. Therefore, the X-ray shutter was controlled by spec accordingly. Typically four dark videos, 200 bright videos and again four dark videos were taken. Each video contained 40 images. The maximum frame rate of the camera was limited to 12.5 kHz due to the needed image size. To increase the frame rate an interleaving was done resulting in final frame rate of around 40 kHz. So the 200 recorded bright videos consisted of sets of videos of shifted time delays. All images of one measurement were directly sorted and averaged according to their delay time. The dark current was subtracted. On basis of these averaged data the multi-contrast analysis was performed.

Scattering sensitivity shift due to white beam illumination and beam hardening in the cavitation bubble

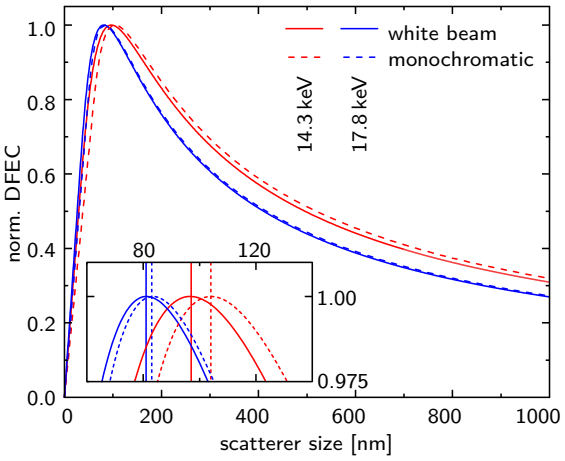

Fig. 4.4: Shift of the Dark-Field Extinction Coefficient (DFEC) due to white beam illumination and beam weakening in the cavitation bubble. The DFEC maximum shifts only minor between monochromatic and white beam illumination (from 104 nm to 97 nm at 14.3 keV). In addition, the shift, which is introduced by a changed peak energy (from 14.3 keV to 17.8 keV), is not very strong (from 97 nm to 81 nm). The assumed sample-to-detector distance is 4.4 cm and the spot pattern pitch is 65 µm.

The scatterer size sensitivity in SEMCI as known from literature[39] is calculated only for a monochromatic illumination. If the scattering imaging is performed in white beam illumination the size sensitivity

only changes slightly as shown in Fig. 4.4. A stronger change is observed, if the peak energy shifts. The peak energy increases due to the energy-dependent absorption of the sample and is referred to as beam hardening.[203,204] In this work the peak energy is expected to change from 14.3 keV to 17.8 keV when the X-rays have to pass through the additional 5 mm of water in the ablation chamber. Thereby the DFEC maximum shifts from 97 nm to 81 nm. During the ablation, however, a water column decrease from 5 mm to 2.7 mm was observed. Hence the change in peak sensitivity is only around 10 nm. This shows, that in first approximation the maximum of the DFEC can be calculated assuming a monochromatic illumination and also the change in peak sensitivity due to a changed X-ray spectra during the cavitation bubble appearance is not very strong.

Nanoparticle detection ability of the SEMCI technique

The particle sizes of the ablated material during PLAL ranges from single atoms up to NPs with diameters of roughly 100 nm (see subsection 2.1.6). The two mainly investigated size fractions in literature are the primary (5 nm to 15 nm) and secondary (20 nm to 80 nm) NPs.[27,31,117] The more abundant size fraction are clusters with sizes between 1 nm and 3 nm as revealed by Letzel et al.[28] using an analytical ultracentrifuge.

In scattering imaging the peak sensitivity μ_ξ^{max} depends according to:

$$\mu_\xi^{max} \propto \frac{L}{E \cdot p} \quad , \tag{4.1}$$

with L the sample-to-detector distance, E the X-ray energy and p the spot pattern pitch. For the detection of primary NPs or even clusters L has to be small or E and p large. The first two are technically limited by the setup geometry and the beamline parameters. The pitch also can not be varied independently as it determines the resolution of the final contrast images. Therefore one can only detect the secondary particles with the SEMCI technique used in this work. With the used CARL a $\mu_\xi^{max} = 100\,\text{nm}$ was obtained, which allowed the detection of zinc NPs after an ablation on a wire. The size quenching of gold NPs due to electrolytes was investigated with a Hartmann mask with a $\mu_\xi^{max} = 55\,\text{nm}$. Here the absence of secondary particles in a micromolar solution of sodium chloride (NaCl) could be shown by a scattering intensity reduction in contrast to a pure water liquid phase. These results are presented in section 6.3.

Expected origins of spurious scattering signals

The scattering contrast normally is referred to small-angle scattering of the sample.[35,39] As explained in subsection 3.4.4, the scattering contrast can also have other origins.[41,197,199–201,203] Not all of them are expected to arise in SEMCI as most of them were originally observed in GI.

Two points can be excluded. First, the breakdown of the dilution approximation, which would change the expected small-angle scattering distribution[151] and second the lens effect[200] leading to a changed pattern period. The latter is only relevant for GI but not for Hartmann mask-like imaging. Here the patterned beam can be resolved by the detector. Hence, a positional shift of the spots can directly be imaged leading to differential phase contrast and not to a spurious scattering signal.

Several aspects of scattering contrast origin are very likely to happen also in SEMCI. At sharp edges,[199] where parts of one beamlet are affected and others not, the beamlet shape will inevitably change and hence lead to a scattering signal. A phase shift at structures, which are not resolvable,[197] also leads to a broadening of the beamlet. A scattering signal from inelastic scattering,[201] which normally is attributed to a smoothly varying background signal,[146] can also not be excluded. Beam hardening,[203] or in our case beam softening due to a reduced absorption, will take place. It was already shown that this will slightly change the scattering sensitivity distribution. The changed X-ray energy will furthermore change the focal length of CARLs by 16 % (peak energy change from 16.6 keV to 17.8 keV for water thickness change from 2.7 5mm). In white beam, the depth of focus is very large, so that a spot size change due to the shifted focus point cannot be completely excluded. Only with Hartmann masks this should be avoided as no focusing takes place. Algorithm errors, as reported for the Fourier analysis,[41] take place as shown later in section 4.4.

4.2 Implementation of multi-contrast reconstruction methods

The reconstruction of the three contrasts transmission, differential phase and scattering can be performed by several algorithms, but not all of them are suitable to retrieve all contrasts. Additionally, their performance with regard of scatterer size sensitivity differs a lot. Within this work the following four reconstruction algorithms are used:

- Fourier analysis: Separation of the contrasts from different harmonic orders in Fourier space.[35]
- Gaussian fitting: Least-square fitting of a 2D Gaussian distribution to each beamlet.[40]
- Image moment analysis: Calculation of the central moments of each beamlet.[41]
- Visibility: Calculated from the maximum and minimum values with one beamlet zone or from the Gaussian parameters.

They are explained in this section in detail. They have their unique strengths and therefore are used for the different analysis required. A comparison of the capabilities and limitations of the different algorithms is given in section 4.4.

The most common one is a Fourier analysis where a Fast Fourier Transformation (FFT) is used to calculate the harmonic images representing the different contrasts. This can be done in 1D[35, 188, 237] or 2D[36, 189, 190, 238–241] depending on whether the optical element is a 1D line grid or a 2D hole grid. The Fourier analysis is a robust technique with the drawback of a crosstalk from transmission and sometimes differential phase to the scattering contrast.[205] This crosstalk leads to a spurious scattering signal and has to be removed by an additional decorrelation.

The second group of algorithms is based on individual beamlet analysis. Here the beamlet position and shape can be retrieved by pixel intensity comparison,[192] centroiding algorithms[52] (also called center of mass determination[242]), image correlation,[191] image moments calculation[41, 193, 197] or by Gaussian fitting.[40, 163, 238] Only the three last methods allow the retrieval of all three contrasts, while the first ones are only suitable for the retrieval of the differential phase contrast in combination with the transmission contrast. In image correlation, however, the scattering contrast is defined by the correlation strength, which is a weak statement for measurements with a high noise level. Therefore it will not be considered in this work. It turned out that the image moment analysis only allows quantitative statements on the

phase contrast and the scattering sensitivity is not very reliable. The Gaussian fitting is very sensitive on the actual beamlet properties and the scatterer size sensitivity is not stable in terms of changing setup parameters (see section 4.3). The advantage of the Gaussian fitting is the direct access to the beamlet parameters, which is required for the characterization of lens arrays.

In Grating Interferometry (GI) the image formation is a different one compared to the here used SEMCI. In the most GI setups one of the gratings is scanned in position and the intensity change of each pixel is analyzed. In SEMCI, on the other hand, only one image is taken and the contrasts are retrieved witch a lower resolution than the camera by analysis of the structured beam. The analysis concept for the scattering contrast in GI is to determine the change in visibility. This is a measure for the contrast of an image. In principle it can also be used in SEMCI to retrieve the scattering contrast as the contrast reduces in case of X-ray scattering. But as it will be shown by simulations in section 4.3, these results are not very reliable. For determining the focal length of a lens array, however, visibility is a good measure of the position of the highest contrast, i.e. the focal point. The visibility V_{BZ} is defined as:

$$V_{bz} = \frac{I_{max} - I_{min}}{I_{max} + I_{min}} , \tag{4.2}$$

where I_{max} and I_{min} stand for the maximum and minimum intensity, respectively, within one beamlet zone. The source code can be found in the appendix B.3. This calculation of the visibility can result in too high values if noisy data are analyzed. Without a previous smoothing single dark or hot pixels lead to an increased visibility. A smoothing, however, might remove small signal changes. There is a second way to determine the visibility via the results of the Gaussian fitting. I_{max} corresponds to the sum of the *offset* and *height* while I_{min} is equal to the *offset*:

$$V_{Gauss} = \frac{height}{height + 2 \cdot offset} . \tag{4.3}$$

With this single defective pixels are eliminated due to the Gaussian fitting of the complete beamlet area. Note that problems in the Gaussian fitting resulting on wrong *height* of *offset* values will propagate to this visibility.

The Fourier analysis and the Gaussian fitting with initial guess calculation by image moment determination are described in the two following subsection. The image moment analysis is a part of the Gaussian fitting algorithm. The first three image moments represent the sum, the center of mass and the variance of an image.[243] In case of a Gaussian beamlet shape this can directly be interpreted as the height, position and width of the beamlet. If the pure image moments are of interest they can directly be calculated by the function `moment_skimage` in the Gaussian source code in appendix B.1.

The complete reconstruction algorithms were implemented in the Python programming language (Python Software Foundation, `www.python.org`). They can be used in both versions, 2.7 and 3.6. The basic scripts can be found in the appendix B.

4.2.1 Contrast retrieval by Gaussian fitting

By Gaussian fitting the parameters height, offset, position and width of each beamlet are calculated.[40,41] The source code for analyzing single beamlets (`fitgaussian` function) and also rectangular 2D pattern of evenly spaced beamlets (`fitmultigaussian` function) can be found in appendix B.1.

The `fitmultigaussian` function divides the received image into zones of equal size, depending on the number of spots in the image. The pixel of maximum intensity is identified in each zone. Then around each maximum point a crop of the image is performed with the calculated zone size. This ensures that even if the beamlet is shifted out of the middle of the zone still the Gaussian fitting is performed on basis of data with a centered beamlet. Each crop then is analyzed by the single beamlet analysis `fitgaussian` function.

First an initial guess of the Gaussian parameters is calculated by the `moment` function. The offset is the average value of the corner pixels and the height the difference between the maximum value and the offset. The center in both directions is calculated by the first image moments, which represent the center of mass.[244] The beamlet width in vertical and horizontal direction is calculated by the second image moments. This moment represents the variance of the data.[244]

These initial parameters are then used for a least-square optimization of the 2D Gaussian function g:

$$g = o + h \cdot exp\left\{ -\frac{1}{2} \cdot \left[\left(\frac{x-\mu_x}{\sigma_x^2} \right)^2 + \left(\frac{y-\mu_y}{\sigma_y^2} \right)^2 \right] \right\} , \tag{4.4}$$

with o the offset, h the height, $\sigma_{x,y}$ the width and $\mu_{x,y}$ the peak position in horizontal and vertical direction, respectively. Note that the offset is no additional contrast itself but is necessary for a proper fitting. Otherwise the fitting algorithm would assume the Gaussian function to approach zero for large distances from the center. A certain offset can always be expected either from an increased dark current or a residual transmission through the optical element. The CARLs used here have even a quite high transmission, as shown later. Since this transmission is also scaled with the transmission of the sample, the offset can also represent a kind of transmission signal.

The raw beamlet parameters can be used for the characterization of the lens arrays. Here the width can be a measure for the beamlet focusing and the height in comparison to the offset a measure for the intensity gain.

Until now, only the pure beamlet properties are determined. The changes of these properties (height, width and position) by the sample are of central interest for SEMCI. These changes between an undisturbed (denoted by *flat*) and a disturbed (denoted by *radio*) image have to be calculated. The transmission (T), the differential phase ($dP_{x,y}$) and the scattering ($S_{x,y}$) in x- and y-direction are calculated by the following equations:

$$T = \frac{h_{radio}}{h_{flat}} , \tag{4.5}$$

$$dP_x = \mu_{x,radio} - \mu_{x,flat} \quad \text{and} \quad dP_y = \mu_{y,radio} - \mu_{y,flat} , \tag{4.6}$$

$$S_x = \sigma_{x,radio} - \sigma_{x,flat} \quad \text{and} \quad S_y = \sigma_{y,radio} - \sigma_{y,flat} . \tag{4.7}$$

This Gaussian fitting is limited to samples with an isotropic scattering distribution. For the investigated NPs this assumption holds true. In some cases also anisotropic samples can be analyzed. Therefore the scattering directions have to be aligned in the horizontal and the vertical direction leading to an elliptical Gaussian function. For randomly aligned scattering samples the Gaussian function has to be extended by a rotation to align with the rotated elliptical shape.

In literature the Gaussian fitting was shown to be less prone to crosstalk compared to Fourier analysis.[41] However, this could not be confirmed in this work. Additionally, Single defective spots lead to stronger error features in the resulting images than in Fourier analysis. Furthermore, high transmission changes in one beamlet zone, hence an increased transmission curvature, lead to errors in both, the scattering and the differential phase signal. In subsection 4.3.2 this will be explained in detail. One way to reduce these errors is a pre-analysis pedestal correction as described in subsection 4.3.3. For this pedestal correction, the raw image is divided by a low-pass filtered duplicate before the analysis. The averaging size corresponds to the beamlet zone size. A comparison of the Gaussian fitting with the algorithms is done in section 4.4. It is shown that the Gaussian fitting is only suitable for the characterization of lens arrays.

4.2.2 Contrast retrieval by Fourier transformation

The second reconstruction algorithm is a fast Fourier analysis.[35, 36, 189] The source code for the pure Fourier analysis can be found in the appendix B.2.

The recorded image has first to be properly cropped. This means that the crop has to be rectangular and have an even pixel number. Furthermore, the number of periodic structures (the number of beamlets in this work) has to be even. Second the cropping position with respect to the pattern position is of importance. This cropped image is then analyzed by the `reconstruct` function.

The image I is Fourier transformed to $I_{FFT} = \mathscr{F}(I)$. Before the transformation the image is multiplied by a Hann window function[245] to suppress errors from discontinuities at the image edges. Normally only the first orders are used. The higher the sampling per spot, the higher the orders, which can be calculated. Whether higher orders contain further information (e.g. another scattering size sensitivity) is still under discussion.[188] Simulations within this work showed a changing scatterer size sensitivity for different Fourier orders (see subsection 4.3.4). The different harmonic orders are cropped and back transformed to $I^{x,y}_{iFFT} = \mathscr{F}\left(I^{x,y}_{FFT}\right)$. Here x and y stand for the horizontal and the vertical directions of the array, respectively. Before this transformation a Hann window function is multiplied to the data. The Fourier transformation is symmetrical in Fourier space, this is why only positive orders are used. The negative ones show the same signal with an inverted sign.

The contrasts transmission, scattering and differential phase are again calculated by the change of the beam pattern due to the sample. Hence, the separation of the contrasts by taking different harmonic orders in Fourier space and the flat correction with the undisturbed images is explained in the following. (Note that the flat correction is not performed in the script shown in the appendix. This script only returns the different harmonic images.)

The central harmonic represents the pure attenuation and therefore the transmission image (T) and is derived by:

$$T = \frac{I^{0,0}_{iFFT,radio}}{I^{0,0}_{iFFT,flat}} \,. \tag{4.8}$$

The amplitude of the beam pattern in horizontal and vertical direction is represented in the first harmonics. These orders are not only attenuated by scattering but also by transmission. Hence the scattering data is additionally corrected by the central harmonic image. The scattering is further linearized to the

thickness of the sample by the negative logarithm. The scattering channels ($S_{x,y}$) therefore are calculated by:

$$S_{x,y} = -ln\left[\left(\frac{I^{x,y}_{iFFT,radio}}{I^{x,y}_{iFFT,flat}}\right) \Big/ \left(\frac{I^{0,0}_{iFFT,radio}}{I^{0,0}_{iFFT,flat}}\right)\right] . \tag{4.9}$$

The shift of the beam pattern corresponds to the differential phase contrast ($dP_{x,y}$). It is derived from the angle ($\angle$) of the complex back transformed harmonic orders:

$$dP_{x,y} = \angle\left(I^{x,y}_{iFFT,radio}\right) - \angle\left(I^{x,y}_{iFFT,flat}\right) . \tag{4.10}$$

4.2.3 Decorrelation to remove transmission crosstalk

The different contrasts in multi-contrast imaging are not necessarily independent of each other. It was shown in literature that a crosstalk from transmission as well as from edge-diffraction effects to the scattering signal does exist when data are analyzed by fast Fourier analysis.[41,205] This crosstalk is not exclusive for one measurement technique. It exists for GI as well as for SEMCI. Sometimes a linear dependence between the transmission and scattering signal is observed and is shown to be material dependent.[35,208,237]

Two possible ways were proposed to reduce or overcome this crosstalk. Either by decorrelation[205] or by using a different analysis routine like the moment analysis.[41] The moment analysis was not used to analyze the data measured in this work because the simulations did show a changed scatterer size sensitivity as shown in section 4.3.

The scattering data measured during PLAL in this work showed a strong correlation between transmission and scattering contrast. One must not forget, that normally scattering imaging is used in low absorption contrast samples, which is in contrast to the here observed transmission increase of up to 30 % induced by the cavitation bubble. Therefore it is not obvious that a crosstalk is observed. The data were decorrelated to obtain the pure scatting signal.[238] In Kaeppler et al.[205] a decorrelation routine for a single set of contrast images was proposed. A polynomial dependence up to the order of four was expected for the dependence between transmission and scattering contrast. Within this work a linear decorrelation was used as the higher orders did not show any advantages.

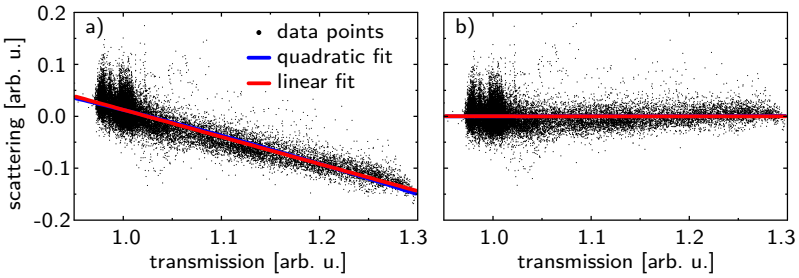

Fig. 4.5: Exemplary pixel-wise scatter diagrams before (a) and after (b) decorrelation of an ablation event. Only a minor difference in the linear and quadratic fitting is observed before the decorrelation. The data are from the measurement at the short sample-to-detector distance as described in subsection 6.3.2. Reproduced from Reich et al.[238] **[SI1]**

Fig. 4.5 shows the scatter plots for the scattering and the transmission contrast before (a) and after (b) the decorrelation for a typical PLAL measurement. In the raw scatter plot a slight difference between the linear and quadratic regression can be found. After a linear decorrelation no further difference was

recognizable. The scattering signal for both, a linear and a quadratic decorrelation did not show considerable differences. Therefore, only linear regression was used in this work. It can be argued whether a quadratic regression could compensate for a spectral response of the transmission signal when measured under white beam conditions.

For the decorrelation all pixels of interest in all images around the cavitation bubble appearance are included in the scatter plot. Then a linear regression was performed on these data points. Images without a cavitation bubble, hence *flat* images, are excluded to reduce the number of data points lying in the center of the scatter plot (scattering = 0 and transmission = 1). This can lead to too high weight on this area in the regression. As last step the intensity values of the scattering contrast are decorrelated according to the linear regression.[238] The source code can be found in the appendix B.4.

4.2.4 Phase reconstruction by zonal wavefront estimation

One of the three contrasts in multi-contrast imaging is the differential phase representing beamlet deviations introduced by the sample. This contrast can be used for wavefront sensing.[246] A change in the wavefront results in changes in the beamlet positions. These optical elements can be used, for example, to characterize X-ray lenses.[163,216] To reconstruct this wavefront change (also called phase) the measured differential phase has to be integrated. In this work the modified Southwell algorithm[247] is used, which is a zonal wavefront estimation primary introduced by Southwell.[248] Additionally to the original algorithm, which used the vertical and horizontal phase slopes, the diagonal slopes are used to improve the phase estimations.

The source code for the wavefront reconstruction can be found in the appendix B.5. The two differential phase images as received from the contrast retrieval, the number of used iterations and a scaling factor h are required. Around ten iterations are suitable for a good reconstruction as shown by the proposers of this algorithm.[247] The factor h is the separation distance between two adjacent spots. If just the relative change in the wavefront is of interest, h can be set to unity.

First, the slope values are calculated. In this algorithm no boundary conditions are needed, which is advantageous if no flat conditions are present at the border of the analyzed area. The errors at the edge of the reconstructed area are larger as the slopes are estimated from a smaller amount of data points. In the second step, which is iterated several times, the phase in each pixel is calculated by adding up the slope values corresponding to the next neighbor pixels. Here it is assumed that the slope between two adjacent points is linear. In the case of infinitesimal distances between neighboring points this assumption holds true.[247]

In Fig. 4.6 the reconstructed phase of an air bubble in water as reference sample measured with a Hartmann mask is shown. The raw data were taken with a short and a large sample-to-detector distance and were analyzed by Fourier analysis and Gaussian fitting. The reconstructed contrasts can be found in section 4.4, where a comparison of the different reconstruction algorithms is done. Here only the reconstruction of the phase is shown. The phase introduced by the vapor bubble in water is reconstructed well. The Gaussian fitting shows a higher contrast compared to the Fourier analysis. However, as will be described later, this higher contrast might come from an overestimation of the beamlet shift towards the bubble edge. Individual misfitted beamlet positions in the Gaussian fitting lead to strong phase errors, as can be seen at the dark spot in the Gaussian image of the large distance measurement. The larger

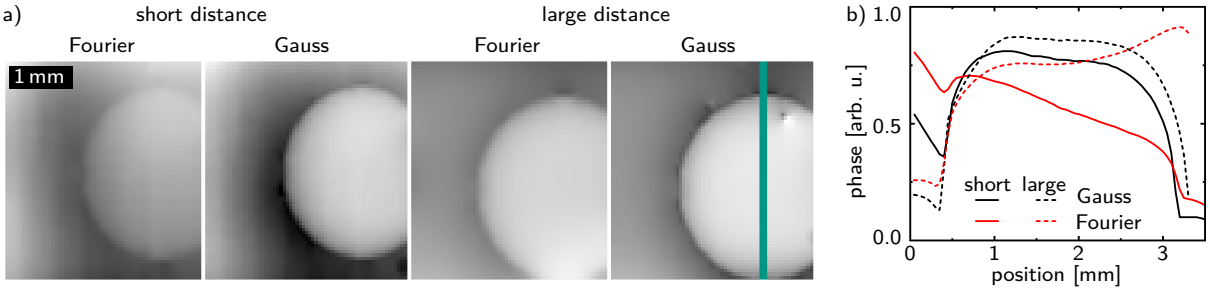

Fig. 4.6: (a) Reconstructed phase of an air bubble in water for the two imaging conditions (short (4.7 cm) and large (40 cm) sample-to-detector distance) and the two multi-contrast reconstruction algorithms Fourier analysis and Gaussian fitting. The grey scale is arbitrary but equal for all images. (b) Line section taken at the green line in (a). With the Gaussian fitting the contrast is higher while there are only minor differences between the short and large distance. The reconstructed contrasts can be found in section 4.4. **[SI2]**

distance only improves the contrast slightly showing that already with the short distance of 4.7 cm a good wavefront measurement is possible.

4.2.5 SH-WaveRecon as published reconstruction software for multi-contrast images

Within this work the complete reconstruction algorithms containing the Fourier analysis, the Gaussian fitting and the phase reconstruction were published as the stand alone software ”SH-WaveRecon” under the creative commons liscence ”CC BY-NC-SA 4.0”.[249] It is not limited for X-ray multi-contrast imaging. This software is not limited to X-ray images as also data from visible light measurements can be analyzed.

The user interface is shown in Fig. 4.7. This software is designed to handle single measurements rather than whole sets of measurements as only one *radio* image can be used at once. The user can choose the reconstruction algorithm and whether an additional phase reconstruction should be done. Phase reconstruction can only be performed if differential phase data are already available.

There are some minor errors in the output of the visualized images in version 1.0, but the raw output images (as TIFF files) are correct. These bugs have been fixed in version 1.2.

4.3 Simulation of scattering imaging

The ablation process with the induced cavitation bubble is not a sample with low absorption contrast, as usually studied with SEMCI, under which the reconstruction algorithms suffer. To learn more about these misinterpretations, typical measurement data were simulated. Afterwards these simulated data were analyzed with all four algorithms mentioned above. The scripts are the same as those used to analyze the measurement data from PLAL.

First, an array of 40×40 spots with a Gaussian shape was produced. This image was used as a *flat* image. Then the transmission increase of a typical bubble of 30 % was multiplied onto this *flat* image. Such an image is shown in Fig. 4.8. On the one hand, this image served as a reference without scattering. On the other hand, on basis of this image the actual sample distorted image (denoted as *radio*) was calculated by a kind of convolution with the theoretical scattering distribution shown in equation (3.7)

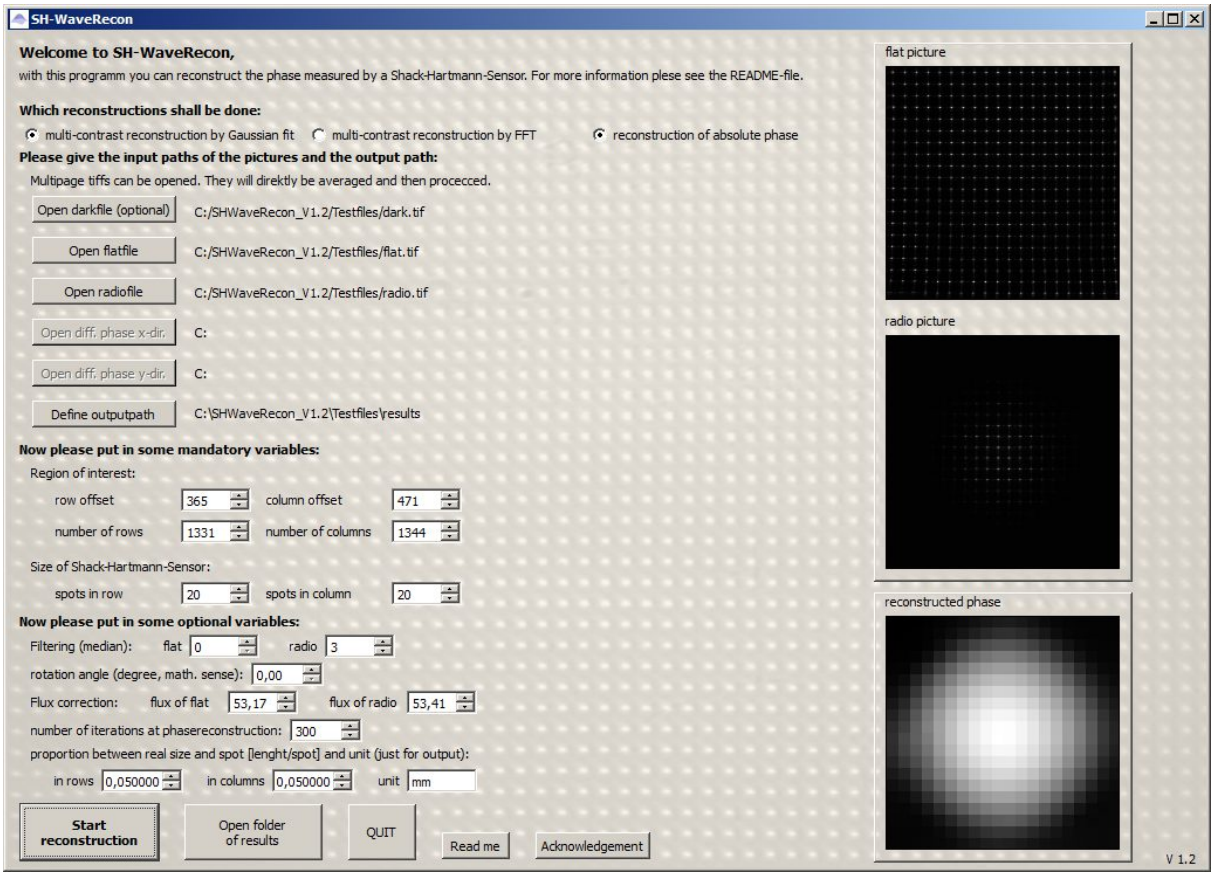

Fig. 4.7: User interface of the multi-contrast reconstruction software SH-WaveRecon in version 1.2.[249] The distributed test files of the characterization of a diamond X-ray lens are displayed.

and (3.8). The scattering distribution was scaled according to the local intensity and the bubble size. The bubble size scaling was used to account for an homogeneous filling of the bubble with scatterers. Before adding the scattering signal, the specific pixel intensity was reduced by the sum of the scattering distribution to fulfill the conservation of intensity. The scattering distribution was calculated for a fixed volume fraction of scatterers as a 2D distribution. This distribution was 3×3, 4×4 or 5×5 beamlet zones in size.

All these images were simulated with a high resolution of $100\,\mathrm{px} \times 100\,\mathrm{px}$ per beamlet zone. Afterwards they were down scaled to a certain sampling (pixels per beamlet zone) with a bi-linear interpolation. The typical sampling of the measurements is around 13 px / beamlet. The basic parameters used for the simulation are summarized in Table 4.2.

4.3.1 Influence of beamlet width on visibility and fitted beamlet parameters

First, the influence of the beamlet parameters on the visibility was simulated. For that only the flat beamlet pattern was simulated with a changing Gaussian width of the single beamlets (see inset of Fig. 4.9 (a) insets). As expected, the visibility V_{bz} has a distinct peak for a beamlet width equal to 20 % of the beamlet zone as shown in Fig. 4.9 (a). For larger spots, the beamlet zone is too small for the intensity to drop to the background level leading to an increased I_{min}. This case also changes the offset value of Gaussian fitting, which increases for larger beamlet sizes as shown in Fig. 4.9 (b). At the other limit, for small beamlets,

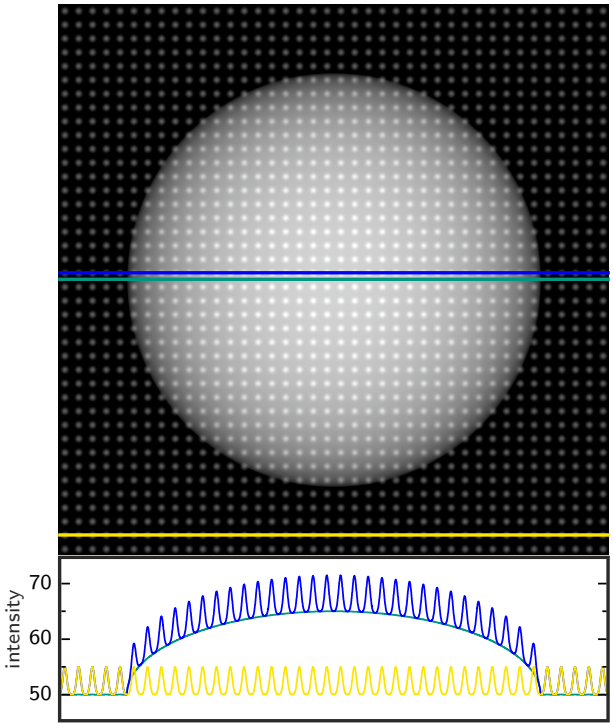

Fig. 4.8: Simulation of a multi-contrast measurement. 40×40 Gaussian spots with a height of 5 on top of a background of 50 represent the *flat* image. Here an additional transmission increase of a factor up to 1.3 due to an air bubble in water is shown in the image on top. Three representative line section as depicted in the image are shown in the bottom graph.

Table 4.2: Basic parameters and their range used in the simulation of the scattering imaging of nanoparticles during laser ablation. Detailed description of the used parameters in the different simulations can be found in the corresponding sections of the "List of experiments". They are referenced in the text in bold square brackets, e.g. **[Sim1]**.

X-ray energy [keV]	15
sample-to-detector distance [cm]	4.5 to 26.6
beamlet pitch [µm]	65
beamlet width [% of beamlet zone]	0.05 to 1
beamlet height	1 to 10
background intensity	0 to 50
scatterer diameter [nm]	2 to 600
sampling [px / beamlet]	7, 13 and 19

the intensity drops too fast to obtain a high visibility. Here even the central pixel contains a substantial amount of lower intensity lowering his intensity. This leads to a decreased I_{max}. This is also visible in the strongly decreasing detected height of the beamlets for small beamlet sizes as shown in Fig. 4.9 (b). The height decrease for larger beamlet sizes, on the other hand, originates from the increasing offset.

There is a strong difference between the visibility calculated from the image intensity (V_{bz}) and the Gaussian parameters (V_{Gauss}). For larger beamlet widths the Gaussian fitting can still quite well estimate the Gaussian parameters despite the strong cutting at the beamlet zone edges. This leads to a much higher V_{Gauss} compared to V_{bz}. Both visibility calculations start to differ at the point, where V_{bz} peaks. This is

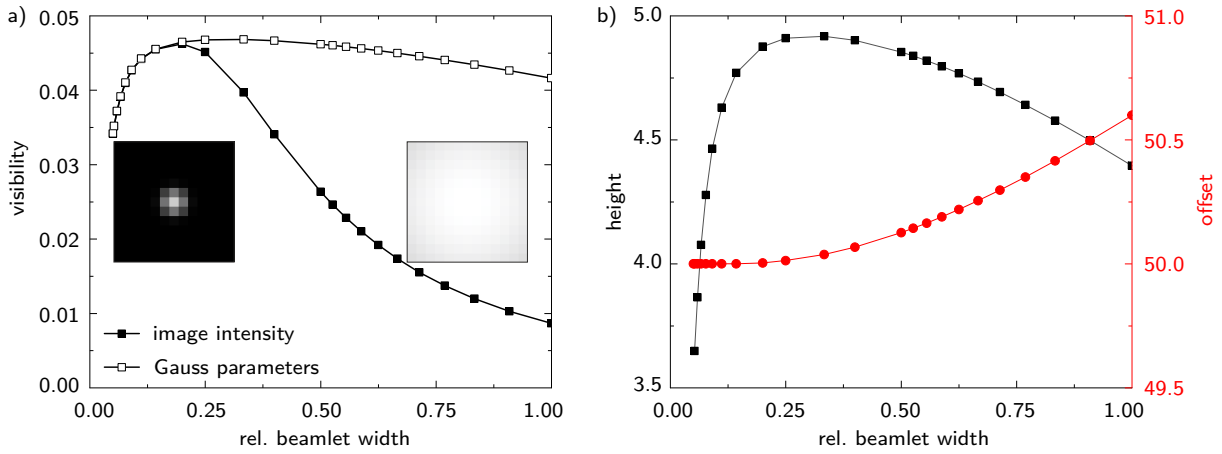

Fig. 4.9: Detected beamlet raw parameters of a simulation of varied beamlet widths (insets in (a) show the two extrema, gray scale [50, 55]). The visibility (a) calculated from the beamlet zone intensity peaks for a beamlet size of 20 % of the the beamlet zone while the visibility calculated from the Gaussian parameters peaks at 33 % beamlet width. The offset increases for larger beamlet widths while the height also has a distinct peak at around 33 % beamlet width. **[Sim1]**

the point, where the beamlet starts to get cut off at the edge of the beamlet zone. Hence, the usage of the Gaussian parameters for the visibility calculation is only valid if the spot drops down to the background signal within the beamlet zone.

The specific values presented here depend on the sampling of each beamlet. This simulation was done with a sampling of 13 px × 13 px per beamlet zone. For a higher sampling the visibility increases slightly and the peak value shifts to smaller beamlet sizes. Correspondingly, the height increases and their peaks shift to smaller beamlet sizes. The offset, in contrast, decreases in this case. For a decreasing sampling the visibility and height decrease and their peak values shift to higher beamlet sizes. The offset increases in this case.

Besides the offset and the height, also the widths are not always well fitted by the Gaussian fitting. For small beam sizes, the width is overestimated and vice versa. The zero crossing is at 1/3 beamlet width, the point where the height and V_{Gauss} peak.

In summary, it can be stated that it is important to find the suitable parameters of the measurement setup in order to achieve a high visibility. Sampling and beam width should be chosen accordingly. Otherwise, a high visibility of the optical element may not be imaged through setup. Visibility is an important factor in reducing sample interference in the reconstruction algorithms, as shown below.

4.3.2 Influence of steep transmission changes on beamlet parameter reconstruction

The strong transmission change induced by the present ablation bubble leads to difficulties in the reconstruction. This effect is more pronounced if a high background signal combined with a low visibility is present in the measurement. As shown later in section 4.4 there is a certain crosstalk between the different channels. In Fig. 4.10 the results of the Gaussian fitting of two neighboring beamlets are shown. One beamlet is outside (b) and one directly inside of the bubble (c) as illustrated already in Fig. 4.8. From the contour plot, representing the results of the Gaussian fitting, it is obvious that in the case of a strong transmission gradient inside the beamlet zone the analysis is disturbed strongly.

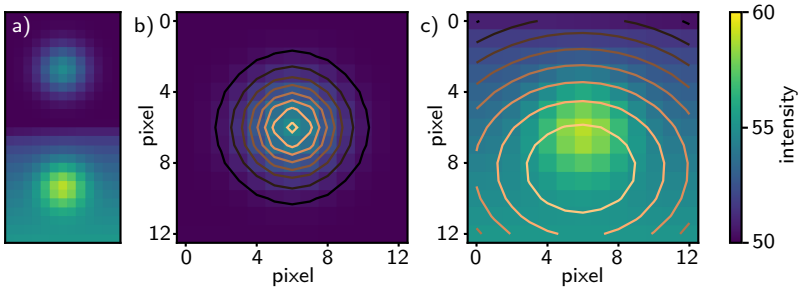

Fig. 4.10: Change of Gaussian fitting results due to strong transmission increase within one beamlet zone. (a) Overview of the two analyzed beamlets in (b) and (c). The analysis results are shown as contour plots in (b) and (c). The beamlet with a flat transmission background (top in (a) and (b)) is analyzed correctly while the beamlet located at a rising transmission background (bottom of (a) and (c)) does not get analyzed correctly. For numerical results see Table 4.3. **[Sim2]**

Table 4.3: Gaussian parameters of two beamlets, one outside and one inside a transmission increasing bubble.

	simulated	outside bubble	inside bubble
height	5.0	4.8	10.3
offset	50.0	50.0	46.3
position x	6.0	6.0	5.9
position y	6.0	6.0	8.3
width x	1.86	1.90	8.62
width y	1.86	1.90	7.00

Table 4.3 shows the very good agreement of the simulated Gaussian with the fitting results for the beamlet located outside the bubble while the values of the beamlet inside the bubble differ strongly. The slight differences outside the bubble were already mentioned and addressed above. The amount of this misfitting depends on the beamlet width. Inside the bubble the height is increased while the offset is decreased. Additionally the position is shifted in direction of the transmission increase towards the higher background signal. The width of the beamlet is strongly increased in both directions. If the same data are simulated without the offset of 50 only marginal changes in the analyzed parameters compared to the design values are observed.

Even in the middle of the simulated bubble, where only a very small background level curvature is present, a slight change in the analyzed beamlet width is observed. The misfit of the width is furthermore dependent on the beamlet width. For larger beamlets the misfit increases. Fig. 4.11 shows the effect of the wrongly determined beamlet width for changes of the height (a), the offset (b) and a scaling of the whole image (c). For the flat images, where no bubble is present, the width stays at a constant value for all situations. This is in agreement with the fact that the Gaussian width is invariant on changes of the height, offset and scaling. However, inside the bubble the width is determined to be larger than the actual value. With an increasing height the amount of misfit decreases. The amount of misfit depends also on the offset. For a height change with no offset, the analyzed width stays constant in all cases. The width is linearly dependent on the offset as shown in Fig. 4.11 (b). Only the scaling does not change the width although it is higher in the bubble compared to the flat scenario (height = 5 and offset = 50). The scaling

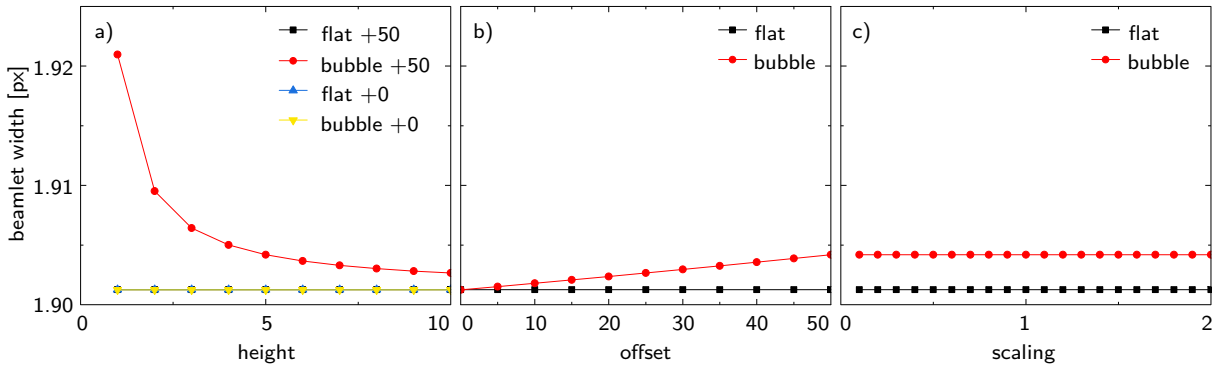

Fig. 4.11: Influence of the bubble curvature on the reconstructed beamlet width. The beamlet width in the middle of the bubble is analyzed for changes in beamlet height (a), offset (b) and a scaling of the whole image (c). The height change was simulated for an offset of 50 (denoted by +50) and no offset (denoted by +0). For the flat images without the bubble the width stays always the same. In the bubble images, however, the width decreases with increasing height and increases with increasing offset. Only scaling does not change the width. **[Sim2]**

of factor 1.3 in the flat scenario corresponds to the simulated transmission increase in the center of the bubble. As the width in the flat scenario does not change under scaling, the increased beamlet width in the bubble must originate from the bubble curvature. The linear dependence of the width on the offset can also be explained with a linear increase of the curvature of the bubble.

A large height as well as a small offset correspond to a higher visibility. The higher the visibility, the lower the disturbing effect of a steep transmission increase.

4.3.3 Pre-analysis pedestal correction to reduce problems during reconstruction

As shown before, a curvature in the background level leads to errors in the contrast reconstruction. Only the ideal case of measurements with no background signal gives the correct values. A pre-analysis pedestal correction can improve the results considerably. In Fig. 4.12 this improvement is shown by simulations of bubbles of different shape with one representative image in (a). The bubble radius was increased while the maximum transmission was kept constant at 30 % leading to a decreasing background curvature.

To remove the background curvature and hence improve the reconstruction capabilities the original image is divided by a low-pass filtered duplicate before the analysis. For the low-pass filtering the mean intensity of each beamlet was calculated. As no scattering or phase signal is considered in this case this background image represents exactly the transmission contrast. This image now is scaled up to fit to the original image. In this step sharp edges as occurring at the bubble edge get smeared out leading to new problems. This already shows that such a pre-analysis correction has its own limits.

In the normal Gaussian fitting the analyzed beamlet width increases with an decreasing bubble size, hence increasing background curvature, as shown in the graph of Fig. 4.12. Below a bubble radius of five beamlet zones the width jumps up to very huge values. Already before the real edge of the bubble is in the region of interest the increased curvature leads to high errors in the reconstruction. When the background correction is performed before the analysis, the beamlet width stays (almost) constant down to a bubble size of four zones.

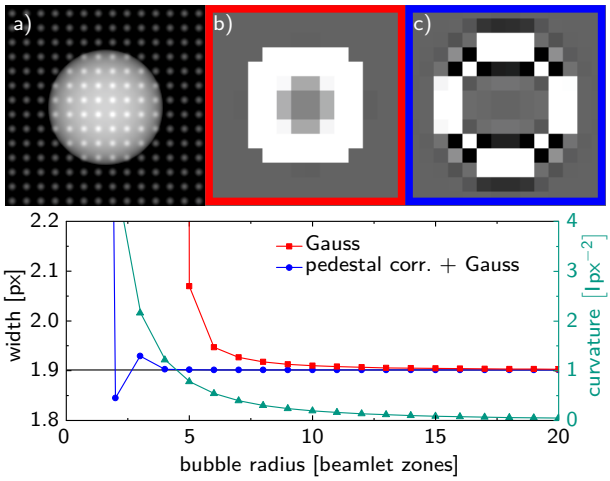

Fig. 4.12: Improvements in the beamlet width analysis due to a pre-analysis pedestal correction. Different bubble sizes with constant maximum transmission, hence different curvature, are simulated. (a) shows an example image with a bubble radius of four beamlet zones. (b) and (c) show the reconstructed width of the image in (a) for both, the normal Gaussian fitting and the pre-analysis pedestal correction, respectively. (b) and (c) have the same scale as the graph, which shows the mean value of the width of the four central beamlets and the curvature as a function of bubble size. **[Sim3]**

As one can see in Fig. 4.12 (b) and (c), the beamlets at the edge of the bubble are not reconstructed correctly in both cases. For the normal Gaussian fitting the beamlets get wrongly analyzed when a finite background curvature is present. The area in the bubble with good values is increased for the pedestal corrected analysis. In other words, much stronger curvatures can be accepted while still achieving good values. On the sharp edge of the bubble also this correction fails. Additionally, outside the bubble more beamlets are misfitted compared to the normal Gaussian fitting due to the long ranging nature of the used low-pass filter.

Validation of the pre-analysis pedestal correction by measurement data

To prove this concept with real measured data a wavefront measurement of a diamond CRL was used as depicted in Fig. 4.13 (a). The wavefront analysis with the detailed setup description is already published by dos Santos Rolo et al.[163] For the wavefront analysis a 2D lens array consisting of crossed cylinder lenses was used. This 2D lens array was produced by 3D direct laser writing.

This wavefront measurement was done to analyze the shape and focusing ability of the diamond CRL. It was shown, that the measured wavefront distortion fitted well to the design value. Additionally, no strong scattering of the lens material was observed. Hence, in contrast to the simulations these data showed a strong beamlet deflection and only minor broadening, while in the simulations only the transmission increase of an empty bubble was used. To mimic an increasing background curvature a calculated background signal was added to the data several times. In Fig. 4.13 (b) a line section of the original image (denoted by 0) and one after ten-fold background addition are shown. The increased background curvature is evident.

In Fig. 4.13 (c) and (d) the beamlet width in the center of the diamond lens and the differential phase at an outer position of the diamond lens are shown. When the data are analyzed with the normal Gaussian fitting an increasing width and an increasing beamlet shift are observed with the increasing background curvature. For the Gaussian fitting with the pre-analysis pedestal correction the increasing behavior van-

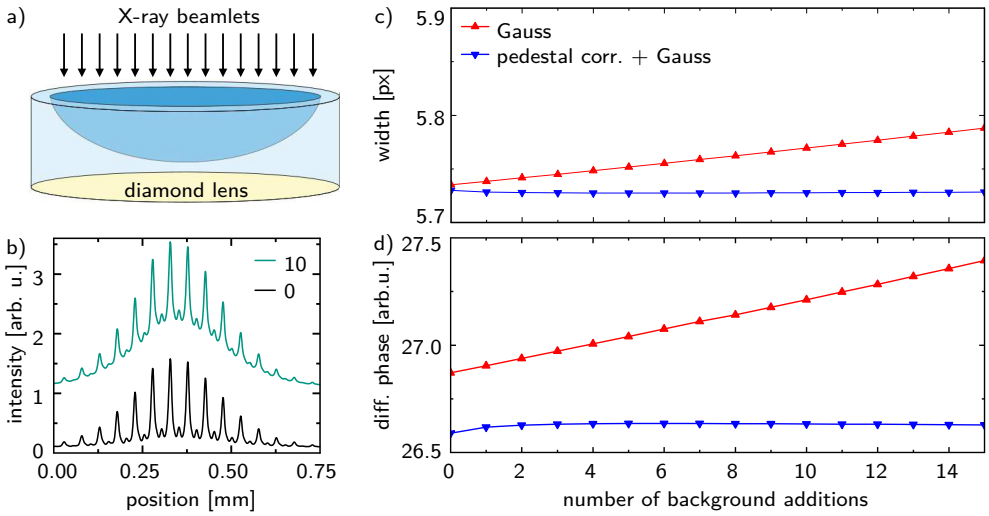

Fig. 4.13: Proof of concept of pre-analysis pedestal correction with measured data of the wavefront of a diamond X-ray lens as depicted in (a). The background curvature was increased by adding up to 15 times the original background. In (b) two representative line sections are shown, the original one (denoted by 0) and after tenfold addition. The resulting values of beamlet width and differential phase (both in horizontal direction) are shown in (c) and (d), respectively. Both increase for normal Gaussian fitting while they stay (almost) constant with additional the pedestal correction. Raw data are taken from dos Santo Rolo et al.[163] **[Sim4]**

ishes. With real data exhibiting a distinct broadening and shift due to the sample, the performance of the analysis improves with the pedestal correction.

The width of the beamlet for both analysis routines almost coincide for the original data with no additional background. Only a minor decrease of the scattering signal would have been observed with the new analysis strategy. No differences in the spatial scattering distribution is observed with the improved reconstruction. For the differential phase, the difference between the two algorithms is greater even for the original data. Therefore it cannot be excluded that the reconstructed values of the differential phase in dos Santos Rolo et al.[163] are slightly too large. The values of the normal Gaussian fitting are up to 2 % larger than those of the pre-analysis pedestal correction. The horizontal direction is slightly larger than the vertical one. The high visibility of 0.93 of the 2D lens array used prevented larger errors.

In summary, it must be noted that the pre-analysis pedestal correction can significantly reduce the misfitting due to background curvatures. It should be noted, however, that steep edges in the transmission still lead to errors and that surrounding beamlets may also be affected due to the far-reaching low-pass filter. In order to reduce the error genesis, the optical element should guarantee the highest possible visibility.

4.3.4 Scattering sensitivity distribution

In this subsection the scattering sensitivity distribution established by Lynch et al.[39] as explained in subsection 3.4.4 is validated. For this purpose, a series of *radio* images with changed scatterer sizes but constant volume fraction were simulated and analyzed. Fig. 4.14 shows the scattering intensity as function of the scatterer diameter in comparison to the expected DFEC for the four different analysis algorithms.

Only the image moment analysis and the Fourier analysis have a comparable peak value as the proposed DFEC (94 nm, 106 nm and 101 nm, respectively). Especially for the Fourier analysis also the decay

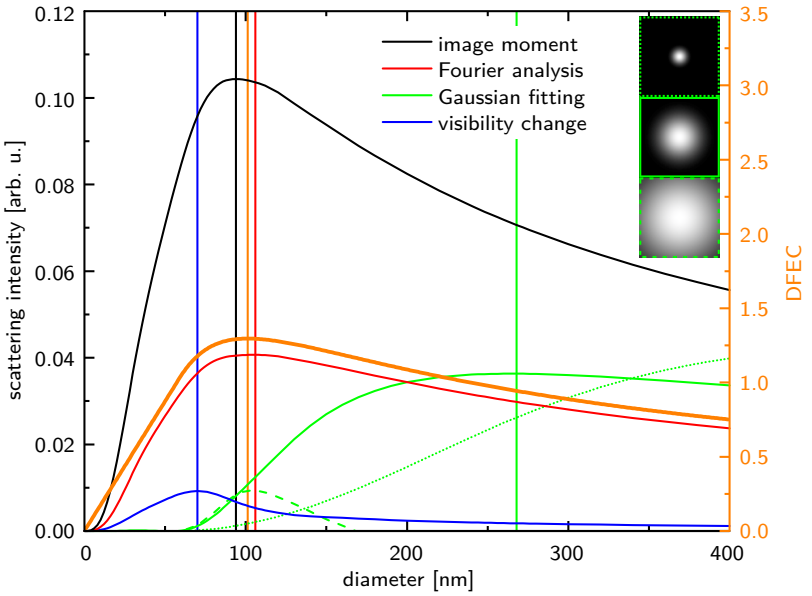

Fig. 4.14: Results of simulated scattering data (auto-correlation length = 57 nm) analyzed with four different algorithms. The Fourier analysis and the image moment determination show good agreements with the Dark-Field Extinction Coefficient (DFEC) with only a minor shift of the peak value. The visibility change exhibits a reduced peak value and the decay of the scattering signal for large scatterers is faster than expected. By Gaussian fitting a 2.5 higher peak value is observed. The peak position of the Gaussian fitting can be changed by changing the beamlet width (smaller width green dotted line, larger width green dashed line). As inset the three simulated beamlet widths. **[Sim5]**

to large and small scatterers fits well to the DFEC. Minor changes are observed for very small scatterers, which can be attributed to the limited q-range of the simulated scattering distribution of the scatterers. Simulations with larger q-ranges showed an improved agreement with the DFEC. The peak value shifts to the expected value of 101 nm. Fig. 4.14 shows the scattering sensitivity with a image background of zero. The same simulations with a background of 50 did not change the sensitivity distribution for both, the Fourier analysis and the moment analysis. The Fourier analysis obtained the same values while the moment analysis resulted in much smaller values. This is to be expected, since the second image moments (the variance) is smaller at a higher background level.

The visibility change inside one beamlet zone has its peak value for somewhat smaller scatterers than the DFEC. Furthermore, the decay for larger scatterers is faster than for the DFEC. For an offset of 50 the shape of the scattering curve changes completely making the results unreliable. The visibility calculated from the Gaussian fitting parameters showed similar unreliable changes. Even the pre-analysis pedestal correction did not improve the results.

The Gaussian fitting showed the largest deviation from the expected values. It peaks at a roughly 2.5 higher scatterer size than the proposed DFEC. A background level of 50 in the simulation only shifted the sensitivity curve to higher values, as expected from the results in subsection 4.3.2. The proposed pre-analysis pedestal correction showed a shift of the scattering intensity down to the values observed without the offset. The peak value did not change. The changed scattering sensitivity peak may result from a contrast shift from the expected scattering contrast to the offset. The smaller scatterers have a broad scattering distribution leading to a global background signal. This background, however, is detected as an increased offset and not as beamlet width change. Thus, the scattering from smaller scatterers might be retrieved by the Gaussian fitting but the disentanglement of the real offset and the spurious scattering

signal in it is still unknown. Despite the controllable shifts in intensity and the shifted scattering contrast into the offset, the Gaussian fitting is not good for scattering sensing. Simulations with changed beamlet width showed a further shift of the peak to larger (smaller beamlet width, green doted line in Fig. 4.14) and smaller scatterer sizes (larger beamlet width, green dashed line). Hence, the sensitivity to certain size levels is strongly dependent on the beamlet shape. Even a contrast inversion to negative values was observed for large beamlet widths. This makes the Gaussian fitting not reliable, especially if different setups are compared.

The beamlet width change is no problem for the other algorithms as they do not show strong shape changes. The visibility slightly shifts the peak value to higher scatterer sizes with increasing beamlet width. Both visibility and image moments show strong changes in the scattering intensity, which can be explained by the nature of these algorithms. Fourier analysis is almost independent of the beamlet width with only tiny intensity and peak position changes.

Some of the algorithms show a varying scattering intensity for different setup parameters. This indicates that no direct conclusions can be drawn about the scattering cross section of the sample. The two promising algorithms, at this point, are the Fourier analysis and the image moment analysis. They both show a good agreement with the proposed DFEC. A closer comparison of these algorithms will be given in the next section.

Scattering sensitivity changes by higher order analysis

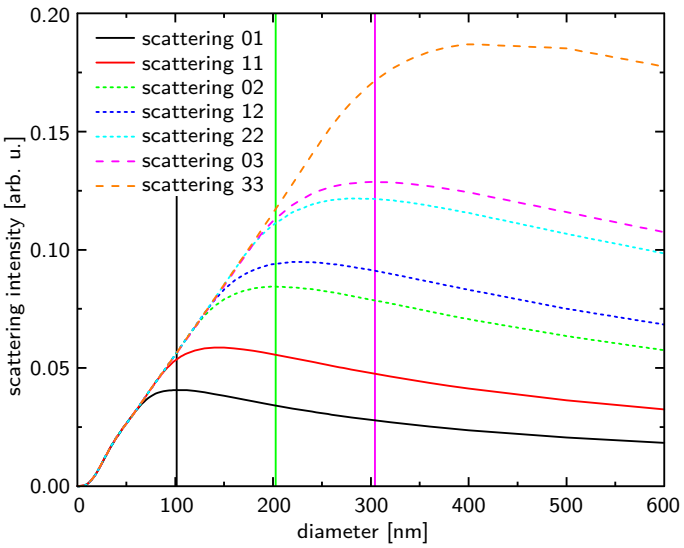

Fig. 4.15: Simulated scattering sensitivity (auto-correlation length = 57 nm) for different orders of Fourier analysis. The linear peak shift with increasing order (see vertical lines) prove the proposed sensitivity to larger scatterers for higher orders by Wen et al.[188] Also Fourier orders with a higher distance to the center inside one order (see 02, 12 and 22) show an increasing peak value. **[Sim5]**

In literature it was proposed that the higher orders are sensitive to larger scatterers.[188] Fig. 4.15 shows a very good agreement with this proposal. During the fast Fourier analysis, the scattering signals of higher order were also calculated. The scattering intensity peak for the first (01), second (02) and third (03) order scale linearly. The equivalent orders (10, 20 and 30) showed the same intensities. From the shift of the further orders within one level (see e.g. 02, 12 and 22) one can conclude that the peak value

shifts linearly with the distance of the Fourier order center to the central point in Fourier space. Note that usually the signal intensities decrease at higher orders in Fourier space due to the counting statistics and hence the errors increase. It seems to be possible to distinguish directly between different size levels by using the higher orders. The discussed improved scattering sensitivity by measuring at two different ACLs (see subsection 3.4.4 and Fig. 3.13) might be also possible by only using the different orders in Fourier space. However, for an increase in the ACL by one order of magnitude one needs a high sampling and good image quality to be able to reconstruct seven or more orders sufficiently. This high sampling rate is additionally accompanied by a reduced image size, since the pixel size of the detectors is limited.

4.4 Comparison of the abilities of different reconstruction algorithms

The four multi-contrast reconstruction algorithms Fourier analysis, Gaussian fitting, image moment and visibility do not give the same results. As has been shown in parts before, they all have advantages and disadvantages. In this section, a comparison of the algorithms and suggestions for their usefulness will be given. The aspects of comparison are (i) the possible contrasts to be obtained, (ii) the differential phase signal and its miscalculation on strong transmission curvatures, (iii) the crosstalk behavior into the scattering signal and (iv) the robustness. For this comparison, on the one hand an air bubble was measured in water. Only transmission and phase contrast are expected here. On the other hand, a simulation with a pure transmission increase without beamlet displacement or broadening is used. In this case, no scattering or differential phase signal is to be expected.

In Fig. 4.16 the retrieved contrasts of all four algorithms for an air bubble in water are shown. It was measured in white beam at the Topo-Tomo instrument of the Synchrotron Radiation Source at KIT with a Hartmann mask consisting of a gold mesh on a graphite plate.[162] Except from the visibility calculation all three other algorithms allow the reconstruction of all contrasts, namely transmission, scattering and differential phase. By visibility analysis only the scattering contrast with no directional information can be obtained. When analyzing by Gaussian fitting one obtains additionally the offset. However, the offset does not represent an additional contrast as it represents only the rest transmission through the optical element and maybe scattering of large q-values.

Transmission contrast

The transmission contrast of the different algorithms do not show strong differences. The Fourier analysis can be seen as a low pass filter as only the central harmonic order is used for the transmission reconstruction. Therefore, a small smearing out can be recognized at sharp transmission edges, which represents the edge of the bubble in this case. The Gaussian fitting has problems with strong transmission curvatures as already shown in subsection 4.3.2. Not only the position but also the peak height get wrongly fitted. The image moment analysis, on the other hand, only showed minor problems at sharp transmission edges.

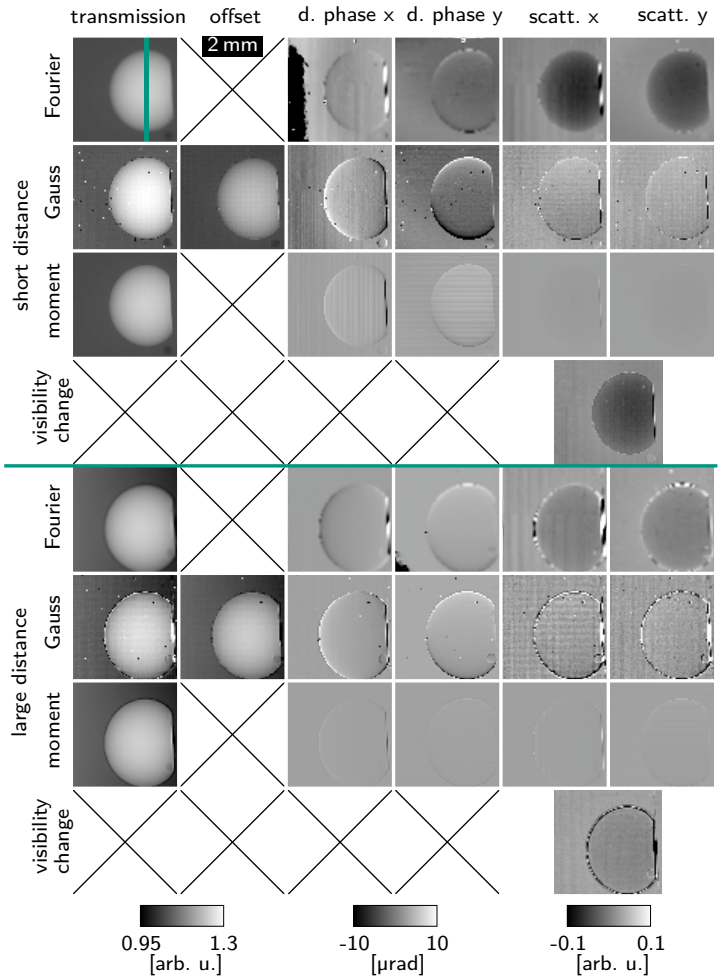

Fig. 4.16: Comparison of the multi-contrast retrieval with Fourier analysis, Gaussian fitting, image moment and visibility analysis. The sample is a static air bubble in water imaged with two sample-to-detector distances (short: 4.7 cm, large: 40 cm) with a Hartmann mask as optical element.[162] The auto-correlation lengths are 78 nm and 661 nm, respectively. Note that the scattering contrasts are the results obtained directly from the algorithms without decorrelation or pre-correction. Details on the capabilities and drawbacks of the different algorithms can be found in the text. **[SI2]**.

Differential phase contrast

The differential phase is calculated from the position change of the beamlets. The noise of the differential phase is reduced for measurements with a larger sample-to-detector distance (see Fig. 4.16). In Fig. 4.17 line sections through the center of a simulated air bubble (a) and the measured air bubble (b) of the large sample-to-detector distance of Fig. 4.16 are shown. In the simulation a background intensity of 50 was used and only a transmission increase but no beamlet shift was simulated. Hence, in the simulated data no differential phase is expected while in the measured data the beamlets observed a shift due to the refracting power of the water-air boundary. The global offset obtained in the measured data comes from a global shift of the optical element between the *flat* and the *radio* image.

The Fourier analysis shows no increased differential phase for the simulated bubble except at the bubble edge. This is in accordance with the simulation parameters, where only a transmission increase but no beamlet shift was introduced.

The image moment analysis in this simulation shows no strong differential phase signal. However, for the measured data, where the beamlets experienced a shift, a decreased differential phase signal com-

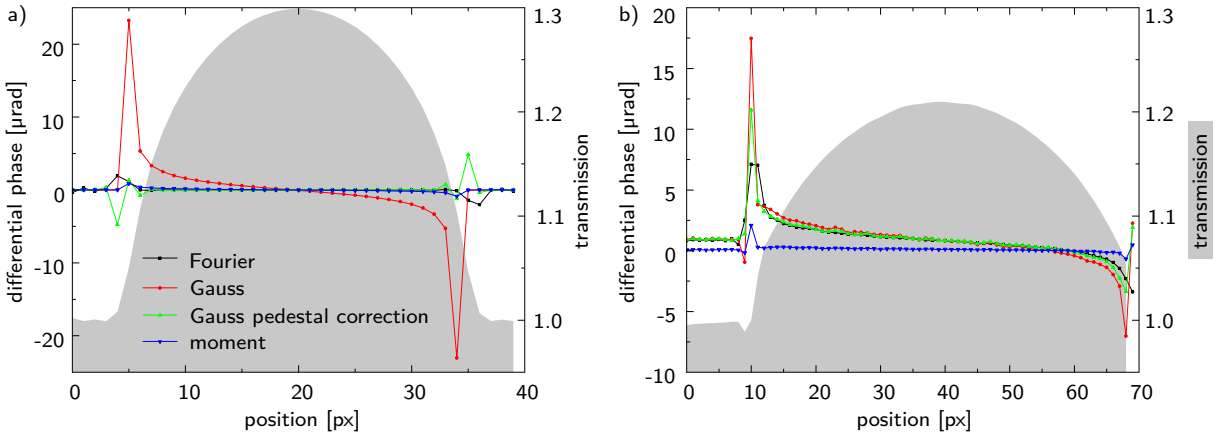

Fig. 4.17: Line section of the differential phase through the center of a simulated bubble (a) and a measured air bubble (b) retrieved with different algorithms. Fourier analysis retrieves only at the edge of the simulated bubble wrong differential phase values. By Gaussian fitting one gets a misfitted increased differential phase inside the simulated bubble, which can be suppressed by a pre-analysis pedestal correction. Moment analysis shows a low but non-zero differential phase. In the measurements in (b) the Gaussian fitting can be improved slightly by using pedestal correction. The moment analysis can also retrieve the differential phase but with a changed absolute value. Note that the difference phase for the simulation is arbitrary, since no beam propagation was simulated. **[Sim5] [SI2]**

pared to the other algorithms is observed. It is one order of magnitude smaller than by Gaussian fitting or Fourier analysis. Simulations with changed a *offset*, furthermore, showed an increase of the wrongly determined differential phase with increased *offset* for both, the moment analysis and the Gaussian fitting. In case of no *offset*, the amount of wrongly determined differential phase of Gaussian fitting and moment analysis was equal. This leads to the conclusion that in moment analysis the differential phase is wrongly calculated qualitatively and quantitatively. This can directly be explained by the nature of the first image moment, which only represents the peak position of a Gaussian distribution. This image moment represents the center of mass of the analyzed image. If a considerable transmission change occurs within one beamlet zone this center of mass is shifted. The increase of the error on the beamlet position with increasing *offset* is therefore obvious.

The Gaussian fitting shows problems in analyzing the positions of the beamlets when there is a finite transmission curvature in the sample. This problem can be improved by a pre-analysis pedestal correction. This was already demonstrated in subsection 4.3.3 and also holds true for the simulated data, where no beamlet shift was introduced. The wrong differential phase of the Gaussian fitting is removed almost completely by the pedestal correction as shown in Fig. 4.17 (a). Only problems at the edge of the bubble remain. They are comparable to the ones of the Fourier analysis. In the real data set in Fig. 4.17 (b), the pedestal correction also improves the slightly to large determined beamlet shifts.

The main advantage of the Gaussian fitting (and also the moment analysis) is that no problems with phase wrapping (phase jump by 2π) occur during reconstruction as it is often observed in Fourier analysis[40] (see Fig. 4.16 differential phase x at short distance). The Fourier analysis is very sensitive on the region of interest used for the analysis. Already single pixel shifts can reduce or increase phase wrapping considerably.

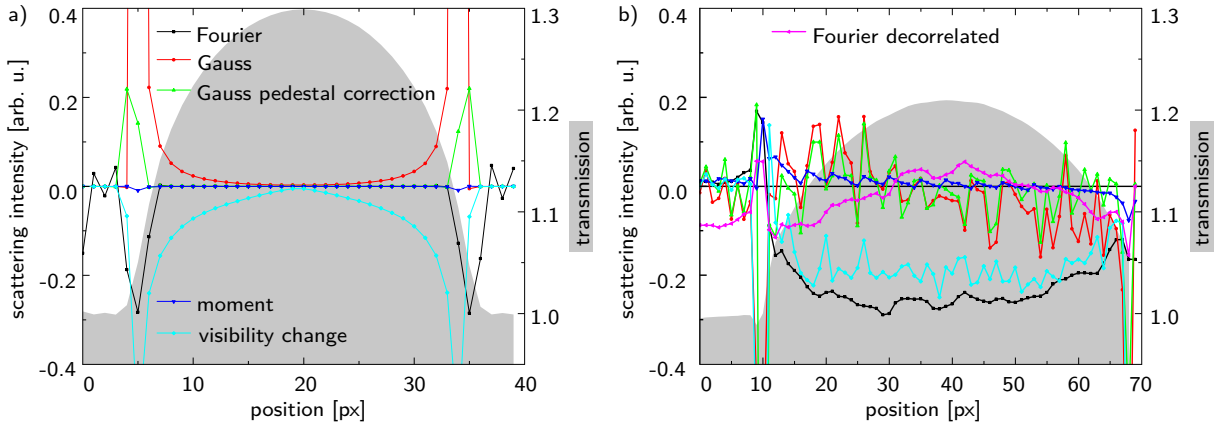

Fig. 4.18: Line section of the scattering contrast through the center of a simulated bubble (a) and a measured air bubble (b) retrieved with different algorithms. Fourier analysis and image moments retrieve only at the edge of the simulated bubble increased scattering values. By Gaussian fitting one gets a faulty increased scattering signal inside the bubble, which can be suppressed by a pre-analysis pedestal correction. The visibility change also shows a faulty decreased signal. In the measurements in (b) the Gaussian fitting and moment analysis do not show an increased scattering intensity. Fourier analysis and the visibility change both show a decreased scattering signal resulting from crosstalk. By decorrelation the faulty scattering signal in Fourier analysis can be improved. Note that the scattering intensity for the visibility change is a quantitatively different value than for the other algorithms. **[Sim5] [SI2]**

Scattering contrast

The scattering contrast is obtained by the beamlet width increase, which can be retrieved by all four mentioned algorithms. In Fig. 4.18 line sections of the scattering intensity through the center of the simulated air bubble (a) and the measured air bubble (large sample-to-detector distance) (b) are shown. No scattering signal is expected as only an empty air bubble in water environment is simulated and measured.

The results of the four algorithms for retrieval of scatter contrast are more diverse than for the differential phase contrast. The algorithms do not only behave differently for both contrasts, they even show different behaviors between simulation and measurement. The Gaussian fitting is known to have problems with a finite transmission curvature. This leads to higher signals in the outer area of the simulated bubble as shown in Fig. 4.18 (a). This erroneous behavior can be improved by the pre-analysis pedestal correction mentioned already before. In the measured data no scattering signal was observed, neither for Gaussian fitting nor for pedestal correction. However, one has to keep in mind the strong difference in the scatterer size sensitivity obtained in the simulations (see subsection 4.3.4).

The visibility, as the most used algorithm in GI, has by nature large problems with a curved transmission background. In both cases, of simulation and measurement a negative scattering signal is observed for the visibility change, which means an increased visibility. A pedestal correction comparable to the one for Gaussian fitting did not improve the results. Only if no *offset* was simulated (zero transmission in non beamlet area) the visibility was unchanged. Hence, only for optical elements with a very high primary visibility this algorithm might be suitable. One has to keep in mind the changed scatterer size sensitivity compared to the predictions.

The fast Fourier analysis is known to show a crosstalk from transmission contrast to scattering contrast.[41, 205, 238] This is not observed in the simulation, but not in the measurement. The difference in

behavior between simulation and measurement may result from the non-periodic boundary conditions in the measurement compared to the periodic simulation. In the measured air bubble the scattering signal drops comparably to the transmission rise. Furthermore, the scattering signal is higher for a measurement with a shorter sample-to-detector distance. One can speculate if this crosstalk is not only linked to the transmission contrast but also to the beamlet shift. The decorrelation, as presented in subsection 4.2.3, reduces the spurious scattering signal. Only some minor variations with space remain (see Fig. 4.18).

The fourth algorithm, the image moment analysis, shows no strong scatter signal at all. A slight increase in scattering to the edge of the bubble still could be observed. This was sensitive to the value of *offset*, but not completely removed for none *offset*. By a pre-analysis pedestal correction this could be reduced, showing only errors directly at the bubble edge. The scattering intensity distribution for different scatterer sizes is very similar to the expected one but the intensity is not stable under changing conditions. A change in beamlet size as well as a change in background intensity changes the scattering intensity easily over more than two orders of magnitude as simulations showed. For pure relative measurements this might still be feasible but not for comparisons with different setups. In contrast to the image moment analysis the scattering curve obtained by Fourier analysis is, with minor deviations, always the same. Hence, the Fourier analysis seems to be the more stable algorithm, especially if the setup conditions are changed. In this work mainly the change in scattering intensity due to NPs appearance is measured. Since this depends only on relative scattering intensity changes, the image moment analysis can still be useful.

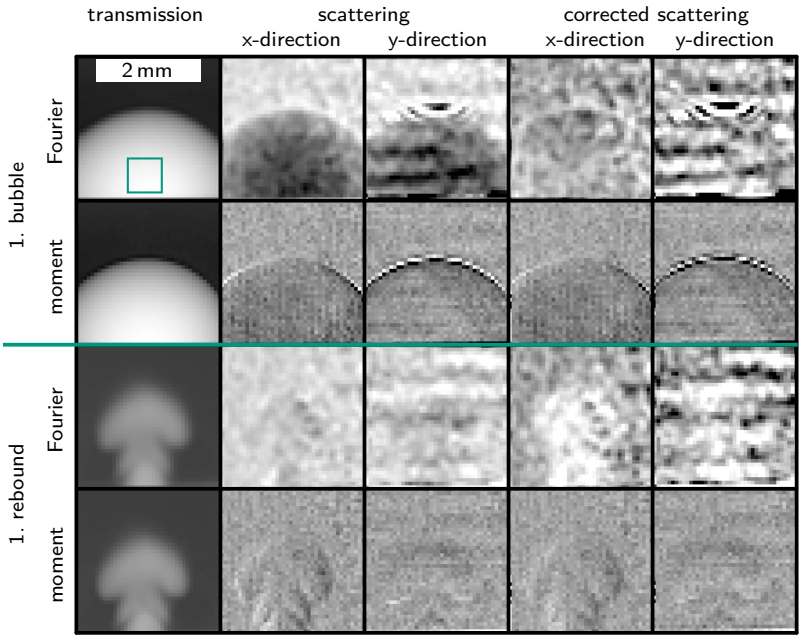

Fig. 4.19: Comparison of the resulting scattering images obtained with Fourier and image moment analysis. Snapshots of transmission and scattering contrast of the laser-induced cavitation bubble 100 µs (1. bubble) and 275 µs (1. rebound) after laser excitation (coming from top) on a zinc wire (horizontal at bottom). The Fourier analysis shows strong crosstalk from transmission and only minor from phase contrast. This crosstalk can be removed mostly by decorrelation. The moment analysis shows stronger crosstalk from phase contrast but the proposed pre-analysis pedestal correction did not improve the scattering signal. The grey scales are [0.95; 1.3] for transmission, [-0.16; 0.06] for scattering with Fourier analysis, [-0.005, 0.005] for scattering with moment analysis and [-0.05; 0.05] for the decorrelated scattering with Fourier analysis. **[SI1]**

For measurements at PLAL, the moment analysis performed worse than expected. In Fig. 4.19 snapshots of the transmission and scattering contrasts analyzed by Fourier and moment analysis of an ablation

event are shown. A zinc wire (1 mm diameter) was ablated with a 1064 nm, 7 ns laser with a pulse energy of 11 mJ. A long sample-to-detector distance with 40 cm was used. This corresponds to a peak sensitivity of around 900 nm, hence a higher sensitivity to larger structures compared to the expected NPs. Only the ability of scattering contrasts is to be discussed here. The detailed discussion on the phenomena of PLAL are explained in subsection 6.3.2.

The first bubble appears dark in the scattering signal due to crosstalk. This is more pronounced in Fourier analysis. In moment analysis, however, a stronger crosstalk from phase contrast at the edge of the bubble is observed. The first rebound is almost invisible in Fourier analysis while in moment analysis the crosstalk from phase dominates.

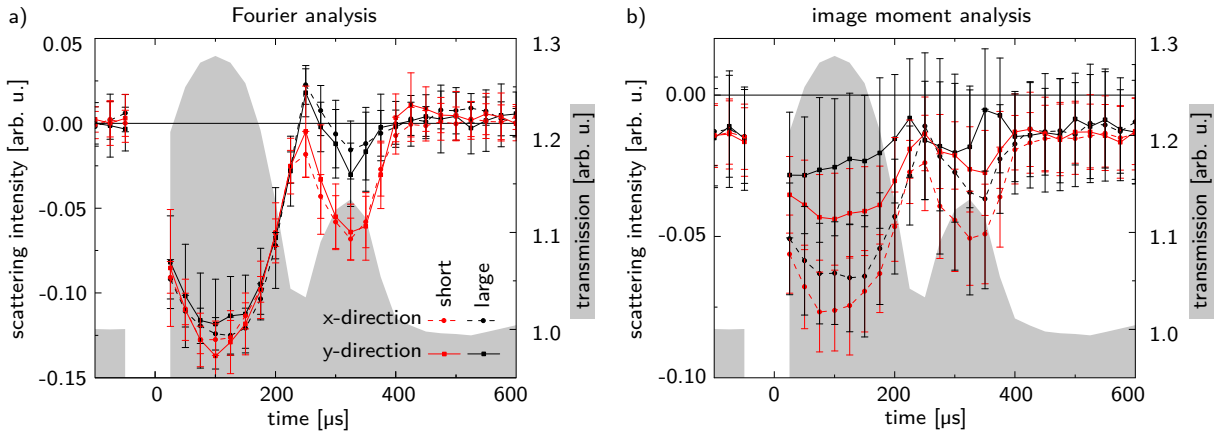

Fig. 4.20: Temporal evolution of the raw scattering intensity after laser ablation retrieved with Fourier and moment analysis investigated at the green square of Fig. 4.19. Measurement with two different sample-to-detector distances (short: 4.5 cm, large: 40 cm) are shown. While Fourier analysis results in similar signals for both directions the moment analysis differs much more. **[SI1]**

The temporal evolution of the scattering signal investigated in the green square of Fig. 4.19 allows for a more detailed statement of the abilities of both algorithms. In Fig. 4.20 the scattering intensities for both directions are plotted for a short (4.5 cm) and a long (40 cm) sample-to-detector distance for both algorithms. As almost spherical NPs are investigated, no difference in the scattering direction is expected. For Fourier analysis this holds true. Only a change between the two distances are observed (details on that difference see subsection 6.3.2). But for the moment analysis the scattering signal for both directions differ a lot. Furthermore some undefined internal structures in the first bubble are observed in the y-direction for the moment analysis.

For both algorithms corrections of the crosstalk are proposed, a decorrelation for the Fourier analysis and a pre-analysis pedestal correction in the case of moment analysis. They showed both good results in simulations and reference measurements (see above). For Fourier analysis, the scattering contrast changes slightly above the background value for the first bubble and for the first rebound to a bright appearance. The scattering contrast retrieved by moment analysis does not change significantly when retrieved with the pre-analysis pedestal correction.

In contrast to the simulations and reference measurements with an empty bubble, the real scattering measurements during PLAL showed an unreliable scattering signal for the moment analysis. This does

not reflect the results showed by Vittoria et al.,[41] where they showed that the moment analysis is of advantage compared to the pure fast Fourier analysis.

Robustness

The analysis of different measured and simulated data showed a varying robustness of the algorithms in sense of the calculation and not the retrieved signals. The fast Fourier analysis is very sensitive on the boundary conditions and hence on the choice of the proper region of interest. Technically, it is also limited to areas with an even number of pixels and an even number of beamlets. This reduces the flexibility, which leads to problems with phase wrapping and possibly a crosstalk from transmission to scattering contrast. In addition, the perpendicular alignment of the optical element to the camera is very important. Single defective pixels of even beamlets do not lead to strong artifacts. The advantage of the fast Fourier analysis is the low calculation efforts leading to a fast analysis. Only the required decorrelation for a pure scattering contrast reduces the speed slightly.

The visibility is also a fast algorithm and has relaxed requirements on the proper crop area. However, the absolute value of the visibility changes with the choice of the footprint size of the minimum and maximum calculation. As long as only changes within one measurement are of interest, this is no serious problem. Defective pixels lead directly to artifacts. This can be improved by a smoothing before the analysis with the drawback of simultaneously reducing the measured signals.

The Gaussian fitting is the slowest algorithm. The least-square optimization of the 2D Gaussian function for each beamlet is very time consuming. A parallelization is easy possible to reduce the calculation time. In contrast to the other algorithms here the calculation time and not the data reading time is the bottleneck. The requirements on the proper crop are relaxed. If necessary, the primary selection can even be optimized. The Gaussian fitting is prone to single defective beamlets and sometimes the optimization routine does not converge or converges to a wrong secondary minima. By plausibility tests of the results and a followed reevaluation with restricted parameters this problem should be reduced.

From calculation robustness point of view the image moment analysis was found to be the best one of those four. The requirement on the proper choice of the region of interest is relaxed. As for the Gaussian fitting, the proper crop can even be improved by a optimized before the analysis. The calculation efforts are low leading to a short calculation time. Single defective pixels do not lead to strong artifacts. Only defective beamlets lead to faulty pixels in the resulting images.

Conclusion

In conclusion, the following image can be drawn as shown in table 4.4. The **Fourier analysis** is the only real multi-contrast algorithm allowing to reconstruct all three contrasts reliably. The drawback of the crosstalk into the scattering contrast exists, which can be reduced by a decorrelation. Additionally, Fourier analysis allows to shift the scatterer size sensitivity to higher values by using higher orders (see Fig. 4.15 and discussion). For the analysis of lens arrays the Fourier analysis is not suitable as it does not provide a direct access to the beamlet parameters.

The **Gaussian fitting** gives competitive results for the differential phase contrast. The minor problem with the accuracy, if a high transmission curvature is present, can be improved by a pre-analysis pedestal

Table 4.4: Conclusion on the comparison of the four contrast reconstruction algorithms Fourier analysis, Gaussian fitting, image moment analysis and visibility change. Reliable results are highlighted in **bold**. The only real multi-contrast algorithm is the Fourier analysis as all others show problems in at least one contrast. In specific cases also the other algorithms have their advantages.

	phase contrast	scattering contrast	lens array characterization
Fourier analysis	**good**	**good with decorrelation**	no direct access to beamlet parameter
Gaussian fitting	**minor problem in accuracy**	changing sensitivity with setup parameters	**good**
image moment	only quantitative results	no stable reliability	only Gaussian beamlet width
visibility change	not possible	bad, crosstalk and inconsistent sensitivity	**good for focal point determination**

correction or by using optical elements with a high visibility, hence small background level. For the scattering contrast it is not suitable despite the fact that no crosstalk into the scattering contrast was observed. However, the sensitivity of the scattering cannot be predicted reliably because it depends strongly on the beamlet parameters. The strength of the Gaussian fitting is the characterization of lens arrays. Here, one has direct access to the beamlet parameters. The beamlet pattern can be analyzed by the positions and the beam shape consistency from the widths. To determine the focal length, either the point with minimum spot size or the visibility V_{Gauss} can be used. As shown in the section 5.2, V_{Gauss} is advantageous because the spot widths varied more within the beamlet pattern.

Image moment analysis does not provide reliable results for differential phase contrast and scattering contrast. The values depend strongly on the setup parameters, since the *offset*, for example, changes these values considerably. Despite the good agreement of the differential phase in Vittoria et al.[41] for the image moment and fast Fourier analysis, the results of the simulated and the measured air bubble did not confirm this. A qualitative statement seems to be possible, but not a quantitative one, since the absolute values differ strongly. The scattering contrast showed promising results in the simulation with only a minor error level. This even could be reduced by a pre-analysis pedestal correction. In real measurements during PLAL this was not confirmed and is, again, in contrast to previous results.[41] The scattering contrast showed a similar crosstalk from transmission as the fast Fourier analysis and the proposed correction failed, different scattering signals in horizontal and vertical direction (despite of isotropic scatterers) and unreliable structures inside the cavitation bubble. For the lens array characterization the image moment analysis is only suitable for the beamlet width. Furthermore, only in the case of Gaussian beamlet shapes the second moments can directly be transferred to beamlet width.

With **visibility** one has no access to transmission and differential phase contrast. So it is not a multi-contrast retrieval algorithm. The change in visibility can be related to a scattering signal, but the simulations showed a crosstalk from other contrasts and additionally a inconsistent sensitivity. The visibility is a measure of how strong the beam patterning is and therefore characterizes the optical elements. It

allows a quick estimation of the correct working cycle of a Hartmann mask and the distance to the focal point of a lens array.

5 Production of Compound Array Refractive Lenses for hard X-rays

This chapter focuses on the production of 2D lens arrays, so-called Compound Array Refractive Lenses (CARLs), and their characterization. Focusing lenses for hard X-rays are typically stacked lenses due to the low refraction power. The 2D lens arrays are intended to replace Hartmann masks in Single-Exposure Multi-Contrast Imaging techniques to increase the flux efficiency. Therefore they need to have small lens pitches as well as a short focal length.

Within this work different possibilities of the production of CARLs were developed. The 2D lens arrays were embossed into plastic foils and afterwards stacked to reduce the focal length. The different production schemes were:

- serial spiral embossing with sewing needle and stacking under an optical microscope,
- serial line-by-line embossing with custom-made needle and
- single-step embossing with needle array and stacking under X-ray illumination.

The 2D lens arrays are analyzed in terms of regularity. The distance to neighboring lenses and the relative position of the lenses to the grid were determined for the regularity evaluation. With the first one you can easily recognize misalignments of single lenses. The second one accounts for more changes in pitch over the entire array. Furthermore, the focal length and homogeneity of the stacked lens arrays was determined.

Parts of this chapter have already been published.[59] Details on the characterization are listed in the "List of Experiments". They are referenced in the text in bold square brackets, e.g. ***[XRI2]****.*

5.1 Fabrication of 2D lens arrays

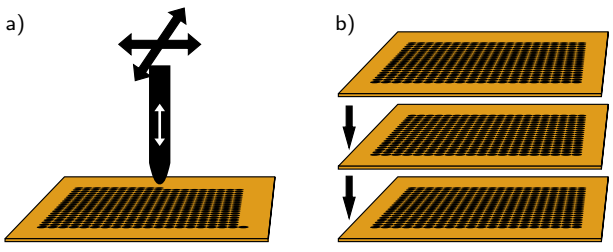

Fig. 5.1: Fabrication of a Compound Array Refractive Lens. First a 2D array of dents is embossed into a plastic foil (a). This can be done either serially with one needle as depicted here or in a single-step with a needle array. Afterwards several of these 2D lens arrays are stacked on top of each other and fixated (b).

X-ray focusing lenses have to be concave as the index of refraction is slightly below unity. The refraction of materials, which have a considerably high transmission is weak. Hence, small radii or large stacks

of lenses are needed. The CARLs developed within this work are a compromise of both. They have apex radii of 8 µm and 25 µm and are stacked up to six times. The fabrication is illustrated in Fig. 5.1. First, the individual lenses of a 2D array are embossed with a needle or a needle array (a) and then these 2D lens arrays are stacked on top of each other (b). Different production schemes were developed in this work and are presented in the following subsections.

Several conditions must be fulfilled for the correct embossing of the lens arrays. First, the lens material must have the correct X-ray parameters. The lens materials of choice are polyimide (Kapton®) and biaxially-oriented polyethylene terephthalate (Mylar®). Both have a low absorption in the hard X-ray regime (below 5 % for a thickness of 100 µm and X-ray energies above 10 keV)[232] and competitive focusing capabilities.[222,250,251] The absorption aperture for parabolic lenses (of 1 m focus length) is in the range of 300 µm to 700 µm.[251] This is much larger than the maximum of 65 µm used here. In addition, these materials have a high X-ray durability to resist radiation damage.[252]

The mechanical properties are also important. The lens material must be ductile enough to enable embossing, but at the same time stiff enough not to lose its shape after embossing. The stamp must be hard enough to withstand several thousand embossing steps without changing the shape. The shape of the stamp is also of central importance. To avoid spherical aberrations, the perfect shape is a rotational parabola. The apex radius defines the focal length and must be small (in the µm range) to avoid obtaining too long focal lengths.

The CARLs fabricated here are used for SEMCI to detect NPs. The spatial resolution of the resulting contrast images is defined by the pitch of the lens array. A spatial resolution of about 65 µm was considered to be suitable for an acceptable mapping of the ablation process. The size of the investigated NPs is expected to be below 100 nm as shown by SAXS measurements before.[30,118] Peak sensitivities, as described in subsection 3.4.4, below 100 nm are very challenging. The X-ray energies are limited by (i) the beamline parameters and (ii) the producible focal length with CARLs. Additionally, the minimal sample-to-detector distance is limited due to the mechanical properties of the camera systems.

5.1.1 Serial embossing with a single needle

The embossing or pressing of X-ray lenses has been carried out almost since their invention.[51,253] These spherical or parabolic lenses were always single lenses and not 2D arrays. An important step towards the achievement of 2D lens arrays was carried out in this work.

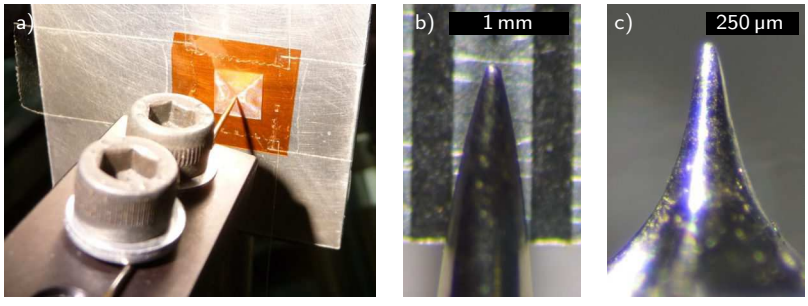

Fig. 5.2: (a) Setup for serial embossing a 2D lens array (after embossing) with the movable needle at the front and the mounted polyimide foil (orange) in the background. (b) Commercial steal needle with apex radius ≈25 µm and (c) custom-made steal needle with apex radius of 8 µm. Both were used for the embossing of the lens arrays.

For the serial embossing of the 2D lens arrays two different needles were used. These are a commercially available sewing needle with controlled shape and a custom-made needle produced of hardened steel as shown in Fig. 5.2 (b) and (c). The latter was produced with a CNC-milling machine and the apex radius was only 8 µm. In addition to the precise needles also the embossing machine itself must be very precise. The movement must be accurate not only for a few steps, but for tens of thousands of repetitive steps. This precision should be below 1 µm. An additional aspect is a proper alignment of the lens foil versus the needle movement. Again, two development steps were carried out in this work. In the beginning a hexapod (PI miCos HP-550) was used and finally linear stages and rotary axes with encoders for absolute positioning. In Fig. 5.2 (a) the sewing needle mounted on the hexapod standing in front of the already embossed array is shown.

Lens array embossed with sewing needle

The sewing needle was selected for a proper apex shape as most tested specimen are unsuitable due to ridges established during the production process. The apex radius was determined to be (25 ± 5) µm. The needle was mounted on a hexapod to easily align the embossing plane to the lens foil. This foil (Kapton®) was fixed with adhesive tape on an electrically conductive plate as shown in Fig. 5.2 (a). The edges were kept free of tape for the alignment. The plate was optically prealigned to be perpendicular to the needle. The electrical conductivity between the needle and the holding plate was measured for precise alignment. Outside the foil area the needle was approached to the plate until an electric conductivity was established. The tilt between the holding plate and the needle movement plane was removed by rotating the hexapod. The Kapton® foils had a defined thickness of 75 µm, making the alignment of the holding plate sufficient for the subsequent embossing process.

As already hinted in Fig. 5.1 (a), the embossing procedure started with a central lens followed by rectangular spirals of increasing size. An embossing line-by-line was not possible with this setup. The foil was slightly deformed due to material expulsion. By the spiral embossing this deformation was distributed homogeneously over the complete area leading only to a slight pyramidal shape of the lens array. With line-by-line embossing, the deformation added up with an increasing number of lines, resulting in strong wrinkles that make the embossing inaccurate or even impossible. The slight pyramidal shape of the lens array was also visible in the beamlet properties during use, as shown later in the section 5.2. Lens arrays with 97×97 lenses or larger were produced. Each following lens array was two lens rows and columns larger. This was necessary for the stacking, as explained later in subsection 5.1.3.

In Fig. 5.3 an optical microscope image of a lens array is shown. At first glance it looks very regular. However, a detailed analysis of the single lens positions shows the already mentioned slight pyramidal shape. From this image the position of each lens was calculated by the Gaussian fitting (see subsection 4.2.1).

The distance between two lenses is shown in Fig. 5.4 (a) and (b) for the vertical and horizontal direction, respectively. One can see a slight variance of the distances from the design value of 65 µm. The Standard Deviations (SDs) are 0.8 µm and 0.9 µm for the vertical and the horizontal distance, respectively. The mean value of the lens distances was set to 65 µm as no absolute scaling of the micrograph was available. The next neighbor distance is not the only measure of the regularity. The global positioning on a rectangular grid is also of importance. In Fig. 5.4 (c) and (d) the relative positions in vertical

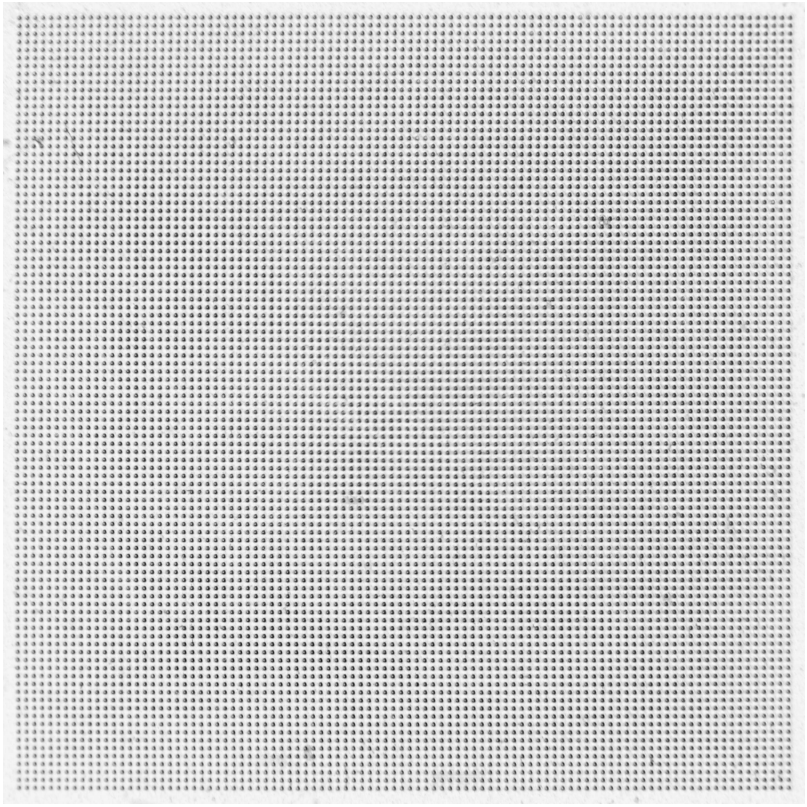

Fig. 5.3: Micrograph of one 2D lens array with 97 × 97 lenses and a pitch of 65 µm after spiral embossing. The pyramidal shape (in this case not very strong pronounced) is only slightly visible at the edges of the lens array by the defocusing and the lens distance as shown in Fig. 5.4.

and horizontal direction are shown. In the vertical direction it can clearly be seen that the array can be split into four triangular sections representing the flanks of the pyramidal shape. The strong difference in the horizontal direction comes from the barrel distortion of the microscope and should not be over emphasized.

The hexapod was a convenient way for a fast alignment of the needle to the lens plane. However, the missing encoder resulted in a high amount of wrongly embossed lens arrays. For the embossing of around 10.000 lenses with more than 40.000 movement steps a repetitive absolute movement is of central importance. This can only be guaranteed by motors with encoders, which can correct previous wrong steps.

Despite these deficiencies an acceptable regularity of lens arrays was achieved. This allowed to stack several of these lens array foils to one CARL and perform scattering imaging at the ablation process as discussed in subsection 6.3.2.

Lens array embossed with milled needle

In the next development step, the needle shape and the embossing machine were improved. The needle used was custom-made with higher precision and a smaller apex radius. The development of the pyramidal shape of the lens arrays during the embossing process was eliminated by an improved foil mounting and the usage of thicker foils.

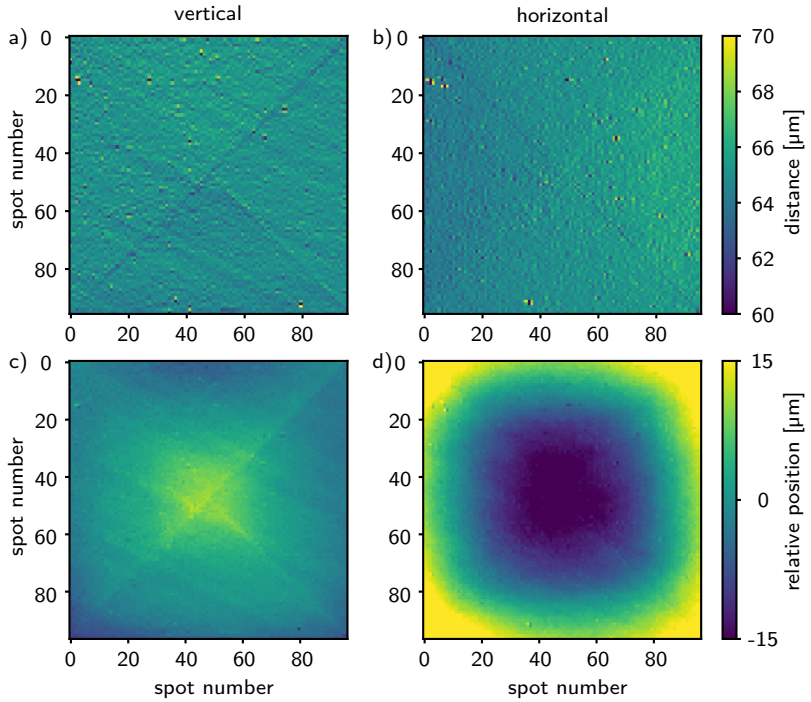

Fig. 5.4: Test of regularity of the spiral embossed lens array of Fig. 5.3. The distance in vertical (a) and horizontal (b) direction between neighboring lenses shows a low deviation from the mean distance of 65 µm. In (c) and (d) the relative positions compared to the expected one are shown. The pyramidal shape is visible by the diagonal lines of changed distance and relative position. Note, that the much increased relative position in horizontal direction comes from artifacts of the microscope.

The needle was produced with a CNC-milling machine by the Institute for Biological Interfaces (IBG-2) at the KIT. The design function $f(x)$ of the needle was:

$$f(x) = 62.5\,\mathrm{mm}^{-1} \cdot x^2 \qquad \text{with} \qquad r(0) = \frac{1}{2 \cdot 62.5\,\mathrm{mm}^{-1}} = 8\,\mu\mathrm{m}\,, \tag{5.1}$$

with x being the distance from the central axis and $r(0)$ the radius at the apex. An image of this needle was shown in Fig. 5.2 (c). With this decrease in apex radius also the focal length of a single lens was reduced by a factor of around three.

The embossing setup was improved by using linear stages with encoders for the movement of the needle and a set of rotational axes for the perpendicular alignment. This enhanced the accuracy of the absolute movements as wrong steps of the previous movement are corrected with the next one. The embossing movement with an approaching step and a separate embossing step was the same as before. As lens material 125 µm thick Mylar® foils were used. They were fixed on glass slides at the entire area with acrylate glue. The glue could easily be removed afterwards with acetone. This allowed to emboss the lenses line-by-line with no wrinkles observed at all. This could be due to the increased thickness and hence higher stiffness or the gluing.

In Fig. 5.5 the regularity of such a 2D lens array (100×100 spots of pitch 50 µm embossed in Mylar®) is represented as the distance between neighboring lenses in (a) and (b) and the relative position in (c) and (d). Note that here an X-ray image of the focused spots was used instead of a micrograph as for the previous lens array. This increased the probability of fit errors, since the contrast in such X-ray images is significantly lower compared to microscope images. However, X-ray image analysis is the better way

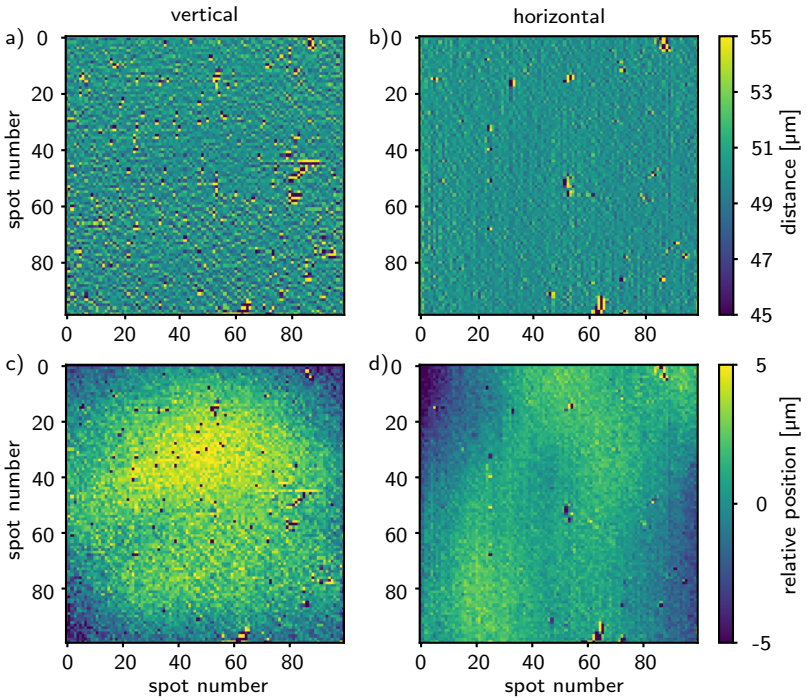

Fig. 5.5: Regularity of a lens array (100×100 lenses with pitch 50 µm) embossed line-by-line with a 8 µm apex radius needle. The distance in vertical (a) and horizontal (b) direction between neighboring lens spots shows a homogeneous variance from the mean distance with a standard deviation of 1 µm in both directions. In (c) and (d) the relative positional shifts of the spot compared to the expected positions are shown. **[XRI2]**

to determine regularity, since the optical microscope image visualizes only reduced transmission and not the actual X-ray focusing capabilities. The regularity in sense of distance to the neighboring spots of this lens array was not improved compared to the first one. However, the relative positioning improved a lot (note the different scaling). Only a small variation of ±5 µm of the relative position over the complete array of 100×100 lenses is observed. The single strong deviations from the mean values are due to faulty fitting and do not represent strong errors in the lens array.

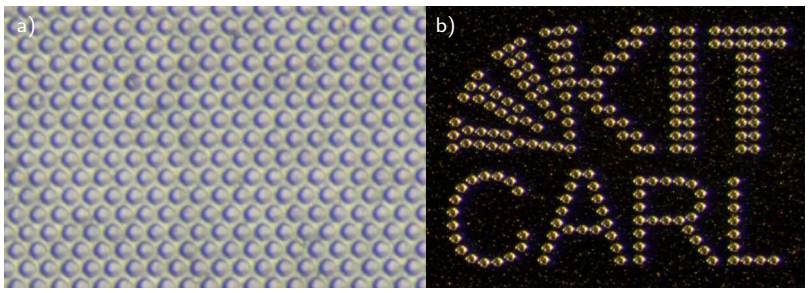

Fig. 5.6: Examples of lens arrays with non-rectangular patterns in form of a hexagonal pattern (a) and the KIT-Logo (b). The micrographs show an embossed foil in (a) and a stamper (see subsection 5.1.2 for more details on the production) in (b).

With the very flexible process of serial embossing also non-rectangular patterns can easily be realized. This has been tested by a hexagonal pattern and the KIT logo as shown in Fig. 5.6 (a) and (b), respectively. Both have a nominal pitch of 50 µm. The hexagonal pattern gives a higher fill factor of the lens apertures when produced in this way but complicates the reconstruction, especially in the case of Fourier analysis. For this reason only a proof of principle was performed and no further measurements were done.

Limitations in fill factor of serial embossed lens arrays

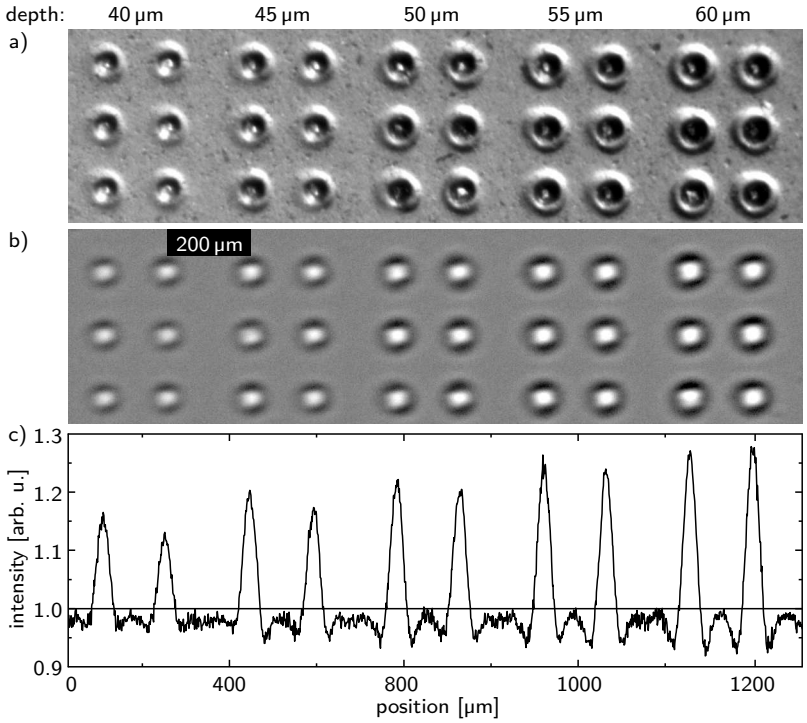

Fig. 5.7: Embossing depth dependence on lens performance. By increasing the embossing depth the lens diameter and the expulsion rim (shown in (a) as optical micrograph) likewise the beamlet intensity (shown in (b) as X-ray image and (c) as line plot of lowest lens row) increases. **[XRI3]**

The fill factor of the lens apertures is limited in an serial embossing scheme. During the embossing process material gets expulsed and builds up a rim around each lens. This rim increases with increasing embossing depth as can be seen in Fig. 5.7 (a). This leads to a limited depth of embossing for a fixed pitch. If the depth is too deep the neighboring lenses get distorted leading to a changed focal length. From X-ray images (white beam, central energy 15 keV) at a distance of $1/4$ of the focal length a clear peak intensity increase with rising lens depth is observed as shown in Fig. 5.7 (b) and (c). In addition, at greater depths an increase in the depleted area is visible. This corresponds well to the increasing area of focusing due to the increasing lens aperture. Furthermore, the deflection of X-rays away from the lenses on the outer side of the expulsed rims is visible by slightly bright rings around the dark depletion rings in Fig. 5.7 (b).

5.1.2 Single-step embossing with a 2D needle array

To pave the way to lens arrays with a fill factor of the lens apertures of almost 100 %, stamping with a needle arrays was studied. Besides the probably of higher fill factors also the embossing process time reduces from 15 h down to seconds. The production of such a needle array is a challenge. Within the scope of this work, only a first realization as proof of principle could be realized. There are many aspects for further improvements.

The ideal CARL in points of efficiency is an area filled array of truncated parabolic lenses. A design of a 4×4 array of such an ideal CARL is shown in Fig. 5.8 (a) with a crosscutting in (b). To fill the whole

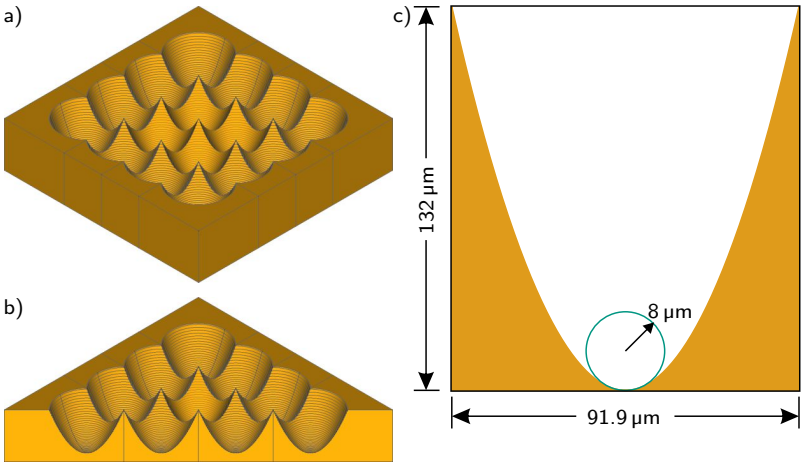

Fig. 5.8: (a) Ideal shape of a Compound Array Refractive Lens with a pitch of 65 µm and a cross section of it along the diagonal in (b). For a realization with an apex radius of 8 µm a lens depth of 132 µm is required to achieve a fill factor of 100 % of the lens aperture as shown in the diagonal lens slice in (c).

area in a rectangular pattern the edges of the lenses have to be much higher than the nodes leading to an egg carton like shape. Lets assume the lenses to have an apex radius of 8 µm and a pitch of 65 µm. When the lens should cover the complete diagonal of 91.9 µm of one lens zone, the required lens depth is 132 µm as can be calculated from equation (5.1). This is illustrated in Fig. 5.8 (c). It is arguable if the sharp edges at the lens boarders give a scattering signal that is detectable and hence reduces the sensitivity. One step into this direction was published just recently where one CRL with lenses of such a shape were produced by 3D laser writing.[254] However, a lateral stacking of many of these CRLs to a 2D lens array was not carried out.

In order to produce CARLs in such a form by embossing, a corresponding stamp in the form of a needle array is required. This is not commercially available. Here a needle array was produced by electroplating, but without a full coverage. The first step was again serial embossing was performed, so that the same filling factor restrictions as described above still apply. A series of lens arrays with different pitches and lens depths were serially embossed in a 4 " poly(methyl methacrylate) (PMMA) plate with the 8 µm needle. The needle array stamps were then produced by nickel electroplating by microworks GmbH (Karlsruhe, Germany). In a galvanic bath a layer of about 2 mm nickel was deposited on it. An overview image of the stamp and a zoom showing single needles of the array are shown in Fig. 5.9 (a) and (b), respectively.

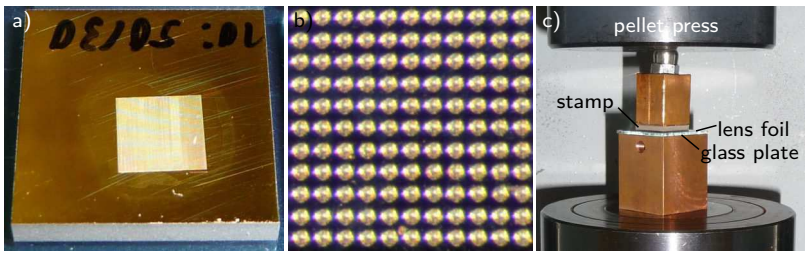

Fig. 5.9: Images of the 2D needle arrays as stamps for lens array embossing. In (a) an overview of a stamp with a pitch of 50 µm and in (b) a micrograph of an array with 65 µm pitch are shown. In (c) the embossing in a pellet press is shown.

The embossing of CARLs using these needle arrays is no longer possible with linear stages because the required forces are too high. The number of needles is increased from 1 to 10.000. The expulsion of material during embossing has also to be encountered. As shown before, during the embossing the material gets expulsed and builds up a rim around each lens. With the needle array all lenses are embossed in once. Therefore this material movement is stronger limited as before. It has to be moved according to the stamp geometry, which additionally increases the needed force.

The embossing was performed in a commercial pellet press (Model 4350, Carver Inc., USA). The setup is shown in Fig. 5.9 (c). To ensure an even lens backside, the foils were placed on a glass plate. The stamp was soldered onto a copper rod with a round back to ensure a balanced force distribution over the entire surface of the lens array. With that the stamp could be placed parallel to the lens foils and the force was loaded perpendicular irrespective of some tilts due to the production process. The lenses were embossed with a load of around 3.5 t. Since no significant changes in the shape of the lens array have been observed for different waiting times, it can be concluded that no long lasting material flow processes have taken place and that the lens arrays are embossed immediately.

The obtained fill factor fits well to the design values of the embossing. The embossing depth was 50 µm at a pitch of 65 µm, resulting in a fill factor of 59 % expected from the embossing depth and less than the maximum possible value of 79 %. This shows the very good replication of the embossed master to the stamp by electroplating and the following single-step embossing of lens arrays. The good embossing replication also can be seen in Fig. 5.7. The aperture diameters fit closely to the expected needle diameters. During the master production this embossing depth was considered to be a safe value to not distort the already embossed neighboring lenses. Further improvements in the stamp shape are beyond the scope of this work. One possible way might be to use 3D direct laser writing to produce a better master for the electroplating process.

In Fig. 5.10 the regularity of a lens array (pitch 65 µm) produced by single-step embossing is shown. In vertical direction the results are very similar to the lens array embossed serially. Again, this shows the good replication. In horizontal direction, however, stripy structures are observed. The SD of the distance between neighboring spots is 1.5 µm and so three times higher compared to the vertical direction (0.6 µm). This decrease in regularity must be explained by the serial embossing of the electroplating master. The embossing setup was changed slightly compared to the previous one. The horizontal axes was the slow axes during the embossing process. In this case a linear stage without an encoder was used for the slow axes. The single-step precision even for the slow axis was less than expected.

One further observation during single lens foil investigation is, that the line-by-line embossed lens arrays are slightly better to analyze compared to the single-step embossed ones. The visibility was slightly reduced. Hence, the line-by-line embossed ones seem to have a bit higher focusing ability. Lens arrays with a higher pitch could be produced with a deeper embossing without distorting the neighboring lenses. Hence, the higher pitch of the lens array in Fig. 5.10 compared to the one in Fig. 5.5 led to a better focusing of the X-rays, thus to a better visibility of the spots and therefore to a reduced number of wrongly analyzed spots.

To sum up the embossing of 2D lens arrays one can state that this is a suitable way to produce large area 2D lens arrays, which can be stacked to CARLs. If a well defined needle and precise stages are used for the embossing process, lens arrays with a good regularity can be achieved. Even galvanic replication, which permits single-step embossing, does not strongly reduce the lens quality. Needle arrays with a

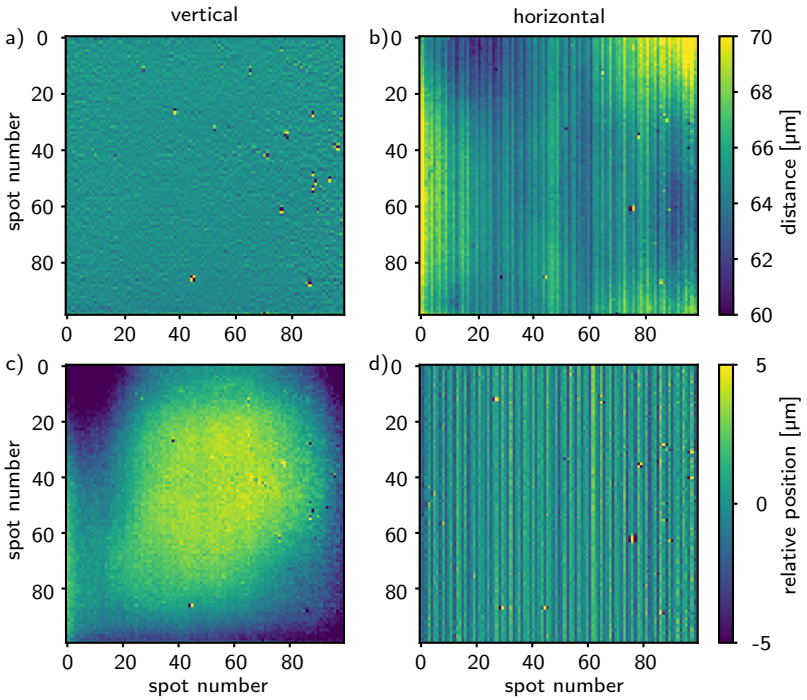

Fig. 5.10: Regularity of a lens array (100×100 lenses with pitch 65 µm) embossed by a needle array (apex radius of the needles 8 µm). The distance between neighboring lens spots differs in vertical (a) and horizontal (b) direction. While in vertical direction the distances are very similar (standard deviation from the mean distance 0.6 µm), stripe like changes are observed in horizontal direction (standard deviation 1.5 µm. In (c) and (d) the relative positional shifts of the spots compared to the expected positions are shown. Besides the stripy structure in horizontal direction again a slowly varying positioning is observed. **[XRI2]**

higher fill factor should improve the lens arrays a lot in the future. Unless a further reduced needle apex radius can be simultaneously achieved, only improvements in the focusing efficiency can thereby be achieved. As the lens arrays show a high precision, the reduction of the focal length can also be obtained by stacking of several foils.

5.1.3 Stacking for focal length reduction

The final step to CARLs is the stacking of the individual 2D lens arrays. The stacking has to be done to reduce the focal length to a suitable value of roughly 1 m. As already mentioned before, a small misalignment of the lenses is not changing the focusing properties but slightly the overall transmission.[222, 225] The first way of stacking lens arrays is under an optical transmission microscope with manual alignment. The second possibility is a stacking under X-ray illumination with a motorized alignment. The alignment under the microscope is easier in terms of requirements but lacks of accuracy compared to the alignment with X-rays.

Lenses are known to have a comatic aberration, when they are not illuminated paraxially. In Fig. 5.11 the focal spots of a 3×2 lens array is shown in dependence of the tilt angle. The lens array plane was rotated from 0° to 45° with respect to the incident beam. For small angles (below 20°) no change in the spot shape is observable. The requirements on a perfect perpendicular alignment are not very strict for single lens arrays. Note that the pitch changes slightly with rotation (6 % for a rotation of 20°). However, this no longer applies to stacks of lenses. Here the requirements are much stricter. Already small tilts

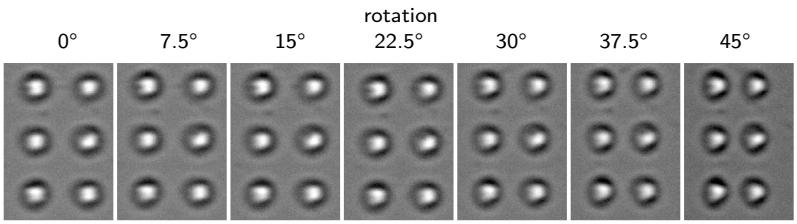

Fig. 5.11: Changes in spot shape due to lens rotation out of paraxial illumination. For small angles no comatic aberration can be detected while for angles above 20° a change in spot shape gets visible. Lens array of Fig. 5.7 with 60 µm depth. **[XRI3]**

result in a changed beamlet shape starting from elongation to complete smearing out. After stacking of five foils the stack height is much larger than the lens pitch resulting in a fast misalignment.

Stacking under an optical microscope

The lower lens array was fixed on the optical table of the microscope while the upper one was mounted onto a goniometer head, which itself was also fixed on the optical table. The lens arrays were aligned in rotation and position with respect to each other. Due to the fact that the lens arrays themselves showed a good regularity only the outer most lenses of both lens foils were aligned to each other. The lens foils were fixed with acrylate glue. After drying of the glue the next smaller lens foil was aligned on top of the previous ones. This process was used to produce stacks of up to six foils with acceptable spot homogeneity, as shown in the next section.

Stacking under X-ray illumination

The better way to align the lens arrays is under X-ray illumination. A small tilt of a CARL (beginning with two stacked foils) already decreases the spot quality strongly. This can only be addressed during an alignment under X-ray illumination. With optical alignment, good positioning is only possible for rotations along the optical axis, but not for an tilt to the optical axis. This comes into account especially for larger stacks.

For the alignment under X-ray illumination, one foil was mounted on a goniometer with all three rotational axes and two translation axes. The second lens foil was mounted on a two-dimension linear stage. Then the lens foils were aligned with respect to rotation and position. The focused spots of both lens arrays can be seen simultaneously. Hence no enlargement of the lens arrays as for the alignment under a microscope is required. To reduce the time of gluing hot glue was used for fixation. As soon as two foils are aligned to each other the tilt of these with respect to the optical axes has to be taken into account before alignment. Therefore the already stacked lenses have to be mounted onto the goniometer. The fifth stacked lens foil did not show a further improvement in spot intensity.

Alignment under X-ray illumination has the disadvantage that beam time at a synchrotron is required. However, the quality of the resulting CARL is better compared to the alignment under an optical microscope, as shown in the next section.

5.2 Focal length and homogeneity determination of CARLs

Two types of CARLs were produced and characterized for their focal length and homogeneity of the spot pattern. Results from a CARL stacked out of six lens arrays (pitch 65 µm), which were serially embossed with the sewing needle[238] and a CARL stacked out of five lens arrays (pitch 65 µm) embossed in single-step mode with a needle array as stamp are presented in this section. The latter shows an improvement compared to the first one in focal length and homogeneity. However, the visibility is reduced, which must be attributed to a smaller fill factor of the lens arrays. Some improvements in the characterization of the first one compared to the publication are explained.

CARL produced by serial embossing

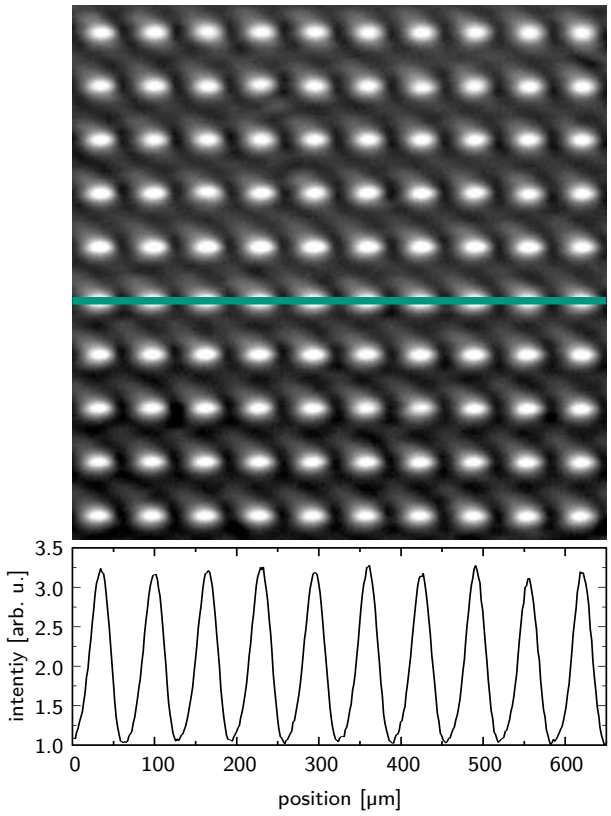

Fig. 5.12: Radiogram of a Compound Array Refractive Lens with six stacked foils of serially embossed lens arrays. Image crop of 10×10 spots together with a line plot of one lens column. The distance between the lens array and the detector is 125 cm, which represents approximately the focal length at 9 keV (see Fig. 5.13). **[XRI4]**

The CARL produced by serial embossing with a sewing needle showed a good 2D spot pattern. In Fig. 5.12 a crop of 10×10 spots together with a line plot of one spot column is shown. The spots are a bit elongated in horizontal direction. This elongation can not only be attributed to the horizontally elongated source size. A size reduction by slits did not change the elongation strongly. Thus, there must be some misalignment of the lens foils leading to elongated spots. For larger misalignment the different lenses in the stack produce spots, which do not coincide but rather are placed next to each other. This results in elongated spots.

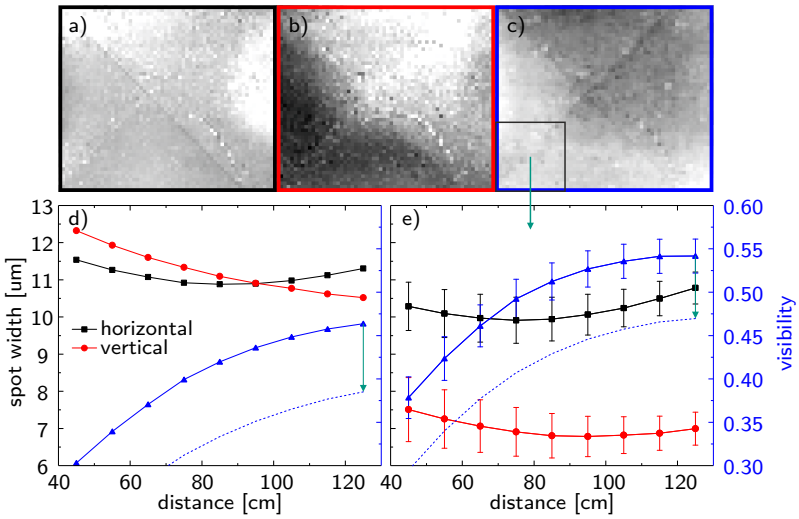

Fig. 5.13: Determination of the focus position (at 9 keV) of a Compound Array Refractive Lens with six stacked foils of serially embossed lens arrays. In (a), (b) and (c) the horizontal and vertical width of the spots and the visibility at distance of 125 cm are shown (scales as in the plots), respectively. The pyramidal shape of this Compound Array Refractive Lens can be seen in all three parameters leading to a high standard deviation over the array. By changing the lens-to-detector distance the spot size and visibility change as shown in (d) as mean for the complete measured array and in (e) as mean for a crop of 20×20 spots as depicted in (c). The three parameters do not give a consistent estimate of the focal length. For more details see the text. Reproduced from Reich et al.[238] **[XRI4]**

In Fig. 5.13 the results from a scan of the distance between the CARL and the detector is shown. In (d) and (e) the horizontal and vertical width as well as the visibility as function of the distance are plotted. Note that the visibility in solid line represents V_{bz}, which is calculated from the image extrema and the dashed line V_{Gauss} calculated from the Gaussian parameters. For (d) the average values of the complete measured array of 53×62 lenses are shown while in (e) the average of only 20×20 lenses are shown. This separation is done because the complete array showed a large variance as can be seen in the three images of horizontal (a) and vertical width (b) and visibility (c). Therefore also the error bars in (d) have been omitted.

As one can clearly see, the minimal spot width and the visibility do not necessarily coincide. For the complete array the horizontal width has its minimum at 85 cm while the vertical width decreases at least up to 125 cm. The visibility maximum is also located above 125 cm. For the small crop, however, the widths have their minimum at 76 cm (horizontal) and 96 cm (vertical) while the visibility saturates at 125 cm. This shows that the widths do more strongly vary than the visibility.

The expected focal length for a stack of six lens array foils made of Kapton® with $\delta = 3.77 \times 10^{-6}$ at 9 keV[232] and an expected apex radius of the lenses of (25 ± 5) µm is $f_{theo} = (110 \pm 22)$ cm. In comparison with the measured distances of minimal width and highest visibility, this value seems to be in fair agreement. The visibility of a smooth area peaks slightly above the expected focal length at 125 cm as shown in Fig. 5.13 (e). The peak visibility of the complete array, as shown in Fig. 5.13 (d), seems to peak at only a bit larger distances but still in the interval of confidence. The widths, however, are deviating stronger. They indicate both a smaller focal length in the crop of 20×20 spots. For the complete array they differ strongly from each other. The horizontal width indicates again a smaller focal length while the vertical direction indicates a focal length larger than the expected value.

The *height* is not necessarily a good measure for the focal point. It not only depends on the focusing abilities of the lens array but also on the air absorption. The latter increases with a larger distance leading to a reduced global intensity and also a reduced peak height. When the peak parameters are determined with division by the mean intensity before the analysis, the *height* peaks according to the visibility. This shows, that here the air absorption overcomes the focusing abilities of the CARL. For lens arrays with high gain and high visibility, the *height* depends only slightly on air absorption. In this case it still can peak around the distance of maximal visibility and minimal width, respectively.

If the *height* is considered in combination with the *offset* it is still a good measure of the focal point. The *offset* takes into account the increased air absorption during the scan of the distance. This combined consideration results in the visibility V_{Gauss} calculated from the Gaussian spot parameters as discussed in chapter 4.2. In Fig. 5.13 (d) and (e) the visibility V_{bz} calculated from the intensity extrema values (solid lines) and V_{Gauss} (dashed lines) show a similar behavior with only a shifted value.

For the simulated data in subsection 4.3.1 it was found, that both calculation algorithms do not necessarily result in the same visibility values. The condition of small beamlets, where both algorithms resulted in the same values, holds true for the measurements. The origin of the difference are the noise level and defective pixels. By calculating the image intensity extrema, higher maximum and lower minimum levels are detected compared to the *height* and *offset* values in Gaussian fitting. This shows that the absolute value of the visibility is not perfectly defined. In order to be able to compare different optical elements correctly with each other, attention must be paid to the exact calculation of the visibility.

The obtained visibility is around 0.5, which is above typical values in GI.[158] This shows the good focusing abilities of this CARL. One reason for this is the high fill factor. With the design values (pitch 65 µm, apex radius 25 µm and embossing depth 20 µm) the calculated fill factor is 75 %. This is very close to the maximum achievable value of 79 % for rectangular closest packed circles.

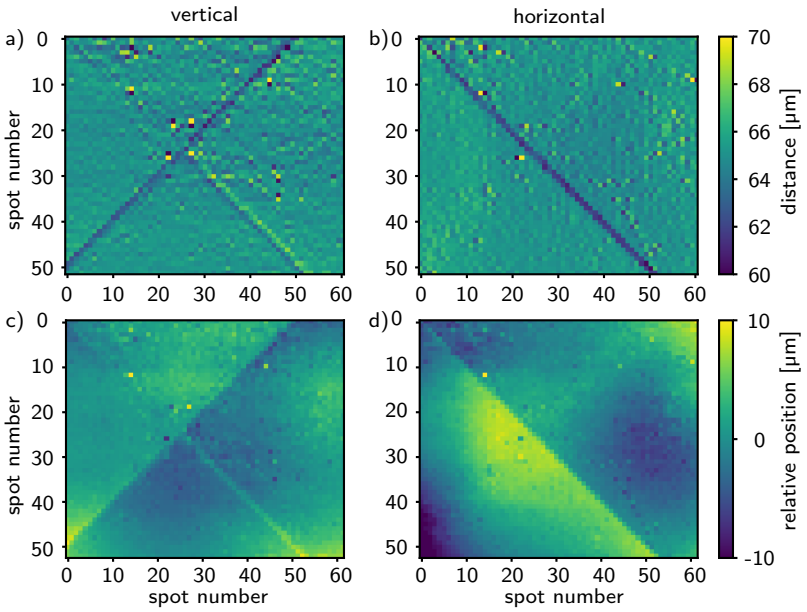

Fig. 5.14: Regularity of a Compound Array Refractive Lens with six stacked foils of serially embossed lens arrays. Except of the two diagonal lines at the edges of the pyramidal shape the distance between the spots varies only minor (standard deviation 1 µm in both direction). The relative position of the spots has a higher standard deviation of 2.3 µm in vertical and 3.8 µm in horizontal direction, respectively. Again the pyramidal shape is visible. The distance between the Compound Array Refractive Lens and the detector was 125 cm. **[XRI4]**

The regularity of the spot pattern did not change strongly during the alignment compared to the single lens arrays. In Fig. 5.14 the distance between neighboring spots in vertical (a) and horizontal (b) direction as well as the relative position in both directions in (c) and (d) are shown. The pyramidal shape observed at the single lens arrays is still present in the stacked CARL. The distance between neighboring spots varies only slightly from the mean value (SD 1 µm) and is comparable to the single lens arrays. The only strong deviations are present at the edges of the triangle sections induced by the pyramidal lens array shape. The relative positions show stronger steps at the diagonals and in the four triangles some smooth variations are present. The SD is 2.3 µm in vertical and 3.8 µm in horizontal direction for the complete area.

In summary, it can be concluded that this CARL, which consists of six stacked foils of lens arrays embossed serially by a sewing needle, has a focal length of about 125 cm. Due to the production some variations in the absolute values of the spot parameters and the visibility within the array do exist. The spots are positioned with a precision of around 5 % of the pitch. With a maximum visibility of 0.5 already a strong gain in the spots is achieved. With these promising parameters this CARL is suitable for the investigation of the ablation process. The results of the SEMCI of laser ablation on a zinc wire are shown in subsection 6.3.2.

CARL produced by single-step embossing

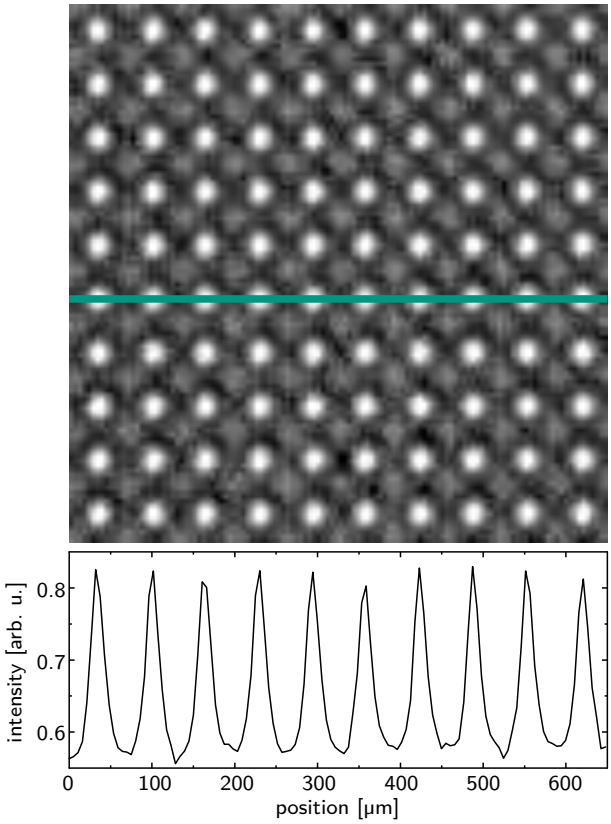

Fig. 5.15: Radiogram of a Compound Array Refractive Lens with five stacked foils of single-step embossed lens arrays. Image crop of 10×10 spots together with a line plot of one lens column. The distance between the Compound Array Refractive Lens and the detector is 59.7 cm, which represents the focal length at 8.5 keV (see Fig. 5.16). **[XRI5]**

The second CARL produced and analyzed consists of five stacked Mylar® foils with an array size of 100×100 lenses. Fig. 5.15 shows a crop of 10×10 spots measured at the focal length (see below). The spots are fairly round, which is an improvement compared to the previous CARL. On the other hand, the visibility of the spots is strongly reduced. In the anti-registry, roundish spot-like structures are also visible. The mentioned depletion zone could mimic such a pattern. They must therefore belong to those areas in which no lenses are present.

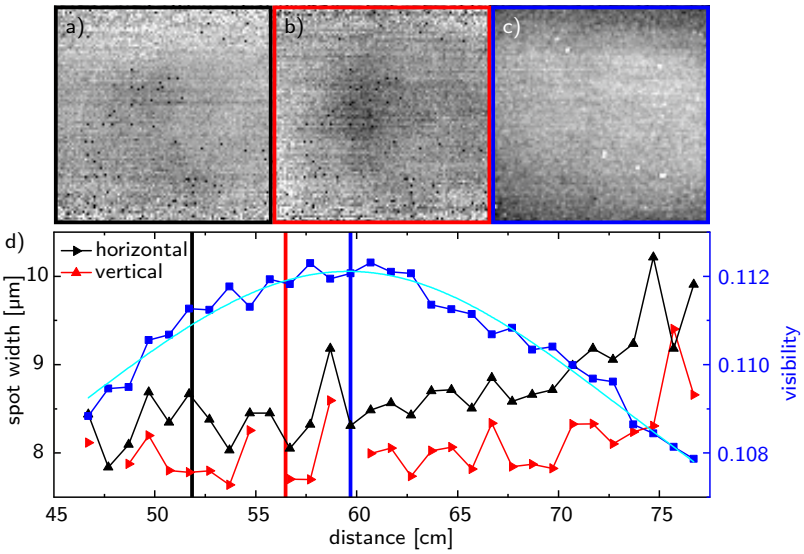

Fig. 5.16: Determination of focus position (at 8.5 keV) of a Compound Array Refractive Lens with five stacked foils of single-step embossed lens arrays. The images (a), (b) and (c) show the width in horizontal and vertical direction (scale [5 µm, 11 µm]) and the visibility (scale [0.07, 0.15]), respectively, imaged at the focal length. In (d) the distance dependence of the widths and the visibility are plotted. The visibility peaks at a distance of 59.6 cm as determined by a Lorentz fit (turquoise line). The standard deviation of the complete array (100×100 spots) is large due to the low primary beam intensity at the top and bottom. For smooth areas in the middle the standard deviations are 0.5 µm for the widths and 0.006 for the visibility. **[XRI5]**

Fig. 5.16 shows the horizontal (a) and vertical spot width (b) and the visibility (c) of this CARL at the focal length. The visibility peaks at the distance of 59.6 cm as shown in the plot (d). The fitted minima of the spot widths are located at 52.4 cm for the horizontal width and 57.4 cm for the vertical width. Since the spot widths vary only slightly and the errors are comparatively high, they are not a good measure for determining the focus. Especially the top and bottom parts of the CARL show a high noise level due to the low intensity of the primary beam there. In monochromatic mode the vertical size of the primary X-ray beam is strongly limited.

The expected focal length for this CARL ($\delta = 4.20 \times 10^{-6}$ at 8.5 keV,[232] apex radius 8 µm) is $f_{theo} = 38.1$ cm. The focal length determined from the visibility is 59.6 cm and is larger than the expected one. The spot widths indicate a somewhat smaller focal length but still considerably larger than expected. An explanation for the increased focal length might be a not perfect replication of the lens shape, although the apertures showed a good agreement.

The visibility of this CARL is by a factor of five lower than for the first one. This can directly be addressed to the lower achieved fill factor. A deeper embossing in the stamp master production could have improved the fill factor and consequently the visibility. A lens shape distortion of neighboring lenses is not directly expected from the results here.

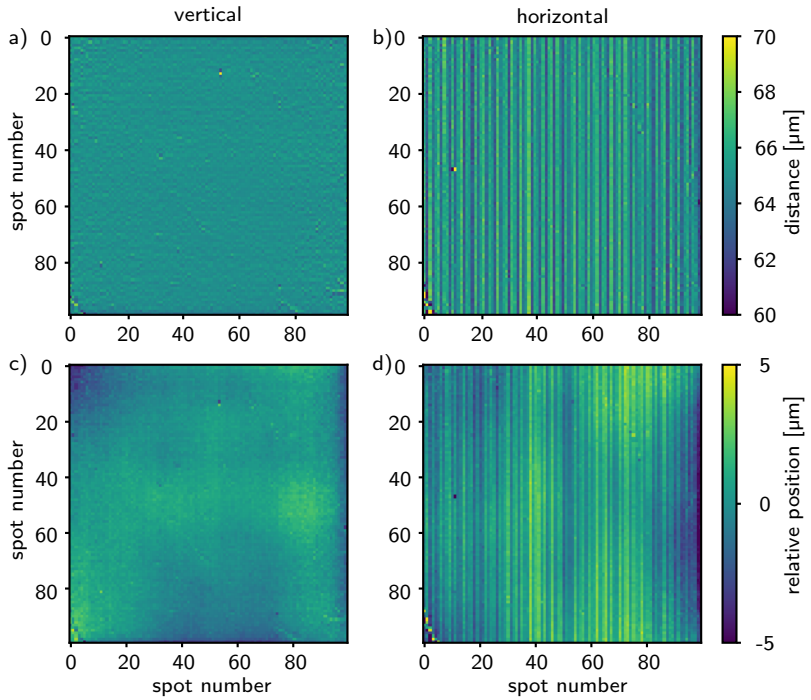

Fig. 5.17: Regularity of a Compound Array Refractive Lens with five stacked foils of single-step embossed lens arrays. The distance between the spots is comparable to the single foils. It varies only minor (standard deviation 0.4 µm) in vertical and has again the stripe like structure in horizontal direction (standard deviation 1.6 µm). The relative positions improved compared to the single foil (standard deviation 0.9 µm in vertical and 1.5 µm in horizontal direction). The distance between the Compound Array Refractive Lens and the detector was 59.7 cm, representing the focal length. **[XRI5]**

The regularity, again, shows the same features as the single foils of this CARL. In vertical direction only a small variance with a SD of 0.4 µm for the neighbor distance and 0.9 µm for the relative position is observed. In horizontal direction the stripy structures are visible again. At least no further error increase was introduced by the stacking (SD 1.6 µm for the neighbor distance and 1.5 µm for the relative distance).

5.3 Summary and definition of optimal production parameters

The embossing of 2D lens arrays in combination with stacking of several of them is a suitable method to produce CARLs. The production schemes shown here led to CARLs with good 2D spot arrays. However, the detailed analysis showed differences in pattern quality and focusing abilities. From these results, an optimized production scheme is concluded here.

The spiral embossed CARL showed a pyramidal shape, which was also observed in the resulting spot pattern. In addition, the alignment under an optical microscope led to a slightly inhomogeneous positioning of the lenses in the stack. This resulted in an inhomogeneous spot shape and focal length over the entire array. Nevertheless, good focusing was achieved with a visibility of about 0.5 at the focal length.

The CARL fabricated by single-stage embossing with a 2D needle array showed an improved regularity of the 2D spot pattern. Alignment under X-ray illumination was advantageous in order to take tilts into account. A homogeneous spot shape and focal length was achieved over the complete array. The visibility was lower compared to the other CARL due to a reduced fill factor of the lens apertures.

For future CARL productions the following points should be considered.

- Serial embossing of the lenses must be carried out by using stages with encoders in order to ensure the correction of minor movement errors.
- The lens foils must be rigid enough and glued surface-filled to avoid deformation during embossing.
- The needle should have a precise shape and, especially for short focal lengths, a small apex radius.
- A high fill factor of the lens apertures must be ensured and therefore a single-step embossing is advantageous.
- A stamp production by electroplating is an appropriate way because replication is good.
- In case of CARLs with more than two stacked foils the stacking is preferably done under X-ray illumination.

Visibility is the more reliable parameter for determining the focus point because it is independent of the measurement scheme. The widths of the spots, as typically examined for CRLs, showed a higher variation of distance dependence compared to the visibility for the CARLs examined here. In the case of an inhomogeneous alignment of the lens foils, the two widths can easily indicate two different focal points.

The visibility V_{bz} obtained from the extrema of the beamlet zone intensity can lead to high values at low sampling or high noise levels. In such cases, the visibility V_{Gauss} calculated from the Gaussian parameters *height* and *offset* is advantageous. It reduces artificial high values resulting from single pixel errors, but is limited to spots significantly smaller than the beamlet zone. With the exception of the absolute values, both algorithms for determining the visibility show the same behavior with respect to the lens-to-detector distance of the CARLs.

6 Summary of new insights of the hierarchical processes of pulsed laser ablation

This chapter presents the new knowledge about PLAL gained in this work. The fundamental processes during ablation were investigated using a combination of several investigation techniques. This is necessary because PLAL is a hierarchical process in time and space. The ablated material already ranges from single atoms to NPs of diameters up to 100 nm while the induced cavitation bubble reaches sizes in the millimeter range. The relevant time regimes range from femtosecond laser pulses over nanoseconds for the ablation process[3] and microsecond cavitation bubble lifetimes to minutes or even days for the ripening of the NPs.[127]

Many research in the field of PLAL is done *ex situ*, which means after the real ablation process. Investigating the NP suspension by absorption spectroscopy, dynamic light scattering, analytical centrifugation or electron microscopy are suitable options with regard to the use of the final suspension. These techniques, in some cases, even allow indirect conclusions to be drawn about the native ablation process, but special care must be taken to ensure that the NPs do not change during the preparation processes such as drying.

With optical imaging and absorption spectroscopy the plasma ignition fluence threshold and the incubation effect are analyzed in section 6.1. A certain fluence is required for an efficient plasma ignition and therefore a sufficient ablation yield. On pristine targets with a smooth surface and low laser pulse energies the energy localization is strongly reduced due to high loss mechanisms. With an increasing number of shots the losses are reduced leading to an increased cavitation bubble size, plasma intensity and ablation yield.

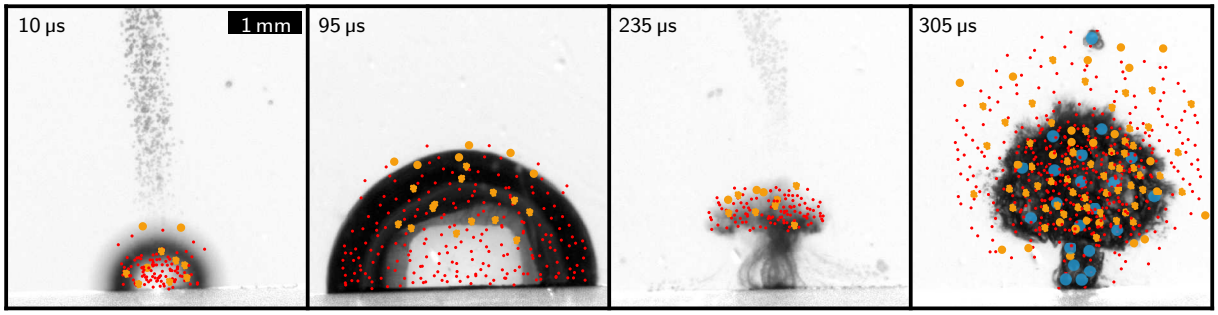

Fig. 6.1: Cavitation bubble dynamics after laser excitation (1064 nm, 7 ns, 11 mJ) of a free wire target (zinc, 1 mm diameter) with a cartoon of the nanoparticle and microbubble distribution. The four images show the cavitation bubble short after genesis (10 µs), at the maximum suspension of the first bubble (95 µs), at the collapse (235 µs) and at the maximum suspension of the first rebound (305 µs). The primary (red) and secondary (orange) nanoparticles and microbubbles (blue) are schematically overlaid. The nanoparticles are magnified by around a factor of 1000. **[OI2]**

For the understanding of the fundamental processes during the ablation and cavitation bubble lifetime investigations with a high temporal resolution are required. Fig. 6.1 shows optical images of the cavitation bubble (different delays after excitation) acquired in stroboscopic mode with a suggestive NP and microbubble distribution overlaid. This ablation image can only be drawn by the combination of several investigation techniques. The optical imaging allows an easy visualization of the cavitation bubble. However, a proper investigation of the bubble interior is not feasible due to strong light refraction at the bubble-water interface. For this X-ray methods are required as they do only show minor problems with refraction. The cavitation bubble dynamics can be visualized with X-ray absorption imaging. To obtain the spatial and the bimodal size distribution of the NPs during the cavitation bubble lifetime, X-ray scattering methods are required.

Small- and wide-angle X-ray scattering are used to determine the spatial distribution of the NPs and their size distribution *in situ* during the cavitation bubble lifetime as shown in section 6.2. With the high temporal resolution (down to 100 ps[255]) the early appearance of large NPs as well as the almost homogeneous filling of the cavitation bubble with small and large NPs are manifested. The large NPs, which are located at or even in front of the cavitation bubble, have large crystalline domains indicating that they are already solidified and not generated by an agglomeration of smaller ones. A strong agglomeration takes place during the bubble collapse.

However, SAXS is just probing a small point (typically below 100 µm × 100 µm). To obtain an overview over the complete cavitation bubble, either SAXS measurements at different positions or a scattering imaging method are required. The latter can be performed by SEMCI with Hartmann masks or CARLs, as shown in section 6.3. One looses the detailed size discrimination of SAXS, but gets a complete image over a range of about 2 mm × 2 mm at once. By changing the setup parameters even a coarse size differentiation is possible. The number of large gold NPs can strongly be reduced by *in situ* size quenching with NaCl. Polyvinylpyrrolidone PVP also leads to a reduced mean size of gold NPs after the ablation, however the mechanism is a different one compared to NaCl as no *in situ* size quenching in the bubble is observed. During ablation on free wire targets the cavitation bubble detaches from the target (see Fig. 6.1. The opaque appearance of the first rebound in optical imaging did not allow conclusions to be drawn on whether it consists of NPs or small vapor bubbles. By changing the scattering sensitivity of a SEMCI with a CARL as optical element between 100 nm and 900 nm, it was determined that the first rebound consists of micrometer-sized vapor bubbles and not of NP clouds.

Parts of this chapter are results achieved in the context of this work. Most of them have already been published.[15, 58–61, 119] In this chapter only the brief experimental parameters are described. Details of the measurement are listed in the "List of Experiments" and are referenced in the text in bold square brackets, e.g. ***[SI1]****.*

6.1 Laser-matter interaction leading to threshold and incubation effects

The interaction of the laser with the target material is one very important aspect for the disintegration of the material. Without a sufficient coupling of the laser energy into the target the ablation efficiency is

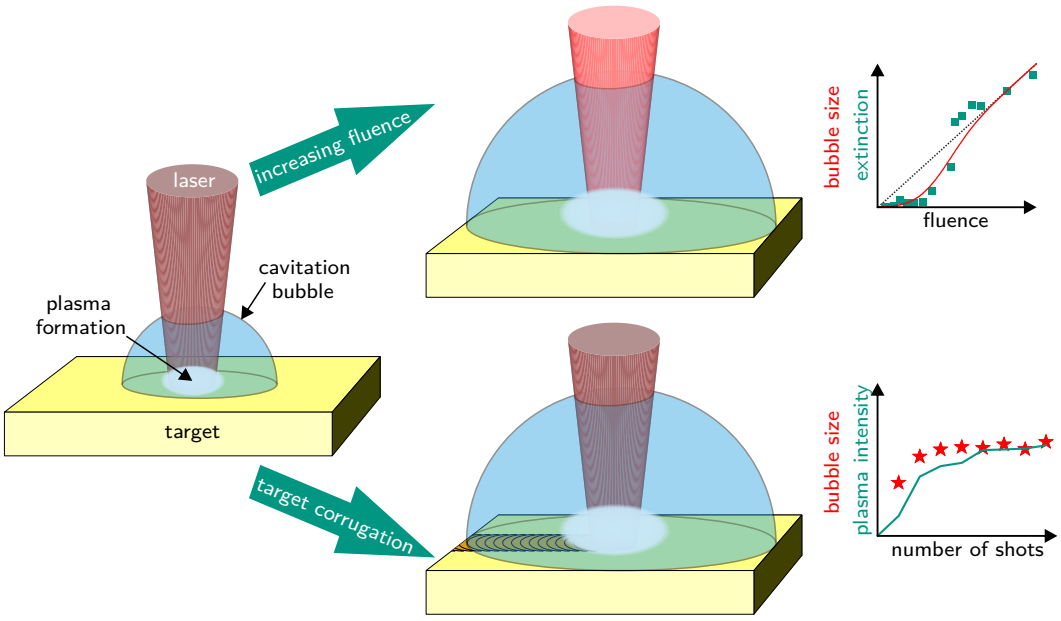

Fig. 6.2: Schematic drawing of the plasma fluence threshold and incubation effect. For low pulse energies on pristine targets no efficient energy localization occurs leading to low plasma intensities and small cavitation bubbles (left). With increasing pulse energy the threshold fluence for an efficient plasma ignition can be overcome resulting in a sigmoidal increasing bubble size and ablation yield with pulse energy (right top). When subsequent laser shots hit the same target position it gets corrugated also increasing the bubble size, the ablation yield and the plasma intensity (right bottom).

low.[58,60] Fig. 6.2 schematically shows two possibilities of an improved energy localization. First, the bubble size and the extinction of the NP suspension show a sigmoidal behavior depending on the laser fluence as illustrated in the right top. Second, the bubble size as well as the plasma intensity increase with the number of applied shots on the same position due to an increased target surface corrugation. These two aspects of improved energy localization into the target and hence increased NP yield were investigated within this work and are explained in the next two subsection in more detail.

6.1.1 Fluence threshold for efficient ablation

In literature often a linear relationship between the ablation rate or cavitation bubble volume and the laser fluence is reported for moderate fluences[58,129,143] with a drop above very high fluences due to optical breakdown in the liquid phase.[256] This indicates that the laser energy is almost quantitatively converted into the bubble and thus into the ablated material.

The linear behavior does not longer hold true for small fluences[58,111,257] as shown in Fig. 6.3. Below a fluence of about 50 J/cm^2 the maximum cavitation bubble volume and the colloidal extinction are both reduced compared to the linear dependence. At higher fluences, the extinction does not show a linear increase either. As the extinction was measured after 150 subsequent shots, the NP shielding effect already manifests. In accordance to that the extinction has to be rescaled by extrapolation of the linear extinction increase of small pulse numbers as shown by the two red circles in Fig. 6.3. For the bubble volume this point is irrelevant as it was measured with liquid flow.

The sigmoidal behavior in the low fluence range can not be explained by a simple fluence threshold for energy localization as assumed in the case of the optimal target distance (see Fig. 2.11 and discussion). This could only explain the reduced bubble size below 50 J/cm^2 but would lead to inhibited cavitation

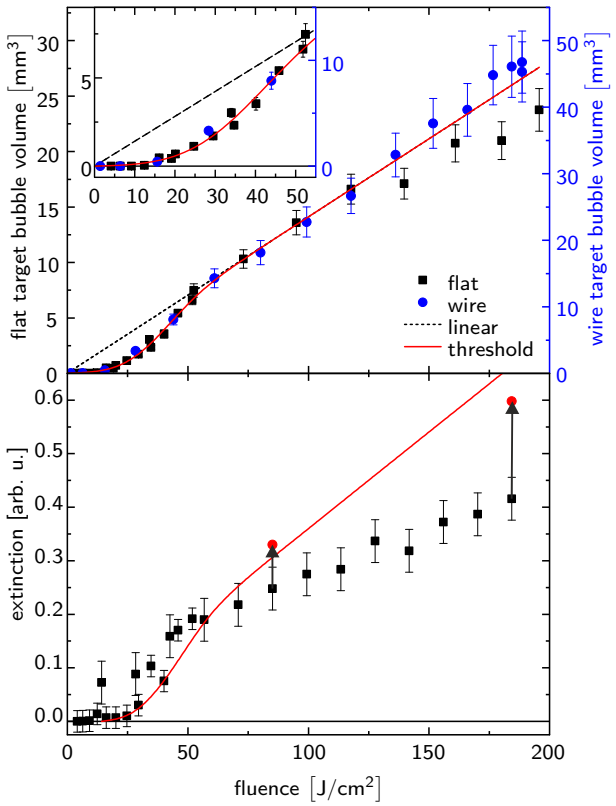

Fig. 6.3: Fluence threshold for bubble size and ablation yield in Pulsed Laser Ablation in Liquids (1064 nm, 7 ns). Top: Maximum cavitation bubble on a flat and wire shaped target. The two lines show models for linear increase (black dashed) and a threshold behavior (red) as explained in the text. Bottom: Colloidal extinction (400 nm to 420 nm) after 150 shots where saturation takes place (black squares). For higher fluences the nanoparticle shielding increases why the extinction has to be corrected to the expected values (red circles). Reproduced from Reich et al.[58] **[OI7]**

bubbles below the threshold fluence.[58] The sigmoidal behavior can be explained by a self-amplified conversion of laser energy into water evaporation. The high heat conduction of metal targets (here silver) in contrast to water and a high boundary resistance at the interface[258] excludes a pure heating of the water phase from the target.

At least for nanosecond lasers the ignited plasma plays an important role. It scales with the cavitation bubble size.[60] Hence, if one assumes a plasma threshold, the sigmoidal shape can be explained. At very low fluences, high energy losses appear, which lead to very small bubbles. They can be detected down to a fluence of approximately 3 J/cm^2.[58] Once a plasma is ignited at the water-target interface,[46,256] it absorbs efficiently the laser. Now the energy is no longer introduced into the metal but is deposited directly into the plasma and consequently into the water. The red lines in Fig. 6.3 display a fitting of a sigmoidal function with a plasma threshold of 39 J/cm^2. The absolute value has to be viewed critically as it varies with pulse length and material.[22] However, this explains well the dependence of the maximum bubble size as well as the ablation efficiency.

The plasma fluence threshold is independent of the target surface state. As shown in Fig. 6.4, a similar sigmoidal bubble size behavior is found for pristine and corrugated targets of gold and silver. The overall reduced sizes for pristine targets are described in more details in the next subsection by an incubation effect occurring within the first 30 shots.

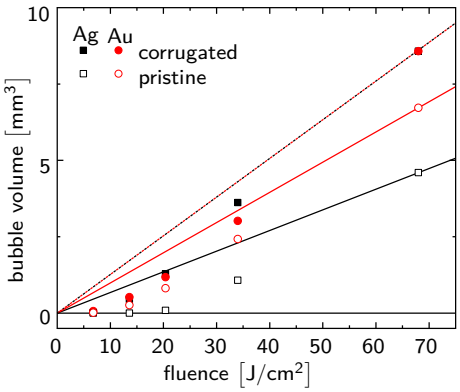

Fig. 6.4: Maximum cavitation bubble sizes as function of laser fluence (1064 nm, 7 ns). Pristine and corrugated targets show a plasma fluence threshold behavior for both, silver (Ag) and gold (Au) flat targets. The lines indicate the linear dependencies appearing for high fluences. **[OI8]**

For an efficient ablation mechanism it is important that the plasma is sufficiently ignited and thus leads to a proper energy localization. This takes place if a certain fluence threshold is exceeded. This effect is independent of the laser pulse duration as observed for nano- and subpicosecond lasers.[58,111,257]

6.1.2 Incubation promoting the ablation

The second aspect for an improved energy localization is the target surface state. Pristine targets with a smooth surface are not favorable for a high ablation rate.[60] Reflection is one of the loss mechanisms reducing the portion of the laser energy used for ablation (see Fig. 2.1 and discussion). On pristine targets the reflectivity is higher compared to roughened ones.[69,259] Additionally to the change of reflectivity due to the surface roughening subsurface voids develop leading to a changed thermal conductivity in the target. This effect is reported to be stronger than reflectivity changes with respect to the ablation efficiency.[68,110,111] The improved ablation and reduced threshold fluences is called incubation.[33,60,68,260,261]

In Fig. 6.5 top part images of the maximum of the cavitation bubbles on three different pristine targets are shown as function of the number of applied shots on the same position with a nanosecond laser. In the case of small pulse energies, hence low fluences (1 mJ or 6.8 J/cm^2), the first bubbles are considerably smaller than the later ones. Both metals, silver and gold, have a high reflectivity of 0.987 and 0.991, respectively.[73] This explains the low coupling of laser energy into water evaporation. The germanium target, on the other hand, has a much lower reflectivity (0.398[73]), which explains the larger bubble already at the first shot.

Metals have attenuation lengths for the laser light of about 10 nm.[58] In semiconductors the attenuation length is larger. In germanium it is still low (0.7 µm) but not for silicon (0.9 mm).[262] A corresponding experiment on a silicon target did not show bubbles for at least 300 shots, occasionally even 600 shots. This shows that for a sufficient ablation the energy must be localized at the target surface and not dissipated into the target or reflected. In the case of silicon, the thresholds for ablation and plasma ignition are not reached. Only with the large number of applied shots some defects might develop and lead to an increased absorption and consequently an energy localization.[60]

In the case of incubation it was found that the plasma intensity increases comparably to the bubble size, as shown in the bottom part of Fig. 6.5. The integrated intensity of the plasma scales very well

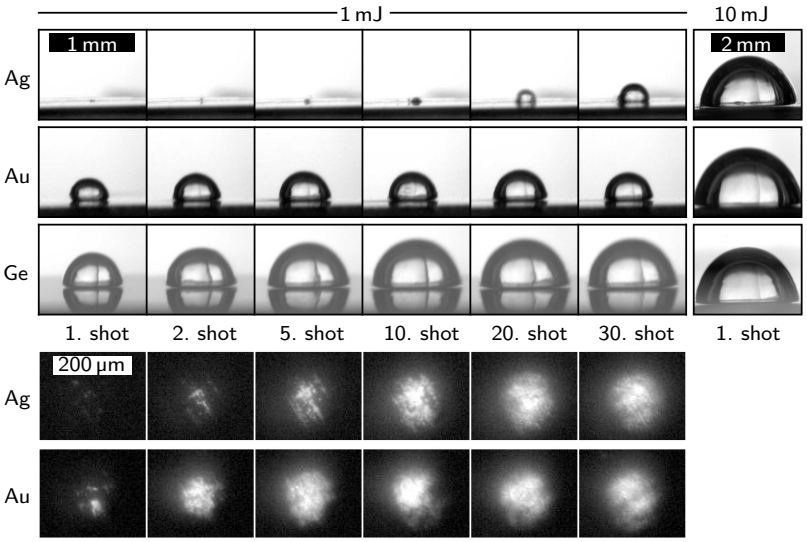

Fig. 6.5: Top: Maximum bubble size on a silver (Ag), gold (Au) and germanium (Ge) target showing an increasing size with the number of applied shots (1064 nm, 7 ns) on the same position of the before pristine target (1 mJ). Bottom: Plasma intensity (5 µs integration time after laser excitation) imaged coaxial with the laser beam showing a similar intensity increase as the bubble size. This effect is called incubation and belongs to an increasing surface roughness induced by the laser shots. Incubation is only dominant for low pulse energies as the differences of the materials and the increasing size almost vanish for high pulse energies (10 mJ). Reproduced from Reich et al.[60] **[OI8]**

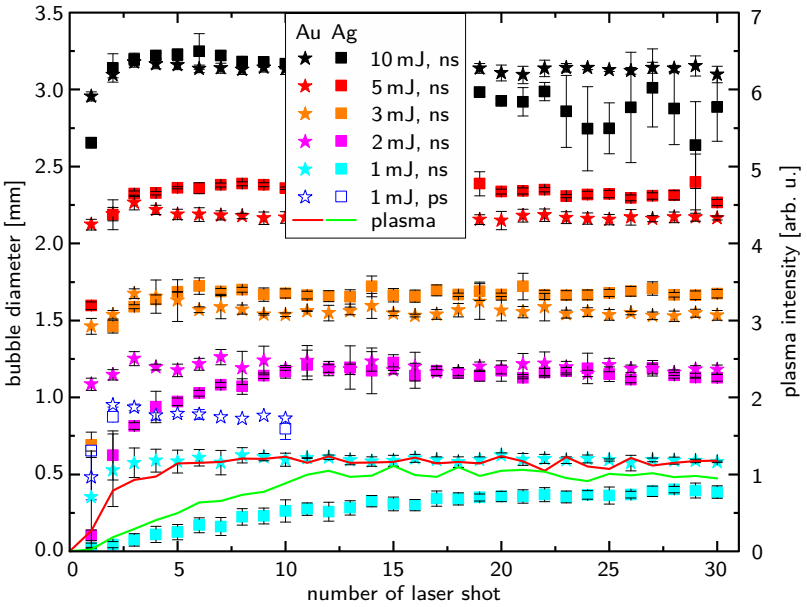

Fig. 6.6: Maximum cavitation bubble diameter as function of the number of applied shots (1064 nm, 7 ns) on the same position. For low pulse energies the bubbles are small first and rise with increasing number due to an increased energy localization. With increasing pulse energy this incubation effects gets smaller being only present at the very first shot. The differences between the two materials gold (Au) and silver (Ag) also disappear. For picosecond laser pulses the incubation effect is much smaller compared to nanosecond pulses due to the overall higher fluence. Reproduced from Reich et al.[60] **[OI8]**

with the bubble diameter as plotted in Fig. 6.6 for 1 mJ. This indicates the close connection between plasma ignition and energy localization in the water phase to end up as the cavitation bubble. If the laser fluence is above the plasma threshold (see subsection before) a plasma can be ignited sufficiently. In this case the material parameters have less influence. The first bubble of all three materials, silver, gold and

germanium, have a similar size in this case (see Fig. 6.5 10 mJ). The same can be observed in Fig. 6.6, where the differences between gold and silver for the first some shots vanish for pulse energies of 3 mJ and higher.

A comparable experiment with a picosecond laser reveals the better energy deposition into the target for shorter laser pulses. The bubble size, as shown in Fig. 6.6, shows only a minor incubation effect and a overall larger bubble size compared to the nanosecond laser ablation with the same pulse energy. On the one hand, the threshold fluence can be reached easier with the shorter pulse duration of similar energy. On the other hand the plasma heating by the trailing part of the laser pulse is reduced for a shorter pulse duration. Hence, the plasma can be ignited sufficiently, however due to the short pulse duration a larger amount of the laser energy is deposited into the target before the plasma is ignited. Furthermore the heat dissipation in the target is reduced for short pulse duration as it is happening in the order of some nanoseconds.[263] As a result, there is a higher energy localization for short pulses, leading to overall larger cavitation bubbles. At the same time, the larger amount of energy deposited into the target results in a stronger surface modification and thus a reduced incubation effect.

With increasing pulse energy the required number of pulses for a steady-state condition reduces and also the differences between materials decrease. In Fig. 6.6 one can clearly see that even on a silver target, where for low fluences the incubation effect is strong, already after the second laser pulse with 10 mJ the maximum bubble size is reached. The cavitation bubbles of several materials, metals and semiconductors, all show a similar bubble size for excitation with 10 mJ of a nanosecond laser pulse. Even on silicon, where no bubbles arise for 1 mJ, cavitation bubbles of the same size as on metals appear.[60] This underlines on the one hand that if a plasma is ignited sufficiently, the material parameters are only of minor importance. On the other hand it implies that a specific dose is required to overcome the unfavorable reduced energy localization.[60] It was shown that this effective dose for steady-state bubble sizes correlates with material parameters such as Young's modulus and energy required for material heating, melting and evaporation.[60] Soft materials (like lead and indium) require a very low effective dose, which is exceeded already within the first shot. Hard materials (such as iron and molybdenum) require a high effective dose.

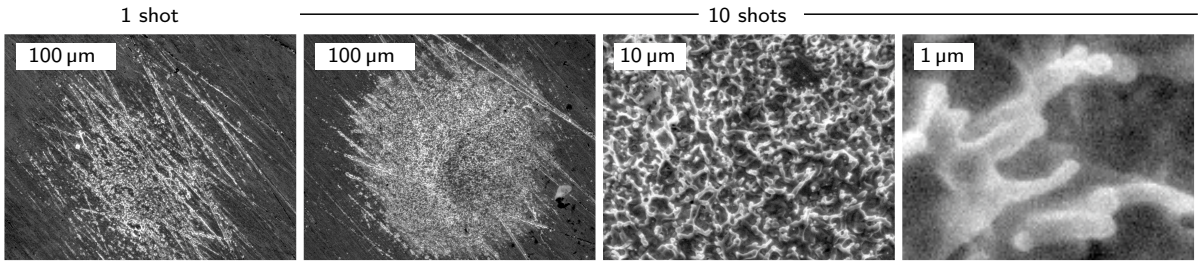

Fig. 6.7: Scanning electron microscope images showing the increasing target corrugation during continuous laser ablation (1064 nm, 7 ns, 1 mJ) of the same spot of a gold target. The damaged area increases between the first and tenth shot and the corrugation gets more homogeneous. The induced surface structure is irregular and shows melt-induced fingering structures. Images were acquired on a "Philips XL 30" with an anode voltage of 20 kV. Reproduced from Reich et al.[60]

The ablation crater size enlarges and the surface morphology changes with an increasing number of shots on the same position[60,68] as shown by electron microscopy images in Fig. 6.7. For low pulse

energies and the first some shots surface modifications are mainly found in the center of the spot and at macroscopic scratches. The latter is caused by field enhancements at the edges. Note that a macroscopic roughness (different polishing states) did not change the incubation effect considerably. The microstructure induced by laser excitation shows sizes comparable to the wavelength. For nanosecond lasers these structures are not ordered like at laser-induced periodic surface structures (LIPSS) obtained after femtosecond ablation.[60, 264, 265]

For large pulse energies already the first shot showed a large ablation spot with the same microstructure occurring after several shots with low intensity. Additionally, splash like structures are observed at the outer part of the crater indicating that substantial amounts of material are in the molten phase during ablation.[60]

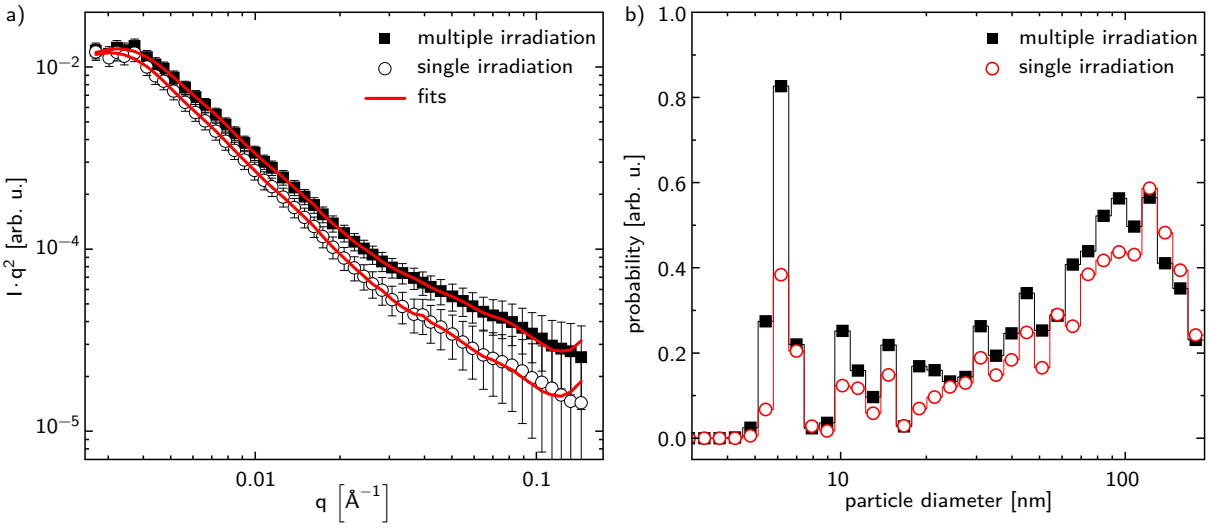

Fig. 6.8: Scattering curves and nanoparticle size histograms of Small-angle X-ray Scattering (SAXS) measurements during laser ablation (1064 nm, 12 ps, 1 mJ, 1 kHz) of a gold target showing an incubation effect. In (a) the Kratky representation of SAXS curves taken 15 s after starting a continuous ablation for single spot irradiation as well as multiple shot irradiation are shown. The red lines are fits by a reverse Monte Carlo approach (McSAS[266]). The higher signal for multiple irradiation indicates the higher ablation rate. In (b), the histograms of size distributions assuming spherical particles for single and multiple irradiation do not differ much, indicating similar nanoparticle size distributions. Reproduced from Reich et al.[60] **[XRS1]**

Plasma intensity and bubble size are only indirect parameters for ablation efficiency.[58, 60] With *in situ* SAXS measurements also further details of the incubation effect could be clarified. For Fig. 6.8 X-ray scattering was performed in the liquid phase besides the laser path and the cavitation bubble location. To mimic the incubation the target was moved with different speed during the continuous ablation (12 ps, 1064 nm, 1 mJ, 1 kHz) of a gold ribbon. In Fig. 6.8 (a) the scattering curves after 15 s of ablation are shown. For multiple irradiation the ribbon was moved slowly resulting in around 30 shots per position, while the fast moving ribbon ensured a real single irradiation. Despite the low incubation effect for picosecond laser pulses, the higher scattering intensity for the multiple irradiation reveals clearly the higher ablation rate in this case. With a reverse Monte Carlo approach (McSAS[266]), the size distribution was calculated for both cases. The resulting histograms in Fig. 6.8 (b) show very similar distributions. This either comes from an independence of the NP genesis with respect of the target surface state or the high number of applied shots. The latter can easily lead to a fragmentation of already existing NPs due to reirradiation. Furthermore, a high agglomeration rate due to the high NP concentration in the suspension

can not be excluded. The size distributions show the typical observed bimodality with one size fraction below 10 nm and a second one at roughly 100 nm.

Incubation with increasing bubble size, plasma intensity and ablation rate is a process that can be found in the first few tens of shots to the same position. When the ablation time is prolonged for several hundreds of shots on the same spot a hole is drilled, which again decreases the bubble size.[28] In Fig. 6.6 the bubble size after laser excitation with 10 mJ of a silver target already starts to decrease after 15 shots. A thin ribbon was used (in comparison to a thick gold plate), which already changed macroscopically the shape by introducing a hole within the applied 30 shots. For much larger numbers of shots not only the size but also the shape of the cavitation bubble changes, while the NP size distribution is almost unchanged.[28]

A certain target roughness in the micrometer range is of advantage for a high ablation rate per laser pulse. For a continuous NP production this is normally fulfilled but if the fundamental processes of single laser shots are investigated this has to be kept in mind. A not perfectly smooth target with the disadvantage of small symmetry breaks should be used. Alternatively, high laser pulse energies must be used, since the incubation effect is considerably lower due to a better energy coupling through a more efficient plasma ignition.

6.2 Mechanisms of nanoparticle genesis

From earlier SAXS measurements[27,31] it is known that the ablated NPs are confined in the cavitation bubble. In addition, an almost homogeneous filling of the bubble was observed. There are two size levels of NPs, the primary and the secondary. The origin of the latter has not yet been clarified in detail. Besides an agglomeration of primary NPs, as indicated by measurements,[27] simulations suggested a direct formation of large solid NPs.[3] This section first shows the early appearance of such solid and crystalline NPs by SAXS and WAXS measurements with a higher temporal resolution than before. The detected NP mass underlines the model of a homogeneously filled bubble with a high concentration for small bubbles and a decrease during bubble expansion. In subsection 6.2.2 the second path of the genesis of the secondary NPs is studied. During the bubble collapse the NP concentration increases again and favors an agglomeration of the primary NPs. This leads to a high amount of secondary NPs and a strongly reduced amount of primary NPs in the first rebound.

6.2.1 Early appearance of crystalline nanoparticles

To gain *in situ* information about the NP sizes, spatial distributions and consequently obtain the picture of ablation shown in Fig. 6.1 X-ray scattering methods are required. With SAXS the NP size distribution and the corresponding relative mass distribution can be investigated. Complementary to that, WAXS probes the crystalline domain size of the NPs. During this work such a combined X-ray scattering measurement was performed at ESRF (Grenoble, France) and SLS (Villingen, Switzerland).

In Fig. 6.9 the measurement scheme as a side view is shown. Within the first 5 µs after the laser excitation the cavitation bubble is too small to be detected by the X-ray beam. For later times the X-ray beam probes a small tube through the bubble (suggested by the elliptical rim as view in beam propagation). Hence, the detected signal is the line integral of the scattering of the NPs located inside this pencil beam.

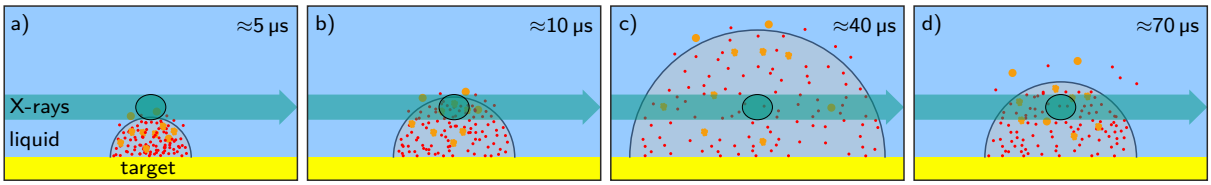

Fig. 6.9: Schematic drawing of the cavitation bubble dynamics and nanoparticle distribution during X-ray scattering. The transparent X-ray beam illustrates the side view while the ellipse with rim depicts the view with beam propagation. Within the first 5 µs the bubble is to small to reach the probe position of the X-rays. Afterwards the nanoparticles get detected by the X-ray beam until the collapse of the bubble. The bubble is roughly homogeneously filled with primary and secondary nanoparticles resulting in a reduced concentration for the bubble of maximum suspension.

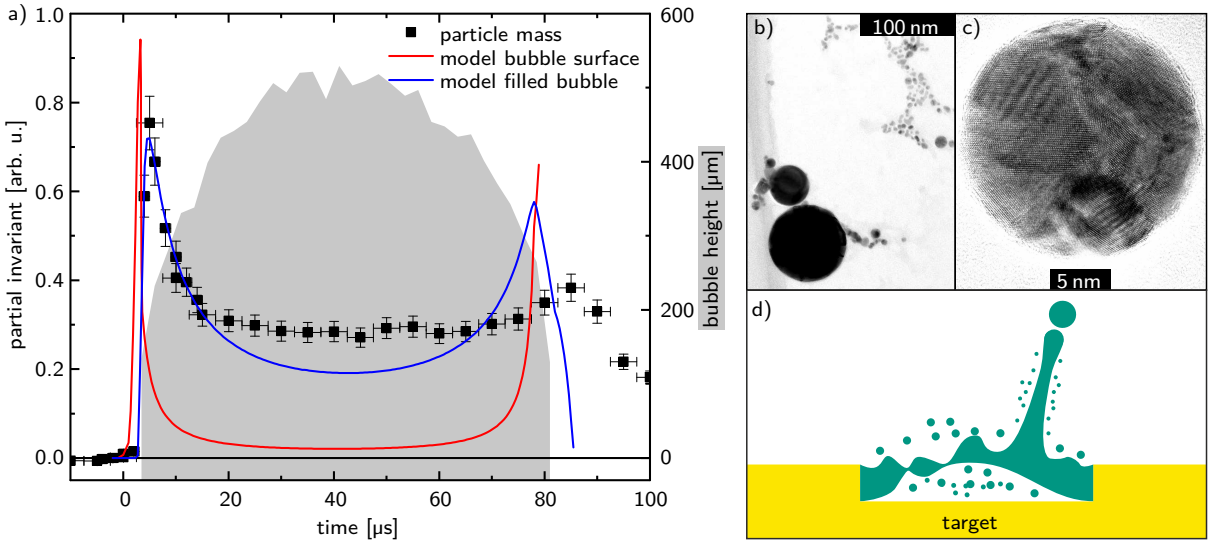

Fig. 6.10: (a) Temporal evolution of the ablated secondary nanoparticle mass (Porod invariant) during the cavitation bubble lifetime on a silver target (1064 nm, 12 ps, 1 mJ) measured by Small-angle X-ray Scattering. The detected nanoparticle mass fits well to the model of a homogeneously filled bubble (blue line) and not to a model of nanoparticles located only at the bubble surface (red line). In (b) and (c) transmission electron micrographs of gold nanoparticles (800 nm, 2 ps, 2.7 mJ) are shown. In (c) large crystalline domains up to 20 nm are visible. (d) Sketch of the material blow-up after laser excitation showing the genesis of differently sized nanoparticles. Electron microscopy was performed with a "Zeiss EM 910" with 120 kV anode voltage in (b) and a "FE Titan" with 300 kV anode voltage in (c) at the Laboratory for Electron Microscopy (LEM) at KIT. Reproduced from Reich et al.[61] **[XRS2]**

In Fig. 6.10 (a) the temporal evolution of the ablated mass (ablation with 1 mJ of a 12 ps, 1064 nm laser of a silver target) of secondary NPs together with two models of NP distribution inside the cavitation bubble are shown. With the arrival of the bubble front at the X-ray beam position, the NP mass reaches its peak and decreases as the bubble expands further. During the shrinkage phase of the bubble, the mass detected rises again slightly and only drops after the collapse. This follows well the model of a homogeneously filled bubble (blue line), as also assumed earlier,[31] where the concentrations are high for small bubbles (rise and shrinkage) and decreased during maximum expansion. The model of NPs being strongly bound to the bubble-water interface (red line) would suggest a much stronger drop of the signal for the expanded bubble. The same investigations for an ablation with a 2 ps (800 nm, 2.7 mJ) laser and 100 ps time resolution even showed an earlier appearance of particle mass than the crossing of the bubble front and the X-ray beam.[61] This confirms the presence of secondary NPs already at the

advancing front of the bubble as simulations recently predicted.[3] Furthermore, the model of film lift-off and Rayleigh instabilities at the liquid metal surface as shown in Fig. 6.10 (d) is underlined.

Similar results as for the secondary NPs are observed for primary NPs and also for an ablation of gold.[61] As no strong shifts from one particle size fraction to the other are observed during the cavitation bubble lifetime, a significant early agglomeration can be omitted. This is further emphasized by the ratio of primary to secondary NPs, which slightly varies and peaks at maximum bubble expansion.[61] If an agglomeration would occur during the bubble lifetime the portion of primary NPs should reduce with time. This can be the reason for the slight reduction of the portion of primary NPs during shrinking phase. It was already shown that at least during the collapse the amount of primary NPs decreases strongly to the benefit of secondary NPs.[27,58]

During maximum bubble suspension the mass of primary and secondary NPs is a bit higher compared to the model of a homogeneous filled bubble as shown in Fig. 6.10 (a). There are two possible explanations for this effect. For nanosecond ablation it was shown that the secondary NPs are more prone to be located at the front of the bubble.[30] The investigation here took place around the middle of the bubble height and again this shifted mass towards the top part can lead to the increased mass during maximum bubble suspension. The fact that also the primary NPs show a higher abundance compared to the model is in contrast to earlier investigations where a homogeneous filling of them was observed.[31] Here a picosecond laser was used, which might cause this change in NP distribution. The second explanation for the increased mass during maximum bubble suspension is an ongoing emerge of NPs during bubble rise. This also would lead to an increased mass for later times.

With SAXS only the NP size and not the crystallinity can be probed. The observed secondary NPs can be aggregates of primary NPs or single large NPs. This can be probed by WAXS, which is sensitive on crystalline grains and their size. Hence, aggregates of small particles are not different from isolated small particles. From the scattering intensity the crystalline mass and from the width of the scattering peak the size of the crystalline domains can be obtained.[156]

In Fig. 6.11 the temporal evolution of the scattering intensity and calculated crystalline domain size is shown for a picosecond ablation (2 ps, 800 nm, 2.7 mJ) of gold. The crystalline mass follows a similar trend as the mass observed in SAXS (see Fig. 6.10). It peaks around the beginning of the bubble crossing the X-ray beam and decays for later times. In addition, a weak signal can also be detected before and when the bubble crosses the X-ray beam. The domain size of these early crystals are with 15 nm to 20 nm considerably larger than in the bubble (down to 8 nm). Hence, the NPs observed at the expansion front of the bubble consist rather of large single NPs then agglomerates of small ones. The detectable crystal scattering furthermore reveals, that these NPs are already cooled down and solidified, which is a result of being in contact with the liquid.[258] In contrast to that, the NPs in the bubble show a smaller domain size coinciding with the larger amount of primary particles in SAXS.

In Fig. 6.10 (b) and (c) electron micrographs of a gold NP distribution and a large spherical NP with visible domains up so 20 nm are shown. These *ex situ* measurements underline furthermore the existence of two size fractions, crystalline domains in the large NPs as well as the low number of secondary NPs. The latter are well visible in terms of mass and potentially harmful effects in an application.[61]

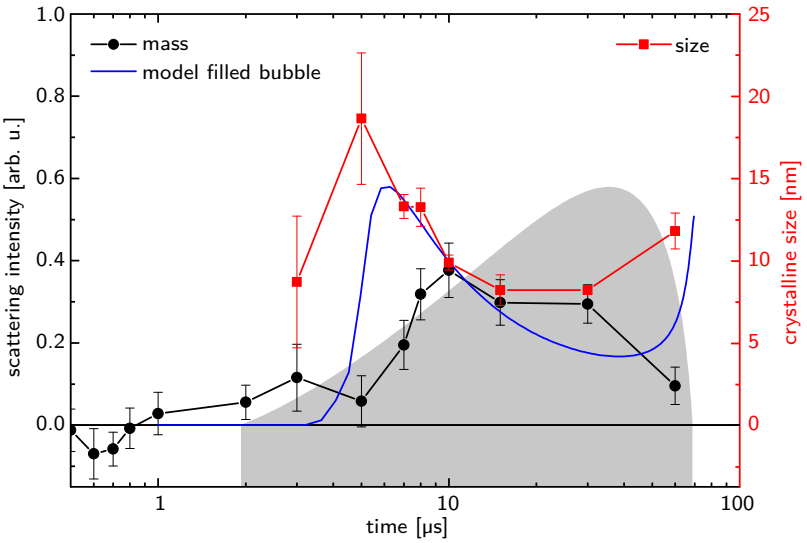

Fig. 6.11: Temporal evolution of the crystalline mass and crystalline domain size for ablation (800 nm, 2 ps, 2.7 mJ) of gold. The blue line shows the model of a homogeneously filled bubble and in gray the bubble size is shown. The mass shows a similar dependence as the model and the trend observed in Small-angle X-ray Scattering in Fig. 6.10. The crystal domain size of the first detected nanoparticles is large and decreases during bubble expansion. A small scattering signal is already observed before and when the bubble crosses the X-ray beam. Reproduced from Reich et al.[61] **[XRS3]**

6.2.2 Nanoparticle agglomeration during bubble collapse

The direct genesis of large spherical NPs with crystal grains, as shown in the last subsection, is not the only possibility of generating secondary NPs. As already mentioned, agglomeration can also occur if the NP density is high enough. This leads to increased NP sizes in SAXS measurements but not to increased crystal domain sizes investigated by WAXS. For flat targets, the bubble collapse occurs on the target surface. In this case the NP concentration rises sharply due to the their confinement in the bubble.[27,30,31,125]

In Fig. 6.12 the temporal evolution of the mass of primary and secondary NPs is shown for two different heights above the target. The mass of primary and secondary NPs increases similar with the cavitation bubble rise, irrespective of the measurement height. This again indicates a homogeneous filled bubble. During bubble shrinking the mass of the primary NPs decreases and stays at a low value but finite for later times. The amount of secondary NPs, however, further increases during bubble collapse and rebound. The values for a height above the target of 0.5 mm drops after 200 µs. The bubble rebounds are much smaller than the first bubble and therefore do not reach this height anymore. This again indicates a strong confinement of the NPs in the bubbles. It was shown earlier, that a substantial release of NPs into the liquid only takes place during the second rebound.[27] The second increase of the secondary NPs for a height of 0.17 mm after 300 µs also indicates a release of NPs after the final collapse. Laser scattering has also shown that after the final bubble collapse, significant amounts of NPs are located near the target.[46]

These SAXS measurements revealed a second process of production of secondary NPs. In the previous subsection an early appearance of solid and crystalline NPs was shown. This confirmed simulations.[3] Here the strongly increased mass of secondary NPs after bubble collapse implies an agglomeration process, which has already been shown before.[27,31] Finding ablation parameters that do not generate sec-

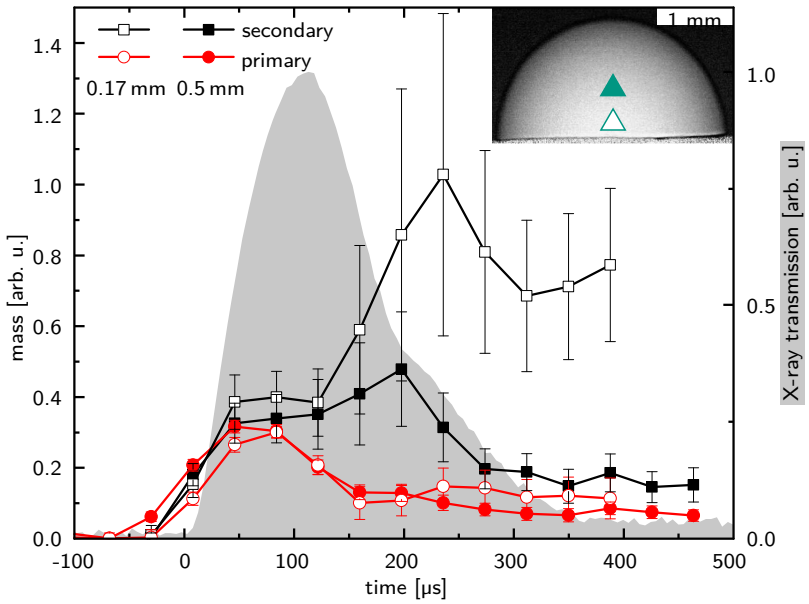

Fig. 6.12: Temporal evolution of the mass (Porod invariant) of primary and secondary nanoparticles after ablation (1064 nm, 6 ns, 10 mJ) of a gold target. In gray the X-ray transmission measured at 0.5 mm height above the target. As inset an X-ray radiograph with the positions of the two investigated heights above the target. The primary nanoparticles are mainly observed during the lifetime of the first bubble while the amount of secondary nanoparticles increases strongly after bubble collapse (around 200 µs). This originates from an agglomeration process occurred during bubble collapse. Reproduced from Reich et al.[15] **[XRS4]**

ondary NPs is a crucial point for an application. One possible way is the quenching by additives, which is shown in subsection 6.3.1.

6.3 Hierarchical imaging for nanoparticle localization during ablation

PLAL is a hierarchical process with nanometer-sized particles being distributed over some millimeters in space. By SAXS the NPs can be detected *in situ* very efficiently, however only a single positions can be investigated at a time. Thus, a multiplexing of SAXS measurements is required for a real imaging of the NP distribution during the cavitation bubble lifetime. This can be realized by SEMCI with Hartmann masks or CARLs. A 2D array of tiny beamlets, which get broadened by the scattering of the NPs, is produced by cutting a broad beam by an hole array of by focusing it into many spots with a lens array. The pitch of the beamlet array determines the spatial resolution of the scattering image at the end but also defines the scatterer size sensitivity (see eq. (3.17) and discussion).

Fig. 6.13 illustrates the SEMCI technique, where from each X-ray beamlet penetrated through the sample the scattering power on the sample in retrieved. The three subimages illustrate the results obtained within this work with this scattering imaging technique. In (a) the already well known NP distribution at maximum cavitation bubble suspension is shown. By comparing these results with an ablation of gold in a millimolar NaCl solution the *in situ* size quenching is observed as shown in Fig. 6.13 (b). The scatterer size sensitivity changes with the distance between the sample and the detector and allows to determine the existence of a large number microbubbles in the first rebound of an ablation on a free wire target, as illustrated in Fig. 6.13 (c). Both results are discussed in the two following subsections.

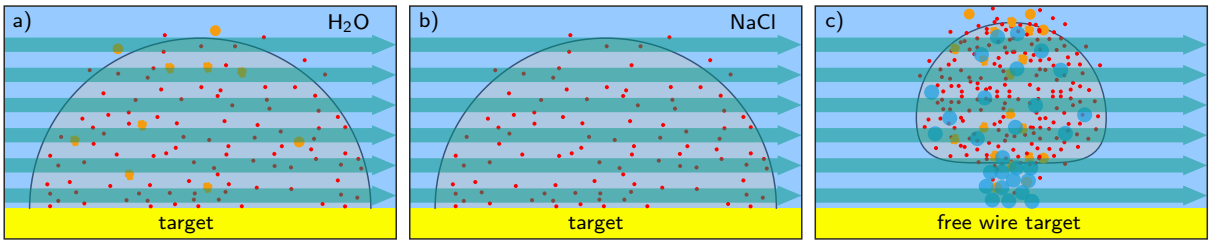

Fig. 6.13: Sketch of the Single-Exposure Multi-Contrast Imaging technique with illustration of the two observed results. From the size change of each X-ray beamlet (green arrows) the scattering strength of the samples is determined. By comparing the ablation of gold in pure water (a) and millimolar sodium chloride (NaCl) (b), the *in situ* size quenching is observed as no secondary nanoparticles (orange) are detected anymore. During ablation on a wire target the rebound detaches from the target and consists of a high amount of microbubbles (blue) as illustrated in (c).

6.3.1 Size quenching of nanoparticles by electrolytes already in the cavitation bubble

Normally a multi-modal NP size distribution is observed during PLAL. The genesis of secondary NPs can be reduced by additives such as NaCl or PVP in the case of gold NPs. The mechanisms of these two additives are different because NaCl already acts in the cavitation bubble, while the macromolecular PVP does not prevent the formation of secondary NPs during the lifetime of the bubble. The experiments presented in this subsection were performed in close cooperation with S. Barcikowski and A. Letzel at the University of Duisburg-Essen in Germany. Here the main focus is on the SEMCI measurement technique as the underlying phenomenology of the size quenching was central part of the dissertation of A. Letzel[45] and was published in literature.[117,119]

The size of gold NPs can be controlled by adding several additives such as polymers or electrolytes to the liquid phase, as the group of Barcikowski has shown.[42–44,117,119] The size quenching of secondary NPs is also observed for other metals like palladium[267] or platinum.[268] The ions of millimolar electrolytes in the liquid phase get into contact with the ignited plasma very early.[269] The dissolved ions can be detected in the plasma by plasma spectroscopy, at least for pulses of 100 ns duration.[122] Therefore they can interact with the ablated material even before the cavitation bubble genesis. For macromolecular ligands, however, it can not be excluded that they degrade by intense laser irradiation.[42,44,270]

In literature the *in situ* size quenching effect of additives is normally referred to the addition of them in advance of the ablation[42,121,271] while *ex situ* is referred to an addition after ablation.[43,44] Both show size quenching effects.

The *in situ* size detection of nanoparticles can, as discussed before, only be performed by X-ray scattering methods. By SAXS it was shown that already after 90 µs, which was at the maximum suspension of the first bubble, the amount of secondary NPs is reduced during a nanosecond ablation on gold with NaCl addition.[117] By *ex situ* NP analysis the reduced size was also confirmed, as shown in Fig. 6.14 (b). The amount of secondary NPs is strongly reduced and the mean size of the primary NPs decreases slightly. This underlines that not only the sizes during the ablation are decreased but also an agglomeration afterwards is diminished.

To disentangle the different quenching processes, ablation in water, millimolar NaCl and PVP were investigated by scattering imaging. A Hartmann mask (25 µm thick platinum foil, pitch 65 µm) was used to produce a 2D array of beamlets with an energy of 17.9 keV. With a distance between the ablation

spot and the detector of 3 cm this results in an ACL of $\xi = 32\,\text{nm}$, hence a maximum sensitivity of $\mu_\xi^{max} = 55\,\text{nm}$. With this setup only the secondary NPs can be detected, because the scattering sensitivity for NPs with sizes below 10 nm is marginal, as discussed in subsection 4.3.4.

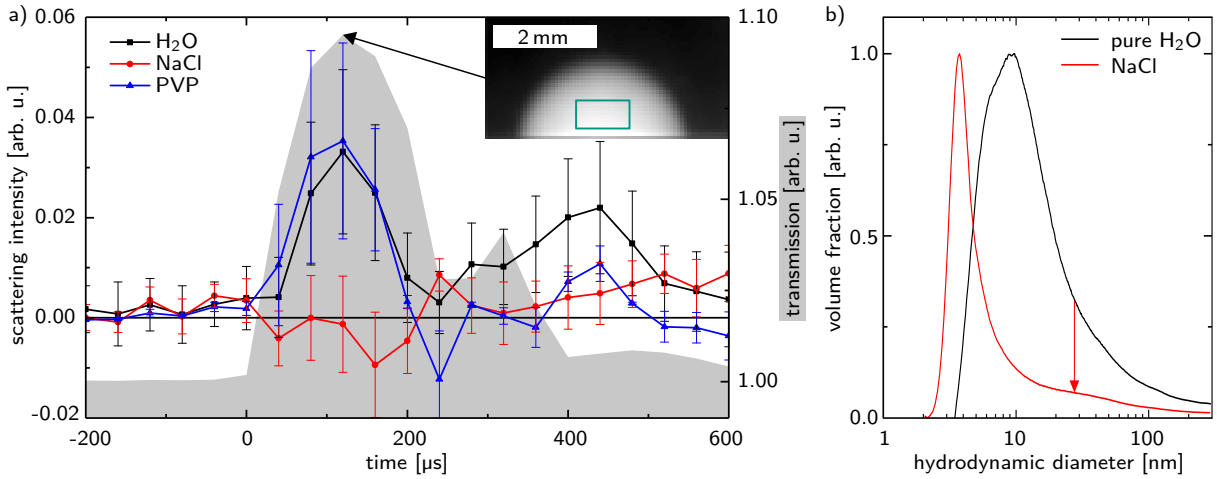

Fig. 6.14: (a) Scattering signal of gold nanoparticles ablated (1064 nm, 7 ns, 11 mJ) in water, sodium chloride (NaCl) and polyvinylpyrrolidone (PVP). The scattering imaging setup had an auto-correlation length = 32 nm, hence was only sensitive to secondary nanoparticles (peak sensitivity at 55 nm). The *in situ* size quenching effect of millimolar NaCl is observed by the reduced scattering signal during the cavitation bubble lifetime compared to a pure water or millimolar PVP solution. (b) Nanoparticle size distribution measured by analytic disc centrifuge of batch ablation (1064 nm, 12 ps, SI11mJ) of gold in water and NaCl showing the reduced secondary nanoparticle amount *ex situ*. Reproduced from Letzel et al.[119] and Reich et al.[61] **[SI3]**

In Fig. 6.14 (a) the scattering signal as function of delay after laser excitation is shown for all three liquid environments. For ablation in water an increased scattering signal is observed during the first bubble with a peak at the maximum bubble extension. The temporal evolution of the scattering intensity obtained from SAXS measurements in a similar way as in Fig. 6.10 can not be determined as the temporal resolution of the SEMCI with 40 µs is much lower. In accordance to previous SAXS results for size quenching of gold NPs by NaCl,[117] the scattering signal vanishes in the SEMCI measurements. Very small amounts of secondary NPs can not be excluded but are below the detection limit. Due to the exclusive sensitivity on the secondary NPs their disappearance in saline solution can be observed.

In *ex situ* experiments PVP also showed a size quenching effect for silver NPs[89] and is used in chemical synthesis of gold NPs.[272] Here, the ablation of gold was performed directly in a millimolar PVP solution. In Fig. 6.14 (a) no change in scattering intensity is visible for ablation in PVP compared to pure water in the first cavitation bubble indicating that no *in situ* size quenching takes place. This is surprising as it was reported that macromolecular ligands can reduce the NP size at least *ex situ*.[42,121,271] However, none of these references investigated the NP size distribution during the cavitation bubble lifetime. Hence, the results obtained by SEMCI indicate that PVP is not able to quench the size of the secondary NPs inside the cavitation bubble.

In contrast to electrolytes, which are detectable in plasma spectroscopy early after laser excitation, plasma spectra obtained in water and PVP (even with a much higher concentration at otherwise similar conditions than here) did not show differences.[89] Concentration-dependent *ex situ* size determination showed that the used 0.5 mM PVP in the SEMCI was well above the required threshold concentra-

tion for an efficient size quenching.[119] This emphasizes that macromolecular ligands can not enter the cavitation bubble due to the harsh conditions during laser excitation, as this leads to their decomposition.[42,44,117,270]

In conclusion it can be stated that both, NaCl and PVP, do reduce the size of NPs. The primary NPs are reduced slightly in size while the secondary NPs are strongly reduced in amount. However the mechanisms are different. NaCl already acts *in situ* inside the cavitation bubble and reduces the ripening by an increased energy barrier between the NPs due to increased surface charges.[119] PVP, in contrary, does not change the abundance of secondary NPs inside the cavitation bubble. It only interacts *ex situ* in the suspension by steric stabilization and thereby suppresses growth processes and agglomeration.[119,127]

Furthermore, the number of large solid spheres is reduced in NaCl compared to PVP. This indicates again an *in situ* size quenching effect of NaCl, which prevents directly the emergence of solid spheres, which are supposed to be formed out of the liquid target phase.[3] PVP can only prevent the aggregation of smaller NPs to larger ones, because it acts delayed.

6.3.2 Micrometer-sized air bubbles after ablation of a free wire target

During PLAL on a free wire target the bubble collapse and rebounds are not located on the target as already shown in Fig. 2.5. The first bubble detaches from the target during the shrinking phase and the subsequent bubble oscillations show a net velocity away from the target. The first rebound is seen as a dark cloud in optical imaging. The nature of this opaqueness can be a cloud of either dense NPs or of microbubbles. It shows a high transmission in X-ray imaging, which already indicates that it consists of a high amount of vapor. However this does not exclude a parallel existence of NPs. This was investigated by SEMCI with a CARL produced in this work.

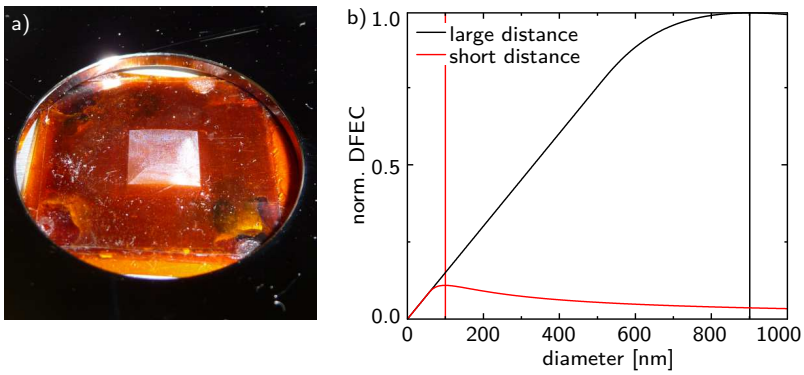

Fig. 6.15: (a) The Compound Array Refractive Lens mounted in the holder. The 2D lens array of the top foil is visible as a bright square in the middle. (b) Scattering sensitivity expressed as Dark-Field Extinction Coefficient (DFEC) for the sample-to-detector distances of the measurements. The peak values are 100 nm and 900 nm.

In Fig. 6.15 (a) an image of the used CARL (produced by spiral embossing and stacking under a microscope) is shown. The focal length at an X-ray energy of 9 keV is arround 125 cm. For more details on the characterization of the CARL see section 5.2. To differentiate between NPs and microbubbles, measurements at two different sample-to-detector distances were performed, which results in different scattering sensitivities as shown in Fig. 6.15 (b). With the short distance one is mainly sensitive on NPs as the peak sensitivity is at 100 nm. Micrometer-sized structures only contribute weakly to the scattering signal. As in subsection 6.3.1, only the secondary NPs can be detected because the primary ones are

too small to gain a considerably scattering signal. For the large distance, where the peak sensitivity is at 900 nm, the setup is still sensitive on the NPs but additionally to much larger structures such as micrometer-sized air bubbles. For the same volume fraction, the scattering intensity for large structures is much larger than for small NPs.

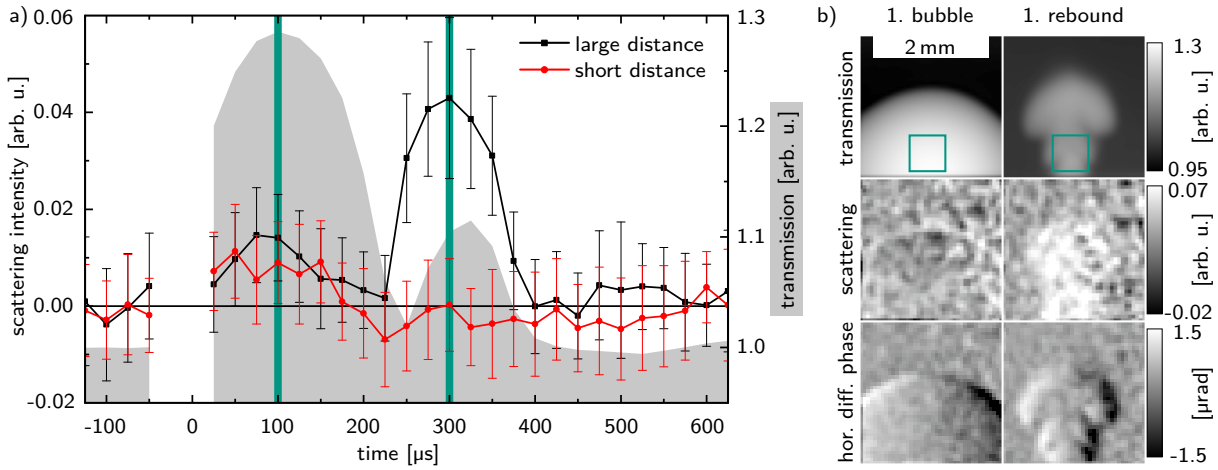

Fig. 6.16: (a) Scattering imaging intensity evolution after ablation (1064 nm, 7 ns, 10 mJ) on a free zinc wire (1 mm diameter) allowing a differentiation between nanoparticles and micrometer-sized bubbles. In (b) the contrast images transmission, scattering and differential phase in horizontal direction for the large distance are shown for the maximum suspension of the first bubble and first rebound as indicated by green lines in (a). The short distance is only sensitive on small structures while the large distance is more sensitive on large ones as shown in Fig. 6.15 (b). During the first bubble the scattering increases for both distances while it only rises for the larger one in the first rebound. Hence, the first bubble is filled with nanoparticles while the first rebound consists of micrometer-sized bubbles. Recalculated from Reich et al.[238] **[SI1]**

In Fig. 6.16 (a) the temporal evolution of the scattering intensity for the ablation (1064 nm, 7 ns, 10 mJ) of a free zinc wire (diameter 1 mm) is shown. In (b) the contrast images transmission, scattering and differential phase in horizontal direction are shown for the maximum suspension of the first bubble and the first rebound for the large sample-to-detector distance. The location of scattering intensity determination for (a) is shown by the green squares in (b).

The scattering intensity increases during the lifetime of the first bubble for both distances. For the first rebound only the scattering signal of the large distance is strongly boosted while it stays around zero for the short distance. This reveals that in the first bubble a large amount of secondary NPs are present, which is in accordance to the already shown results of the Hartmann mask measurements in H_2O and PVP. As both signals, for the short and large distance, are the same within the error margins, the scattering signal must result from NPs rather than from larger structures. The scattering intensity for both distances is similar for NPs, as shown in Fig. 6.15 (b). If a significant amount of micrometer-sized structures would be present during the first bubble lifetime, the scattering signal of the large distance must have been increased compared to the short distance. This allows for the conclusion, that the first bubble consists of one homogeneous bubble with a smooth surface as not micrometer-sized structures introduced scattering.

The first rebound, however, consists mainly of micrometer size structures. Ablated particles in this size can be excluded as they are only rarely found after PLAL. These micrometer-sized structures are small cavitation bubbles and partly also persistent bubbles, as displayed in subsection 2.1.5. As the scattering

signal for the short distance only varies around zero, no significant amount of NPs can be present in the stem of the first rebound. Furthermore, in the main cavity of the first rebound no increased scattering signal is observed indicating that already a large amount of NPs must have left the cavitation bubbles and be dispersed in the liquid.

During PLAL on free wire targets, where the cavitation bubbles detaches from the target, the NPs captured in the first bubble can not be redeposited onto the target during the collapse phase. This is of advantage for an increased NP yield as regularly shown in literature.[21,47,59,143] In contrast to ablation on flat targets, where also in the first rebound a high mass of secondary NPs was observed,[27] the first rebound on a free wire target contains a much decreased amount of secondary NPs. This indicates an early release of NPs into the liquid during the detached collapse. This collapse is much less symmetric compared to the flat target leading to higher turbulences and therefore a higher probability to release NPs into the liquid phase.

In optical imaging only opaque structures are visible during the first rebound allowing no reliable conclusion of the origin. X-ray imaging already showed that a high amount of vapor must be present in the first rebound due to the high transmission signal. Only the scattering imaging can manifest the statement, that the rebound consists of a large number of microbubbles. Due to the strong scattering signal even a visual recognition of the first rebound in the scattering image in Fig. 6.16 (b) is possible.

The differential phase, which is the third possible contrast in multi-contrast imaging, measures the angle of beamlet deflection. The cavitation bubble represents a biconcave cavity for the X-rays. This leads, as in the case of lenses, to a focusing of the beamlets. In Fig. 6.16 (b) the differential phase in horizontal direction is shown. It clearly shows the beamlet deflection towards the bubble center. With a SD of 0.18 µrad of the undisturbed beam a good angular resolution is achieved.[163]

7 Conclusion and Outlook

In this work the fundamental processes of Nanoparticle (NP) genesis in Pulsed Laser Ablation in Liquids (PLAL) were investigated. The multi-scale nature of PLAL required a set of complementary measurement techniques and hierarchical imaging to investigate the different processes occurring *in situ*.

After laser excitation of the target a cavitation bubble with a size in the millimeters range is induced by the evaporation of the liquid. By simultaneously imaging the bubble and the ignited plasma and measuring the extinction of the suspension it was found that a close correlation between the bubble size, the ablation yield and the plasma intensity exists. With the combination of these three linked quantities, parameters for an improved ablation efficiency were determined. During ablation on pristine targets with low laser fluences, an incubation effect occurs with high loss mechanisms, which in turn leads to a low ablation efficiency. The subsequent excitation of the same target position roughens the surface and thus reduces losses and increases the ablation yield.

At high laser fluences, however, the surface state of the target plays only a minor role. Above a certain threshold value, a plasma can be ignited sufficiently and dominates the energy localization. In this case, the incubation effect is reduced to the very first pulse, while several tens of shots are required at low fluences. The threshold fluence for sufficient plasma ignition manifests itself in a sigmoidal dependence of ablation efficiency and cavitation bubble size on the applied fluence. This effect is independent of the state of the target surface and has been found for pristine and corrugated targets. Favorable parameters are therefore an ablation with high fluences or on pre-irradiated targets.

Small- and wide-angle X-ray scattering (SAXS and WAXS) are the only techniques that allow an *in situ* investigation of NPs during the lifetime of the cavitation bubble. By combining both, the NP size distribution and the crystalline domain sizes were observed to confirm the most recent models of ablation derived from simulations. With SAXS it could be shown that secondary NPs are located at or even in front of the cavitation bubble boundary. These NPs are solidified and have large crystal domain sizes as revealed by WAXS. This indicates that these NPs are rather solid spheres than agglomerates of smaller ones. Agglomerates and spherical NPs, both observed in the final suspension, have different mechanisms of genesis. Agglomeration occurs mainly during bubble collapse and not during material disintegration from the target. The detected NP mass during the lifetime of the cavitation bubble follows well the model of a homogeneously filled bubble.

A multi-contrast imaging, where the scattering contrast represents a multiplexing of SAXS, can be performed by the Hartmann mask-like Single-Exposure Multi-Contrast Imaging (SEMCI) technique. This was used in the field of PLAL in this work for the first time. The electrolyte sodium chloride (NaCl) and the macromolecular ligand polyvinylpyrrolidone (PVP) both reduce the size of the NPs. However, the actual mechanism of action, which is different for the two, has not yet been clarified. In cooperation with A. Letzel and S. Barcikowski at the Institute of Technical Chemistry I of the University of Duisburg-Essen this was investigated by scattering imaging. While NaCl acts already inside the cavitation bubble

PVP does not. The latter can only prevent the later agglomeration of small NPs to larger ones while NaCl directly inhibits the genesis of large NPs.

During ablation on free wire targets, the bubble rebounds are detached from the target, increasing the ablation efficiency. In optical imaging, only an opaque mushroom like first rebound is visible, but the nature of it was unknown until now. SEMCI showed that the first rebound consists mainly of micrometer-sized vapor bubbles. Therefore, the opacity in optical imaging originates from vapor bubbles and not from a large amount of NPs. The amount of NPs detected in the first bubble is not detected in the first rebound any more. This indicates that due to the higher turbulence of the detached bubble collapse, a higher amount of NPs is released into the liquid than during ablation on flat targets.

For the SEMCI technique used in this work, a wide incident X-ray beam was divided into a 2D array of beamlets. This was realized by a 2D hole array in an otherwise absorbing foil and by the newly developed Compound Array Refractive Lenses (CARLs). The latter were manufactured to improve X-ray efficiency by switching spot pattern production from absorption to focusing. Apart from the low absorption of the lens material, the entire X-ray intensity can be used. The 2D lens arrays were produced either by serial embossing with one needle or by single-step embossing with a 2D needle array. The production of the needle array by first embossing with a single needle and subsequent electroplating showed good replication. Embossing with precise linear stages led to an accuracy of beam positioning with deviations of less than 1 µm from the ideal 2D array. The lens foils were stacked up to six times to reduce the focal length. With this, focal lengths between 60 cm and 125 cm for X-ray energies of 9 keV were realized. The maximum visibility was about 0.5.

Due to the serial embossing, the maximum fill factor is limited to 79 %. The most perfect form of a 2D lens array are parabolic truncated lenses with a fill factor of 100 %. Therefore, in future the production of the master for the electroplating process must be improved compared to the serial embossing used in this work. One possibility would be the 3D laser writing of the master with an egg carton shape of parabolically truncated lenses. Other current approaches for the production of CARLs are direct 3D laser writing of lens arrays and X-ray lithography. Both methods are currently being investigated in collaboration at the Institute of Microstructure Technology (IMT) at KIT. With these techniques a fill factor of nearly 100 % should be possible. For the fabrication of a larger number of lens arrays, however, stamping seems to be the only suitable method, since the other approaches do not allow low-tech replication of CARLs.

By combining simulations of SEMCI data and measurements, it was shown that only the fast Fourier analysis in combination with a subsequent decorrelation of transmission crosstalk to scattering contrast is suitable for reliable scattering data interrogation. The Gaussian fitting, the visibility change and the image moment analysis, which are also described in literature, showed scattering sensitivities that are strongly dependent on the specific setup parameters. The first two, however, are suitable for the characterization of the lens arrays as they allow the direct determination of the beamlet spot parameters and the focus point.

Future advances in CARL production, which will result in higher gain factors, will hopefully lead to a reduced noise level, especially in the scattering contrast of SEMCI. Thus, not only the strong scattering signal of microbubbles, but also the scattering of NPs during PLAL should lead to directly visible scattering patterns. This makes it possible to investigate the NP distribution during the ablation process even more precisely and leads to a further improved knowledge of the fundamental processes during PLAL. With the help of this the way to designed NPs can be paved further. Many other applications of

hierarchical imaging, such as the evaluation of additively manufactured objects,[273] are conceivable in order to answer central societal challenges such as energy, mobility and information technology.

List of Experiments

Optical imaging

Optical imaging was performed mainly in stroboscopic mode. This means that for each image a separate laser pulse was probed and the delay between laser excitation and image acquisition was shifted. General details of the imaging setup can be found in subsection 4.1.3. Here only the parameters of the measurements are listed.

OI1 - Ablation bubble dynamics on flat target

- data: 19.01.2018, folder: `003`
- laser: Nd:YAG laser "Continuum Minilite I", pulse duration 7 ns, wavelength 1064 nm, 3 mJ pulse energy, ≈0.1 Hz repetition rate
- target: brass plate of 5 mm thickness (technical grade); target transported continuously to ensure fresh target for each shot
- ablation chamber: large plastic vessel with plano-convex lens (Thorlabs, effective focal length with water on the planar side 38 mm) as incoupling wall; lens-target distance slightly smaller than focal length comparable to standard flow-chambers; water (Millipore) flushed in between two laser shots to refresh ablation region
- image acquisition in stroboscopic mode

OI2 - Ablation bubble dynamics on wire target

- published in paper: *X-ray spectroscopic and stroboscopic analysis of pulsed-laser ablation of Zn and its oxidation*[59]
- data: paraxial to wire: 22.08.2017, folder `009`; perpendicular to wire: 09.08.2017, folder `003`
- laser: Nd:YAG laser "Continuum Minilite I", pulse duration 7 ns, wavelength 1064 nm, 11 mJ pulse energy, 1 Hz repetition rate
- target: Zn wire with 1 mm diameter (Advent, 99.99 %); continuously transported
- ablation chamber: paraxial: cuvette for free wire, perpendicular: 3D printed ablation chamber for free wire; continuous water (Millipore) flow
- image acquisition in stroboscopic mode

OI3 - Appearance of nanoparticle fog and persistent gas bubble

- data: 15.02.2018, folder: `longtime`
- laser: Nd:YAG laser "Continuum Minilite I", pulse duration 7 ns, wavelength 1064 nm, 1 mJ pulse energy

- target: brass plate of 5 mm thickness (technical grade)
- ablation chamber: large plastic vessel with plano-convex lens (Thorlabs, effective focal length with water on the planar side 38 mm) as incoupling wall; lens-target distance slightly smaller than focal length comparable to standard flow-chambers
- image acquisition in videographic mode with 95 Hz repetition rate
- burst generator (33210A, Agilent) for camera triggering

OI4 - Bubble shielding effect at high repetition rates

- data: 21.09.2017, folder `018`, first run, images: 31, 34, 44
- laser: "EdgeWave InnoSlab PX400-1-GM SN769", pulse duration 12 ps, wavelength 1064 nm, 1 mJ pulse energy, 26 kHz repetition rate
- target: gold ribbon (99.9 %) with 4 mm width and 200 µm thickness
- ablation chamber: 3D printed ablation chamber for ribbon targets
- image acquisition in stroboscopic mode

OI5 - Nanoparticle shielding effect

- data: 19.01.2018, folder `002`, images: 46, 47
- laser: Nd:YAG laser "Continuum Minilite I", pulse duration 7 ns, wavelength 1064 nm, 3 mJ pulse energy, 0.5 Hz repetition rate
- target: brass plate of 5 mm thickness (technical grade); transported continuously to ensure fresh target for each shot
- ablation chamber: large plastic vessel with plano-convex lens (Thorlabs, effective focal length with water on the planar side 38 mm) as incoupling wall; lens-target distance slightly smaller than focal length comparable to standard flow-chambers
- image acquisition in stroboscopic mode

OI6 - Ablation efficiency compared to target the position

- published in paper: *Fluence Threshold Behaviour on Ablation and Bubble Formation in Pulsed Laser Ablation in Liquids*[58]
- data:
  - Stroboscopy: 20160912
  - image as inset: 20160912 - `014_22mm-0002.tiff`
  - Spectroscopy: 20161010
- laser: Nd:YAG laser "Continuum Minilite I", pulse duration 7 ns, wavelength 1064 nm, 10 mJ pulse energy for stroboscopy and 12 mJ pulse energy for spectroscopy, 5 Hz repetition rate for spectroscopy and 0.5 Hz for stroboscopy repetition rate
- target: silver ribbon (99.9 %) with 4 mm width and 100 µm thickness; transported continuously
- ablation chamber: cuvette (1 cm × 1 cm) where bottom was replaced by a plano-convex lens (Thorlabs, effective focal length with water on the planar side 38 mm); lens-target distance was varied; water (Millipore) continuously flowed for stroboscopy and only replaced in between measurements for spectroscopy

- spectroscopy:
  - fiber spectrometer (Ocean Optics, USB2000, 200-850 nm) with halogen lamp (DH-2000, Ocean Optics)
  - fibers were connected to ablation cuvette via fiber couplers
  - 150 shots with 5 Hz repetition rate per distance
  - volume normalized extinction
  - measurement 10 s after ablation stopped; integration time 2 ms, averaging 50, boxcar 4; integrated intensity from 370 nm to 500 nm
- image acquisition in stroboscopic mode

OI7 - Fluence threshold for bubble size and ablation efficiency

- published in paper: *Fluence Threshold Behaviour on Ablation and Bubble Formation in Pulsed Laser Ablation in Liquids*[58]
- data:
  - Spectroscopy extinction versus energy: 20161007 and 20161018 - `exticntion_volume_VsFluence.opj`
  - Spectroscopy extinction versus number of shots: 20161010 - `resultsextVsnrshot.opj`
  - Stroboscopy flat: Schönfeld - Auswertung - Run 6 - 01.04.16 - `volumen.opj`
  - Stroboscopy wire: Schönfeld - Auswertung - Run 2 - 27.01.16 - `16-01-27_2.opj`
- laser: Nd:YAG laser "Continuum Minilite I", pulse duration 7 ns, wavelength 1064 nm, 1 mJ to 30 mJ pulse energy, 1 Hz repetition rate
- target: silver ribbon (99.9 %) with 4 mm width and 100 µm thickness and silver wire (99.9 %) with diameter 0.7 mm; both transported continuously
- ablation chamber: bubble imaging: 3D printed ablation chamber for wire and ribbon targets; water (Millipore) continuously flowed; spectroscopy: cuvette for wire target
- spectroscopy:
  - fiber spectrometer (Ocean Optics, USB2000, 200-850 nm) with halogen lamp (DH-2000, Ocean Optics)
  - fibers were connected to ablation cuvette via fiber couplers
  - 150 shots with 5 Hz repetition rate per pulse energy
  - measurement 10 s after ablation stopped; integration time 2 ms, averaging 50, boxcar 4; integrated intensity from 400 nm to 420 nm
  - extinction versus number shots: at 400 nm during continuous ablation
- image acquisition in stroboscopic mode

OI8 - Incubation effect during ablation

- published in paper: *Incubation effect of pre-irradiation on bubble formation and ablation in laser ablation in liquids*[60]
- data:
  - Stroboscopy: 20180720, folders `003,008,009,010,011,012`; high pulse energies

  - plasma imaging: `20180802_plasma-003,005`
- laser: Nd:YAG laser "Continuum Minilite I", pulse duration 7 ns, wavelength 1064 nm, 1 mJ to 10 mJ pulse energy, 1 Hz repetition rate
- EdgeWave InnoSlab PX400-1-GM SN769 1064 nm, max 2 mJ, max 80 kHz, 12 ps
- target: gold ribbon (99.9 %) with 4 mm width and 200 µm thickness; silver ribbon (99.9 %) with 4 mm width and 100 µm thickness thickness; germanium wafer (≈5 mm width and 512 µm thickness; all continuously transported
- ablation chamber: large plastic vessel with plano-convex lens (Thorlabs, effective focal length with water on the planar side 38 mm) as incoupling wall; lens-target distance slightly smaller than focal length comparable to standard flow-chambers; water (Millipore) flushed in between two laser shots to refresh ablation region
- plasma imaging: coaxial imaging of plasma intensity with basler camera with a tube lens and the laser focusing lens for imaging the target plane; exposure time delay to laser −5 µs to 5 µs; average plasma intensity calculated from the average value of equally sizes images
- image acquisition in stroboscopic mode

X-ray imaging

XRI1 - Cavitation bubble dynamics on a wire target

- data: 20.02.2017, batch 12, `run99`
- laser: Nd:YAG laser "Continuum Minilite I", pulse duration 7 ns, wavelength 1064 nm, 11 mJ pulse energy, 2 Hz repetition rate
- target: Zn wire with 1 mm diameter (Advent, 99.99 %); continuously transported
- ablation chamber: 3D printed ablation chamber for free wire; continuous water (Millipore) flow
- Topo-Tomo instrument of the Synchrotron Radiation Source at KIT
- white beam from a bending magnet filtered by 0.25 mm beryllium and 0.2 mm aluminum leading to a central energy of 15 keV
- 50 µm LuAg:Ce scintillator lens coupled (magnification 2.3) to a PCO.dimax CMOS camera
- image size 560 px × 720 px, exposure time 30 µs, repetition rate 10 kHz, Trigger mode ext. exp. start
- image sequence recording: one image sequence of 40 images per laser shot with around seven images before laser impact (*flat*); in total 208 image sequences taken per run consisting of four sequences without X-ray illumination (*dark*), 200 sequences with X-ray illumination (*radio*) and again four sequences *dark*; time delay shift (0 µs, 25 µs, 50 µs and 75 µs) between subsequent sequences leading to 50 parts with each having four sequences of shifted delay
- image acquisition in interleaved mode
- image processing: averaging of all images with same delay; flat correction with images before laser impact to remove beam patterning of the CARL

XRI2 - Regularity of Compound Array Refractive Lenses

- data: 30.01.2019; folders: `ragularityFoils\2.gen_mylar_p50_1foil_1` and `regularityFoils\3.gen_mylar_65-50_1foil_1`

- production of lens arrays:
  - serially embossed lens array: embossed at 24.04.2017 in 125 µm Mylar®, #028, pitch 50 µm, depth around 15 µm, array of 100 × 100 lenses, CNC-milled steel needle with parabolic shape and 8 µm apex radius
  - single-step embossed lens array: master for electroplating embossed at 21.12.2017 in 5 mm PMMA plate, #007, pitch 65 µm, depth 50 µm, array of 100 × 100 lenses, CNC-milled steel needle with parabolic shape and 8 µm apex radius, electroplating by microworks GmbH (Karlsruhe, Germany), embossing in pellet press (Model 4350, Carver Inc., USA) with a load of around 3.5 t
- Topo-Tomo instrument of the Synchrotron Radiation Source at KIT
- white beam filtered by 0.5 mm aluminum and 0.25 mm beryllium, primary slits 3 mm × 3 mm
- Phantom v2640 camera lens coupled to 50 µm LYSO scintillator, magnification 2.5, 700 µs exposure time, 100 Hz acquisition rate, distance lens array to scintillator 149 cm
- recording of 100 images for dark current, flat image and radio image each
- data analysis:
  1. averaging of all 100 images for each contrast
  2. flat division before beamlet parameter analysis by Gaussian fitting (`fitmultigaussian` in appendix B.1)
  3. regularity: relative position by subtraction of a plane fitted to the median filtered center images and neighbor distance by calculating difference of center of neighboring spots

XRI3 - Lens properties with embossing depth and rotation

- data: 21.04.2017; folder: `20170421_CARL2.0_ANKA\001_8um_Tiefenprofil` and `20170421_CARL2.0_ANKA\005_8um_Tiefenprofil_rotation`
- production of lens array (30.03.2017): serially embossed lens array (#009) in 125 µm Mylar®, 13 different depths from 0 µm to 60 µm in 5 µm steps, each 10 × 2 lenses, pitch 150 µm with 200 µm distance to next depth array, CNC-milled steel needle with parabolic shape and 8 µm apex radius
- Topo-Tomo instrument of the Synchrotron Radiation Source at KIT
- white beam filtered by 0.2 mm aluminum and 0.25 mm beryllium
- PCO.dimax camera lens coupled to scintillator, magnification 10, 20 ms exposure time, distance lens array to scintillator 185 cm for depth dependence and 146 cm for rotation dependence, recording of dark, flat and radio image

XRI4 - Focal length of serially embossed CARL

- data: 09.11.2016, folder: `CARL_1_1`
- production of CARL: serially embossed lens array: embossed at 23.06.2016 in 75 µm Kapton®, #004, #005, #007, #008, #009, #010, pitch 65 µm, depth around 20 µm, array of 100 × 100 lenses, sewing needle with apex radius of around 25 µm
- Topo-Tomo instrument of the Synchrotron Radiation Source at KIT
- monochromatic beam with 9 keV X-ray energy

- Andor neo camera lens coupled to 200 µm LuAG:Ce scintillator, magnification 3.6, distance CARL to scintillator changed from 45 cm to 125 cm in steps of 10 cm
- data analysis:
  1. determination of the beamlet parameters by Gaussian fitting (`fitmultigaussian` in appendix B.1)
  2. determination of visibility of complete array with I_{max} and I_{min} determined for each beamlet zone (appendix B.3) and from Gaussian parameters
  3. regularity (at 125 cm sample-to-detector distance): relative position by subtraction of a plane fitted to the median filtered center images and neighbor distance by calculating difference of center of neighboring spots

XRI5 - Focal length of single-step embossed CARL

- data: 30.01.2019, folders: `focalpoint\3gen_5foils_Nr1`
- production of CARL: single-step embossed lens array: master for electroplating embossed at 21.12.2017 in 5 mm PMMA plate, #007, pitch 65 µm, depth 50 µm, array of 100 × 100 lenses, CNC-milled steel needle with parabolic shape and 8 µm apex radius, electroplating by microworks GmbH (Karlsruhe, Germany), embossing in pellet press (Model 4350, Carver Inc., USA) with a load of around 3.5 t, stacking under X-ray illumination of 5 lens foils
- Topo-Tomo instrument of the Synchrotron Radiation Source at KIT
- monochromatic beam with 8.5 keV X-ray energy
- Phantom v2640 camera lens coupled to 50 µm LYSO scintillator, magnification 2.5, 700 µs exposure time, 100 Hz acquisition rate, distance CARL to scintillator changed from 46.7 cm to 76.7 cm in steps of 1 cm
- recording of 100 images for dark current, flat image and radio images each
- data analysis:
  1. determination of the beamlet parameters by Gaussian fitting (`fitmultigaussian` in appendix B.1)
  2. determination of visibility of complete array with I_{max} and I_{min} determined for each beamlet zone (appendix B.3)and from Gaussian parameters
  3. regularity (at 59.7 cm sample-to-detector distance): relative position by subtraction of a plane fitted to the median filtered center images and neighbor distance by calculating difference of center of neighboring spots

Small- and wide-angle X-ray scattering

XRS1 - Incubation effect

- published in paper: *Incubation effect of pre-irradiation on bubble formation and ablation in laser ablation in liquids*[60]
- data: `2017-e16654\analysis\Au_fastslowmove`
- laser: EdgeWave InnoSlab PX400-1-GM SN769 1064 nm, 1 mJ, 1 kHz, 12 ps
- target: gold ribbon (99.9 %) with 4 mm width and 200 µm thickness; continuously transported

- ablation chamber: 3D printed ablation chamber for ribbon wire
- cSAXS beamline at the Swiss Light Source (PSI Villigen, Switzerland)
- monochromatic beam with 13.6 keV X-ray energy
- Pilatus 2M detector with a sample-to-detector distance (evacuated flight tube) of 7.1 m
- continuous ablation for 90 s with 1 kHz repetition rat
- different target speeds such that either a single shot was applied per target area or each part of the surface was irradiated by about 30 shots
- analysis: 2D scattering data subjected to standard corrections, transformed into curves of scattering intensity versus scattering vector by azimuthal integration; size distribution calculated by reverse Monte Carlo approach with McSAS[266]

XRS2 - Early appearance of crystalline nanoparticles - SAXS

- published in paper: *Early appearance of crystalline nanoparticles in pulsed laser ablation in liquids dynamics*[61]
- data: `2017-ma3821\SAXS\agruns138to141`
- laser: EdgeWave InnoSlab PX400-1-GM SN769 1064 nm, 1 mJ, 1 kHz, 12 ps
- target: gold ribbon (99.9 %) with 4 mm width and 200 µm thickness; continuously transported
- ablation chamber: 3D printed ablation chamber for ribbon wire
- cSAXS beamline at the Swiss Light Source (PSI Villigen, Switzerland)
- monochromatic beam (6 µm × 24 µm) with 13.6 keV X-ray energy 0.17 mm above the target
- Pilatus 2M detector with a sample-to-detector distance (evacuated flight tube) of 7.1 m; exposure time 2 µs and 5 µs by electronic active gate
- timing for different delays between laser excitation and detector with delay generator (DG645, Stanford Research Instruments), temporal precision of at least 0.5 µs
- analysis: 2D scattering data subjected to standard corrections, transformed into curves of scattering intensity versus scattering vector by azimuthal integration; calculation of the Porod invariant as partial integrals

XRS3 - Early appearance of crystalline nanoparticles - WAXS

- published in paper: *Early appearance of crystalline nanoparticles in pulsed laser ablation in liquids dynamics*[61]
- data: `2017-ma3821\WAXS\auruns089to094\Ag_089`
- laser: Coherent Legend Ti:Sa-based regenerative amplifier with 800 nm, 2.7 mJ, 2 ps and 1 kHz
- target: silver ribbon (99.9 %) with 4 mm width and 100 µm thickness; continuously transported
- ablation chamber: 3D printed ablation chamber for ribbon wire
- ID09 beamline at the European Synchrotron Radiation Facility (ESRF, Grenoble, France)
- monochromatic beam (60 µm × 80 µm) with 15.2 keV X-ray energy 0.2 mm above the target
- Rayonix HS170 detector with a sample-to-detector distance of 120 mm; accumulated exposure time 30 s, hence 30 000 shots
- temporal resolution $<$100 ps with a precision of 5 ps; achieved by isolating single X-ray pulses from the storage ring with a mechanical chopper and synchronized laser emission

- analysis: removal of liquid scattering by polynomial modeling; fitting of the (111) peak by Gaussian function; height as measure of mass and width transferred by Scherrer formula[156] to crystal grain size

XRS4 - Agglomeration of nanoparticles during bubble collapse

- published in paper: *Pulsed laser ablation in liquids: Impact of the bubble dynamics on particle formation*[15]
- data: `timescans_SAXS_2011\cuts.opj`
- laser: single mode EdgeWave HD-40I-E with 1064 nm, 10 mJ, 6 ns and 200 Hz
- target: gold ribbon (99.99 %) with 4 mm width and 200 µm thickness; continuously transported
- ablation chamber: steel chamber comparable to 3D printed ablation chamber for ribbon wire
- cSAXS beamline at the Swiss Light Source (PSI Villigen, Switzerland)
- monochromatic beam (6 µm × 24 µm) with 13.6 keV X-ray energy
- Pilatus 2M detector with a sample-to-detector distance (evacuated flight tube) of 7.1 m; exposure time 30 µs by electronic active gate; averaging of around 5000 laser shots
- analysis: 2D scattering data subjected to standard corrections, transformed into curves of scattering intensity versus scattering vector by azimuthal integration; calculation of the Porod invariant as partial integrals

Scattering imaging

SI1 - Scattering imaging of laser ablation for differentiation between nanoparticles and microbubbles

- published in paper: *Scalable, large area compound array refractive lens for hard X-rays*[238]
- data: 20.02.2017; `batch11` (9 runs) and `batch12` (26 runs)
- laser: Nd:YAG laser "Continuum Minilite I", pulse duration 7 ns, wavelength 1064 nm, 11 mJ pulse energy, 2 Hz repetition rate
- target: Zn wire with 1 mm diameter (Advent, 99.99 %); continuously transported
- ablation chamber: 3D printed ablation chamber for free wire; continuous water (Millipore) flow
- delay generator "Research Instruments, DG535"; burst generator "Agilent, 33210A"
- CARL produced by serial embossing (see section 5.2)
- Topo-Tomo instrument of the Synchrotron Radiation Source at KIT
- white beam from a bending magnet filtered by 0.25 mm beryllium and 0.2 mm aluminum leading to a central energy of 14.3 keV
- distance between ablation spot and detector 4.5 cm and 40 cm, CARL-to-detector distance 107 cm
- 50 µm LuAg:Ce scintillator lens coupled (magnification 2.3) to a PCO.dimax CMOS camera
- image size 560 px × 720 px, exposure time 30 µs, repetition rate 10 kHz, single image triggering
- image sequence recording: one image sequence of 40 images per laser shot with around seven images before laser impact (*flat*); in total 208 image sequences taken per run consisting of four sequences without X-ray illumination (*dark*), 200 sequences with X-ray illumination (*radio*) and again four sequences *dark*; time delay shift (0 µs, 25 µs, 50 µs and 75 µs) between subsequent sequences leading to 50 parts with each having four sequences of shifted delay

- contrast reconstruction:
  1. averaging images of same delay (script `averaging_run_direct-flat_V2.py` without flat division) and dark subtraction, thereby taking into account the logarithmic mean increase of the *dark* sequences, the different mean levels of *dark* sequences before and after the *radio* sequences as well as the logarithmic decrease in mean intensity in the whole run
  2. Fourier analysis of averaged video (script `singleshot_fromavg_V3_settingsimport.py`)
  3. averaging all contrasts of all runs of one batch (script `averaging_runs_V3_improved_code.py`)
  4. decorrelation of transmission crosstalk to scattering channels (script `crosscorrelation_V3_realvalue.py`)

SI2 - Multi-contrast test with empty air bubble

- data: 21.06.2018; bubbletest: `bubbletest_long_2`, `bubbletest_long_far`
- horizontal lying PMMA cuvette sealed with hot glue and filled with ultrapure water (Millipore); after the flat image acquisition an air bubble was injected by a syringe and placed into the beam; sample-to-detector distance 4.7 cm and 40 cm, Hartmann mask-to-detector distance 7 cm and 42.3 cm
- Hartmann mask: gold mesh on graphite, duty cycle 0.6 (60 % mesh and 40 % opening), pitch 50 µm; thanks for provision to M. Zakharova.[162]
- Topo-Tomo instrument of the Synchrotron Radiation Source at KIT
- 50 µm LuAg:Ce scintillator lens coupled (magnification 1.5) to a PCO.dimax CMOS camera
- image size 548 px × 720 px, exposure time 1.5 ms, repetition rate 100 Hz
- image sequence recording: 500 images for flat and radio conditions
- contrast reconstruction of all images:
  1. (1) Fourier analysis (script `singleshot_fromavg_FFT_V3_settingsimport.py`),
     (2) Gaussian fitting (script `singleshot_fromavg_gauss_V3_settingsimport.py`),
     (3) Gaussian fitting with pre-analysis pedestal correction (script `singleshot_fromavg_gauss_V4_backcorr.py`),
     (4) image moment analysis (script `singleshot_fromavg_moment_V1.py`),
     (5) visibility (script `Lensarray_visibility_fix-OEV2.py`)
  2. averaging all 500 images of each contrast.
  3. for visibility change: $1 - \frac{V_{radio}}{V_{flat}}$
  4. decorrelation of transmission and scattering data obtained by Fourier analysis with 50 images for correlation determination (script `crosscorrelation_V3_realvalue.py`)
  5. Reconstruction of the absolute phase with SHWave-Recon V1.2[249]

SI3 - Scattering imaging of laser ablation for *in situ* size quenching of gold nanoparticles with NaCl

- published in paper: *On the time and mechanism of nanoparticle functionalization by macromolecular ligands during pulsed laser ablation in Liquids*[119]

- data: 28.09.2016; `batch6` (20 runs), `batch7` (5 runs), `batch8` (11 runs), `batch9` (20 runs), `batch12` (12 runs) and `batch13` (35 runs)
- laser: Nd:YAG laser "Continuum Minilite I", pulse duration 7 ns, wavelength 1064 nm, 11.5 mJ pulse energy, 1 Hz repetition rate
- target: gold ribbon (99.9 %) with 4 mm width and 200 µm thickness; continuously transported
- ablation chamber: 3D printed ablation chamber for wire targets; continuous water flow (Millipore, NaCl and PVP solutions with 0.5 mM concentration)
- delay generator "Research Instruments, DG535"; burst generator "Agilent, 33210A"
- Hartmann mask: 25 µm thick platinum foil (Chempur, 99.9 %); 2D array of regular holes of about 10 µm in diameter and pitch 65 µm, drilled by pulsed fs-laser micromachining (Spectra Physics Spitfire Ace, 800 nm, 100 fs) with a fluence of 2 J/cm^2 and a repetition rate of 5 kHz.
- ID19 beamline at the European Synchrotron Radiation Facility (ESRF, Grenoble, France)
- pink beam from single-line undulator with an energy of 17.9 keV
- distance between ablation spot and detector 3 cm, Hartmann mask-to-detector distance 7 cm
- 100 µm YAG scintillator lens coupled (magnification 1) to a PCO.dimax CMOS camera
- image size 580 px × 480 px, exposure time 40 µs, repetition rate 12.5 kHz, single image triggering
- image sequence recording: one image sequence of 40 images per laser shot with around seven images before laser impact (*flat*); in total 212 image sequences taken per run consisting of six sequences without X-ray illumination (*dark*), 200 sequences with X-ray illumination (*radio*) and again six sequences *dark*; time delay shift (0 µs and 40 µs) between subsequent sequences leading to 100 parts with each having two sequences of shifted delay
- contrast reconstruction:

  1. averaging images of same delay (script `averaging_run_direct-flat_V2.py` without flat division) and dark subtraction, thereby taking into account the logarithmic mean increase of the *dark* sequences and the different mean levels of *dark* sequences before and after the *radio* sequences
  2. Fourier analysis of averaged video (script `singleshot_fromavg_V3_settingsimport.py`)
  3. averaging all contrasts of all runs of one batch (script `averaging_runs_V3_improved_code.py`)
  4. decorrelation of transmission crosstalk to scattering channels (script `crosscorrelation_V3_realvalue.py`)

Simulation

The simulations were performed with Python 2.7.14. The following published packages were used: `numpy` version '1.15.2', `tifffile` version '2018.05.10', `PIL` version '5.3.0'. The two packages developed within this work to reconstruct were used: `FFT_reconstruct` version '`V2.2_2017.05.17`', `gaussfit` version '`V10_2018.11.29`'.

If positions of an array are specified in the following descriptions, the numbering belongs to the Python label beginning with 0.

Sim1 - Influence of beamlet width on visibility

- 2D beamlet pattern of 40×40 spots, each spot area is $100\,\text{px} \times 100\,\text{px}$ large
- Gaussian beamlet distribution in one beamlet zone with varied $width_x$ and $width_y$ from 5 px to 100 px:
  $g = 5 \cdot exp\left\{ -\left[\left(\frac{49.5-y}{width_y} \right)^2 + \left(\frac{49.5-x}{width_x} \right)^2 \right] \right\} + 50$
- down sampling of images from $4000\,\text{px} \times 4000\,\text{px}$ to $520\,\text{px} \times 520\,\text{px}$ corresponding to a sampling of $13\,\text{px} \times 13\,\text{px}$ per beamlet zone
- data analysis:
  1. calculation of the visibility in each beamlet zone (script `Lensarray_visibility_fix-OEV2.py`)
  2. Gaussian fitting of the beamlets raw parameters (script `singleshot_fromavg_gauss_V3_settingsimport.py`)

Sim2 - Influence of transmission changes on beamlet parameter reconstruction

- 2D beamlet pattern of 40×40 spots, each spot area is $100\,\text{px} \times 100\,\text{px}$ large
- Gaussian beamlet distribution in one beamlet zone with varied
  1. *height* from 1 to 10:
     $g = height \cdot exp\left\{ -\left[\left(\frac{49.5-y}{14.3} \right)^2 + \left(\frac{49.5-x}{14.3} \right)^2 \right] \right\} + 50$
  2. $offset$ from 0 to 50:
     $g = 5 \cdot exp\left\{ -\left[\left(\frac{49.5-y}{14.3} \right)^2 + \left(\frac{49.5-x}{14.3} \right)^2 \right] \right\} + offset$
  3. *scale* factor from 0.1 to 2:
     $g = \left(5 \cdot exp\left\{ -\left[\left(\frac{49.5-y}{14.3} \right)^2 + \left(\frac{49.5-x}{14.3} \right)^2 \right] \right\} + 50 \right) \cdot scale$
- bubble transmission simulation:
  radius of bubble: $r = 1500\,\text{px}$,
  thickness of bubble: $t(x,y) = \sqrt{r^2 - (x-2000)^2 - (y-2000)^2}$,
  transmission: $T = \frac{t}{t_{max}} \cdot 0.3 + 1$,
  multiplication of 2D beamlet pattern with T
- down sampling of images from $4000\,\text{px} \times 4000\,\text{px}$ to $520\,\text{px} \times 520\,\text{px}$ corresponding to a sampling of $13\,\text{px} \times 13\,\text{px}$ per beamlet zone
- analysis of raw 2D beamlet pattern and transmission increased pattern by Gaussian fitting of the beamlets raw parameters (script `singleshot_fromavg_gauss_V3_settingsimport.py`)

Sim3 - Pre-analysis pedestal correction to reduce transmission problems during Gaussian reconstruction

- 2D beamlet pattern of 40×40 spots, each spot area is $100\,\text{px} \times 100\,\text{px}$ large
- Gaussian beamlet distribution in one beamlet zone:
  $g = 5 \cdot exp\left\{ -\left[\left(\frac{49.5-y}{14.3} \right)^2 + \left(\frac{49.5-x}{14.3} \right)^2 \right] \right\} + 50$

- bubble transmission simulation:
  radius of bubble varied from $r_1 = 100\,\text{px}$ to $r_{20} = 2000\,\text{px}$,
  thickness of bubble: $t(x,y) = \sqrt{r^2 - (x-2000)^2 - (y-2000)^2}$,
  transmission: $T = \frac{t}{t_{max}} \cdot 0.3 + 1$,
  multiplication of 2D beamlet pattern with T
- down sampling of images from 4000 px × 4000 px to 520 px × 520 px corresponding to a sampling of 13 px × 13 px per beamlet zone
- data nalysis:
  1. Gaussian fitting of the beamlets raw parameters (script `singleshot_fromavg_gauss_V3_settingsimport.py`)
  2. Gaussian fitting of the beamlets raw parameters with subtraction of low-pass filtered background intensity (script `singleshot_fromavg_gauss_V4_backcorr.py`)

Sim4 - Background correction before Gaussian fitting at real data

- raw data from,[163] median filtered with $size = 2\,\text{px}$
- 11.08.2016; Topo-Tomo instrument of the Synchrotron Radiation Source at KIT
- monochromatic X-ray at 8.5 keV, filtered by 0.25 mm beryllium and 0.2 mm aluminum; exposure time 5 sec; Andor NEO CMOS camera lens coupled to 10 µm LSO:TB scintillator
- stack of eight diamond X-ray lenses (radius of curvature at appex 200 µm) as sample;[216] sample-to-detector distance 16 cm
- calculate background signal of different intensity from native background:
  1. Gaussian blurring with $\sigma = 5\,\text{px}$ of *radio* image
  2. minimum filter with $size = 34\,\text{px}$ of filtered image
  3. Gaussian blurring with $\sigma = 30\,\text{px}$ of minimum filtered image
- simulate increased curvature by adding background multiplied by 0 to 15 to *radio* image
- data analysis:
  1. Gaussian fitting of the beamlets raw parameters (script `singleshot_fromavg_gauss_V3_settingsimport.py`)
  2. Gaussian fitting of the beamlets raw parameters with subtraction of low-pass filtered background intensity (script `singleshot_fromavg_gauss_V4_backcorr.py`)

Sim5 - Scattering sensitivity distribution

- 2D beamlet pattern of 40 × 40 spots, each spot area is 100 px × 100 px large
- Gaussian beamlet distribution in one beamlet zone with $offset$ 0 and 50 and with $width_x$ and $width_y$ 14.3; additionally for $offset = 0$ with $width_x$ and $width_y$ 5 and 33.3:
  $g = 5 \cdot exp\left\{-\left[\left(\frac{49.5-y}{width_y}\right)^2 + \left(\frac{49.5-x}{width_x}\right)^2\right]\right\} + offset$
- bubble transmission simulation:
  radius of bubble: $r = 1500\,\text{px}$,
  thickness of bubble: $t(x,y) = \sqrt{r^2 - (x-2000)^2 - (y-2000)^2}$,
  transmission: $T = \frac{t}{t_{max}} \cdot 0.3 + 1$,
  multiplication of 2D beamlet pattern with T

- parameters of simulated scattering setup: X-ray energy 15 keV, pitch of optical element 65 µm, sample-to-detector distance 4.5 cm, auto-correlation length $\xi = 57$ nm, peak value of the Dark-Field Extinction Coefficient at $\mu_d^{max} = 101$ nm
- 2D scattering distribution $I(q(x,y),r)$ for nanoparticles of sizes from 1 nm to 200 nm radius with constant volume fraction in the three sizes of 300 px × 300 px with $q(149.5,149.5) = 0$, 400 px × 400 px with $q(199.5,199.5) = 0$ and 500 px × 500 px with $q(249.5,249.5) = 0$:
  $I(q(x,y),r) = \left(4/3 \cdot \pi \cdot r^3\right) \cdot \left(3 \cdot \frac{\sin(q \cdot r) - q \cdot r \cdot \cos(q \cdot r)}{(q \cdot r)^3}^2\right) \cdot 10^{17}$
- convolution like scattering simulation for each pixel with considering conservation of X-ray flux:
  1. scaling of scattering distribution according to convolution pixel intensity
  2. scaling of scattering distribution according to bubble transmission at convolution pixel to simulate homogeneous filling
  3. addition of scattering distribution to area around convolution pixel
  4. subtraction of the sum of scattering distribution from convolution pixel
- down sampling of images from 4000 px × 4000 px to 520 px × 520 px corresponding to a sampling of 13 px × 13 px per beamlet zone
- data analysis:
  1. Fourier analysis up to order four (script `singleshot_fromavg_V3_settingsimport.py`)
  2. Gaussian fitting (script `singleshot_fromavg_gauss_V3_settingsimport.py`)
  3. Gaussian fitting with pre-analysis pedestal correction (script `singleshot_fromavg_gauss_V4_backcorr.py`)
  4. image moment analysis (script `singleshot_fromavg_moment_V1.py`)
  5. calculation of the visibility in each beamlet zone (script `Lensarray_visibility_fix-OEV2.py`)

Sim6 - Scattering sensitivity distribution depending on the auto-correlation length

- 2D beamlet pattern of 40 × 40 spots, each spot area is 100 px × 100 px large
- Gaussian beamlet distribution in one beamlet zone:
  $g = 5 \cdot exp\left\{-\left[\left(\frac{49.5-y}{14.3}\right)^2 + \left(\frac{49.5-x}{14.3}\right)^2\right]\right\} + 0$
- bubble transmission simulation:
  radius of bubble: $r = 1500$ px,
  thickness of bubble: $t(x,y) = \sqrt{r^2 - (x-2000)^2 - (y-2000)^2}$,
  transmission: $T = \frac{t}{t_{max}} \cdot 0.3 + 1$,
  multiplication of 2D beamlet pattern with T
- parameters of simulated scattering setup: X-ray energy 15 keV, pitch of optical element 65 µm, sample-to-detector distance 4.5 cm to 26.6 cm, auto-correlation length $\xi = 57$ nm to 338 nm, peak value of the Dark-Field Extinction Coefficient at $\mu_d^{max} = 101$ nm to 600 nm
- 2D scattering distribution $I(q(x,y),r)$ for nanoparticles of sizes from 10 nm to 300 nm radius of constant volume fraction in the size of 300 px × 300 px with $q(149.5,149.5) = 0$:
  $I(q(x,y),r) = \left(4/3 \cdot \pi \cdot r^3\right) \cdot \left(3 \cdot \frac{\sin(q \cdot r) - q \cdot r \cdot \cos(q \cdot r)}{(q \cdot r)^3}^2\right) \cdot 10^{15}$
- convolution like scattering simulation for each pixel with considering conservation of X-ray flux:

1. scaling of scattering distribution according to convolution pixel intensity
2. scaling of scattering distribution according to bubble transmission at convolution pixel to simulate homogeneous filling
3. addition of scattering distribution to area around convolution pixel
4. subtraction of the sum of scattering distribution from convolution pixel

- down sampling of images from 4000 px $\times$ 4000 px to 520 px $\times$ 520 px corresponding to a sampling of 13 px $\times$ 13 px per beamlet zone
- data analysis:

1. Fourier analysis up to order four (script `singleshot_fromavg_V3_settingsimport.py`)
2. Gaussian fitting (script `singleshot_fromavg_gauss_V3_settingsimport.py`)
3. image moment analysis (script `singleshot_fromavg_moment_V1.py`)
4. calculation of the visibility in each beamlet zone (script `Lensarray_visibility_fix-OEV2.py`)

References

[1] A. Fojtik and A. Henglein. *Ber. Bunsen-Ges. Phys. Chem.*, 97(2):252–254, **1993**.

[2] V. Amendola and M. Meneghetti. *Phys. Chem. Chem. Phys.*, 15(9):3027–3046, **2013**. doi:10.1039/C2CP42895D.

[3] C.-Y. Shih, R. Streubel, J. Heberle, A. Letzel, M. V. Shugaev, C. Wu, M. Schmidt, B. Gökce, S. Barcikowski, and L. V. Zhigilei. *Nanoscale*, 10(15):6900–6910, **2018**. doi:10.1039/c7nr08614h.

[4] J. D. Blakemore, H. B. Gray, J. R. Winkler, and A. M. Müller. *ACS Catal.*, 3(11):2497–2500, **2013**. doi:10.1021/cs400639b.

[5] E. Pizzolato, S. Scaramuzza, F. Carraro, A. Sartori, S. Agnoli, V. Amendola, M. Bonchio, and A. Sartorel. *J. Energy Chem.*, 25(2):246–250, **2016**. doi:10.1016/j.jechem.2015.12.004.

[6] S. Kohsakowski, R. Streubel, I. Radev, V. Peinecke, S. Barcikowski, G. Marzun, and S. Reichenberger. *Appl. Surf. Sci.*, 467-468:486–492, **2019**. doi:10.1016/j.apsusc.2018.10.145.

[7] H. A. Atwater and A. Polman. *Nat. Mater.*, 9(3):1–11, **2010**. doi:10.1038/nmat2629.

[8] M. Flores-Castañeda, E. Camps, M. Camacho-López, S. Muhl, E. García, and M. Figueroa. *J. Alloys Compd.*, 643:S67–S70, **2015**. doi:10.1016/j.jallcom.2014.12.054.

[9] F. Chen, M. Chen, C. Yang, J. Liu, N. Luo, G. Yang, D. Chen, and L. Li. *Phys. Chem. Chem. Phys.*, 17(2):1189–1196, **2015**. doi:10.1039/c4cp04380d.

[10] J. Lee, D. K. Chatterjee, M. H. Lee, and S. Krishnan. *Cancer Lett.*, 347(1):46–53, **2014**. doi:10.1016/j.canlet.2014.02.006.

[11] G. Gonçalves and G. Tobias, editors. *Nanooncology*. Springer International Publishing, **2018**. doi:10.1007/978-3-319-89878-0.

[12] S. Koenen, C. Rehbock, H. E. Heissler, S. D. Angelov, K. Schwabe, J. K. Krauss, and S. Barcikowski. *ChemPhysChem*, 18(9):1108–1117, **2017**. doi:10.1002/cphc.201601180.

[13] R. Intartaglia, G. Das, K. Bagga, A. Gopalakrishnan, A. Genovese, M. Povia, E. D. Fabrizio, R. Cingolani, A. Diaspro, and F. Brandi. *Phys. Chem. Chem. Phys.*, 15(9):3075–3082, **2013**. doi:10.1039/c2cp42656k.

[14] D. Zhang, B. Gökce, and S. Barcikowski. *Chem. Rev.*, 117(5):3990–4103, **2017**. doi:10.1021/acs.chemrev.6b00468.

[15] S. Reich, P. Schönfeld, P. Wagener, A. Letzel, S. Ibrahimkutty, B. Gökce, S. Barcikowski, A. Menzel, T. dos Santos Rolo, and A. Plech. *J. Colloid Interface Sci.*, 489:106–113, **2017**. doi:10.1016/j.jcis.2016.08.030.

[16] M.-R. Kalus, N. Bärsch, R. Streubel, E. Gökce, S. Barcikowski, and B. Gökce. *Phys. Chem. Chem. Phys.*, **2017**. doi:10.1039/c6cp07011f.

[17] V. Amendola, S. Polizzi, and M. Meneghetti. *Langmuir*, 23(12):6766–6770, **2007**. doi:10.1021/la0637061.

[18] T. Sakka, S. Masai, K. Fukami, and Y. H. Ogata. *Spectrochim. Acta, Part B*, 64(10):981–985, **2009**. doi:10.1016/j.sab.2009.07.018.

[19] C. L. Sajti, R. Sattari, B. N. Chichkov, and S. Barcikowski. *J. Phys. Chem. C*, 114(6):2421–2427, **2010**. doi:10.1021/jp906960g.

[20] P. Wagener, A. Schwenke, B. N. Chichkov, and S. Barcikowski. *J. Phys. Chem. C*, 114(17):7618–7625, **2010**. doi:10.1021/jp911243a.

[21] S. Kohsakowski, A. Santagata, M. Dell'Aglio, A. de Giacomo, S. Barcikowski, P. Wagener, and B. Gökce. *Appl. Surf. Sci.*, 403:487–499, **2017**. doi:10.1016/j.apsusc.2017.01.077.

[22] R. Streubel, S. Barcikowski, and B. Gökce. *Opt. Lett.*, 41(7):1486, **2016**. doi:10.1364/OL.41.001486.

[23] R. Streubel, G. Bendt, and B. Gökce. *Nanotechnology*, 27(20):205602, **2016**. doi:10.1088/0957-4484/27/20/205602.

[24] A. V. Kabashin and M. Meunier. *J. Appl. Phys.*, 94(12):7941, **2003**. doi:10.1063/1.1626793.

[25] J.-P. Sylvestre, A. V. Kabashin, E. Sacher, and M. Meunier. *Appl. Phys. A*, 80(4):753–758, **2005**. doi:10.1007/s00339-004-3081-4.

[26] W. T. Nichols, T. Sasaki, and N. Koshizaki. *J. Appl. Phys.*, 100(11):114912, **2006**. doi:10.1063/1.2390641.

[27] S. Ibrahimkutty, P. Wagener, T. dos Santos Rolo, D. Karpov, A. Menzel, T. Baumbach, S. Barcikowski, and A. Plech. *Sci. Rep.*, 5:16313, **2015**. doi:10.1038/srep16313.

[28] A. Letzel, M. Santoro, J. Frohleiks, A. R. Ziefuß, S. Reich, A. Plech, E. Fazio, F. Neri, S. Barcikowski, and B. Gökce. *Appl. Surf. Sci.*, 473:828–837, **2019**. doi:10.1016/j.apsusc.2018.12.025.

[29] M. Sztucki, T. Narayanan, and G. Beaucage. *J. Appl. Phys.*, 101(11):114304, **2007**. doi:10.1063/1.2740341.

[30] S. Ibrahimkutty, P. Wagener, A. Menzel, A. Plech, and S. Barcikowski. *Appl. Phys. Lett.*, 101(10):103104, **2012**. doi:10.1063/1.4750250.

[31] P. Wagener, S. Ibrahimkutty, A. Menzel, A. Plech, and S. Barcikowski. *Phys. Chem. Chem. Phys.*, 15(9):3068–3074, **2013**. doi:10.1039/C2CP42592K.

[32] L. Zhigilei. *Appl. Phys. A*, 76(3):339–350, **2003**. doi:10.1007/s00339-002-1818-5.

[33] C.-Y. Shih, M. V. Shugaev, C. Wu, and L. V. Zhigilei. *J. Phys. Chem. C*, 121(30):16549–16567, **2017**. doi:10.1021/acs.jpcc.7b02301.

[34] X. Chen, J. Schröder, S. Hauschild, S. Rosenfeldt, M. Dulle, and S. Förster. *Langmuir*, 31(42):11678–11691, **2015**. doi:10.1021/acs.langmuir.5b02759.

[35] H. Wen, E. E. Bennett, M. M. Hegedus, and S. Carroll. *IEEE Trans. Med. Imag.*, 27(8):997–1002, **2008**. doi:10.1109/TMI.2007.912393.

[36] Y. Liu, B. Ahr, A. Linkin, G. J. Diebold, and C. Rose-Petruck. *Opt. Lett.*, 36(12):2209, **2011**. doi:10.1364/OL.36.002209.

[37] A. Momose, S. Kawamoto, I. Koyama, and Y. Suzuki. *Proc. SPIE*, 5535:352–360, **2004**. doi:10.1117/12.557572.

[38] T. Weitkamp, A. Diaz, C. David, F. Pfeiffer, M. Stampanoni, P. Cloetens, and E. Ziegler. *Opt. Express*, 13(16):6296–6304, **2005**. doi:10.1364/opex.13.006296.

[39] S. K. Lynch, V. Pai, J. Auxier, A. F. Stein, E. E. Bennett, C. K. Kemble, X. Xiao, W.-K. Lee, N. Y. Morgan, and H. H. Wen. *Appl. Opt.*, 50(22):4310–4319, **2011**. doi:10.1364/ao.50.004310.

[40] F. A. Vittoria, M. Endrizzi, P. C. Diemoz, A. Zamir, U. H. Wagner, C. Rau, I. K. Robinson, and A. Olivo. *Sci. Rep.*, 5:16318, **2015**. doi:10.1038/srep16318.

[41] F. A. Vittoria, G. K. N. Kallon, D. Basta, P. C. Diemoz, I. K. Robinson, A. Olivo, and M. Endrizzi. *Appl. Phys. Lett.*, 106(22):224102, **2015**. doi:10.1063/1.4922189.

[42] S. Petersen and S. Barcikowski. *Adv. Funct. Mater.*, 19(8):1167–1172, **2009**. doi:10.1002/adfm.200801526.

[43] C. L. Sajti, A. Barchanski, P. Wagener, S. Klein, and S. Barcikowski. *J. Phys. Chem. C*, 115(12):5094–5101, **2011**. doi:10.1021/jp1093405.

[44] C. Rehbock, V. Merk, L. Gamrad, R. Streubel, and S. Barcikowski. *Phys. Chem. Chem. Phys.*, 15(9):3057–3067, **2013**. doi:10.1039/c2cp42641b.

[45] A. Letzel. *Size evolution of laser-generated nanoparticles before and after cavitation bubble confinement*. PhD thesis, University of Duisburg-Essen, **2018**.

[46] A. De Giacomo, M. Dell'Aglio, A. Santagata, R. Gaudiuso, O. De Pascale, P. Wagener, G. C. Messina, G. Compagnini, and S. Barcikowski. *Phys. Chem. Chem. Phys.*, 15(9):3083–3092, **2013**. doi:10.1039/c2cp42649h.

[47] S. Kohsakowski, B. Gökce, R. Tanabe, P. Wagener, A. Plech, Y. Ito, and S. Barcikowski. *Phys. Chem. Chem. Phys.*, 18(24):16585–16593, **2016**. doi:10.1039/c6cp01232a.

[48] M. Zakharova, V. Vlnieska, H. Fornasier, M. Börner, T. dos Santos Rolo, J. Mohr, and D. Kunka. *Appl. Sci.*, 8(3):468, **2018**. doi:10.3390/app8030468.

[49] M. Zakharova, S. Reich, A. Mikhaylov, V. Vlnieska, T. dos Santos Rolo, A. Plech, and D. Kunka. *Opt. Lett.*, 44(9):2306, **2019**. doi:10.1364/ol.44.002306.

[50] A. Snigirev, V. Kohn, I. Snigireva, and B. Lengeler. *Nature*, 384(6604):49–51, **1996**. doi:10.1038/384049a0.

[51] B. Lengeler, C. G. Schroer, J. Tümmler, B. Benner, M. Richwin, A. Snigirev, I. Snigireva, and M. Drakopoulos. *J. Synchrotron Rad.*, 6(6):1153–1167, **1999**. doi:10.1107/S0909049599009747.

[52] S. C. Mayo and B. Sexton. *Opt. Lett.*, 29(8):866, **2004**. doi:10.1364/ol.29.000866.

[53] V. P. Nazmov, J. Mohr, H. Vogt, R. Simon, and S. Diabaté. *J. Micromech. Microeng.*, 24(7):075005, **2014**. doi:10.1088/0960-1317/24/7/075005.

[54] A. Snigirev, I. Snigireva, M. Grigoriev, V. Yunkin, M. Di Michiel, S. Kuznetsov, and G. Vaughan. *Proc. SPIE*, 6705:670506, **2007**. doi:10.1117/12.733609.

[55] V. P. Nazmov, J. Mohr, I. Greving, M. Ogurreck, and F. Wilde. *J. Micromech. Microeng.*, 25(5):055010, **2015**. doi:10.1088/0960-1317/25/5/055010.

[56] M. Lyubomirskiy, I. Snigireva, V. Kohn, S. Kuznetsov, V. Yunkin, G. Vaughan, and A. Snigirev. *J. Synchrotron Rad.*, 23(5):1104–1109, **2016**. doi:10.1107/s160057751601153x.

[57] E. Kornemann, O. Márkus, A. Opolka, T. Zhou, I. Greving, M. Storm, C. Krywka, A. Last, and J. Mohr. *Opt. Express*, 25(19):22455–22466, **2017**. doi:10.1364/oe.25.022455.

[58] S. Reich, P. Schönfeld, A. Letzel, S. Kohsakowski, M. Olbinado, B. Gökce, S. Barcikowski, and A. Plech. *ChemPhysChem*, 18(9):1084–1090, **2017**. doi:10.1002/cphc.201601198.

[59] S. Reich, J. Göttlicher, A. Letzel, B. Gökce, S. Barcikowski, T. dos Santos Rolo, T. Baumbach, and A. Plech. *Appl. Phys. A*, 124(1):71, **2018**. doi:10.1007/s00339-017-1503-3.

[60] S. Reich, A. Letzel, B. Gökce, A. Menzel, S. Barcikowski, and A. Plech. *ChemPhysChem*, 20(8):1036–1043, **2019**. doi:10.1002/cphc.201900075.

[61] S. Reich, A. Letzel, A. Menzel, N. Kretzschmar, B. Gökce, S. Barcikowski, and A. Plech. *Nanoscale*, 11(14):6962–6969, **2019**. doi:10.1039/c9nr01203f.

[62] G. M. Hale and M. R. Querry. *Appl. Opt.*, 12(3):555, **1973**. doi:10.1364/ao.12.000555.

[63] W. T. Nichols, T. Sasaki, and N. Koshizaki. *J. Appl. Phys.*, 100(11):114913, **2006**. doi:10.1063/1.2390642.

[64] B. N. Chichkov, C. Momma, S. Nolte, F. von Alvensleben, and A. Tünnermann. *Appl. Phys. A*, 63(2):109–115, **1996**. doi:10.1007/bf01567637.

[65] J. Bonse, S. Baudach, J. Krüger, W. Kautek, and M. Lenzner. *Appl. Phys. A*, 74(1):19–25, **2002**. doi:10.1007/s003390100893.

[66] A. Kanitz, D. J. Förster, J. S. Hoppius, R. Weber, A. Ostendorf, and E. L. Gurevich. *Appl. Surf. Sci.*, 475:204–210, **2019**. doi:10.1016/j.apsusc.2018.12.184.

[67] O. Armbruster, A. Naghilou, M. Kitzler, and W. Kautek. *Appl. Surf. Sci.*, 396:1736–1740, **2017**. doi:10.1016/j.apsusc.2016.11.229.

[68] N. Lasemi, U. Pacher, L. Zhigilei, O. Bomatí-Miguel, R. Lahoz, and W. Kautek. *Appl. Surf. Sci.*, 433:772–779, **2018**. doi:10.1016/j.apsusc.2017.10.082.

[69] A. Y. Vorobyev and C. Guo. *J. Appl. Phys.*, 110(4):043102, **2011**. doi:10.1063/1.3620898.

[70] O. Benavides, L. de la Cruz May, E. B. Mejia, J. A. R. Hernandez, and A. F. Gil. *Laser Phys.*, 26(12):126101, **2016**. doi:10.1088/1054-660x/26/12/126101.

[71] K. Sugioka, M. Meunier, and A. Piqué, editors. *Laser Precision Microfabrication*. Springer Berlin Heidelberg, **2010**. doi:10.1007/978-3-642-10523-4.

[72] W. Demtröder. *Experimentalphysik 2: Elektrizität und Optik*. Springer Berlin Heidelberg, **2017**. doi:10.1007/978-3-662-55790-7.

[73] D. R. Lide, editor. *CRC Handbook of Chemistry and Physics CD-ROM, Version 2010*. CRC Press, **2009**.

[74] C. Momma, B. N. Chichkov, S. Nolte, F. von Alvensleben, A. Tünnermann, H. Welling, and B. Wellegehausen. *Opt. Commun.*, 129(1-2):134–142, **1996**. doi:10.1016/0030-4018(96)00250-7.

[75] L. V. Zhigilei, P. B. S. Kodali, and B. J. Garrison. *J. Phys. Chem. B*, 102(16):2845–2853, **1998**. doi:10.1021/jp9733781.

[76] L. V. Zhigilei, Z. Lin, and D. S. Ivanov. *J. Phys. Chem. C*, 113(27):11892–11906, **2009**. doi:10.1021/jp902294m.

[77] P. Lorazo, L. J. Lewis, and M. Meunier. *Phys. Rev. Lett.*, 91(22):225502, **2003**. doi:10.1103/physrevlett.91.225502.

[78] J. H. Yoo, S. H. Jeong, X. L. Mao, R. Greif, and R. E. Russo. *Appl. Phys. Lett.*, 76(6):783–785, **2000**. doi:10.1063/1.125894.

[79] D. Perez and L. J. Lewis. *Phys. Rev. B*, 67(18):184102, **2003**. doi:10.1103/physrevb.67.184102.

[80] T. Tsuji, Y. Okazaki, Y. Tsuboi, and M. Tsuji. *Japan J. Appl. Phys.*, 46(4R):1533, **2007**. doi:10.1143/JJAP.46.1533.

[81] T. T. P. Nguyen, R. Tanabe-Yamagishi, and Y. Ito. *Appl. Surf. Sci.*, 470:250–258, **2019**. doi:10.1016/j.apsusc.2018.10.160.

[82] R. Russo, X. Mao, H. Liu, J. Yoo, and S. Mao. *Appl. Phys. A*, 69(7):S887–S894, **1999**. doi:10.1007/s003390051553.

[83] S. S. Mao, X. Mao, R. Greif, and R. E. Russo. *Appl. Phys. Lett.*, 77(16):2464–2466, **2000**. doi:10.1063/1.1318239.

[84] R. Fabbro, J. Fournier, P. Ballard, D. Devaux, and J. Virmont. *J. Appl. Phys.*, 68(2):775–784, **1990**. doi:10.1063/1.346783.

[85] A. Vogel, J. Noack, K. Nahen, D. Theisen, S. Busch, U. Parlitz, D. Hammer, G. Noojin, B. Rockwell, and R. Birngruber. *Appl. Phys. B*, 68(2):271–280, **1999**. doi:10.1007/s003400050617.

[86] D. Perez, L. K. Béland, D. Deryng, L. J. Lewis, and M. Meunier. *Phys. Rev. B*, 77(1):014108, **2008**. doi:10.1103/physrevb.77.014108.

[87] T. Sakka, S. Iwanaga, Y. H. Ogata, A. Matsunawa, and T. Takemoto. *J. Chem. Phys.*, 112(19):8645–8653, **2000**. doi:10.1063/1.481465.

[88] T. Sakka, K. Takatani, Y. H. Ogata, and M. Mabuchi. *J. Phys. D: Appl. Phys.*, 35(1):65–73, **2002**. doi:10.1088/0022-3727/35/1/312.

[89] T. Tsuji, D.-H. Thang, Y. Okazaki, M. Nakanishi, Y. Tsuboi, and M. Tsuji. *Appl. Surf. Sci.*, 254(16):5224–5230, **2008**. doi:10.1016/j.apsusc.2008.02.048.

[90] S. Zhu, Y. F. Lu, M. H. Hong, and X. Y. Chen. *J. Appl. Phys.*, 89(4):2400–2403, **2001**. doi:10.1063/1.1342200.

[91] C. L. Sajti, R. Sattari, B. Chichkov, and S. Barcikowski. *Appl. Phys. A*, 100(1):203–206, **2010**. doi:10.1007/s00339-010-5572-9.

[92] M. Dell'Aglio, R. Gaudiuso, O. De Pascale, and A. De Giacomo. *Appl. Surf. Sci.*, 348:4–9, **2015**. doi:10.1016/j.apsusc.2015.01.082.

[93] M. Dell'Aglio, A. Santagata, G. Valenza, A. De Stradis, and A. De Giacomo. *ChemPhysChem*, 18(9):1165–1174, **2017**. doi:10.1002/cphc.201601231.

[94] M. Dell'Aglio, A. De Giacomo, S. Kohsakowski, S. Barcikowski, P. Wagener, and A. Santagata. *J. Phys. D: Appl. Phys.*, 50(18):185204, **2017**. doi:10.1088/1361-6463/aa652a.

[95] A. De Giacomo and J. Hermann. *J. Phys. D: Appl. Phys.*, 50(18):183002, **2017**. doi:10.1088/1361-6463/aa6585.

[96] F. R. Gilmore. *Calif. Inst. Tech. Eng. Rep.*, 26(4):1–40, **1952**.

[97] M. S. Plesset and A. Prosperetti. *Annu. Rev. Fluid Mech.*, 9(1):145–185, **1977**. doi:10.1146/annurev.fl.09.010177.001045.

[98] Shima, A. Shima, and Y. Sato. *Ingenieur-Archiv*, 48(2):85–95, **1979**. doi:10.1007/BF00536833.

[99] M.-R. Kalus, V. Reimer, S. Barcikowski, and B. Gökce. *Appl. Surf. Sci.*, 465:1096–1102, **2019**. doi:10.1016/j.apsusc.2018.09.224.

[100] L. Escobar-Alarcón, J. Iturbe-García, F. González-Zavala, D. Solis-Casados, R. Pérez-Hernández, and E. Haro-Poniatowski. *Int. J. Hydrogen Energy*, 44(3):1579–1585, **2019**. doi:10.1016/j.ijhydene.2018.11.158.

[101] W. Soliman, T. Nakano, N. Takada, and K. Sasaki. *Japan J. Appl. Phys.*, 49(11):116202, **2010**. doi:10.1143/JJAP.49.116202.

[102] K. L. de Graaf, I. Penesis, and P. A. Brandner. Comparison of the Rayleigh - Plesset and Gilmore Equations and Additional Aspects for the Modelling of Seismic Airgun Bubble Dynamics. In: *18th Australasian Fluid Mechanics Conference*, **2012**.

[103] Z. Hu. *Comparison of Gilmore-Akulichev equation and Rayleigh-Plesset equation on therapeutic ultrasound bubble cavitation*. PhD thesis, Iowa State University, **2013**.

[104] M. Koch, C. Lechner, F. Reuter, K. Köhler, R. Mettin, and W. Lauterborn. *Comput. Fluids*, 126:71–90, **2016**. doi:10.1016/j.compfluid.2015.11.008.

[105] M. Jiang, X. Wu, Y. Wei, G. Wilde, and L. Dai. *Extreme Mech. Lett.*, 11:24–29, **2017**. doi:10.1016/j.eml.2016.11.014.

[106] A. Siems, S. A. L. Weber, J. Boneberg, and A. Plech. *New J. Phys.*, 13(4):043018, **2011**. doi:10.1088/1367-2630/13/4/043018.

[107] L. V. Zhigilei, P. B. S. Kodali, and B. J. Garrison. *J. Phys. Chem. B*, 101(11):2028–2037, **1997**. doi:10.1021/jp9634013.

[108] L. V. Zhigilei and B. J. Garrison. *J. Appl. Phys.*, 88(3):1281–1298, **2000**. doi:10.1063/1.373816.

[109] S. Anisimov, B. Kapeliovich, and T. Perel'man. *Zh. Eksp. Teor. Fiz.*, 66(2):375–377, **1974**.

[110] C. Wu, M. S. Christensen, J.-M. Savolainen, P. Balling, and L. V. Zhigilei. *Phys. Rev. B*, 91(3):035413, **2015**. doi:10.1103/physrevb.91.035413.

[111] J.-M. Savolainen, M. S. Christensen, and P. Balling. *Phys. Rev. B*, 84(19):193410, **2011**. doi:10.1103/physrevb.84.193410.

[112] D. S. Ivanov and L. V. Zhigilei. *Phys. Rev. B*, 68(6):064114, **2003**. doi:10.1103/physrevb.68.064114.

[113] E. Leveugle, D. Ivanov, and L. Zhigilei. *Appl. Phys. A*, 79(7):1643–1655, **2004**. doi:10.1007/s00339-004-2682-2.

[114] M. V. Shugaev, C. Wu, O. Armbruster, A. Naghilou, N. Brouwer, D. S. Ivanov, T. J.-Y. Derrien, N. M. Bulgakova, W. Kautek, B. Rethfeld, and L. V. Zhigilei. *MRS Bull.*, 41(12):960–968, **2016**. doi:10.1557/mrs.2016.274.

[115] M. E. Povarnitsyn, V. B. Fokin, P. R. Levashov, and T. E. Itina. *Phys. Rev. B*, 92(17):174104, **2015**. doi:10.1103/physrevb.92.174104.

[116] C.-Y. Shih, C. Wu, M. V. Shugaev, and L. V. Zhigilei. *J. Colloid Interface Sci.*, 489:3 – 17, **2017**. doi:10.1016/j.jcis.2016.10.029.

[117] A. Letzel, B. Gökce, P. Wagener, S. Ibrahimkutty, A. Menzel, A. Plech, and S. Barcikowski. *J. Phys. Chem. C*, 121(9):5356–5365, **2017**. doi:10.1021/acs.jpcc.6b12554.

[118] A. Letzel, B. Gökce, A. Menzel, A. Plech, and S. Barcikowski. *Appl. Surf. Sci.*, 435:743–751, **2018**. doi:10.1016/j.apsusc.2017.11.130.

[119] A. Letzel, S. Reich, T. dos Santos Rolo, A. Kanitz, J. Hoppius, A. Rack, M. P. Olbinado, A. Ostendorf, B. Gökce, A. Plech, and S. Barcikowski. *Langmuir*, 35(8):3038–3047, **2019**. doi:10.1021/acs.langmuir.8b01585.

[120] S. I. Kudryashov, A. A. Nastulyavichus, A. K. Ivanova, N. A. Smirnov, R. A. Khmelnitskiy, A. A. Rudenko, I. N. Saraeva, E. R. Tolordava, A. Y. Kharin, I. N. Zavestovskaya, Y. M. Romanova, D. A. Zayarny, and A. A. Ionin. *Appl. Surf. Sci.*, 470:825–831, **2019**. doi:10.1016/j.apsusc.2018.11.201.

[121] J. Tomko, J. J. Naddeo, R. Jimenez, Y. Tan, M. Steiner, J. M. Fitz-Gerald, D. M. Bubb, and S. M. O'Malley. *Phys. Chem. Chem. Phys.*, 17(25):16327–16333, **2015**. doi:10.1039/C5CP01965F.

[122] A. Matsumoto, A. Tamura, T. Honda, T. Hirota, K. Kobayashi, S. Katakura, N. Nishi, K. Amano, K. Fukami, and T. Sakka. *J. Phys. Chem. C*, 119(47):26506–26511, **2015**. doi:10.1021/acs.jpcc.5b07769.

[123] J. Söderlund, L. B. Kiss, G. A. Niklasson, and C. G. Granqvist. *Phys. Rev. Lett.*, 80(11):2386–2388, **1998**. doi:10.1103/physrevlett.80.2386.

[124] L. B. Kiss, J. Söderlund, G. A. Niklasson, and C. G. Granqvist. *Nanotechnology*, 10(1):25–28, **1999**. doi:10.1088/0957-4484/10/1/006.

[125] W. Soliman, N. Takada, and K. Sasaki. *Appl. Phys. Express*, 3(3):035201, **2010**. doi:10.1143/APEX.3.035201.

[126] D. Zhang, B. Gökce, C. Notthoff, and S. Barcikowski. *Sci. Rep.*, 5:13661, **2015**. doi:10.1038/srep13661.

[127] S. Jendrzej, B. Gökce, V. Amendola, and S. Barcikowski. *J. Colloid Interface Sci.*, 463:299 – 307, **2016**. doi:10.1016/j.jcis.2015.10.032.

[128] V. Merk, C. Rehbock, F. Becker, U. Hagemann, H. Nienhaus, and S. Barcikowski. *Langmuir*, 30(15):4213–4222, **2014**. doi:10.1021/la404556a.

[129] M. Maciulevičius, A. Vinčiūnas, M. Brikas, A. Butsen, N. Tarasenka, N. Tarasenko, and G. Račiukaitis. *Appl. Phys. A*, 111(1):289–295, **2013**. doi:10.1007/s00339-012-7535-9.

[130] A. Schwenke, P. Wagener, S. Nolte, and S. Barcikowski. *Appl. Phys. A*, 104(1):77–82, **2011**. doi:10.1007/s00339-011-6398-9.

[131] F. Mafuné, J. Kohno, Y. Takeda, and T. Kondow. *J. Phys. Chem. B*, 107(18):4218–4223, **2003**. doi:10.1021/jp021580k.

[132] S. I. Kudryashov, I. N. Saraeva, V. N. Lednev, S. M. Pershin, A. A. Rudenko, and A. A. Ionin. *Appl. Phys. Lett.*, 112(20):203101, **2018**. doi:10.1063/1.5026591.

[133] S. Besner, A. V. Kabashin, and M. Meunier. *Appl. Phys. Lett.*, 89(23):233122, **2006**. doi:10.1063/1.2402944.

[134] S. Scaramuzza, S. Agnoli, and V. Amendola. *Phys. Chem. Chem. Phys.*, 17(42):28076–28087, **2015**. doi:10.1039/c5cp00279f.

[135] P. Camarda, L. Vaccaro, F. Messina, and M. Cannas. *Appl. Phys. Lett.*, 107(1):013103, **2015**. doi:10.1063/1.4926571.

[136] P. Camarda, F. Messina, L. Vaccaro, G. Buscarino, S. Agnello, F. M. Gelardi, and M. Cannas. *J. Appl. Phys.*, 120(12):124312, **2016**. doi:10.1063/1.4963720.

[137] D. Segets, J. Gradl, R. K. Taylor, V. Vassilev, and W. Peukert. *ACS Nano*, 3(7):1703–1710, **2009**. doi:10.1021/nn900223b.

[138] B. Gökce, D. D. van't Zand, A. Menéndez-Manjón, and S. Barcikowski. *Chem. Phys. Lett.*, 626:96–101, **2015**. doi:10.1016/j.cplett.2015.03.010.

[139] V. Kotaidis and A. Plech. *Appl. Phys. Lett.*, 87(21):213102, **2005**. doi:10.1063/1.2132086.

[140] R. Tanabe, T. T. P. Nguyen, T. Sugiura, and Y. Ito. *Appl. Surf. Sci.*, 351:327–331, **2015**. doi:10.1016/j.apsusc.2015.05.030.

[141] A. Resano-Garcia, Y. Battie, A. Koch, A. En Naciri, and N. Chaoui. *J. Appl. Phys.*, 117(11):113103, **2015**. doi:10.1063/1.4915277.

[142] A. R. Ziefuß, S. Reichenberger, C. Rehbock, I. Chakraborty, M. Gharib, W. J. Parak, and S. Barcikowski. *J. Phys. Chem. C*, 122(38):22125–22136, **2018**. doi:10.1021/acs.jpcc.8b04374.

[143] G. C. Messina, P. Wagener, R. Streubel, A. De Giacomo, A. Santagata, G. Compagnini, and S. Barcikowski. *Phys. Chem. Chem. Phys.*, 15(9):3093–8, **2013**. doi:10.1039/c2cp42626a.

[144] F. Waag, B. Gökce, and S. Barcikowski. *Appl. Surf. Sci.*, 466:647–656, **2019**. doi:10.1016/j.apsusc.2018.10.030.

[145] A. Menéndez-Manjón, P. Wagener, and S. Barcikowski. *J. Phys. Chem. C*, 115(12):5108–5114, **2011**. doi:10.1021/jp109370q.

[146] J. Als-Nielsen and D. McMorrow. *Elements of Modern X-ray Physics*. John Wiley & Sons, Inc., **2011**. doi:10.1002/9781119998365.

[147] E. C. McCullough. *Med. Phys.*, 2(6):307–320, **1975**. doi:10.1118/1.594199.

[148] A. Sarapata, M. Willner, M. Walter, T. Duttenhofer, K. Kaiser, P. Meyer, C. Braun, A. Fingerle, P. B. Noël, F. Pfeiffer, and J. Herzen. *Opt. Express*, 23(1):523, **2015**. doi:10.1364/oe.23.000523.

[149] R. W. James. *The Optical Principles of the Diffraction of X-rays*. The crystalline state. G. Bell and Sons, London, **1950**.

[150] L. Lavisse, J.-L. Le Garrec, L. Hallo, J.-M. Jouvard, S. Carles, J. Perez, J. B. A. Mitchell, J. Decloux, M. Girault, V. Potin, H. Andrzejewski, M. C. Marco de Lucas, and S. Bourgeois. *Appl. Phys. Lett.*, 100(16):164103, **2012**. doi:10.1063/1.4703930.

[151] S. Gkoumas, P. Villanueva-Perez, Z. Wang, L. Romano, M. Abis, and M. Stampanoni. *Sci. Rep.*, 6:35259, **2016**. doi:10.1038/srep35259.

[152] A. Guinier and G. Fournet. *Small-angle scattering of x-rays*. J. Wiley & Sons, **1955**. doi:10.1063/1.3060069.

[153] G. Porod. *Kolloid-Zeitschrift*, 125(1):51 and 108, **1952**. doi:10.1007/bf01519615.

[154] G. Beaucage. *J. Appl. Crystallogr.*, 28(6):717–728, **1995**. doi:10.1107/S0021889895005292.

[155] G. Beaucage, H. K. Kammler, and S. E. Pratsinis. *J. Appl. Crystallogr.*, 37(4):523–535, **2004**. doi:10.1107/s0021889804008969.

[156] P. Scherrer. Bestimmung der inneren Struktur und der Größe von Kolloidteilchen mittels Röntgenstrahlen. In: *Nachrichten von der Gesellschaft der Wissenschaften zu Göttingen, Mathematisch-Physikalische Klasse*, pages 98–100. **1918**.

[157] B. E. Warren. *X-ray Diffraction*. Courier Corporation, **1990**.

[158] C. David, B. Nöhammer, H. H. Solak, and E. Ziegler. *Appl. Phys. Lett.*, 81(17):3287–3289, **2002**. doi:10.1063/1.1516611.

[159] B. Pauwels, P. Bruyndonckx, X. Liu, A. Tapfer, A. Velroyen, A. Yaroshenko, M. Bech, F. Pfeiffer, and A. Sasov. *Proc. SPIE*, 8506:85060J, **2012**. doi:10.1117/12.929567.

[160] F. Horn, M. Leghissa, S. Kaeppler, G. Pelzer, J. Rieger, M. Seifert, J. Wandner, T. Weber, T. Michel, C. Riess, and G. Anton. *Sci. Rep.*, 8:2325, **2018**. doi:10.1038/s41598-018-19482-z.

[161] M. Kagias, Z. Wang, P. Villanueva-Perez, K. Jefimovs, and M. Stampanoni. *Phys. Rev. Lett.*, 116(9):093902, **2016**. doi:10.1103/physrevlett.116.093902.

[162] M. Zakharova, S. Reich, A. Mikhaylov, V. Vlnieska, M. Zuber, S. Engelhardt, T. Baumbach, and D. Kunka. *Proc. SPIE*, 11032:110320U, **2019**. doi:10.1117/12.2520723.

[163] T. dos Santos Rolo, S. Reich, D. Karpov, S. Gasilov, D. Kunka, E. Fohtung, T. Baumbach, and A. Plech. *Appl. Sci.*, 8(5):737, **2018**. doi:10.3390/app8050737.

[164] U. Bonse and M. Hart. *Appl. Phys. Lett.*, 6(8):155–156, **1965**. doi:10.1063/1.1754212.

[165] P. Cloetens, R. Barrett, J. Baruchel, J.-P. Guigay, and M. Schlenker. *J. Phys. D: Appl. Phys.*, 29(1):133–146, **1996**. doi:10.1088/0022-3727/29/1/023.

[166] S. W. Wilkins, T. E. Gureyev, D. Gao, A. Pogany, and A. W. Stevenson. *Nature*, 384(6607):335–338, **1996**. doi:10.1038/384335a0.

[167] T. J. Davis, D. Gao, T. E. Gureyev, A. W. Stevenson, and S. W. Wilkins. *Nature*, 373(6515):595–598, **1995**. doi:10.1038/373595a0.

[168] A. Olivo and R. Speller. *Appl. Phys. Lett.*, 91(7):074106, **2007**. doi:10.1063/1.2772193.

[169] F. A. Vittoria, M. Endrizzi, P. C. Diemoz, U. H. Wagner, C. Rau, I. K. Robinson, and A. Olivo. *Appl. Phys. Lett.*, 104(13):134102, **2014**. doi:10.1063/1.4870528.

[170] M. Endrizzi, P. C. Diemoz, T. P. Millard, J. Louise Jones, R. D. Speller, I. K. Robinson, and A. Olivo. *Appl. Phys. Lett.*, 104(2):024106, **2014**. doi:10.1063/1.4861855.

[171] F. Krejci, J. Jakubek, and M. Kroupa. *Rev. Sci. Instrum.*, 81(11):113702, **2010**. doi:10.1063/1.3499372.

[172] K. S. Morgan, D. M. Paganin, and K. K. W. Siu. *Appl. Phys. Lett.*, 100(12):124102, **2012**. doi:10.1063/1.3694918.

[173] H. Wang, Y. Kashyap, and K. Sawhney. *Opt. Express*, 23(18):23310, **2015**. doi:10.1364/oe.23.023310.

[174] H. Wang, Y. Kashyap, and K. Sawhney. *Sci. Rep.*, 6:20476, **2016**. doi:10.1038/srep20476.

[175] A. Momose, S. Kawamoto, I. Koyama, Y. Hamaishi, K. Takai, and Y. Suzuki. *Japan J. Appl. Phys.*, 42(Part 2, No. 7B):L866–L868, **2003**. doi:10.1143/jjap.42.l866.

[176] A. Momose, W. Yashiro, H. Maikusa, and Y. Takeda. *Opt. Express*, 17(15):12540, **2009**. doi:10.1364/oe.17.012540.

[177] A. Momose, W. Yashiro, S. Harasse, and H. Kuwabara. *Opt. Express*, 19(9):8423, **2011**. doi:10.1364/oe.19.008423.

[178] S. Bérujon, E. Ziegler, R. Cerbino, and L. Peverini. *Phys. Rev. Lett.*, 108(15):158102, **2012**. doi:10.1103/physrevlett.108.158102.

[179] H. Wang, S. Berujon, J. Herzen, R. Atwood, D. Laundy, A. Hipp, and K. Sawhney. *Sci. Rep.*, 5:8762, **2015**. doi:10.1038/srep08762.

[180] H. Talbot. *Lond. Edinb. Dublin Philos. Mag. J. Sci.*, 9(56):401–407, **1836**. doi:10.1080/14786443608649032.

[181] V. Weinhardt. *3-D imaging based on hard x-ray grating interferometry: theory, development and application*. PhD thesis, Karlsruher Institut für Technologie, **2014**.

[182] F. Pfeiffer, M. Bech, O. Bunk, P. Kraft, E. F. Eikenberry, C. Brönnimann, C. Grünzweig, and C. David. *Nat. Mater.*, 7(2):134–137, **2008**. doi:10.1038/nmat2096.

[183] W. Yashiro, Y. Terui, K. Kawabata, and A. Momose. *Opt. Express*, 18(16):16890–16901, **2010**. doi:10.1364/oe.18.016890.

[184] F. Pfeiffer, T. Weitkamp, O. Bunk, and C. David. *Nat. Phys.*, 2(4):258–261, **2006**. doi:10.1038/nphys265.

[185] E. Lau. *Ann. Phys.*, 437(7-8):417–423, **1948**. doi:10.1002/andp.19484370709.

[186] S. A. McDonald, F. Marone, C. Hintermüller, G. Mikuljan, C. David, F. Pfeiffer, and M. Stampanoni. *J. Synchrotron Rad.*, 16(4):562–572, **2009**. doi:10.1107/S0909049509017920.

[187] J. Hartmann. *Zeitschrift für Instrumentenkunde*, pages 47–58, **1900**.

[188] H. Wen, E. E. Bennett, M. M. Hegedus, and S. Rapacchi. *Radiology*, 251(3):910–918, **2009**. doi:10.1148/radiol.2521081903.

[189] H. H. Wen, E. E. Bennett, R. Kopace, A. F. Stein, and V. Pai. *Opt. Lett.*, 35(12):1932–1934, **2010**. doi:10.1364/OL.35.001932.

[190] K. J. Harmon, E. E. Bennett, A. A. Gomella, and H. Wen. *PLOS ONE*, 9(1):e87127, **2014**. doi:10.1371/journal.pone.0087127.

[191] K. S. Morgan, D. M. Paganin, and K. K. W. Siu. *Opt. Express*, 19(20):19781–19789, **2011**. doi:10.1364/oe.19.019781.

[192] F. Krejci, J. Jakubek, and M. Kroupa. *J. Instrum.*, 6(01):C01073–C01073, **2011**. doi:10.1088/1748-0221/6/01/c01073.

[193] P. Modregger, T. P. Cremona, C. Benarafa, J. C. Schittny, A. Olivo, and M. Endrizzi. *Sci. Rep.*, 6:30940, **2016**. doi:10.1038/srep30940.

[194] F. Prade, A. Yaroshenko, J. Herzen, and F. Pfeiffer. *EPL (Europhys. Lett.)*, 112(6):68002, **2015**. doi:10.1209/0295-5075/112/68002.

[195] M. Strobl. *Sci. Rep.*, 4:7243, **2014**. doi:10.1038/srep07243.

[196] A. Malecki, G. Potdevin, and F. Pfeiffer. *EPL (Europhys. Lett.)*, 99(4):48001, **2012**. doi:10.1209/0295-5075/99/48001.

[197] P. Modregger, M. Kagias, S. C. Irvine, R. Brönnimann, K. Jefimovs, M. Endrizzi, and A. Olivo. *Phys. Rev. Lett.*, 118(26):265501, **2017**. doi:10.1103/physrevlett.118.265501.

[198] T. Koenig, M. Zuber, B. Trimborn, T. Farago, P. Meyer, D. Kunka, F. Albrecht, S. Kreuer, T. Volk, M. Fiederle, and T. Baumbach. *Phys. Med. Biol.*, 61(9):3427–3442, **2016**. doi:10.1088/0031-9155/61/9/3427.

[199] W. Yashiro and A. Momose. *Opt. Express*, 23(7):9233, **2015**. doi:10.1364/oe.23.009233.

[200] J. Wolf, J. I. Sperl, F. Schaff, M. Schüttler, A. Yaroshenko, I. Zanette, J. Herzen, and F. Pfeiffer. *Biomed. Opt. Express*, 6(12):4812, **2015**. doi:10.1364/boe.6.004812.

[201] A. Ritter, P. Bartl, F. Bayer, K. C. Gödel, W. Haas, T. Michel, G. Pelzer, J. Rieger, T. Weber, A. Zang, and G. Anton. *Opt. Express*, 22(19):23276, **2014**. doi:10.1364/oe.22.023276.

[202] Y. Yang and X. Tang. *Med. Phys.*, 39(12):7237–7253, **2012**. doi:10.1118/1.4764901.

[203] G. Pelzer, G. Anton, F. Horn, J. Rieger, A. Ritter, J. Wandner, T. Weber, and T. Michel. *Med. Phys.*, 43(6):2774–2779, **2016**. doi:10.1118/1.4948671.

[204] M. Chabior, T. Donath, C. David, O. Bunk, M. Schuster, C. Schroer, and F. Pfeiffer. *Med. Phys.*, 38(3):1189–1195, **2011**. doi:10.1118/1.3553408.

[205] S. Kaeppler, F. Bayer, T. Weber, A. Maier, G. Anton, J. Hornegger, M. Beckmann, P. A. Fasching, A. Hartmann, F. Heindl, T. Michel, G. Oezguel, G. Pelzer, C. Rauh, J. Rieger, R. Schulz-Wendtland, M. Uder, D. Wachter, E. Wenkel, and C. Riess. *Signal Decomposition for X-ray Dark-Field Imaging*, pages 170–177. Springer International Publishing, **2014**.

[206] A. F. Stein, J. Ilavsky, R. Kopace, E. E. Bennett, and H. Wen. *Opt. Express*, 18(12):13271, **2010**. doi:10.1364/oe.18.013271.

[207] A. Velroyen, M. Bech, A. Malecki, A. Tapfer, A. Yaroshenko, M. Ingrisch, C. C. Cyran, S. D. Auweter, K. Nikolaou, M. Reiser, and F. Pfeiffer. *Phys. Med. Biol.*, 58(4):N37–N46, **2013**. doi:10.1088/0031-9155/58/4/n37.

[208] E. A. Miller, T. A. White, B. S. McDonald, and A. Seifert. *IEEE Trans. Nucl. Sci.*, 60(1):416–422, **2013**. doi:10.1109/tns.2012.2227803.

[209] L. E. Levine and G. G. Long. *J. Appl. Crystallogr.*, 37(5):757–765, **2004**. doi:10.1107/s0021889804016073.

[210] A. Snigirev and I. Snigireva. *C. R. Phys.*, 9(5-6):507–516, **2008**. doi:10.1016/j.crhy.2008.02.003.

[211] P. Kirkpatrick and A. V. Baez. *J. Opt. Soc. Am.*, 38(9):766, **1948**. doi:10.1364/josa.38.000766.

[212] D. R. Kreger. *Recueil des travaux botaniques néerlandais*, 41(3):603–605, **1949**.

[213] A. V. Baez. *J. Opt. Soc. Am.*, 42(10):756, **1952**. doi:10.1364/josa.42.000756.

[214] S. Suehiro, H. Miyaji, and H. Hayashi. *Nature*, 352(6334):385–386, **1991**. doi:10.1038/352385c0.

[215] B. Lengeler, J. Tümmler, A. Snigirev, I. Snigireva, and C. Raven. *J. Appl. Phys.*, 84(11):5855–5861, **1998**. doi:10.1063/1.368899.

[216] S. Gasilov, A. Mittone, T. dos Santos Rolo, S. Polyakov, S. Zholudev, S. Terentyev, V. Blank, A. Bravin, and T. Baumbach. *J. Synchrotron Rad.*, 24(6):1137–1145, **2017**. doi:10.1107/s1600577517012772.

[217] B. Lengeler, C. G. Schroer, M. Kuhlmann, B. Benner, T. F. Günzler, O. Kurapova, F. Zontone, A. Snigirev, and I. Snigireva. *J. Phys. D: Appl. Phys.*, 38(10A):A218–A222, **2005**. doi:10.1088/0022-3727/38/10A/042.

[218] A. Mikhaylov, S. Reich, A. Plech, M. Zakharova, V. Vlnieska, and D. Kunka. *Proc. SPIE*, 11032:1103208, **2019**. doi:10.1117/12.2520687.

[219] A. Snigirev, V. Kohn, I. Snigireva, A. Souvorov, and B. Lengeler. *Appl. Opt.*, 37(4):653, **1998**. doi:10.1364/ao.37.000653.

[220] V. Nazmov, E. Reznikova, A. Snigirev, I. Snigireva, M. DiMichiel, M. Grigoriev, J. Mohr, B. Matthis, and V. Saile. *Microsyst. Technol.*, 11(4-5):292–297, **2005**. doi:10.1007/s00542-004-0435-y.

[221] U. T. Sanli, H. Ceylan, I. Bykova, M. Weigand, M. Sitti, G. Schütz, and K. Keskinbora. *Adv. Mater.*, 30(36):1802503, **2018**. doi:10.1002/adma.201802503.

[222] H. R. Beguiristain, J. T. Cremer, M. A. Piestrup, R. H. Pantell, C. K. Gary, and J. Feinstein. *Proc. SPIE*, 4144:155–164, **2000**. doi:10.1117/12.405889.

[223] C. G. Schroer and B. Lengeler. *Phys. Rev. Lett.*, 94(5):054802, **2005**. doi:10.1103/PhysRevLett.94.054802.

[224] J. Patommel, S. Klare, R. Hoppe, S. Ritter, D. Samberg, F. Wittwer, A. Jahn, K. Richter, C. Wenzel, J. W. Bartha, M. Scholz, F. Seiboth, U. Boesenberg, G. Falkenberg, and C. G. Schroer. *Appl. Phys. Lett.*, 110(10):101103, **2017**. doi:10.1063/1.4977882.

[225] R. H. Pantell, J. Feinstein, H. R. Beguiristain, M. A. Piestrup, C. K. Gary, and J. T. Cremer. *Rev. Sci. Instrum.*, 72(1):48, **2001**. doi:10.1063/1.1331326.

[226] M. A. Piestrup. X-RAY AND NEUTRON IMAGING. Patent: US 2003/0081724 A1, **2003**.

[227] M. A. Piestrup. *Rev. Sci. Instrum.*, 75(11):4769, **2004**. doi:10.1063/1.1809286.

[228] R. Shack and B. Platt. *J. Opt. Soc. Am.*, 61:656, **1971**. doi:10.1364/JOSA.61.000648.

[229] A. Opolka, S. Reich, E. Kornemann, K. Sawhney, A. Cecilia, J. Mohr, and A. Last. Compound Refractive X-ray Lenses made out of SU-8 as Shack-Hartmann wavefront sensor. In preparation.

[230] B. D. Patterson. *Am. J. Phys*, 79(10):1046–1052, **2011**. doi:10.1119/1.3614033.

[231] B. L. Henke, E. M. Gullikson, and J. C. Davis. Bend Magnet Spectrum. `http://henke.lbl.gov/optical_constants/bend2.html`, 2018-09-04.

[232] B. L. Henke, E. M. Gullikson, and J. C. Davis. *Atomic Data and Nuclear Data Tables*, 54(2), **1993**.

[233] J. A. Golovchenko, R. A. Levesque, and P. L. Cowan. *Rev. Sci. Instrum.*, 52(4):509–516, **1981**. doi:10.1063/1.1136631.

[234] P. Deschamps, P. Engström, S. Fiedler, C. Riekel, S. Wakatsuki, P. Høghøj, and E. Ziegler. *J. Synchrotron Rad.*, 2(3):124–131, **1995**. doi:10.1107/s0909049595001592.

[235] A. Hexemer, W. Bras, J. Glossinger, E. Schaible, E. Gann, R. Kirian, A. MacDowell, M. Church, B. Rude, and H. Padmore. *J. Phys. Conf. Ser.*, 247:012007, **2010**. doi:10.1088/1742-6596/247/1/012007.

[236] E. J. Peterman, F. Gittes, and C. F. Schmidt. *Biophys. J.*, 84(2):1308–1316, **2003**. doi:10.1016/s0006-3495(03)74946-7.

[237] E. E. Bennett, R. Kopace, A. F. Stein, and H. Wen. *Med. Phys.*, 37(11):6047–6054, **2010**. doi:10.1118/1.3501311.

[238] S. Reich, T. dos Santos Rolo, A. Letzel, T. Baumbach, and A. Plech. *Appl. Phys. Lett.*, 112(15):151903, **2018**. doi:10.1063/1.5022748.

[239] F. M. Schunk, D. Rand, and C. Rose-Petruck. *Phys. Chem. Chem. Phys.*, 17(46):31237–31246, **2015**. doi:10.1039/c5cp04508h.

[240] P. Brůža, D. Pánek, M. Vrbová, V. Fidler, and C. Rose-Petruck. *Appl. Phys. Lett.*, 104(25):254101, **2014**. doi:10.1063/1.4884935.

[241] D. Rand, E. G. Walsh, Z. Derdak, J. R. Wands, and C. Rose-Petruck. *Phys. Med. Biol.*, 60(2):769–784, **2015**. doi:10.1088/0031-9155/60/2/769.

[242] S. Wiebe, N. Samadi, G. Belev, M. Martinson, B. Bassey, and D. Chapman. *IEEE Trans. Nucl. Sci.*, 62(5):2031–2035, **2015**. doi:10.1109/tns.2015.2470555.

[243] M.-K. Hu. *IEEE Trans. Inf. Theory*, 8(2):179–187, **1962**. doi:10.1109/tit.1962.1057692.

[244] J. K. Patel and C. B. Read. *Handbook of the normal distribution*, volume 150 of *Statistics*. Dekker, New York [u.a.], 2. ed., rev. and expanded edition, **1996**.

[245] R. B. Blackman and J. W. Tukey. *Bell Syst. Tech. J.*, 37(1):185–282, **1958**. doi:10.1002/j.1538-7305.1958.tb03874.x.

[246] B. C. Platt and R. Shack. *J. Refract. Surg.*, 17(5):S573–S577, **2001**. doi:10.3928/1081-597x-20010901-13.

[247] B. Pathak and B. R. Boruah. *J. Opt.*, 16(5):055403, **2014**. doi:10.1088/2040-8978/16/5/055403.

[248] W. Southwell. *J. Opt. Soc. Am.*, 70(8):998, **1980**. doi:10.1364/josa.70.000998.

[249] S. Reich and A. Plech. Shack-Hartman sensor wavefront reconstruction software, **2018**. doi:10.5445/ir/1000082060.

[250] H. R. Beguiristain. Development of Compound Refractive Lenses for x-rays. In: *AIP Conference Proceedings*. AIP, **2000**. doi:10.1063/1.1291797.

[251] M. Piestrup, H. Beguiristain, C. Gary, J. Cremer, R. Pantell, and R. Tatchyn. *Nucl. Instrum. Methods Phys. Res., Sect. B*, 173(1-2):170–177, **2001**. doi:10.1016/s0168-583x(00)00244-5.

[252] J. Megusar. *J. Nucl. Mater.*, 245(2-3):185–190, **1997**. doi:10.1016/s0022-3115(97)00012-3.

[253] B. Lengeler, C. G. Schroer, M. Richwin, J. Tümmler, M. Drakopoulos, A. Snigirev, and I. Snigireva. *Appl. Phys. Lett.*, 74(26):3924–3926, **1999**. doi:10.1063/1.124225.

[254] M. Lyubomirskiy, F. Koch, K. A. Abrashitova, V. O. Bessonov, N. Kokareva, A. Petrov, F. Seiboth, F. Wittwer, M. Kahnt, M. Seyrich, A. A. Fedyanin, C. David, and C. G. Schroer. *Opt. Express*, 27(6):8639, **2019**. doi:10.1364/oe.27.008639.

[255] M. Wulff, A. Plech, L. Eybert, R. Randler, F. Schotte, and P. Anfinrud. *Faraday Discuss.*, 122:13–26, **2002**. doi:10.1039/b202740m.

[256] G. Cristoforetti, E. Pitzalis, R. Spiniello, R. Ishak, and M. Muniz-Miranda. *J. Phys. Chem. C*, 115(12):5073–5083, **2010**. doi:10.1021/jp109281q.

[257] P. Šmejkal, J. Pfleger, B. Vlčková, and O. Dammer. *J. Phys. Conf. Ser.*, 59:185–188, **2007**. doi:10.1088/1742-6596/59/1/040.

[258] A. Plech, V. Kotaidis, S. Grésillon, C. Dahmen, and G. von Plessen. *Phys. Rev. B*, 70(19):195423, **2004**. doi:10.1103/physrevb.70.195423.

[259] A. Y. Vorobyev and C. Guo. *Phys. Rev. B*, 72(19):195422, **2005**. doi:10.1103/physrevb.72.195422.

[260] P. Mannion, J. Magee, E. Coyne, G. O'Connor, and T. Glynn. *Appl. Surf. Sci.*, 233(1-4):275–287, **2004**. doi:10.1016/j.apsusc.2004.03.229.

[261] A. Naghilou, O. Armbruster, M. Kitzler, and W. Kautek. *J. Phys. Chem. C*, 119(40):22992–22998, **2015**. doi:10.1021/acs.jpcc.5b07109.

[262] M. A. Green. *Sol. Energy Mater. Sol. Cells*, 92(11):1305–1310, **2008**. doi:10.1016/j.solmat.2008.06.009.

[263] D. Issenmann, S. Eon, H. Bracht, M. Hettich, T. Dekorsy, G. Buth, R. Steininger, T. Baumbach, J. L. Hansen, A. N. Larsen, J. W. Ager, E. E. Haller, and A. Plech. *Phys. Status Solidi A*, 213(3):541–548, **2016**. doi:10.1002/pssa.201532462.

[264] C. S. Nathala, A. Ajami, A. A. Ionin, S. I. Kudryashov, S. V. Makarov, T. Ganz, A. Assion, and W. Husinsky. *Opt. Express*, 23(5):5915, **2015**. doi:10.1364/oe.23.005915.

[265] S. Gräf and F. A. Müller. *Appl. Surf. Sci.*, 331:150–155, **2015**. doi:10.1016/j.apsusc.2015.01.056.

[266] B. R. Pauw, J. S. Pedersen, S. Tardif, M. Takata, and B. B. Iversen. *J. Appl. Crystallogr.*, 46(2):365–371, **2013**. doi:10.1107/s0021889813001295.

[267] G. Marzun, J. Nakamura, X. Zhang, S. Barcikowski, and P. Wagener. *Appl. Surf. Sci.*, 348:75–84, **2015**. doi:10.1016/j.apsusc.2015.01.108.

[268] M. Fischer, J. Hormes, G. Marzun, P. Wagener, U. Hagemann, and S. Barcikowski. *Langmuir*, 32(35):8793–8802, **2016**. doi:10.1021/acs.langmuir.6b00685.

[269] A. De Giacomo, M. Dell'Aglio, F. Colao, and R. Fantoni. *Spectrochim. Acta, Part B*, 59(9):1431–1438, **2004**. doi:10.1016/j.sab.2004.07.002.

[270] Y. Takeda, F. Mafuné, and T. Kondow. *J. Phys. Chem. C*, 113(13):5027–5030, **2009**. doi:10.1021/jp809438d.

[271] S. Besner, A. V. Kabashin, F. M. Winnik, and M. Meunier. *J. Phys. Chem. C*, 113(22):9526–9531, **2009**. doi:10.1021/jp809275v.

[272] P. Abdulkin, T. L. Precht, B. R. Knappett, H. E. Skelton, D. A. Jefferson, and A. E. H. Wheatley. *Part. Part. Syst. Charact.*, 31(5):571–579, **2013**. doi:10.1002/ppsc.201300227.

[273] O. J. Kio, J. Yuan, A. J. Brooks, G. L. Knapp, K. Ham, J. Ge, D. V. Loo, and L. G. Butler. *Addit. Manuf.*, 24:364–372, **2018**. doi:10.1016/j.addma.2018.04.014.

A Publications

Publications in reviewed journals

Published:

- **S. Reich**, P. Schönfeld, P. Wagener, A. Letzel, S. Ibrahimkutty, B. Gökce, S. Barcikowski, A. Menzel, T. dos Santos Rolo, and A. Plech. Pulsed laser ablation in liquids: Impact of the bubble dynamics on particle formation. *J. Colloid Interface Sci.*, 489:106–113, **2017**. doi:10.1016/j.jcis.2016.08.030.
- **S. Reich**, P. Schönfeld, A. Letzel, S. Kohsakowski, M. Olbinado, B. Gökce, S. Barcikowski, and A. Plech. Fluence Threshold Behaviour on Ablation and Bubble Formation in Pulsed Laser Ablation in Liquids. *ChemPhysChem*, 18(9):1084–1090, **2017**. doi:10.1002/cphc.201601198.
- A. Plech, S. Ibrahimkutty, **S. Reich**, and G. Newby. Thermal dynamics of pulsed-laser excited gold nanorods in suspension. *Nanoscale*, 9(44):17284–17292, **2017**. doi:10.1039/c7nr06125k.
- **S. Reich**, J. Göttlicher, A. Letzel, B. Gökce, S. Barcikowski, T. dos Santos Rolo, T. Baumbach, and A. Plech. X-ray spectroscopic and stroboscopic analysis of pulsed-laser ablation of Zn and its oxidation. *Appl. Phys. A*, 124(1):71, **2018**. doi:10.1007/s00339-017-1503-3.
- **S. Reich**, T. dos Santos Rolo, A. Letzel, T. Baumbach, and A. Plech. Scalable, large area compound array refractive lens for hard x-rays. *Appl. Phys. Lett.*, 112(15):151903, **2018**. doi:10.1063/1.5022748.
- T. dos Santos Rolo, **S. Reich**, D. Karpov, S. Gasilov, D. Kunka, E. Fohtung, T. Baumbach, and A. Plech. A Shack-Hartmann sensor for single-shot multi-contrast imaging with hard X-rays. *Appl. Sci.*, 8(5):737, **2018**. doi:10.3390/app8050737.
- A. Letzel, M. Santoro, J. Frohleiks, A. Ziefuß, **S. Reich**, A. Plech, E. Fazio, F. Neri, S. Barcikowski, and B. Gökce. How the re-irradiation of a single ablation spot affects cavitation bubble dynamics and nanoparticles properties in laser ablation in liquids. *Appl. Surf. Sci.*, 473:828–837, **2019**. doi:10.1016/j.apsusc.2018.12.025.
- A. Letzel, **S. Reich**, T. dos Santos Rolo, A. Kanitz, J. S. Hoppius, A. Rack, M. Olbinado, A. Ostendorf, B. Gökce, A. Plech, and S. Barcikowski. Time and Mechanism of Nanoparticle Functionalization by Macromolecular Ligands during Pulsed Laser Ablation in Liquids. *Langmuir*, 35(8):3038–3047, **2019**. doi:10.1021/acs.langmuir.8b01585.
- **S. Reich**, A. Letzel, B. Gökce, A. Menzel, S. Barcikowski, and A. Plech. Incubation Effect of Pre-Irradiation on Bubble Formation and Ablation in Laser Ablation in Liquids. *ChemPhysChem*, 20(8):1036–1043, **2019**. doi:10.1002/cphc.201900075.

- **S. Reich**, A. Letzel, A. Menzel, N. Kretzschmar, B. Gökce, S. Barcikowski, and A. Plech. Early nanoparticle genesis and size manifestation during pulsed laser ablation in liquids dynamics. *Nanoscale*, 11(14):6962–6969, **2019**. doi:10.1039/c9nr01203f.
- M. Zakharova, **S. Reich**, A. Mikhaylov, V. Vlnieska, T. dos Santos Rolo, A. Plech, and D. Kunka. Inverted Hartmann mask for single-shot phase-contrast x-ray imaging of dynamic processes. *Opt. Lett.*, 44(9):2306, **2019**. doi:10.1364/ol.44.002306.
- M. Zakharova, **S. Reich**, A. Mikhaylov, V. Vlnieska, M. Zuber, S. Engelhardt, T. Baumbach, and D. Kunka. A comparison of customized Hartmann and newly introduced inverted Hartmann masks for single-shot phase-contrast X-ray imaging. *Proc. SPIE*, 11032:110320U, **2019**. doi:10.1117/12.2520723.
- A. Mikhaylov, **S. Reich**, A. Plech, M. Zakharova, V. Vlnieska, and D. Kunka. 2D lens array for multi-contrast X-ray imaging. *Proc. SPIE*, 11032:1103208, **2019**. doi:10.1117/12.2520687.

In preparation:

- A. Plech, A. Ziefuß, **S. Reich**, C. Rehbock, M. Levantino, and S. Barcikowski. Structural kinetics of picosecond laser fragmentation of suspended gold spheres.
- A. Opolka, **S. Reich**, E. Kornemann, K. Sawhney, A. Cecilia, J. Mohr, and A. Last. Compound Refractive X-ray Lenses made out of SU-8 as Shack-Hartmann wavefront sensor.

Software

- **S. Reich**, and A. Plech. Shack-Hartman sensor wavefront reconstruction software. *Karlsruhe Institute of Technology*. 2018. doi:10.5445/ir/1000082060.

Oral presentation at international conferences

- **S. Reich**, A. Letzel, T. dos Santos Rolo, B. Gökce, S. Barcikowski, T. Baumbach, M. Olbinado, and A. Plech. Fast multi-contrast imaging of the ablation process in liquids adding X-ray bright-field and dark-field methods. *Advanced Nanoparticle Generation & Excitation by Lasers in Liquids (ANGEL) 2018*, Lyon, 9. - 7. June 2018.

Poster presentation at international conferences

- **S. Reich**, S. Ibrahimkutty, A. Letzel, T. dos Santos Rolo, T. Baumbach, A. Menzel, M. Olbinado, J. Göttlicher, B. Gökce, S. Barcikowski, and A. Plech. Adding new information on pulsed laser ablation in liquids (PLAL) by fast X-Ray diagnostics. *International Conference on Laser Ablation (COLA) 2017*, Marseille, 3. - 8. September 2017.

B Source Code

B.1 2D Gaussian fitting and image moment

```
"""
Fit of a 2D Gaussian function to data. Gauss must be in positive direction, but data
    can be in negative region. Fit of one Gauss or of an array of Gauss is possible.
    Also only the pure image moments can be calculated.

gaussfit of one gauss:
 gaussfit.fitgaussian()
  Input: array of data
  Return: list of 6 parameters: height, center_axis=0, center_axis=1, width_axis=0,
      width_axis=1, offset

gaussfit of multiple gauss:
 gaussfit.fitmultigaussian()
  Input: array of data
   crop
   nr of spots
   filtering size (optional, default=None)
  Return: array of gaussfits with of parameters

image moments:
 moment_skimage()
  Input: array of data
  Return: list of 5 parameters: height, center_axis=0, center_axis=1, width_axis=0,
      width_axis=1
"""

import numpy as np
from scipy import optimize
from scipy.ndimage.filters import median_filter
from skimage import measure

__version__ = 'V10_2018.11.29'

######################################################################
def gaussian(height, center_0, center_1, width_0, width_1, offset):
  """Returns a gaussian function with the given parameters"""
```

```
  height = float(height)
  center_0 = float(center_0)
  center_1 = float(center_1)
  width_0 = float(width_0)
  width_1 = float(width_1)
  offset = float(offset)
  return lambda ax0, ax1 : height* np.exp(-(((center_0-ax0) / width_0)**2 +
      ((center_1-ax1) / width_1)**2)/2) + offset

##############################################################################
def moment_skimage(data): #calculate image moments for analysis
  """Returns (height, center_axis=0, center_axis=1, width_axis=0, width_axis=1) the
      moment parameters of an image by calculating its moments"""
  height = np.sum(data)
 #calculate image moments for center and width
  M = measure.moments(data, order=2)
 #center in axis=0 and axis=1
  center_0 = M[1,0]/M[0,0]
  center_1 = M[0,1]/M[0,0]
 #width in axis=0 and axis=1
  width_0 = np.sqrt(M[2,0]/M[0,0] - center_0**2)
  width_1 = np.sqrt(M[0,2]/M[0,0] - center_1**2)

  return height, center_0, center_1, width_0, width_1

#####################################################################
def moment(data):  #initial guess of parameters
  """Returns (height, center_axis=0, center_axis=1, width_axis=0, width_axis=1,
      offset) the gaussian parameters of a 2D distribution by calculating its
      moments"""
 #filter data by median to obtain better guessed parameters, especially for height
     and offset
  data = median_filter(data, size=3)
 #guess offset
  offset = np.average((data[0,0], data[0,data.shape[1]-1], data[data.shape[0]-1,0],
      data[data.shape[0]-1,data.shape[1]-1]))
 #guess hight
  height = data.max() - offset
 #remove offset with min() to still have positive numbers
  data -= np.min(data)
 #calculate image moments for center and width guess
  M = measure.moments(data, order=2)
 #guess center in axis=0 and axis=1
  center_0 = M[1,0]/M[0,0]
  center_1 = M[0,1]/M[0,0]
 #guess width in axis=0 and axis=1
  width_0 = np.sqrt(M[2,0]/M[0,0] - center_0**2)
```

```
  width_1 = np.sqrt(M[0,2]/M[0,0] - center_1**2)

  return height, center_0, center_1, width_0, width_1, offset

##################################################################
def fitgaussian(data):
  """Returns (height, center_axis=0, center_axis=1, width_axis=0, width_axis=1,
      offset) the gaussian parameters of a 2D distribution found by a fit"""
 #find initial guess of parameters
  params = moment(data)
 #generate errorfunction for optimisation
  errorfunction = lambda p: np.ravel(gaussian(*p)(*np.indices(data.shape)) - data)
 #optimize fit by leastsquare
  p, success = optimize.leastsq(errorfunction, params)
 #abs of widths to ensure positive values; important for small peaksizes
  p[3] = np.abs(p[3])
  p[4] = np.abs(p[4])

  return p   #height, center_axis=0, center_axis=1, width_axis=0, width_axis=1, offset

##################################################################
def fitmultigaussian(data, crop, spots, filtering=None):
  """Returns 6 global and two local parameters of gaussian fit of several
      2D-distributed gaussians optional filtering for initial guess, but only symetric
      filterdimension supported
  Input:
   data = array of values of whole area, where the gaussians are located rectangular
       and are equally distributed
   crop = crop around all gaussians:
    0: rowoffset
    1: columoffset
    2: nr of rows
    3: nr of colums
   spots = number of gaussians in:
    0: axis=0
    1: axis=1
   filtering = size of filter, optional
  Output:
   array of parameters:
    0: global center_axis=0
    1: glogal center_axis=1
    2: height
    3: local center_axis=0
    4: local center_axis=1
    5: width_axis=0
    6: width_axis=1
    7: offset
```

```
 """

 spots_row = spots[0]  #gausspeaks in rows
 spots_col = spots[1]  #gausspeaks in colums

 spotrowsize = float(crop[2]) / spots_row #rowsize of one gauss
 spotcolsize = float(crop[3]) / spots_col #columsize of one gauss

#medianfilter on data for maxpointdetection to avoid wrong detection of single
    bright spots
 if filtering != None:
  data_max = median_filter(data, size=filtering)
 else:
  data_max = data

#coordinates of point witch max of peaks; array compared to pic, downward, rigthward
 maxpoints = np.zeros((spots_row, spots_col, 2), dtype=int) #nr. spot down, nr. spot
     right, center_row, center_col
#array of spots, row of gausspeak, column of gaussspeak, hight, center_x, center_y,
    width_x, width_y
 gaussparameters = np.zeros((spots_row, spots_col, 8), dtype=np.float32)

 for i in range(spots_row): #i over rows downward
  for j in range(spots_col): #j over colums rightward
   #coordinates of crop for maxdetection
    startrow = crop[0] + int(i*spotrowsize)
    endrow = startrow + int(spotrowsize)
    startcol = crop[1] + int(j*spotcolsize)
    endcol = startcol + int(spotcolsize)
   #relative position of max in crop
    localmax = np.unravel_index( np.argmax( data_max[ startrow: endrow, startcol:
        endcol]), (int(spotrowsize), int(spotcolsize)))
   #save global position of max
    maxpoints[i,j,0] = localmax[0] + startrow
    maxpoints[i,j,1] = localmax[1] + startcol
   #crop arround max, fit gauss and save data
    peak = data[maxpoints[i,j,0] - int(spotrowsize/2): maxpoints[i,j,0] +
        int((spotrowsize+1)/2), maxpoints[i,j,1] - int(spotcolsize/2):
        maxpoints[i,j,1] + int((spotcolsize+1)/2)]
    gaussparameters[i,j,2:] = fitgaussian(peak)
    gaussparameters[i,j,0] = maxpoints[i,j,0] - int(spotrowsize/2) +
        gaussparameters[i,j,3] #row = center_y
    gaussparameters[i,j,1] = maxpoints[i,j,1] - int(spotcolsize/2) +
        gaussparameters[i,j,4] #col = center_x

 return gaussparameters.reshape(spots_row, spots_col, 8)
```

B.2 Fourier-analysis

```
"""
Fourier analysis of datasets
- FFT of pic
- crop of different regions of orders up to 4th
 - transmission (|0. order|), phase (angle(i. order)), diff (|i. order|)
 - 1. order: phase10, phase01, phase11, diff-10, diff10, diff01, diff11
 - 2. order: phase20, phase21, phase02, phase12, phase22, diff20, diff21, diff02,
     diff12, diff22
 - 3. order: phase30, phase03, phase33, diff30, diff03, diff33
 - 4. order: phase40, phase04, phase44, diff40, diff04, diff44
 - diffraction is uncorrected, must be done afterwords: -log((diff_radio/diff_flat) /
     (abs_radio/abs_flat))
 -! no flatcorrection !
"""

import numpy as np

__version__ = 'V2.2_2017.05.17'

#####################################################################
# RECONSTRUCT PICS
def reconstruct(data, FFT_shape, order): #data= cropped image, FFT_shape=number of
    beamlets in crop, order of FFT analysis
 #positions in data and FFT
  nr, nc = data.shape  #data size
  cr, cc = int(nr / 2), int(nc / 2) #half data size --> centre of image
  zr, zc = FFT_shape , FFT_shape #size of one fft zone
  zhr, zhc = int(FFT_shape / 2), int(FFT_shape / 2) #half size of fft zone

 #real space window to flatten edges
  rsw = np.hanning(data.shape[0]) * (np.ones(data.shape) *
      np.hanning(data.shape[1])).T
 #compute sfs (2D fourier transform the mesh image)
  imgfft = np.fft.fft2(data * rsw)
 #bring the zero frequency to the center (for display)
  imgfft_shifted = np.fft.fftshift(imgfft)

#harmonics labelling: ij corresponds to ith horizontal and jth vertical harmonic
#00 HARMONIC
 #extract 00 harmonic of fft
  fft_00 = imgfft_shifted[cr - zhr:cr + zhr, cc - zhc:cc + zhc]
 #zone hanning-window
  fftw = np.hanning(fft_00.shape[0]) * (np.ones(fft_00.shape) *
      np.hanning(fft_00.shape[1])).T
 #prepare 00 haronic for inverse fft
```

```
 fft_00_shifted = np.fft.fftshift(fft_00 * fftw)
#inverse Fourier transform 00 harmonic
 ifft_00 = np.fft.ifft2(fft_00_shifted)

 if order >= 1:
#-10 HARMONIC
  fft_m10 = imgfft_shifted[cr - zhr:cr + zhr, cc - zc - zhc:cc - zc + zhc]
  fft_m10_shifted = np.fft.fftshift(fft_m10 * fftw)
  ifft_m10 = np.fft.ifft2(fft_m10_shifted)
#10 HARMONIC
  fft_10 = imgfft_shifted[cr - zhr:cr + zhr, cc + zc - zhc:cc + zc + zhc]
  fft_10_shifted = np.fft.fftshift(fft_10 * fftw)
  ifft_10 = np.fft.ifft2(fft_10_shifted)
#01 HARMONIC
  fft_01 = imgfft_shifted[cr - zr - zhr:cr - zr + zhr, cc - zhc:cc + zhc]
  fft_01_shifted = np.fft.fftshift(fft_01 * fftw)
  ifft_01 = np.fft.ifft2(fft_01_shifted)
#11 HARMONIC
  fft_11 = imgfft_shifted[cr - zr - zhr:cr - zr + zhr, cc + zc - zhc:cc + zc + zhc]
  fft_11_shifted = np.fft.fftshift(fft_11 * fftw)
  ifft_11 = np.fft.ifft2(fft_11_shifted)

 if order >= 2:
#20 HARMONIC
  fft_20 = imgfft_shifted[cr - zhr:cr + zhr, cc + 2*zc - zhc:cc + 2*zc + zhc]
  fft_20_shifted = np.fft.fftshift(fft_20 * fftw)
  ifft_20 = np.fft.ifft2(fft_20_shifted)
#21 HARMONIC
  fft_21 = imgfft_shifted[cr - zr - zhr:cr - zr + zhr, cc + 2*zc - zhc:cc + 2*zc +
      zhc]
  fft_21_shifted = np.fft.fftshift(fft_21 * fftw)
  ifft_21 = np.fft.ifft2(fft_21_shifted)
#02 HARMONIC
  fft_02 = imgfft_shifted[cr - 2*zr -zhr:cr - 2*zr + zhr, cc - zhc:cc + zhc]
  fft_02_shifted = np.fft.fftshift(fft_02 * fftw)
  ifft_02 = np.fft.ifft2(fft_02_shifted)
#12 HARMONIC
  fft_12 = imgfft_shifted[cr - 2*zr - zhr:cr - 2*zr + zhr, cc + zc - zhc:cc + zc +
      zhc]
  fft_12_shifted = np.fft.fftshift(fft_12 * fftw)
  ifft_12 = np.fft.ifft2(fft_12_shifted)
#22 HARMONIC
  fft_22 = imgfft_shifted[cr - 2*zr - zhr:cr - 2*zr + zhr, cc + 2*zc - zhc:cc + 2*zc
      + zhc]
  fft_22_shifted = np.fft.fftshift(fft_22 * fftw)
  ifft_22 = np.fft.ifft2(fft_22_shifted)
```

```
 if order >= 3:
#30 HARMONIC
  fft_30 = imgfft_shifted[cr - zhr:cr + zhr, cc + 3*zc - zhc:cc + 3*zc + zhc]
  fft_30_shifted = np.fft.fftshift(fft_30 * fftw)
  ifft_30 = np.fft.ifft2(fft_30_shifted)
#03 HARMONIC
  fft_03 = imgfft_shifted[cr - 3*zr -zhr:cr - 3*zr + zhr, cc - zhc:cc + zhc]
  fft_03_shifted = np.fft.fftshift(fft_03 * fftw)
  ifft_03 = np.fft.ifft2(fft_03_shifted)
#33 HARMONIC
  fft_33 = imgfft_shifted[cr - 3*zr - zhr:cr - 3*zr + zhr, cc + 3*zc - zhc:cc + 3*zc
      + zhc]
  fft_33_shifted = np.fft.fftshift(fft_33 * fftw)
  ifft_33 = np.fft.ifft2(fft_33_shifted)

 if order >= 4:
#40 HARMONIC
  fft_40 = imgfft_shifted[cr - zhr:cr + zhr, cc + 4*zc - zhc:cc + 4*zc + zhc]
  fft_40_shifted = np.fft.fftshift(fft_40 * fftw)
  ifft_40 = np.fft.ifft2(fft_40_shifted)
#04 HARMONIC
  fft_04 = imgfft_shifted[cr - 4*zr -zhr:cr - 4*zr + zhr, cc - zhc:cc + zhc]
  fft_04_shifted = np.fft.fftshift(fft_04 * fftw)
  ifft_04 = np.fft.ifft2(fft_04_shifted)
#44 HARMONIC
  fft_44 = imgfft_shifted[cr - 4*zr - zhr:cr - 4*zr + zhr, cc + 4*zc - zhc:cc + 4*zc
      + zhc]
  fft_44_shifted = np.fft.fftshift(fft_44 * fftw)
  ifft_44 = np.fft.ifft2(fft_44_shifted)

#Reconstruct
 # reconstruct absorption: real and positiv
  absorption = np.abs(ifft_00)
 if order >= 1:
 # reconstruct phase: angle of iFFT
  phase_10 = np.angle(ifft_10)
  phase_01 = np.angle(ifft_01)
  phase_11 = np.angle(ifft_11)
 # reconstruct diffraction: -log(|iFFT xx|/|iFFT 00|) done external
  diff_m10 = np.abs(ifft_m10)
  diff_10 = np.abs(ifft_10)
  diff_01 = np.abs(ifft_01)
  diff_11 = np.abs(ifft_11)

 if order >= 2:
  diff_20 = np.abs(ifft_20)
  diff_21 = np.abs(ifft_21)
```

```
 diff_02 = np.abs(ifft_02)
 diff_12 = np.abs(ifft_12)
 diff_22 = np.abs(ifft_22)
 phase_20 = np.angle(ifft_20)
 phase_21 = np.angle(ifft_21)
 phase_02 = np.angle(ifft_02)
 phase_12 = np.angle(ifft_12)
 phase_22 = np.angle(ifft_22)

if order >= 3:
 diff_30 = np.abs(ifft_30)
 diff_03 = np.abs(ifft_03)
 diff_33 = np.abs(ifft_33)
 phase_30 = np.angle(ifft_30)
 phase_03 = np.angle(ifft_03)
 phase_33 = np.angle(ifft_33)

if order >= 4:
 diff_40 = np.abs(ifft_40)
 diff_04 = np.abs(ifft_04)
 diff_44 = np.abs(ifft_44)
 phase_40 = np.angle(ifft_40)
 phase_04 = np.angle(ifft_04)
 phase_44 = np.angle(ifft_44)

if order >= 1:
 results = {
  "abs" : absorption,
  "phase10" : phase_10,
  "phase01" : phase_01,
  "phase11" : phase_11,
  "diffm10" : diff_m10,
  "diff10" : diff_10,
  "diff01" : diff_01,
  "diff11" : diff_11}

if order >= 2:
 results.update({
  "phase20" : phase_20,
  "phase21" : phase_21,
  "phase02" : phase_02,
  "phase12" : phase_12,
  "phase22" : phase_22,
  "diff20" : diff_20,
  "diff21" : diff_21,
  "diff02" : diff_02,
  "diff12" : diff_12,
```

```
  "diff22" : diff_22})

if order >= 3:
 results.update({
  "phase30" : phase_30,
  "phase03" : phase_03,
  "phase33" : phase_33,
  "diff30" : diff_30,
  "diff03" : diff_03,
  "diff33" : diff_33})

if order >= 4:
 results.update({
  "phase40" : phase_40,
  "phase04" : phase_04,
  "phase44" : phase_44,
  "diff40" : diff_40,
  "diff04" : diff_04,
  "diff44" : diff_44})

return results
```

B.3 Visibility

```
"""
Calculates the visibility of a set of images by calculating (Max-Min)/(Max+Min). The
    minimum and maximum filter is performed in a defined crop and with a footprint
    size suitable to the number of beamlets of the crop. A stable position of the
    beamlet pattern is assumed for all images analyzed.

definitions:
- pin: inpout folder
- pout: output folder
- crop and number of spots tabulated in external file
"""

import os
from glob import glob
import numpy as np
from tifffile import imread, imsave
import scipy.ndimage
import math
import shutil

__version__ = 'V2_2018.10.01'

#####################################################################
if __name__ == "__main__":
  pin = r'C:\Measurements\Darkfield\batchesAuNaCl'
  pout = os.path.join(pin, 'visibility')
  if not os.path.exists(pout): os.makedirs(pout)
 #import crop and nr of spots from external file
  settings = {}
  with open(os.path.join(pin,'settings.txt'), 'r') as f:
    for line in f:
      splitLine = line.split()
      settings[splitLine[0]] = splitLine[1]
  ro, co = int(settings['rowoffset']), int(settings['columnoffset'])
  nr, nc = int(settings['nrrows']), int(settings['nrcolumns'])
  spots = [int(settings['spotrows']), int(settings['spotcolumns'])]

 #search files
  files = sorted(glob(os.path.join(pin, '*radio*.tif')))
  darkpath = os.path.join(pin, '*dark*.tif')
  flatpath = sorted(glob(os.path.join(pin, '*flat*.tif')))

 #import dark image
  dark = imread(darkpath).astype(np.float32)
 #calculate visibility for all files found
```

```
 for nrfile in range(len(files)):
   pic = imread(files[nrfile]).astype(np.float32) - dark
   flat = imread(flatpath[nrfile]).astype(np.float32) - dark
   pic = pic/flat
   if (float(settings['rotangle']) != 0):
     pic = scipy.ndimage.rotate(pic, float(settings['rotangle']), reshape=False)
#size of footprint for minimum and maximum filtering
   footprintsize = math.ceil(0.5 *(nr / float(settings['fftshape']) + nc /
       float(settings['fftshape'])))

   pic_max = scipy.ndimage.maximum_filter(pic, size=footprintsize)
   pic_min = scipy.ndimage.minimum_filter(pic, size=footprintsize)
   visibility = (pic_max-pic_min)/(pic_max+pic_min)

   imsave(os.path.join(pout, "visibility_{}.tif".format(str(nrfile).zfill(5))),
       visibility[ro:ro+nr, co:co+nc].astype(np.float32))

#copy script file into pout for documentation
 shutil.copyfile(os.path.realpath(__file__), os.path.join(pout,
     os.path.basename(os.path.realpath(__file__))))
```

B.4 Decorrelation of absorption and scattering contrast

```
"""
- correlates greyvalues of two pics with each other
- can process whole run
- area of interest choosable
- shift of histogram to uncorrelate and correction of pics

pin: inpout folder, subfolders choosalbe at fileimport
pout: output folder of uncorrelated pic
"""

import os
from glob import glob
import numpy as np
from tifffile import imread, imsave
import shutil

__version__ = 'V3_2018.12.08'

#####################################################################
if __name__ == "__main__":
  pin = r'C:\Measurements\Darkfield\batchesAuNaCl'
  pout = os.path.join(pin, 'scattering01_uncorrelated', 'FFT-FFT')
  if not os.path.exists(pout): os.makedirs(pout)

  absfiles = sorted(glob(os.path.join(pin, 'FFT_analysis', 'abs', '*.tif')))
  difffiles = sorted(glob(os.path.join(pin, 'FFT_analysis', 'scattering_01',
      '*.tif')))

  ro, nr, co, nc = 0, 72, 0, 72 #crop of images to remove bad parts: row offset, nr
      of rows, column offset, nr of colums
  img_bubble = (20, 40)  #images with bubble for decorrelation

#CALCULATE CROSSCORRELATION
 #histogram before decorrelation
  histogram = np.zeros((nr*nc*(img_bubble[1] - img_bubble[0] + 1), 2),
      dtype=np.float32)
  index = 0

  for i in range(len(absfiles)):
   abspic = imread(absfiles[i]).astype(np.float32)[ro: ro+nr, co: co+nc]
   diffpic = imread(difffiles[i]).astype(np.float32)[ro: ro+nr, co: co+nc]

   #produce correlation-picture
   for j in range(abspic.shape[0]):
    for k in range(abspic.shape[1]):
```

```
    if not (np.isnan(abspic[j,k]) or np.isnan(diffpic[j,k])):
     if (i >= img_bubble[0] and i <= img_bubble[1]): #fill histogram for selcted
         frames !size of histogram!
      histogram[index,0] = abspic[j,k]
      histogram[index,1] = diffpic[j,k]
      index += 1
     else:
      if (i >= img_bubble[0] and i <= img_bubble[1]): #fill histogram for selcted
          frames !size of histogram!
       histogram = np.delete(histogram, -1, 0)

#shift of histogram to decorrelate
 m,b = np.polyfit(histogram[:,0], histogram[:,1], 1)

#histogram after decorrelation
 histogram2 = np.zeros((abspic.shape[0]*abspic.shape[1]* (img_bubble[1]-
     img_bubble[0]+ 1),2), dtype=np.float32)
 index = 0

 for i in range(len(absfiles)):
  abspic = imread(absfiles[i]).astype(np.float32)[ro: ro+nr, co:co+nc]
  diffpic = imread(difffiles[i]).astype(np.float32)[ro: ro+nr, co:co+nc]

  for j in range(diffpic.shape[0]):
   for k in range(diffpic.shape[1]):
    if not (np.isnan(abspic[j,k]) or np.isnan(diffpic[j,k])):
     diffpic[j,k] -= abspic[j,k]*m + b
     if (i >= img_bubble[0] and i <= img_bubble[1]):
      histogram2[index,0] = abspic[j,k]
      histogram2[index,1] = diffpic[j,k]
      index += 1
     else:
      diffpic[j,k] = np.nan
      if i >= img_bubble[0] and i <= img_bubble[1]: #fill histogram for selcted
          frames !size of histogram!
       histogram2 = np.delete(histogram2, -1, 0)

  imsave(os.path.join(pout, 'frame_{}.tif'.format(str(i).zfill(3))), diffpic)

#copy script file into pout for documentation
 shutil.copyfile(os.path.realpath(__file__), os.path.join(pout,
     os.path.basename(os.path.realpath(__file__))))
```

B.5 Modified Southwell-algorithm for phase reconstruction

```
"""
MODIFIED SOUTHWELL-ALGORITHM FOR PHASE RECONSTRUCTION
see [Pathak, Baruah, 2014, Journal of Optics, doi:10.1088/2040-8978/16/5/055403]

Input:
 - image of differential phase in x direction
 - image of differential phase in y direction
 - number of iterations to perform
 - scaling factor h, only important for absolute values

Output:
 - phase image
"""
import numpy as np
import sys

__version__ = 'V3_2017.03.21'

#################################################################################
def mSPR(diffphase_x, diffphase_y, nriteration, h):
  if (diffphase_x.shape!=diffphase_y.shape):
   sys.exit("shape of diffphases is different")
  else:
   spots = diffphase_x.shape
   phase = np.zeros((spots[0], spots[1]), dtype=np.float32)
   slope = np.zeros_like(phase)

 #calculate slopes
  for i in range(spots[0]):
   for j in range(spots[1]):
 #interior
    if ((i>0 and i<spots[0]-1) and (j>0 and j<spots[1]-1)):
     slope[i,j] = h/(2*8.) *(diffphase_x[i-1,j-1] + diffphase_y[i-1,j-1] +
         diffphase_x[i,j-1] + diffphase_x[i+1,j-1] - diffphase_y[i+1,j-1] -
         diffphase_y[i+1,j] - diffphase_x[i+1,j+1] - diffphase_y[i+1,j+1] -
         diffphase_x[i,j+1] - diffphase_x[i-1,j+1] + diffphase_y[i-1,j+1] +
         diffphase_y[i-1,j])
 #walls without edges
    elif (i==0 and (j>0 and j<spots[1]-1)): #top
     slope[i,j] = h/(2*5.) *(-diffphase_x[i,j+1] + diffphase_x[i,j-1] -
         diffphase_y[i+1,j] - diffphase_x[i+1,j+1] - diffphase_y[i+1,j+1] +
         diffphase_x[i+1,j-1] - diffphase_y[i+1,j-1])
    elif ((i>0 and i<spots[0]-1) and j==0): #left
```

```
    slope[i,j] = h/(2*5.) *(-diffphase_x[i,j+1] - diffphase_y[i+1,j] +
        diffphase_y[i-1,j] - diffphase_x[i+1,j+1] - diffphase_y[i+1,j+1] -
        diffphase_x[i-1,j+1] + diffphase_y[i-1,j+1])
   elif (i==spots[0]-1 and (j>0 and j<spots[1]-1)): #bottom
    slope[i,j] = h/(2*5.) *(-diffphase_x[i,j+1] + diffphase_x[i,j-1] +
        diffphase_y[i-1,j] + diffphase_x[i-1,j-1] + diffphase_y[i-1,j-1] -
        diffphase_x[i-1,j+1] + diffphase_y[i-1,j+1])
   elif ((i>0 and i<spots[0]-1) and j==spots[1]-1): #right
    slope[i,j] = h/(2*5.) *(diffphase_x[i,j-1] - diffphase_y[i+1,j] +
        diffphase_y[i-1,j] + diffphase_x[i-1,j-1] + diffphase_y[i-1,j-1] +
        diffphase_x[i+1,j-1] - diffphase_y[i+1,j-1])
#edges
   elif (i==0 and j==0):  #left top
    slope[i,j] = h/(2*3.) *(-diffphase_x[i,j+1] - diffphase_y[i+1,j] -
        diffphase_x[i+1,j+1] - diffphase_y[i+1,j+1])
   elif (i==0 and j==spots[1]-1): #rigth top
    slope[i,j] = h/(2*3.) *(diffphase_x[i,j-1] - diffphase_y[i+1,j] +
        diffphase_x[i+1,j-1] - diffphase_y[i+1,j-1])
   elif (i==spots[0]-1 and j==0): #left bottom
    slope[i,j] = h/(2*3.) *(-diffphase_x[i,j+1] + diffphase_y[i-1,j] -
        diffphase_x[i-1,j+1] + diffphase_y[i-1,j+1])
   elif (i==spots[0]-1 and j==spots[1]-1): #right bottom
    slope[i,j] = h/(2*3.) *(diffphase_x[i,j-1] + diffphase_y[i-1,j] +
        diffphase_x[i-1,j-1] + diffphase_y[i-1,j-1])

#reconstruct
 for k in range(nriteration):
  tempphase = np.zeros_like(phase)
  for i in range(spots[0]):
   for j in range(spots[1]):
#interior
    if ((i>0 and i<spots[0]-1) and (j>0 and j<spots[1]-1)):
     tempphase[i,j] = (1/8. * (phase[i,j+1] + phase[i,j-1] + phase[i-1,j] +
         phase[i+1,j] + phase[i+1,j+1] + phase[i-1,j+1] + phase[i-1,j-1] +
         phase[i+1,j-1]) + slope[i,j])
#walls without edges
    elif (i==0 and (j>0 and j<spots[1]-1)): #top
     tempphase[i,j] = (1/5. * (phase[i,j+1] + phase[i,j-1] + phase[i+1,j] +
         phase[i+1,j+1] + phase[i+1,j-1]) + slope[i,j])
    elif ((i>0 and i<spots[0]-1) and j==0): #left
     tempphase[i,j] = (1/5. * (phase[i,j+1] + phase[i-1,j] + phase[i+1,j] +
         phase[i+1,j+1] + phase[i-1,j+1]) + slope[i,j])
    elif (i==spots[0]-1 and (j>0 and j<spots[1]-1)): #bottom
     tempphase[i,j] = (1/5. * (phase[i,j+1] + phase[i,j-1] + phase[i-1,j] +
         phase[i-1,j+1] + phase[i-1,j-1]) + slope[i,j])
    elif ((i>0 and i<spots[0]-1) and j==spots[1]-1): #right
```

```
     tempphase[i,j] = (1/5. * (phase[i,j-1] + phase[i-1,j] + phase[i+1,j] +
         phase[i-1,j-1] + phase[i+1,j-1]) + slope[i,j])
 #edges
    elif (i==0 and j==0):  #left top
     tempphase[i,j] = (1/3. * (phase[i,j+1] + phase[i+1,j] + phase[i+1,j+1]) +
         slope[i,j])
    elif (i==0 and j==spots[1]-1): #rigth top
     tempphase[i,j] = (1/3. * (phase[i,j-1] + phase[i+1,j] + phase[i+1,j-1]) +
         slope[i,j])
    elif (i==spots[0]-1 and j==0): #left bottom
     tempphase[i,j] = (1/3. * (phase[i,j+1] + phase[i-1,j] + phase[i-1,j+1]) +
         slope[i,j])
    elif (i==spots[0]-1 and j==spots[1]-1): #right bottom
     tempphase[i,j] = (1/3. * (phase[i,j-1] + phase[i-1,j] + phase[i-1,j-1]) +
         slope[i,j])

  phase = tempphase
 return phase
```

List of Figures

2.1 Main processes occurring during Pulsed Laser Ablation in Liquids with a nanosecond laser. 6
2.2 Phase diagram of the ablation process. 9
2.3 Typical bubble dynamics during PLAL on flat targets. 11
2.4 Dynamic of the cavitation bubble after laser ablation. 12
2.5 Typical bubble dynamics during PLAL on a free wire targets. 13
2.6 Appearance of nanoparticles and persistent bubbles after cavitation bubble collapse. . . . 14
2.7 Schematic drawing of the material disintegration for short laser pulses. 15
2.8 Illustration of nanoparticle distribution inside the cavitation bubble after laser ablation. . 17
2.9 Images showing bubble shielding due do a high laser repetition rate. 18
2.10 Reduced cavitation bubble size due to nanoparticle shielding. 19
2.11 Influence of the target position on the cavitation bubble volume and the ablation rate. . . 20

3.1 Illustration of wide- and small-angle scattering methods. 25
3.2 Scattering distribution of a solid sphere. 26
3.3 Scattering intensity of three spheres of different size. 27
3.4 Bragg's law of diffraction. 28
3.5 Optical elements used in X-ray multi-contrast imaging techniques. 30
3.6 Single-Exposure Multi-Contrast Imaging principle. 33
3.7 Scattering vector resolution of SEMCI and SAXS. 36
3.8 Comparison of normalized scattering sensitivities reported in literatur. 36
3.9 Evaluation of scattering intensities fitting to the DFEC. 38
3.10 The Dark-field extinction coefficient. 38
3.11 Schematic drawing of the multi-contrast imaging parameters. 39
3.12 Scattering intensity of a single nanoparticle. 40
3.13 Improving the sensitivity of the SEMCI by scanning the auto-correlation length. 41
3.14 Illustration of interchangeable setups for phase contrast imaging. 42
3.15 A parabolic focusing X-ray lens. 43
3.16 Schematic drawing of a 2D lens array. 45
3.17 Bending magnet spectra before and after filtering. 46

4.1 Ablation chamber designs. 51
4.2 Setup of scattering measurement with a CARL. 53
4.3 Acquisition control chain for multi-contrast imaging at a synchrotron. 53
4.4 Shift of the DFEC due to white beam illumination and beam weakening in the cavitation bubble. 54

4.5 Decorrelation of transmission and scattering signal from multi-contrast imaging. 60
4.6 Reconstructed phase of an air bubble for both Gaussian fitting and Fourier analysis. . . . 62
4.7 GUI of the SH-WaveRecon software 63
4.8 Simulated 2D Gaussian beamlet pattern for scattering contrast imaging. 64
4.9 Reconstructed beamlet parameters by varying the beamlet Gaussian width. 65
4.10 Change of Gaussian fitting results due to strong transmission increase. 66
4.11 Influence of the bubble curvature on the reconstructed beamlet width. 67
4.12 Improvements in the beamlet width analysis due to a pre-analysis pedestal correction. . . 68
4.13 Evaluation of pre-analysis pedestal correction with measured data. 69
4.14 Scattering sensitivity calculated from simulated scattering data by with four different algorithms. 70
4.15 Simulated scattering sensitivity for different orders of Fourier analysis. 71
4.16 Comparison of the multi-contrast retrieval with FFT-analysis, Gaussian fitting, image moment and visibility analysis. 73
4.17 Differential phase of simulated and measured empty air bubble obtained by different algorithms. 74
4.18 Scattering intensity of simulated and measured empty air bubble obtained by different algorithms. 75
4.19 Comparison of the resulting scattering images obtained with Fourier and image moment analysis. 76
4.20 Temporal evolution of the raw scattering intensity after laser ablation retrieved with Fourier and moment analysis. 77

5.1 Fabrication of a CARL. 81
5.2 Setup for serial embossing a 2D lens array and images of the used stamping needles. . . 82
5.3 Micrograph of one 2D lens array after spiral embossing. 84
5.4 Regularity of a sewing needle embossed lens array. 85
5.5 Regularity of a custom-made needle embossed lens array. 86
5.6 Examples of lens arrays with arbitrary patterns. 86
5.7 Embossing depth dependence on lens performance. 87
5.8 Ideal shape of a CARL. 88
5.9 Images of the 2D needle arrays as stamps for lens array embossing. 88
5.10 Regularity of a single-step embossed lens array. 90
5.11 Changes in spot shape due to lens rotation out of the paraxial illumination. 91
5.12 Radiogram of a CARL with six stacked foils of serially embossed lens arrays. 92
5.13 Focus position of a CARL with six stacked foils of serially embossed lens arrays. 93
5.14 Regularity of a CARL with six stacked foils of serially embossed lens arrays. 94
5.15 Radiogram of a CARL with five stacked foils of single-step embossed lens arrays. 95
5.16 Focus position of a CARL with five stacked foils of single-step embossed lens arrays. . . 96
5.17 Regularity of a CARL with five stacked foils of single-step embossed lens arrays. 97

6.1 Cavitation bubble dynamics with overlaid figurative nanoparticle and microbubble distribution. . . . 99
6.2 Schematic drawing of the plasma fluence threshold and incubation effect. . . . 101
6.3 Fluence threshold for bubble size and ablation yield. . . . 102
6.4 Bubble size dependence on fluence for fresh and corrugated target. . . . 103
6.5 Increasing bubble size and plasma intensity with number of applied shots due to the incubation effect. . . . 104
6.6 Maximum bubble size with a decreasing incubation effect for increasing pulse energies. . 104
6.7 Scanning electron microscope images showing increasing target corrugation during continuous laser ablation. . . . 105
6.8 Scattering curves and NP histograms of SAXS measurements at laser ablation of a gold target showing an incubation effect. . . . 106
6.9 Schematic drawing of the cavitation bubble dynamics and nanoparticle distribution during X-ray scattering. . . . 108
6.10 Temporal evolution of the ablated nanoparticle mass during the cavitation bubble lifetime. 108
6.11 Temporal evolution of the crystalline mass and crystalline domain size for ablation of gold. 110
6.12 Temporal evolution of the mass of primary and secondary nanoparticles. . . . 111
6.13 Sketch of the Single-Exposure Multi-Contrast Imaging technique with illustration of the two observed results. . . . 112
6.14 Scattering imaging of *in situ* size quenching of gold NPs by NaCl. . . . 113
6.15 Sensitivity for scattering imaging on free wire target and image of the used CARL. . . . 114
6.16 Scattering imaging intensity evolution allowing a differentiation between nanoparticles and micrometer-sized bubbles after laser ablation. . . . 115

List of Tables

4.1 Lasers used in this work together with the used parameters. 50
4.2 Basic parameters and their range used in the simulation of the scattering imaging. 64
4.3 Gaussian parameters of two beamlets, one outside and one inside a transmission increasing bubble. 66
4.4 Conclusion on the comparison of the four contrast reconstruction algorithms for multi-contrast imaging. 79

List of Equations

2.1: Beer-Lambert law . . . 7

3.1: Total scattering length of an atom . . . 23
3.2: Linear attenuation coefficient . . . 24
3.3: Index of refraction in the X-ray regime . . . 24
3.4: Decrement of the index of refraction . . . 24
3.6: Intensity of scattering . . . 25
3.7: Intensity of scattering of a single particle . . . 26
3.8: Form factor of a solid suqere . . . 26
3.9: Guinier approximation of the scattering intensity . . . 26
3.10: Porod approximation of the scattering intensity . . . 26
3.11: Beaucage equation of Unified fit . . . 27
3.12: Bragg's law of diffraction . . . 28
3.13: Scherrer equation . . . 28
3.14: Absorption intensity . . . 28
3.15: Auto-Correlation length of scattering imaging . . . 35
3.16: Dark-field ectinction coefficient . . . 37
3.17: Maximum of the dark field extinction coefficient . . . 38
3.18: Auto-Correlation lenght in simplified version . . . 38
3.20: Scattering vector . . . 39
3.23: Angle of refraction . . . 43
3.24: Focal length of biconcave lenses . . . 43
3.25: Critical energy of a bending magnet . . . 45
3.26: Brilliance of an X-ray beam . . . 47

4.2: Visibility from beamlet zone values . . . 57
4.3: Visibility from Gaussian fitting values . . . 57
4.4: 2D Gaussian distribution . . . 58
4.5: Transmission contrast from Gaussian fitting . . . 58
4.6: Differential phase contrast from Gaussian fitting . . . 58
4.7: Scattering contrast from Gaussian fitting . . . 58
4.8: Transmission contrast from Fourier reconstruction . . . 59
4.9: Scattering contrast from Fourier reconstruction . . . 60
4.10: Differential phase contrast from Fourier reconstruction . . . 60

5.1: Parabola of X-ray lens 85

List of abbreviations

Abbreviations

ACL	Auto-Correlation Length
CARL	Compound Array Refractive Lens
CRL	Compound Refractive Lens
DFEC	Dark-Field Extinction Coefficient
ESRF	European Synchrotron Radiation Facility
FFT	Fast Fourier Transformation
GI	Grating Interferometry
KIT	Karlsruhe Institute of Technology
NP	Nanoparticle
PLAL	Pulsed Laser Ablation in Liquids
SEMCI	Single-Exposure Multi-Contrast Imaging
SAXS	Small-angle X-ray Scattering
SD	Standard Deviation
SLS	Swiss Light Source
TTL	Transistor-Transistor Logic
WAXS	Wide-angle X-ray Scattering

Chemicals

Al	aluminum
Ag	silver
Au	gold
Be	beryllium
H_2O	water

NaCl	sodium chloride
PMMA	poly(methyl methacrylate)
PVP	polyvinylpyrrolidone
Zn	zinc
ZnO	zinc oxide

Symbols

D	diameter
f	focal length
L	sample-to-detector distance
p	pitch of the optical element
q	scattering vector
r	radius
n	index of refraction
Z	atomic number
β	imaginary part of the index of refraction
δ	decrement of the index of refraction
λ	wavelength
μ	linear absorption coefficient
μ_ξ	dark-field extinction coefficient
ξ	auto-correlation length

Acknowledgments

This work would have never been possible without the help of a lot of people. Technical and scientific support are very important for the success of a dissertation. But friends and family are also an essential support, especially when your work demands a lot from you.

Thanks a lot to . . .

. . . my doctoral supervisor **Prof. Dr. Tilo Baumbach** for giving me the opportunity to do my PhD in your institute.

. . . my second supervisor **PD Dr. habil. Plech** for giving me the chance to my PhD in the field of synchrotron science. It was a great experience to enter this field of science with your immense knowledge. The long days and nights during the eleven beam times were demanding, but a great experience that I would not want to miss. Thank you for all the inspiring discussions and direct support at all times. I hope your beam time shirt survives until you retire.

. . . **Prof Dr. Stephan Barcikowski** for the stimulating discussions at conferences and meetings of our cooperation. It is always good to have someone form an other discipline in the team.

. . . **Alexander Letzel**, my co-PhD student in the cooperation. The beam times together were a great time. The combined knowledge of chemistry and physics is fruitful for overcoming challenges. Be careful when the bubblenado comes.

. . . **Tomy dos Santos Rolo** for your numerous ideas for experiments and improvements. Unfortunately the time together at the IPS was so short. I hope for you, you will manage to graduate.

. . . all the **colleges at the IPS**. Special thanks to the people at the beamlines: Macrus Zuber, David Haas, Stefan Uhlemann, Thorsten Müller and Jörg Göttlicher. Without your support the experiments would have failed.

. . . the **beamline staff** at the ESRF and PSI, namely: Alexander Rack, Margie P. Olbinado, Michael Wulff, Matteo Levantino, Norman Kretzschmar, Sakura Pascarelli, Olivier Mathon and Andreas Menzel. You are doing a great job solving the challenges of the experiments every week.

. . . **Daniel Gauder** at the IBG-2 for producing the tiny needle.

. . . **Sergei Gasilov** for provision of the diamond lens.

. . . **Alexander Kanitz and Jan Hoppius** at the Ruhr Universität Bochum for producing the Hartmann mask.

. . . **μicroworks** for the production of the 2D needle arrays by electroplating.

. . . **René Streubel** and **Anna Ziefuß** for the nice beam times at the ESRF.

. . . **Danays Kunka, Margarita Zakharova and Andrey Mikhaylov** for the straightforward good work together and the provision of Hartmann masks and SHARXs when our CARLs did not work. I think it was an enriching cooperation for both sides even without an official collaboration.

... the **IBPT** for running the synchrotron ANKA, now called KARA, at KIT.

... the **ESRF** and the **PSI** for provision of beam times.

... the **LEM** for making the HR-TEM images of our nanoparticles.

... the **DFG** and the **Helmholtz programme MML** for the financial support.

... **all my friends** in the DLRG and at the Physikerstammtisch. After days of hard work you all showed me what else is important in life. Special thanks to **Georg** for reading my complete thesis and all your good comments.

... **my family** for the support throughout all the years.

... **Vanessa**, my girlfriend, not only for also reading my complete thesis but much more for standing by me also in the hard times.

Thanks to all of you!